

# Nano-Fluidic Coupled Membrane Devices for Confinement of Single Extra Cellular Vesicles

Seyed Imman Isaac Hosseini, Bioengineering Department

McGill University, Montreal

August, 2023

A thesis submitted to McGill University in partial fulfillment of the  
requirements of the degree of

Doctor of Philosophy in Biological and Biomedical Engineering

©Seyed Imman Isaac Hosseini

# Abstract

Extracellular Vesicles (EVs) are spherical nano-bio-particles that cells continuously secrete. The secreted EVs can migrate and be absorbed by other cells, affecting the biochemistry of the recipient cells. Considering the heterogeneity of cells in a tissue, and the fact that a single cell can secrete EVs with different contents, the population of EVs in body fluids is highly heterogeneous. This extensive heterogeneity motivates the development of technologies that can analyze the contents of single EVs.

This thesis proposes a membrane-interfaced nanofluidic device for confinement and analysis of a single EVs. The membrane serves as a bonding lid sealing off a nanoslit with embedded cavity bioreactors. The membrane can be deflected via the application of pneumatic pressure during an experiment; this reduces the height of the nanoslit, tending to confine EVs in the bioreactor structures.

The average time required for a confined particle to leave the confinement status depends on the surface charge of the particle as well as the slit height controlled via membrane actuation. Therefore, the surface charge of particles which is related to their surface chemistry can be estimated by measuring the average time that the particle takes to leave the confinement status. We isolated and confined EVs secreted from brain-cell lines. We used the nanofluidic device to measure the EVs' surface charge. We observed that the average surface charge of the EVs secreted from a Glioblastoma astrocytoma (U<sub>373</sub> a type of brain cancer) cell line is less than the surface charge secreted from a Normal Human Astrocytoma (NHA) cell line.

After confirming the possibility of EVs confinement, we modified the nanofluidic device to include the possibility of adding detection reagents inside the bioreactors while the target molecule is fully-confined. We added extra microchannels to load detection reagents. A set of parallel nanochannels was implemented adjacent to the nanocavities which were connected to the reagent loading channels outside the membrane area. This modification lets us bring the detection reagents very close to the nanocavities while the membrane is fully actuated. By creating a gap of several nanometers slit height using our flexible membrane, detection reagents that are smaller than the target molecules can diffuse inside the nanocavities while the target molecules are fully confined. After concentrating NAs molecules in the nanocavities array, the confined NAs are amplified using Loop-mediated isothermal Amplification and Rolling Circle Amplification methods.

# Abrégé

Les vésicules extracellulaires (VE) sont des nano-bio-particules sphériques que les cellules sécrètent en continu. Les VE sécrétés peuvent migrer et être absorbés par d'autres cellules, affectant la biochimie des cellules réceptrices. Compte tenu de l'hétérogénéité des cellules dans un tissu et du fait qu'une seule cellule peut sécréter des VE avec des contenus différents, la population de VE dans les fluides corporels est très hétérogène. Cette grande hétérogénéité motive le développement de technologies capables d'analyser le contenu d'un seul VE.

Cette thèse propose un dispositif nanofluidique à interface membranaire pour le confinement et l'analyse d'un seul VE. La membrane sert de couvercle de liaison scellant une nanofente avec des bioréacteurs à cavité intégrés. La membrane peut être déviée via l'application d'une pression pneumatique au cours d'une expérience ; cela réduit la hauteur de la nanofente, tendant à confiner les VE dans les structures du bioréacteur.

Le temps moyen nécessaire pour qu'une particule confinée quitte l'état de confinement dépend de la charge de surface de la particule ainsi que de la hauteur de fente contrôlée via l'actionnement de la membrane. Par conséquent, la charge de surface des particules qui est liée à leur chimie de surface peut être estimée en mesurant le temps moyen que la particule met pour quitter l'état de confinement. Nous avons isolé et confiné les VEs sécrétés par les lignées de cellules cérébrales. Nous avons utilisé le dispositif nanofluidique pour mesurer la charge de surface des VE. Nous avons observé que la charge de surface moyenne des VE sécrétés par une lignée cellulaire d'astrocytome de



glioblastome (U<sub>373</sub> un type de cancer du cerveau) est inférieure à la charge de surface sécrétée par une lignée cellulaire d'astrocytome humain normal (NHA).

Après avoir confirmé la possibilité d'un confinement des VEs, nous avons modifié le dispositif nanofluidique pour inclure la possibilité d'ajouter des réactifs de détection à l'intérieur des bioréacteurs pendant que la molécule cible est entièrement confinée. Nous avons ajouté des microcanaux supplémentaires pour charger les réactifs de détection. Un ensemble de nanocanaux parallèles a été mis en œuvre à côté des nano-cavités qui étaient connectées aux canaux de chargement de réactif à l'extérieur de la zone membranaire. Cette modification permet d'amener les réactifs de détection très près des nano-cavités alors que la membrane est pleinement actionnée. En créant un espace de plusieurs nanomètres de hauteur de fente à l'aide de notre membrane flexible, les réactifs de détection plus petits que les molécules cibles peuvent diffuser à l'intérieur des nano-cavités tandis que les molécules cibles sont entièrement confinées. Après avoir concentré les molécules d'AN dans le réseau de nano-cavités, les AN confinés sont amplifiés à l'aide des méthodes Loop-mediated Isothermal Amplification (LAMP) et Rolling Circle Amplification (RCA).

# Acknowledgements

Ph.D. at McGill University has been an extremely instructive period of my life. I would like to thank my supervisors, Dr. Sara Mahshid and Dr. Walter Reisner. Dr. Mahshid with her hard work, enthusiasm for bringing science to technology, and great team management has promoted me to catch the goals of my Ph.D. project in the most effective and reliable ways. I want to give my special thanks to my great co-supervisor Dr. Walter Reisner. I found Prof. Reisner as one of the most intelligent and knowledgeable people I have ever seen. His insightful comments on my project have been very problem-solving, and without his comments, this fast progress in my project was not possible. I will definitely be thankful to Dr. Walter Reisner for whole my life. I am happy that I had the chance to be in touch with Prof. Janusz Rak at the Research Institute of the McGill University Health Centre, for the biological aspects of my research. Despite he is very busy with many projects, he passionately and diligently answered my raised questions. And, I am also grateful to Laura Montermini for her helping and teaching me to prepare the required biological samples for my experiments. I thank all my doctoral committee members, Dr. Adam Hendricks, Dr. Milica Popovic, and Dr. Christine Lucas Tardif who spared their precious time for my dissertation and improved my research with their informative comments.

I am fortunate that I had the chance to work with many intelligent and hard worker researchers. First, I would like to thank Xavier Capaldi, a member of Dr. Reisner's group, who as an artist in nanofabrication, helped me with the fabrication procedure in clean-room. I would like to thank my labmate, Zezhou Liu, for being supportive and discussing

different aspects of our experiments around the clock. I want to give special thanks to my friend and advisor Seyed Vahid Hamidi, a postdoc student in Dr. Mahshid's lab, for his unstinting help in biological experiments. To all my labmates in Dr. Reisner and Dr. Mahshid's labs, Lili, Matheus, Roozbeh, Hamed, Arash, Mahsa, Tamer, Sripadh, Carolina, for providing a friendly and relaxed atmosphere for research.

I thank all staff of LMN at INRS, Nanotools at McGill, LMF at polytechnique de mon-treal, especially Boris Le Drogoff, Dr. Zhao Lu, and Marie-Hélène Bernier who patiently trained me to work in the cleanrooms.

# Contribution to original knowledge

The thesis proposes a membrane-interfaced nanofluidic device for the confinement and analysis of single EVs to address the heterogeneity. The device consists of a membrane that acts as a sealing lid, enclosing a nanoslit with embedded cavity bioreactors in real-time. By applying pneumatic pressure, the membrane can be deflected, reducing the height of the nanoslit and confining EVs within the bioreactor structures.

The nanofluidic device is used to measure surface charge of EVs by evaluating the time they take to leave the confinement status. By measuring this time, the surface charge, related to their surface chemistry, can be estimated. The thesis demonstrates the isolation and confinement of EVs secreted by brain-cell lines and measures their surface charge using the nanofluidic device. The findings reveal that EVs secreted from a Glioblastoma astrocytoma (a type of brain cancer) cell line exhibit a lower surface charge compared to EVs secreted from a Normal Human Astrocytoma (NHA) cell line.

Building upon this, the nanofluidic device is further modified to enable the addition of detection reagents inside the bioreactors while the target molecule remains fully confined. Additional microchannels are included to load detection reagents, and parallel nanochannels connected to the reagent loading channels allow close proximity to the nanocavities within the fully actuated membrane. By creating a narrow gap, smaller detection reagents can diffuse into the nanocavities while the target molecules remain

confined. The confined nucleic acid molecules are then amplified using Loop-mediated isothermal Amplification and Rolling Circle Amplification methods.

In summary, this thesis presents a novel nanofluidic device that utilizes a membrane-interfaced system to confine and analyze single EVs. It demonstrates the measurement of EVs' surface charge and introduces modifications that enable the addition of detection reagents for further analysis and amplification of confined molecules.

# Table of Contents

Abstract . . . . .	i
Abrégé . . . . .	iv
Acknowledgements . . . . .	v
Contribution to original knowledge . . . . .	vii
List of Figures . . . . .	xxiii
List of Tables . . . . .	xxiv
<b>1 Introduction</b>	<b>4</b>
1.1 Motivation . . . . .	4
1.2 Thesis objectives . . . . .	12
Connection between Chapter 1 and 2 . . . . .	16
<b>2 Single Extracellular Vesicles</b>	<b>17</b>
2.1 Extracellular Vesicles . . . . .	17
2.2 Molecular Cargo of EVs . . . . .	19
2.3 EVs Biogenesis . . . . .	22
2.4 General definitions for EVs analysis . . . . .	26
2.5 Why there is a need for high throughput multi-dimensional analysis of single EVs . . . . .	30
2.6 Characteristics of ideal single EV analysis approach . . . . .	36
2.7 Current single EVs analysis methods . . . . .	43
Connection between Chapter 2 and 3 . . . . .	51

<b>3</b>	<b>Background</b>	<b>52</b>
3.1	Nanoparticle Confinement in Electrostatic Energy Wells . . . . .	52
3.2	Brownian motion of nanoparticles . . . . .	58
3.3	Pneumatic nanofluidic devices . . . . .	64
3.4	Experimental Steps . . . . .	65
3.4.1	Nanofluidic fabrication . . . . .	65
3.4.2	3D printed chuck: . . . . .	68
3.4.3	Nucleic Acid Amplification . . . . .	71
3.4.4	Extracellular Vesicles Isolation . . . . .	73
	Connection between Chapter 3 and 4 . . . . .	74
<b>4</b>	<b>Nanofluidics for Simultaneous Size and Charge Profiling of Extracellular Vesicles</b>	<b>75</b>
4.1	Abstract . . . . .	75
4.2	Introduction . . . . .	76
4.3	Material and Methods . . . . .	80
4.4	Results and Discussion . . . . .	82
4.5	Conclusion . . . . .	90
4.6	Supplementary Information . . . . .	90
4.6.1	Device Fabrication and Operation . . . . .	90
4.6.2	Slit Height Calibration . . . . .	91
4.6.3	Measurement of Solution Ionic Concentration . . . . .	92
4.6.4	Calculation of Particle Escape Time . . . . .	93
4.6.5	Solution for Electrostatic Potential . . . . .	96
4.6.6	Determining Zeta-Potential of Device Surfaces . . . . .	97
4.6.7	Effect of hydrodynamic coupling between particle and device surfaces	98
4.6.8	Relationship Between Zeta Potential and Charge . . . . .	99
4.6.9	Automation . . . . .	99
4.6.10	Preparation of Extracellular Vesicles . . . . .	100

4.6.11	Data Table for Vesicle Measurements . . . . .	101
4.6.12	Discussion of Technology Scaling . . . . .	101
4.6.13	Supporting Movie . . . . .	103
	Connection between Chapter 4 and 5 . . . . .	105
<b>5</b>	<b>Tunable nanofluidic device for digital nucleic acid analysis</b>	<b>106</b>
5.1	Abstract . . . . .	106
5.2	Introduction . . . . .	107
5.3	Experimental . . . . .	110
5.3.1	Device design . . . . .	110
5.3.2	Device operation . . . . .	112
5.3.3	Nucleic Acid Concentration in Nanocavities . . . . .	114
5.4	Result and Discussion . . . . .	115
5.4.1	DNA in-cavity retention during buffer exchange . . . . .	115
5.4.2	Nanoparticle Retention in Nanocavities . . . . .	117
5.4.3	DNA retention in nanocavities . . . . .	119
5.4.4	Amplification Results . . . . .	120
5.5	Conclusions . . . . .	125
5.6	Author Contributions . . . . .	126
5.7	Conflicts of interest . . . . .	126
5.8	Acknowledgements . . . . .	127
5.9	Supporting Information . . . . .	127
5.9.1	Device Fabrication and Operation . . . . .	127
5.9.2	Temperature Controller . . . . .	128
5.9.3	Slit Height Calibration . . . . .	129
5.9.4	Flow Measurement . . . . .	130
5.9.5	Gel electrophoresis and Real-Time PCR . . . . .	132
5.9.6	Particle size measurement . . . . .	133
5.9.7	Primer Design . . . . .	133



5.9.8	Point-spread function . . . . .	135
5.9.9	Supporting Movie . . . . .	135
<b>6</b>	<b>Discussion and Conclusion</b>	<b>137</b>
6.1	Discussion . . . . .	137
6.2	Future Work . . . . .	142

# List of Figures

1.1	Tumor Heterogeneity a) Cancer heterogeneity arises at two levels: inter-tumor heterogeneity and intra-tumor heterogeneity b) The heterogeneity is rooted in genomic or epigenomic reasons. c) As well as spatial changes, a tumor can be evolved over time. . . . .	6
1.2	Extracellular vesicles (EVs) are interesting biomarkers since: 1- EVs preserve their cargoes from degradation; 2- a large number of EVs can be found in a body fluid; 3- EVs are involved in different physiological activities of cells; 4- a single EV simultaneously carry different biomarkers including proteins, nucleic acids, and lipids; 5- EVs are continuously generated by the different cell types. . . . .	8
1.3	EVs are interesting in cancer detection studies since: 1) EVs influence the immune system responsible directly or by modulating fibroblast cells or tumor-associated macrophages (TAM); 2) EVs participate in angiogenesis to provide more nutrition for tumors; 3- EVs promotes metastasis by extracellular matrix degradation, increasing vascular permeability, creating premetastatic niches, or activating macrophages RNA. . . . .	15
2.1	Molecular cargo encapsulated inside EVs. . . . .	22

2.2	a) EVs biogenesis. EVs can be formed through Intra-Luminal Vesicles (ILVs) pathway which has three main steps: Step 1- Endocytosis; Step 2- MVB formation; Step 3- EVs release. EVs can be also formed through direct budding out from cells plasma membrane. b) (ESCRT) machinery is one of the main pathways for MBVs formation which has four main steps. In each step, one of the ESCRT components including ESCRT-0, ESCRT-I, ESCRT-II, and ESCRT-III attaches to the ESCRT complex. . . . .	25
2.3	EV isolation methods. Three main standard methods exist including a) Ultracentrifugation, b) size exclusion chromatography, and c) ultrafiltration. Also, some microfluidic-base methods are . . . . .	28
2.4	EV focused studies: the EVs studies methods can be divided into a) Studies of fundamental EV biology b) developing new detection technologies and c) harnessing EVs for drug delivery. The detection technologies can be sub-categorized into d) Isolation and e) developing new technologies. The new technologies proposed for EVs can be divided into two main categories: g) fingerprint methods based on different properties such as stiffness, Raman spectra, and surface charge, and h) molecular detection methods such as antibody-based protein identification, and RNA sequencing. . . . .	29
2.5	Single EV analysis enhances the potential use of EV-derived biomarkers for cancer diagnosis and monitoring. These capabilities can be obtained by high-throughput and multiplexed detection. . . . .	35
2.6	An ideal single EV analysis approach should be able to confine and isolate individual EVs, detect EVs molecular cargo, perform high-throughout analysis, perform multi-omic analysis, detect EVs and EV encapsulated biomarkers with high sensitivity and specificity, and work with a low amount of sample. Also, industrial scalability, automatic operation with minimum labor input and reasonable cost are desirable. . . . .	36

2.7	Cancer cells secrete EVs at a higher rate than normal cells. However, a portion of EVs released by cancer cells carry detectable cancerous markers.	41
2.8	Current Single EVs analysis methods. a) Droplet generation method for EVs digitization [125] b) Increasing the sensitivity of flow cytometry [198] c) Single-molecule analysis method for EV isolation in microwells. (SiMoA) [252] d) EV surface immobilization [117] e) Surface-enhanced Raman spectroscopy [259]. . . . .	43
3.1	Finite element calculation of an electrical potential distribution at the interface of a charged surface with an ionic solution obtained by solving the Poisson-Boltzmann equation. a) Color map of electrical potential normalized to the electrical potential at the surface. b) Electrical potential versus distance away from surface. . . . .	55
3.2	Electrical potential between two parallel like-charged plates. a) Colormap corresponding to the electrical potential of two plates at a 40nm separation. b) The electrical potential normalized to surface potential plotted along the vertical axis from the lower plate. . . . .	56
3.3	the electrical potential between two like-charged plates as a function of gap height. a) colormap of the electrical potential at I) 80 and II) 40 nm slit heights. b) The minimum electrical potential normalized to surface potential versus different slit height values. . . . .	57
3.4	local minimum energy induced by creating nanocavities embedded in the slit. a) colormap of minimum energy b) minimum energy along the cavity radius. In this simulation, the depth of the cavity is 100 nm, and the gap is 50 nm. . . . .	58

3.5	The electrical potential between two like-charged parallel plates with embedded nanocavities with different gap heights. a) Colormap of electrical potential for plates with I) 40 and II) 80 nm gap and b) minimum electric potential versus radial coordinate from the center of cavities for the two gap heights. . . . .	59
3.6	Electrical potential inside and outside of the cavity and the depth of potential well induced by the cavity. . . . .	60
3.7	Pneumatically actuated micro/nanofluidic devices. a) PDMS based device for adjusting the height of a channel via pneumatic pressure [230] b) The device called dimple machine which has trapping and refreshing states [200] c) PDMS base device for contact-free trapping and manipulation of nanoparticles [61] d) Convex lens-induced confinement (CLiC) [195].	66
3.8	Overall image of the nanofluidic device representative of its compartments. a) the camera image of the I) front and II) back of the nanofluidic device. b) SEM image of the central area of the nanofluidic device including the nanocavities and nanochannels. c) schematic image of the membrane area of the device d) schematic image of the nanofluidic device and its different layers. . . . .	67
3.9	The fabrication procedure: 1- Cleaning the borosilicate glass. 2- Adding the gold alignment marks. 3- Creating the nanofeatures including the nanocavities and nanochannels using E-beam lithography. 4- creating the microchannels using photolithography following RIE. 5- Obtaining the silicon wafer double-sided coated with SiNx. 6- Bonding the nitride-coated silicon wafer to the prepared glass wafer. 7- opening the windows on SiNx layer. 8- KOH wet etching of the wafer. . . . .	69
3.10	3D printed chuck a) the camera image of the 3D printed chuck connected to the luer tubes. b) the schematic image of the 3D chuck and the retainer plate holding the nanofluidic device against the chuck. . . . .	70

3.11	Isothermal amplification method. a) Loop-mediated isothermal amplification [165]. b) Rolling circle amplification [115] c) PLP method for RCA amplification of targets which are circularized [115]. . . . .	73
4.1	(a) The device consists of a lattice of circular nanocavities bonded to a flexible membrane lid. (b) When pneumatic pressure $P$ is applied to the lid, the lid is deflected downwards, increasing the degree of vertical confinement experienced by the particles. At maximum deflection (c), the confinement is complete and the particles cannot escape from the cavities. (d-f) The imposed confinement alters the electrostatic free energy landscape experienced by the particle, increasing the potential well depth $W$ for a particle confined in a cavity, which in turn decreases the particle escape rate $R$ . (g-h) The device consists of a nanoslit with embedded cavity lattice etched into a borosilicate substrate. A flexible nanoscale nitride lid is exposed at the device center and suspended over the cavity lattice. The nanoslit is interfaced to two loading ports for introducing particle containing solution. (i) SEM of cavities taken through the nanoscale lid. (j) photograph of $1 \times 1$ cm device. . . . .	78
4.2	(a-c) Sequence of fluorescence micrographs of plasmids diffusing in cavity lattice for (a) weak, (b) moderate and (c) strong confinement. The cavity positions are indicated in gray. (d-f) Corresponding trajectories for three example plasmids for (d) weak, (e) moderate and (f) strong confinement. (g-i) The probability of finding the plasmid at a point in the cavity lattice, for (g) weak, (h) moderate and (i) strong confinement. At higher confinement the plasmids remain in the cavities longer relative to the slit, resulting in a higher probability for a plasmid to be found in a cavity. . . . .	80

4.3	Normalized histogram of measured plasmid escape times for (a) slit height of 191 nm with 25 particles and 195 hopping events; (b) slit height of 185 nm with 42 particles and 351 hopping events; and (c) slit height of 180 nm with 74 particles and 295 hopping events. (e) Comparison of experimentally measured averaged escape times for different slit heights with Langevin simulation results. The inset gives the measured average escape time for different DPW on a log-linear scale with an exponential fit to the simulation results. Data points from device class 1 ( $\delta h_{\text{max}} = 0.8 \text{ nm}$ ) are shown as circles with colors that match the corresponding histograms in (a), (b) and (c). Data points from device class 2 ( $\delta h_{\text{max}} = 10 \text{ nm}$ ) are shown as blue triangles. . . . .	84
4.4	Methodology for measuring size and charge of single vesicles. (a) A sample trajectory of a liposome particle at two different slit heights ( $2h = 291 \text{ nm}$ and $2h' = 315 \text{ nm}$ ) and resulting $\langle t_{\text{esc}} \rangle$ . (b) Mean square displacement in slit of 5 vesicles of similar size at the two different slit heights. The inset indicates the definition of the displacement vector $\mathbf{r}$ for a vesicle undergoing Brownian motion in the slit between cavities. (c) Mid-point potential measured for the two different slit heights. . . . .	86

4.5	Size and charge measurement of 100 NHA (red) and 100 U373 (blue) EVs and 30 liposomes (green). (a) Distribution of diameter characterized in device. The small dots give results for individual vesicles measured in device, the bar gives the average over the individual vesicle measurements (with error-bar based on standard-deviation) and the large point to the right of the distributions gives the NTA result for comparison (with error-bar based on standard-deviation). (b) The zeta potential analysis for the same vesicles as in (a). The small dots give results for individual vesicles measured in device, the bar gives the average over the individual vesicle measurements (with error-bar based on standard-deviation) and the large point to the right of the distributions gives the electrophoresis result for comparison (with error-bar based on standard-deviation). (c) Scatter plot of effective charge versus diameter for the vesicles. Inset gives zeta potential versus diameter . . . . .	89
4.6	(a) Photograph of 3D printed chuck interfaced to luer tubing for applying pneumatic pressure to deflect membrane lid and transport solution through flow-cell. (b) Schematic showing chuck/nanofluidic device assembly. . . . .	91
4.7	Relation between slit height and applied pressure used to deflect the membrane lid. The error bars show the variation of slid height in plateau region. The inset shows the plateau region definition. This curve was taken for device class 1. . . . .	93
4.8	Solution conductivity versus ionic concentration. The error bars are smaller than the symbols and the maximum error is less than 0.1 %. . . . .	94



4.9	(a) The mid-point potential Energy as a function of radial distance from the cavity center for a slit height of 200 nm and 250 nm. By decreasing the slit height, the energy barrier increases and the average of escape time increases. The quantity $r_{\text{esc}}$ gives the boundary a particle should pass to be considered as having escaped from the well. The mid-point potential corresponding to a $3 \times 3$ cavity lattice for a slit height of (b) 250 nm and (c) 200 nm. . . . .	95
4.10	Electrostatic potential obtained from COMSOL simulation. (a) Electrostatic potential contours inside the chamber; (b) surface-averaged value of electrostatic potential at mid-plane $\psi_m$ versus the radial distance from cavity center; (c) surface-averaged value of electrostatic potential versus particle radius. . . . .	96
4.11	(a) Histogram of 351 experimentally measured escape times for pBR322 Vector with a hydrodynamic radius of 65 nm and a slit height of 187 nm. (b) Histogram of 10000 simulated escape times using BD simulation for a particle with the same size, charge and the same slit height as experiment. Setting $\psi \sim 2.06(\frac{k_B T}{e})$ yields an average escape time in agreement with experiment. (c) Average escape time versus surface electrostatic potential using BD simulation. . . . .	97
4.12	Flow Chart of python code for syncing microscope camera and LED and pressure controller. . . . .	100
4.13	COMSOL simulation results for the plateau length $L_{\text{plateau}}$ versus membrane width. The effective utilizable membrane area is given by $L_{\text{plateau}} \times L_{\text{plateau}}$ . The total variation in slit height across the plateau region is given by $2 \delta h_{\text{max}}$ . For these simulations $\delta h_{\text{max}} = 0.8 \text{ nm}$ . . . . .	104

5.1	Nanofluidic device and its working principle a) Front and back views of the nanofluidic device b) 3D schematic of the deformable membrane. c) SEM of nanocavity array after the membrane is removed. d) The device has two crossed microchannels (target-loading channel and reagent-loading channel) which intersect at the membrane position. e I) Cut-out view of the nanofluidic device at the reagent-loading channel. When the membrane is pushed down, the membrane prevents the reagents from flowing from the nanochannels to the nanocavities. e II) Cut-out view of the nanofluidic device at the target loading channel. While the membrane is deflected, the reagents can enter the nanochannels as the nanochannels are connected to the reagent-loading channel external to the membrane area. . . . .	111
5.2	a) Schematic image of the membrane region. b) Loading and amplification steps of DNA inside cavities; bI) loading of target DNAs from target loading channel; bII) DNA confinement via membrane deflection; bIII) washing out extra DNAs in side nanochannels and reagent-loading channels; bIV) adding amplification reagents from nanochannels while the target DNAs remain confined in nanocavities. c) Cartoon showing molecule concentration in cavities as the membrane lid is lowered. d) Fluorescent images showing the confinement of YOYO-1 labelled-pBR322 plasmid vectors in nanocavities I) without and II) with the concentrating procedure. . . . .	113
5.3	Labeling of pBR322 plasmid vector with YOYO-1 fluorescent dye in cavities. a) Fluorescent images before and after loading the fluorescent dye in nanochannels while pBR322 plasmid vectors are confined in nanocavities. b) Average fluorescent intensity variation over time. . . . .	116

5.4	Variation of occupancy percentage of a) 15 nm and b) 50 nm particles in nanocavities after waiting over 5 minutes at different slit heights. c) Comparison of final occupancy percentage of 15 and 50 nm nanoparticles for different slit heights after waiting 5min. d) Retention of YOYO-3 labelled-pBR322 plasmid vectors in nanocavities during the introduction of FAM-tagged primers . . . . .	118
5.5	Digital amplification of M13mp18 in nanocavities. a) Real-time average fluorescent intensity measurement from nanocavities using the LAMP method. b) Four primer RCA amplification procedure. c) Fluorescent images before and 18 minutes after loading the RCA amplification reagents. d) Real-time average of fluorescent intensity measurement using the RCA method and comparison of results with the interaction of the fluorescent dye with target-ssDNA without amplification. e) Fluorescent intensity distribution over cavities for two used isothermal amplification methods. . . . .	121
5.6	(a) Schematic image showing chuck/nanofluidic/heater device assembly. (b) Photograph of the assembled system which shows the opening that the microscope objective can image the nanocavity area through. . . . .	128
5.7	a) Photograph of the stage top incubator for applying homogenous heat up to 50°C. b) IR image taken using an infrared camera. The nanofluidic device temperature is increased to $\approx 65^{\circ}\text{C}$ for loop-mediated isothermal amplification. . . . .	129
5.8	Relation between slit height and applied pressure used to deflect the membrane lid. The error bars show the variation of slid height in the center region of the membrane. The inset shows the zoom-in for the slit height smaller than 100 nm . . . . .	130

5.9	Flow and hydrodynamic resistance in the nanofluidic device computed from model a) Symbolic representation of hydrodynamic resistance circuit in the nanofluidic device. b) and c) Fluid velocity and flow rate, respectively, in the slit gap and nanochannels at different slit heights. . . . .	131
5.10	a) Comparison of LAMP and RCA results regarding the size of generated particles. b) Real-time PCR results for comparison of amplification rate for four primers and one primer RCA. . . . .	132
5.11	Point-spread function effect on the fluorescent measurements. a) 3D intensity profile of a 300 nm rhodamine red-labelled liposome imaged with 60× N.A. 1 objective. The scale bar of the inset is 1μm. b) The fluorescent intensity vs the radius distance from the center. . . . .	136

# List of Tables

2.1	EVs microRNAs and messenger RNAs . . . . .	20
2.2	Throughput of well-known methods for EVs analysis . . . . .	38
2.3	Sensitivity of well-known methods for EVs analysis . . . . .	40
2.4	Throughput of well-known methods for EVs analysis . . . . .	49
4.1	The mean diameter, charge and zeta potential for vesicles measured in the device along with their accompanying standard-deviation ( $\sigma$ ). In total, 30 liposomes were measured (device class 1) and 100 U373 and NHA EVs each (70% of EVs in device class 1 for both U373 and NHA, 30% in device class 2). Each mean value is given an error bar determined from the standard-deviation of the mean. . . . .	101
5.1	Radius of gyration of polymerase. . . . .	134
5.2	Radius of gyration of RCA primers. . . . .	134
5.3	Radius of gyration of LAMP primers. . . . .	134
5.4	LAMP primers . . . . .	135
5.5	RCA primers . . . . .	135

# Contributions of Authors

## **Nanofluidics for Simultaneous Size and Charge Profiling of Extracellular Vesicles, Nano Letters, 2021 21 (12).**

Authors: Imman I Hosseini<sup>1</sup>, Zezhou Liu<sup>2</sup>, Xavier Capaldi<sup>2</sup>, Tamer AbdelFatah<sup>1</sup>, Laura Montermini<sup>3</sup>, Janusz Rak<sup>3</sup>, Walter Reisner<sup>2</sup>, Sara Mahshid<sup>1</sup>

1. Department of Bioengineering, McGill University, 3775 Rue University, Montreal, Quebec H3A 2B4, Canada

2. Department of Physics, McGill University, 3600 Rue University, Montreal, Quebec H3A 2T8, Canada

3. Department of Pediatrics, McGill University, Research Institute of the McGill University Health Centre, 1001 Decarie Boul., Montreal, Quebec H4A 3J1, Canada

### **Contributions:**

**IIH:** Conceptualized the problem, performed the experiments, prepared the samples, performed the calibration tests, analyzed the results, discussed the results, prepared the figures and wrote the manuscript.

**ZL:** Mentored to perform the experiments, fabricated devices, provided technical and scientific advice

**XC:** Fabricated devices, provided technical and scientific advice for the fabrication of devices

**TA:** Helped with the calibration of the devices

**LM:** Prepared samples

JR: Provided technical and scientific advice for EVs samples, discussed the result, provided resources and funding.

WR: Conceptualized the problem, provided technical and scientific advice, analyzed the results, discussed the results, wrote the manuscript, provided resources and funding.

SR: Conceptualized the problem, provided technical and scientific advice, analyzed the results, discussed the results, provided resources and funding.

## **Tunable nanofluidic device for digital nucleic acid analysis. (ready to be submitted)**

Authors: Imman I Hosseini<sup>1</sup>, Seyed Vahid Hamidi<sup>1</sup>, Xavier Capaldi <sup>2</sup>, Zezhou Liu<sup>2</sup>, Walter Reisner<sup>2</sup>, Sara Mahshid <sup>1</sup>

1. Department of Bioengineering, McGill University, 3775 Rue University, Montreal, Quebec H3A 2B4, Canada

2. Department of Physics, McGill University, 3600 Rue University, Montreal, Quebec H3A 2T8, Canada

### **Contributions:**

IIH: Conceptualized the problem, performed the experiments, prepared the samples, performed the calibration tests, analyzed the results, discussed the results, prepared the figures and wrote the manuscript.

SVH: Performed the experiments for control tests, provided technical and scientific advice on biological aspects, advised on writing the manuscript

XC: Fabricated devices, provided technical and scientific advice for the fabrication of devices

ZL: Provided technical and scientific advice for the fabrication of devices

WR: Conceptualized the problem, provided technical and scientific advice, analyzed the results, discussed the results, wrote the manuscript, provided resources and funding.

SR: Conceptualized the problem, provided technical and scientific advice, analyzed the results, discussed the results, provided resources and funding.



# Chapter 1

## Introduction

### 1.1 Motivation

**Motivation for EVs analysis:** Cancer is Canada's leading cause of death (28% of deaths among all other causes including heart diseases). In Canada, out of every four people, one dies because of cancer. [211] The cancer mortality rate can be dramatically decreased by early detection. The current approved methods for cancer detection are based on imaging methods such as Magnetic Resonance Imaging (MRI) or molecular tests (such as Polymerase Chain Reaction (PCR) which is a gold standard method for the detection of cancer mutations) on tissue biopsies by a specialist. All these tests are usually performed when noticeable symptoms are observed by the patient. At this late stage, controlling the disease is highly challenging. In the United States, 52% of all primary brain tumors correspond to glioblastoma multiforme (GBM): as the most common brain tumors [114]. Based on a report from 2022 for all cases between 2015-2019, the five-year post-diagnosis survival rate is still low, despite all the invasive treatments such as surgery combined with radiation and chemotherapy [162]. The survival rate has not improved since 2005 [159].

Molecular and cellular heterogeneity in GBM is the main reason for the low survival rate. The tumor heterogeneity arises at two levels:

1- Inter-tumor heterogeneity refers to heterogeneity arising between different patients diagnosed with GBM carrying different mutations. For example, a GBM tumor can be classified based on the existence of isocitrate dehydrogenase (IDH) 1/2 mutations or co-deletions in chromosomes 1p and 19q into three groups: IDH mutant-1p19q co-deleted, IDH mutant,1p19q intact, and IDH wild-type gliomas [216]. Also, each group might have different alternations as well such as EGFR, TERT promoter, PDGFRA, CIC, FUBP1 [133].

2- Intra-tumor heterogeneity refers to heterogeneity in a single tumor. A wide range of transcriptional programs, cell states (i.e., differentiation or stemness), and proliferation capacity can be observed by looking at individual cells of a single tumor. The individual tumor cells compete continuously for nutrients, oxygen, and space in their environment. Based on the genomics and functionality of cells, the cells undergo some adaptations and modify their particular microenvironment by creating localized clones to survive; otherwise, will die or stay quiescent. Therefore, the intra-tumor heterogeneity is genetic (the genome of cells) and the cells' environment variations. In the case of glioblastoma, the genetic mutations can be aneuploidy (variation in the number of chromosomes), gains in chromosome 7, losses in chromosomes 9, 10, 13, and 22, or a combination of these alterations [103,213]. As well as spatial changes, tumors also experience longitudinal changes. For low-graded glioma, only 10% of mutations are clonal (subsequently passed down to all its daughter cells) and 60% of the mutations are subclonal (occurs in only a subset of cells) [216]. For example, it is confirmed that H3K27M, ATRX, and NF1 mutations are clonal and TP53, BRAF, PDGFRA mutations are subclonal in pediatric GBM [237]. The existence of these subclonal mutations confirms the perpetual molecular alteration during tumor growth.

Furthermore, treatment methods such as chemotherapy or radiotherapy, although they can eradicate a portion of clones, also give rise to clonal genetic or environmental changes that promote treatment resistance.. Temozolomide (TMZ) is a type of chemotropy that is mainly used for GBM treatment [215]. In tumor recurrence after treatment with TMZ, the number of mutations per megabase can be increased from 0.2-4.5 to 31.9-90.9,

in which, 97% of these mutations are associated with the TMZ treatment [93]. The mutated clones can grow again and create a resistant tumor and the treatment method is no longer effective.

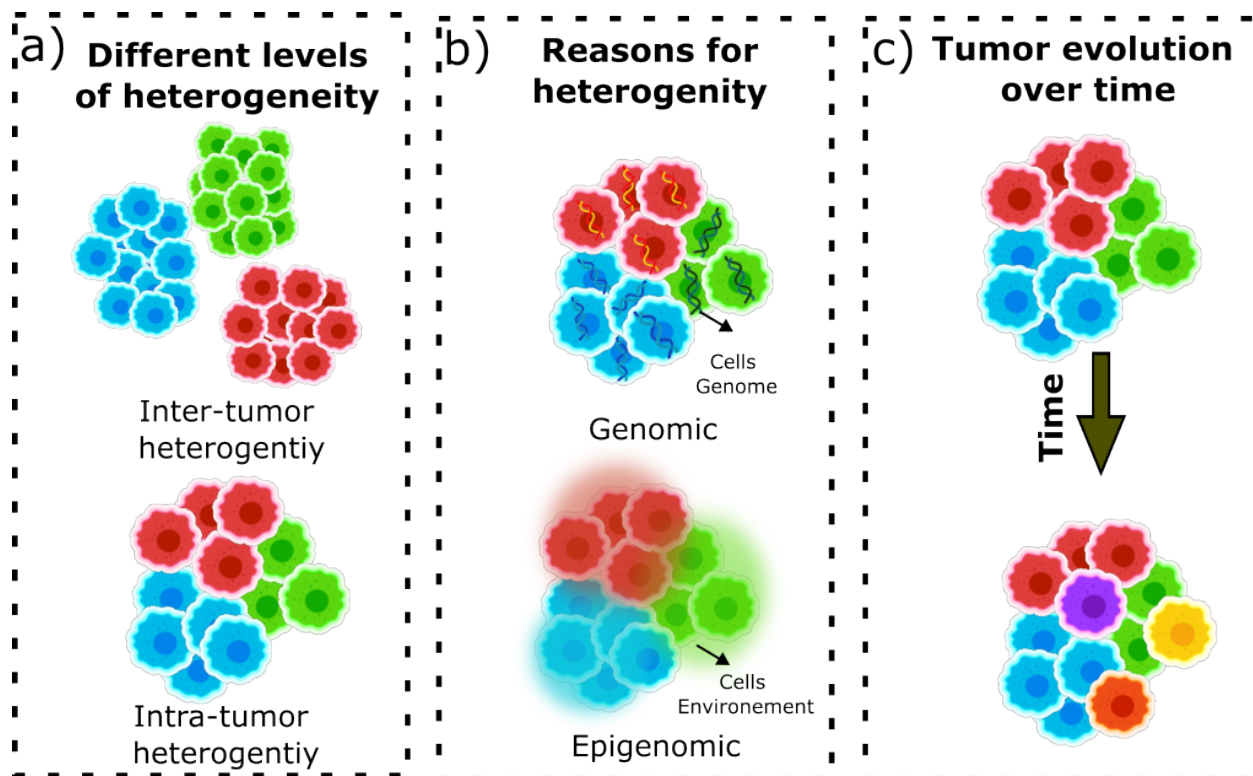


**Figure 1.1:** Tumor Heterogeneity a) Cancer heterogeneity arises at two levels: inter-tumor heterogeneity and intra-tumor heterogeneity b) The heterogeneity is rooted in genomic or epigenomic reasons. c) As well as spatial changes, a tumor can be evolved over time.

Single cell/clonal analysis provides detailed information regarding the incredible degree of intra-tumor heterogeneity. This information can then be used to select a combination of drugs tailored to the specific properties of the given tumor cells/clones. For example, in one study, single tumor cells were extracted from 12 tumor tissue clones, and grown to establish single-cell clones. Several genomic profiling methods such as single nucleotide polymorphism (SNP) arrays, RNA sequencing, and whole genome sequencing (WGS) were performed on 6 clones from the grown cells [5]. None of the drugs were individually effective on all clones. For example, when EGFR genome expression was targeted using Afatinib, although most of the clones were suppressed, two of the clones re-

sisted. However, CDK 4/6 inhibitor (Abemaciclib) and PI3K inhibitor (Buparlisib) could suppress each of the Afatinib-resisted clones. Therefore, a combination of drugs based on the specific genomic signature of single tumor cells/clones can provide more effective treatment. Yet, early detection of cancer due to the limited resolution of tumor imaging methods (MRI) especially for invasive cancers [84], and real-time monitoring due to the considerable risk posed by invasive tissue biopsy are almost impossible. Accordingly, an approach for early cancer detection and real-time monitoring of treatment is needed to be able to decrease the cancer mortality rate.

Liquid biopsy is a promising potential replacement for surgically based invasive solid biopsy [132]. Liquid biopsy refers to analysis approaches based on the extraction of biological fluids including blood (plasma and other cells), urine, saliva, and cerebrospinal fluid (CSF). Different types of cancer biomarkers can be found including proteins, circulating tumor RNA/DNA (ctRNA/DNA), circulating free tumor cells, and Extracellular Vesicles (EVs) [128]. Liquid biopsy has two key advantages. Firstly, the biomarkers extracted via a liquid biopsy can contain information from cells that are not easily accessible with surgery (e.g., brain tumors). Secondly, body fluids can be extracted with much less risk in comparison to tissue biopsy avoiding surgical complications such as bleeding caused by biopsy needles insertion, damage to nearby organs, anesthesia-related risks, and infection by skin incision [132]. For these reasons, liquid biopsy is a promising approach for early cancer detection and the monitoring of cancer progression during treatment.

Extracellular Vesicles (EVs) in particular have shown promising results for cancer detection [128]. EVs are mostly compared with ctDNAs as another liquid biopsy biomarker.

- Single EVs carry different types of biomarkers such as proteins, DNA/RNA, lipids, and metabolites (e.g., carbohydrates) simultaneously [221].
- EVs are generated from living cells, while ctDNAs can be released inside body fluids after cellular apoptosis [79].

- EVs preserve their inner contents from degradation using phospholipid calculation. In contrast, ctDNAs half-life in tissues and body fluids is 15-120 min before being degraded depending on their size and configuration (ssDNA or dsDNA) [112,176].
- Cancer cells generate more EVs than healthy cells by increasing growth factors so that diagnostically relevant EVs originating from cancer cells are present at high levels relative to background signals from normal cells [55].
- EVs have demonstrated functionality in the formation of premetastatic niches; and consequently, can likely be used to detect tumors with metastatic potential before metastasis occurs [250].

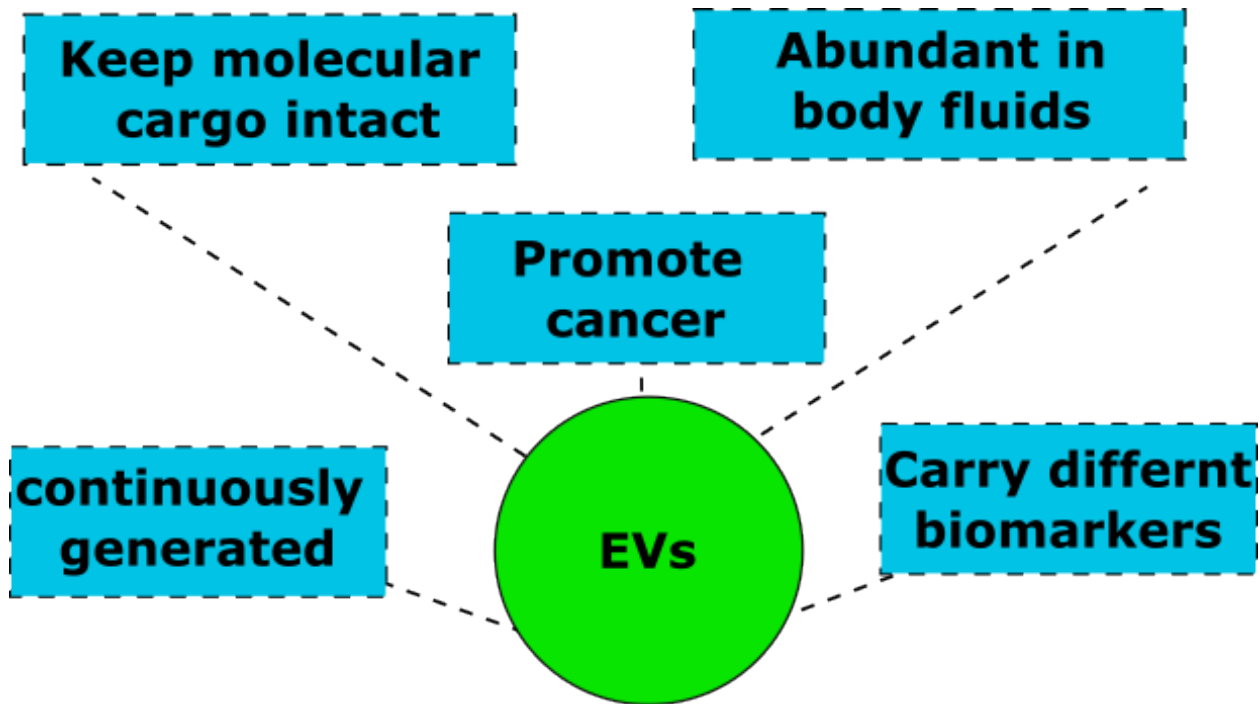


**Figure 1.2:** Extracellular vesicles (EVs) are interesting biomarkers since: 1- EVs preserve their cargoes from degradation; 2- a large number of EVs can be found in a body fluid; 3- EVs are involved in different physiological activities of cells; 4- a single EV simultaneously carry different biomarkers including proteins, nucleic acids, and lipids; 5- EVs are continuously generated by the different cell types.

EVs in growing tumor cells play an important role which makes them a promising cancer biomarker. EVs can regulate immune system functionality by affecting immune cell chemistry. This modulation can suppress and decrease the number of immune cells and subsequently affect the maturation of immune cells and how they interact with circulating tumor cells [1, 24, 126, 266]. Also, EVs can regulate the tumor microenvironment (TME). For example, some studies show that EVs can affect the immune system indirectly by promoting the generation of Tumor-Associated Macrophages (TAM). Macrophages are a type of white blood cell that kill microorganisms and regulates the functionality of other immune cells. TAM cells are produced while a tumor grows and seem to protect the tumor tissue from immune system attack. Recent studies show that tumor-derived EVs preserve the tumor tissue from immune system attack by TAM polarization [179]. Moreover, EVs can facilitate tumor growth by regulating fibroblast cells. Fibroblast cells generate a cellular scaffold in the extracellular environment by secreting extracellular matrix (ECM) components and collagens. EVs lead to the formation of an environment suitable for tumor-tissue growth by promoting the development of fibroblast cells [65]. Tumors need more oxygen and nutrition for their fast growth and metastasis, which they obtain by generating new vessels (angiogenesis). EVs promote the generation of new vessels by communication with endothelial cells [263]. EVs also can be involved in the many steps of the complicated metastatic emerging in sites far from the tumor origin. First, the TAM cells polarized by tumor-derived EVs (TDEs) increase the invasiveness of tumor cells via RNAs (e.g. HIF-1 $\alpha$ -stabilizing lncRNA) capsulated in EVs [30]. Also, TDEs can bind to the ECM and degrade the ECM components including collagens, LNs, and fibronectin. The degradation of ECM helps to promote proliferation and apoptosis resistance of tumor cells as well as prepare new host locations for the metastatic migration of cancer cells [189]. Tumor cells, for migration, need to permeate through the vessels and circulate in the bloodstream. TDEs can destroy tight junction proteins (ZO-1) which increases blood permeability and promote tumor cell migration by expressing miRNAs

(miR-105) [273]. EVs also can prepare the host location for migration at distant sites (pre-metastasis niche) by vascular leakiness, and ECM preparation at the destination [250].

**Motivation for single EVs analysis:** Given the complexity of this discussion, chapter 2 of this thesis is dedicated to a detailed discussion of the importance of single EVs analysis. Here, we summarize the key reasons for why single EVs analysis is important.

The main reason a single EV level analysis is needed is that EVs are highly heterogeneous. The heterogeneity is rooted in the fact a single cell can generate different types of EVs based on their functionality and different biogenesis pathways. Also, cells in a tissue that is in contact with a body fluid are heterogeneous resulting in a high heterogeneity of EVs in the body fluid. This high degree of heterogeneity creates two main challenges: 1- Although the EVs are abundant in body fluid, the target cancer biomarker might be scarce; therefore, high sensitivity is required to detect the scarce biomarkers. 2- The target biomarkers will be hard to detect against the large background signal from other EVs (e.g. secreted by healthy cells); therefore, high specificity is required to eliminate false results. Single EV level analysis will provide a better chance of detecting the few EVs that are carrying diagnostically significant biomarkers. On the other hand, EV heterogeneity creates the opportunity to evaluate different cellular activities in tissue from a single body fluid sample.

A second key motivation for single-level EV assessment is the possibility of multiplexing and observing the correlation between different types of molecular cargo extracted from single EVs (e.g., proteins, lipids, DNAs/RNAs). A single EV carries different multiple biomolecules (a detailed discussion is provided in Chapter 2 which discusses the different molecules that can be found in an EV) and it is hypothesized there is an interdependency between the molecules to confer a specific functionality to a given EV. By analysis of EVs functionality, EVs' parental cells could be deduced [33,105], and consequently reveal interdependencies among differentiation status, local environment, and phenotype to ensure an accurate assessment of cancer progression [55].

In Chapter 2 we discuss in detail what are the characteristics of an ideal single EV analysis approach. In general, an ideal method for EV analysis should have the following features; it should be able to 1- perform the analysis for a large number of EVs simultaneously; 2- be able to access EV molecular cargo; 3- perform multidimensional/multiomic analysis to detect different cargo molecules from individual EVs. Despite the recent advances of single EVs analysis methods, there is no ideal diagnostic method enabling quantitative multiomic analysis of EVs in a single level with high throughput and functionality at a low concentration that is easy to operate, simple to construct, portable, and durable.

One of the well-known methods for EVs analysis is called: Single EVs Analysis (SEA) [117,209]. In this method, the EVs are immobilized on a surface using a capturing antibody, and then the surface EVs proteins are detected using antibodies conjugated with fluorescent dyes. The method provides a high chance of multiple detections of single EVs surface proteins by serial staining and bleaching steps; however, it is limited to the surface proteins of EVs and is unable to detect the encapsulated molecular cargo due to the lack of complete isolation (i.e., the encapsulated molecular cargo can be dispersed after being released in the solution). Some studies have tried to penetrate the detection molecules inside EVs (e.g., detection antibody, fluorescent dyes) after immobilization by cell-penetrating peptides (CPP)-Molecular beacons (MB) [43] or fixation cross-links to preserve the EVs integrity after membrane permeabilization [142]. The efficiency of CPP penetrating depends on the lipid components of EVs and the attached detection molecules to the CPP molecule [91]. Also, using fixation cross-links (e.g., formaldehyde) limits the accessibility of immunodetection molecules inside the EV lumen. These limitations reduce the sensitivity of detecting encapsulated EV cargo. The other well-known method for single particle detection is the droplet generation method [99,261]. The EVs are first captured on the surface of magnetic beads and then partitioned inside droplets and the target molecules are detected using fluorescent dye. Although, this method completely isolates EVs from other particles and consequently increases the sensitivity and specificity of detection using a label-free method, the multiplexing of detection is lim-



ited to 4-6 fluorophores (i.e., due to the spectral overlap between different fluorophores), and also it is not possible to have washing and changing reagents while the particles are confined. Another method for single particle detection is based on flow cytometry [120]. Different modifications have been applied to the traditional flow cytometry method to increase the sensitivity of detection to small particles such as EVs [149]. The method provides a single and high throughput analysis of EVs; nevertheless, the detection will be only limited to 4-6 biomarkers for individual EVs and only limited multiplexing is possible. Other methods for single EV analysis and detection include surface-enhanced Raman spectroscopy [116], Electrochemistry [89], and mechanical properties measurement [239] discussed in chapter 2.

## 1.2 Thesis objectives

Here, we develop a nanofluidic system for the isolation and analysis of single EVs. The system utilizes a flexible nanoscale membrane that can be actuated from above via pneumatic pressure to implement tunable nanoconfinement. By applying pressure, the membrane is deformed, decreasing the height of the nanoslit and increasing the degree of confinement the EVs experience. Upon significant membrane deflection, EVs in the slit are forced into nanocavity bioreactors embedded in the nanoslit; the reactors can be completely closed off, or a small slit left so that the EVs can escape with a probability dependent on their surface charge.

**The first objective:** is to examine the confinement of EVs in nanocavities by adjusting the membrane height. The performance of the nanocavity-coupled membrane can be measured via quantitative analysis of EVs using fluorescent microscopy. We examine the capability of the device for the confinement of EVs and the parameters which affect the confinement. The confinement will be dependent on the geometry of the nanofluidic device including the height of the channel which can be adjusted in real-time by controlling the flexible membrane deflection as well as the size of cavities and their depth. The

correlation between the applied pneumatic pressure and the nanofluidic channel height is measured. The level of confinement as well as the geometry of the nanofluidic device. The EVs surface charge is correlated to surface-associated molecules (e.g. proteins [235], glycans [248] and cholesterol [171]) that are incorporated during the biogenesis of EVs. By measuring the escape time for a single particle at different channel heights using real-time control over the membrane deflection, the surface charge of particles can be estimated according to Kramer's theory. The confinement of EVs secreted from two brain cell lines: 1- glioblastoma astrocytoma (U373) and normal human astrocytoma (NHA) is examined using the nanofluidic device. The size and surface charge distribution of EVs from these cell lines is measured and compared.

**The second objective:** is to examine the capability of the nanofluidic device for adding detection reagent to the nano-bioreactors while the target molecule is fully confined (the target particle stays in a cavity for long hours). The target molecules in this objective are DNA molecules with the future objective being EVs-based mRNA analysis. The aim is to keep the target molecule fully confined while still there is a tiny opening (several nanometers) where the small molecules including fluorescent dyes, polymerases, and primers can be loaded inside the nanocavities. First, the capability of the device to concentrate the target molecules inside the cavities is examined. Then, we modify the nanofluidic device to be able to load detection reagents from a separate channel from the target loading channel to remove the cross-contamination. Also, a set of nanochannels are implemented to bring detection reagents very close to the nano-bioreactors. DNA molecules are confined in the nanocavities to develop an on-chip amplification of DNA inside the nanocavities. DNA amplification inside the cavities provides a better target DNA detection using a fluorescent signal as well as increasing the specificity. Loop-mediated Isothermal Amplification (LAMP) and Rolling Circle Amplification (RCA) are primary options for DNA amplification. These methods can be used to amplify a target DNA at a constant temperature by using extra primers. Different parameters are optimized to achieve the best performance. These include: (I) the temperature, which should be uniformly set over the device and

kept in a steady-state condition; (II) the concentration of each amplification component, which should be adjusted according to the device to have the optimized amplification rate, namely, the master mix, primers, and fluorescent dye, which will be defined as related to the DNA concentration; (III) the transformation rate of the amplification components to the nanocavities and the membrane height, which should be adjusted to keep DNAs confined inside the nanocavities while amplification occurs.

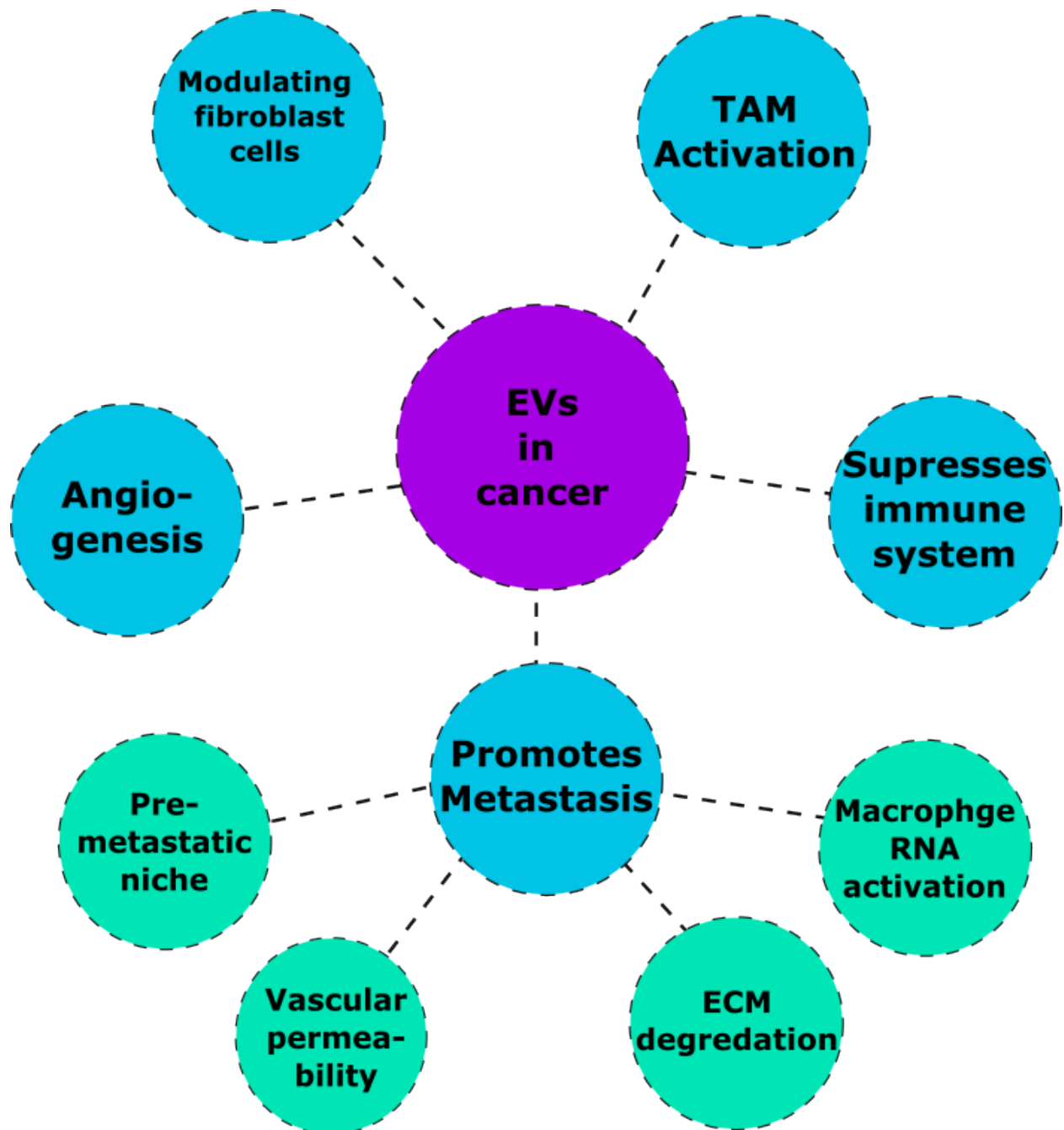


**Figure 1.3:** EVs are interesting in cancer detection studies since: 1) EVs influence the immune system responsible directly or by modulating fibroblast cells or tumor-associated macrophages (TAM); 2) EVs participate in angiogenesis to provide more nutrition for tumors; 3- EVs promotes metastasis by extracellular matrix degradation, increasing vascular permeability, creating premetastatic niches, or activating macrophages RNA.

# Connection between Chapter 1 and 2

Many studies have been conducted to exploit the capability of EVs for different purposes including understanding the biogenesis of EVs, drug delivery, and detection of diseases such as cancer. The field of EVs analysis is a broad topic and researchers are conducting different studies in various directions. This chapter of the thesis is dedicated to disentangling the current studies in this field. First, a short introduction is provided about the structural biology of EVs. Then a general discussion of subgroups of EV analysis is provided. Next, the importance of multidimensional single-level analysis of EVs is discussed. Before reviewing the most well-known examples of single EVs analysis, we outline the characteristics of an optimum single EV analysis approach. Finally, we discuss the current methods proposed for single EV analysis including their development history and outcomes are detailed. Our objective is to understand the limitations and strengths of each approach.

## Chapter 2

# Single Extracellular Vesicles

### 2.1 Extracellular Vesicles

Extracellular Vesicles (EVs) are nanoscale-size particles that cells continuously secrete. EVs have a phospholipid layer that carries diverse biological contents including proteins, nucleic acids, and N-glycoproteins [235]. EVs have been found in almost all body fluids including blood, plasma, cerebrospinal fluid (CSF) urine, and saliva [177]. The reported concentration of EVs in a plasma blood sample, in 37 studies, varies in the range of  $10^6 - 10^{13}$ /ml based on the isolation techniques used (size exclusion chromatography, polyethylene glycol-based precipitation, ultracentrifugation, density gradient ultracentrifugation) and quantification methods (nanoparticle tracking analysis, tunable resistive pulse sensing, flow cytometry, and acetylcholine esterase activity) [92]. EVs play key roles in maintaining physiological balance and homeostasis. For example, EVs are used to send signals from injured cells to stem cells. In turn, stem cells send required RNAs and proteins via EVs to repair the injured tissue and maintain the tissue homeostasis [180].

**Types:** Extracellular Vesicles have been categorized into two main types: exosomes and microvesicles (MVs). This nomenclature is based on the formation and biogenesis of the particles. Exosomes originate in the endosomal pathway as intraluminal vesicles (ILVs) inside multivesicular bodies (MVB); the ILVs become exosomes when they are se-

creted outside the cell during exocytosis. The size range of exosomes is 30 – 150 nm. In bulk exosome samples, the particles with the very lowest size ( $\approx 35$ ) nm do not have lipid structure and are termed ‘exosmeres’ [265]. On the other hand, microvesicles with a size range of 50 – 1000 nm are formed and secreted by direct budding from the plasma membrane. Due to the distinct biogenesis and formation pathway of these particles, it is expected that each of the groups contains different cargoes. The International Society for Extracellular Vesicles (ISEV) recommends that researchers use small EVs (sEVs) and large EVs (lEVs) instead of directly referring to exosomes or microvesicles [249], respectively, if EVs are separated based on their size. This recommendation arises from several factors: 1- the current knowledge and available technologies are not strong enough to completely distinguish the particles based on their contents; 2- considerable overlap in the contents carried by exosomes and MVs; 3- some EVs partially follow both MVs and exosomes biogenesis [151].

**Importance:** EVs have received considerable attention due to their potential as a promising noninvasive biomarker for different pathogens. Due to the presence of EVs in the mentioned body fluids, they are a convenient target for liquid biopsy. EVs have a significant role in different diseases including cardiovascular [45,122], neurodegenerative diseases [122,225], and cancer [10,256]. Also, EVs have been used for drug delivery purposes. Vesicles, including liposomes, have been used for years to control the dose of drugs and target specific sites in the body [228]. EVs have specific advantages for drug delivery purposes including the ability to fuse to specific cells, carry bio-contents possess, lower toxicity, and most importantly have higher stability due to the non-immunogenic nature of EVs [68]. EVs have been used for the preparation of vaccines for different diseases including SARS coronavirus [111], human papillomavirus (HPV) [44] and especially cancer therapy [241]. Furthermore, mesenchymal stem cells (MSC)-derived EVs have been used for therapy of several different diseases, including kidney injury, cardiac injury, and brain injury [96].

## 2.2 Molecular Cargo of EVs

The molecular cargo of EVs can be categorized into four main components: 1- DNAs/RNAs 2- Lipids 3-Proteins 4- Metabolites. Some of these components are involved during biogenesis, but most of them are just encapsulated during EV formation.

**DNAs/RNAs:** EVs carry DNAs and RNAs. Extensive studies have been conducted to profile EVs RNAs. Different types of RNAs can be carried by EVs including messenger RNA (mRNA), microRNA (miRNA), long non-coding RNA (lncRNA), transfer RNA (tRNA), small nucleolar RNA (snoRNA), small nuclear RNA (snRNA), vault RNA (Y-RNA), piwi-interacting RNA (piRNA), mitochondrial RNA (mtRN), and circular RNA (circRNA). Most abundant EVs RNA have 200 nucleotides [164]. Many miRNA and mRNA cancer biomarkers have been found in EVs (Table.1). Some miRNAs can be found in different cancer cell types. DNAs can be also found inside EVs including double-stranded DNA (dsDNA), single-stranded DNA (ssDNA), circular DNA (cDNA), and mitochondrial DNA (mtDNA). 30-80% of EVs are carrying DNA. The DNAs can be simply attached to the membrane of EVs or capsulated inside the lumen area of EVs. The membrane DNAs are mostly found on sEVs and the lumen DNAs are found in lEVs. The size of EV-encapsulated DNAs can range from 100 to 10kb. EV encapsulated DNA can be transferred to the recipient cells' nucleus and passed to at least three daughter cell generations. Cancer-specific mutations have been found for different cancers including colorectal cancer [104], acute myeloid leukemia [102].

**Proteins:** Some EV encapsulated proteins are positioned in the EV plasma membrane and are called membrane protein. These include tetraspanins (e.g., CD63, CD9, and CD81), major histocompatibility complex (MHC) molecules, integrins, ligands (e.g., Hedgehog (Hh), programmed death-ligand 1(PD-L1)), receptors (e.g., epidermal growth factor receptor (EGFR), platelet-derived growth factor receptor (PDGFR)), and flotillins. The membrane proteins are used as immunoaffinity-base capturing molecules or disease biomarkers. CD9/CD63/CD 81 are the most enriched membrane proteins in EVs secreted



**Table 2.1:** EVs microRNAs and messenger RNAs

microRNA					
miRNA	Cancer type	reference	miRNA	Cancer type	reference
miR-10b	Breast Cancer	[13]	miR-200b	Breast cancer	[14]
miR-17-5p	Lung Cancer	[15]	miR-200c	Breast cancer	[14]
miR-21	Breast Cancer	[16, 17]	miR-204-5p	Translocation Renal Cell Carcinoma	[18]
	Hepatocellular Carcinoma	[19]	miR-205	Oral Squamous Cell Carcinoma	[20]
	Lung Cancer	[21]	miR-210	Breast Cancer	[13]
	Pancreatic Neoplasm	[22]		Glioma	[23]
	Glioma	[24]	miR-221	Breast Cancer	[13]
miR-23b	Gastric Cancer	[25]	miR-222	Glioma	[24]
miR-27a	Breast Cancer	[16, 17]	miR-223-3p	Ductal Carcinoma in situ breast cancer	[26]
	Colorectal Cancer	[27]	miR-375	Breast Cancer	[13, 16, 17]
miR-30d-5p	Cervical Cancer	[28]	miR-451a	Pancreatic Cancer	[22]
miR-31	Oral Squamous Cell Carcinoma	[20]	miR-1246	Aggressive Prostate Cancer	[29]
miR-122	Hepatocellular Carcinoma	[19]	miR-6807-5p	Gastric Cancer	[30]
miR-124-3p	Glioma	[24]	miR-6856-5p	Gastric Cancer	[30]
miR-130a	Colorectal Cancer	[27]	miR-7641	Colorectal Cancer	[31]
miR-145	Ovarian Cancer	[32]	miRNA let-7a	Oral Squamous Cell Carcinoma	[20]
miR-191	Pancreatic Cancer	[22]	miRNA let-7d-3p	Cervical Cancer	[28]
miR-200a	Breast cancer	[14]			
massanger RNA					
mRNA	Cancer type	reference	mRNA	Cancer type	reference
EPHA2	Glioblastoma	[33]	FGG	Hepatocellular Carcinoma	[34]
EGFR			AHSG		
PDPN			RBP4		
MGMT			TF		
APNG			TTF-1		
AFP	Hepatocellular Carcinoma	[34]	SLC9A3-AS1	Lung Cancer	[35]
GPC3			PCAT6		
ALB			CK18	Pancreatic Cancer	[36]
APOH			CK63		
FAPB1			ErbB3		
FGB			KRAS		

from many cells; therefore, they have been used in many studies for capturing EVs on a substrate. The level of enrichment might vary in different cell types. For example, in breast cancer cell lines, CD63 and CD81 are the most enriched protein and CD9 is not detected; however, CD9 is the most enriched protein in epithelial adenocarcinoma cell lines and pancreatic carcinoma cell lines. Proteins, known as lumen proteins, can also be encapsulated inside EVs including tumor susceptibility gene 101 (TSG101), ALG-2 interacting protein X (ALIX), heat shock proteins (HSPs), syntenin, and RNA binding protein (RAB) GTPases [221].

**Lipids:** EV encapsulated lipids include glycerolipids (e.g., diglycerides (DG)), phospholipids (e.g., phosphatidylserine(PS), phosphatidylcholine(PC), and phosphatidylinositol(PI)) [134], sphingolipids (sphingomyelin (SM), ceramide (Cer)) [71,229], and sterols (e.g., cholesterol) [171]. Also, EVs can carry bioactive lipids (i.e., the lipids which are involved in signaling pathways) such as eicosanoids (e.g., leukotrienes and prostaglandins) [173]. Studies on EV lipid composition are more limited in comparison to the studies conducted on EV encapsulated DNA/RNA or proteins. The enrichment level of some lipids is different in EVs and their parental cells. For example, PS, PC, PI, SM, and cholesterol can be four times richer in EVs than in their parental cells [70]. The enrichment level of lipids might be correlated to cancer progression. For example, the level of free fatty acids (such as arachidonic acid (AA), linoleic acid (LA), and 15-hydroxyeicosatetraenoic acid (15-HETE)) is higher in lung adenocarcinoma patients [129]. Also, several functionalities are possessed by lipids found in cancer-associated EVs. For example, the fatty acids carried by EVs including palmitic and oleic are involving EVs membrane biogenesis [192]. Different level of lipid enrichment is found in different types of EVs. In lEVs, the sphingolipids and glycerophospholipids are enriched; while, in sEVs, fatty acids and glycolipids are enriched [134].

**Metabolites:** EV encapsulated metabolites include amino acids, carbohydrates, carbonic acids and adenosine. Amino acids include proteinogenic and non-proteinogenic forms. Non-proteinogenic amino acids such as ornithine and aminoadipic acid partici-

pate in different carcinogenesis pathways. Encapsulated carbohydrates include D-ribose 5-phosphate (DR5P). DR5P is a product of the cytosolic pentose-phosphate pathway and plays an important role in determining cancer growth rate. Carbonic acids include lactic acid. Cancer cells employ the strategy of lowering extracellular PH via secreting tumor-derived EVs that contain encapsulated lactic acid to evade immune surveillance. Adenosine is involved in mainly in energy metabolism and cell signaling. The lifetime of adenosine is very low (10s) outside of the cells and EVs encapsulation provides protection from degradation.

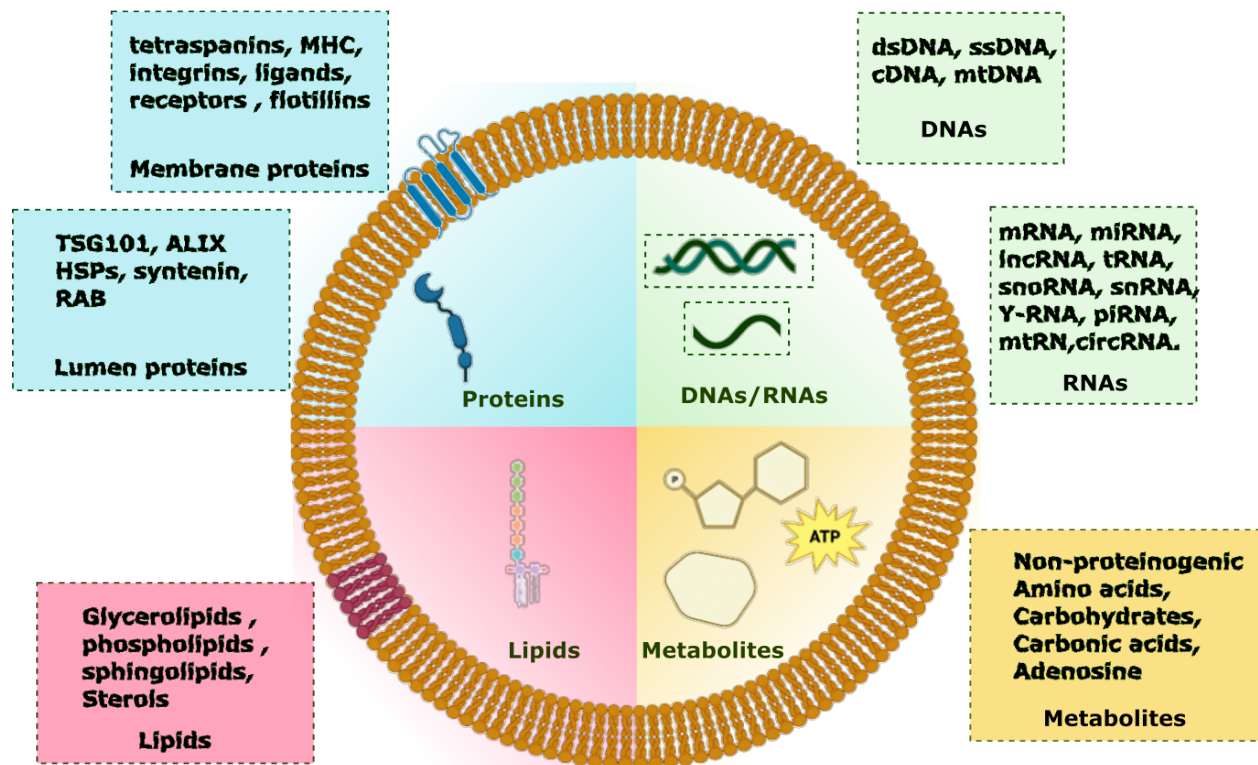


Figure 2.1: Molecular cargo encapsulated inside EVs.

## 2.3 EVs Biogenesis

Here, we will discuss the biogenesis of two common EVs: exosomes and microvesicles. Each of the subgroups can be generated following several pathways, Ongoing studies

continuously suggest new pathways and small changes in the pathways that each subgroup might follow during formation.

**Exosomes biogenesis:** There are three main steps in exosome biogenesis:

1. Endocytosis: By invagination of the plasma membrane, an initial vesicle (called endosome) is formed inside the parental cell. In some cases, the endosomes can be formed by budding from the trans-Golgi network (TGN).
2. Multivesicular body (MVB) formation: In mature endosomes, several small intraluminal vesicles (ILVs) are formed inside the endosomes by invagination of endosomes membrane inside their lumen. The formed endosomes are called the multivesicular body or MVB.
3. Exosome release: the MVBs fuse with the plasma membrane of the parental cell and release the ILVs into the extracellular milieu which then become exosomes. The MVBs can also be degraded by fusing with either lysosomes or autophagosomes.

The MVB can be formed using different pathways. The pathways are classified based on whether "endosome sorting complexes required for transport" (ESCRT) machinery is used. In particular, there are canonical ESCRT-dependent pathways, noncanonical ESCRT-dependent pathways and ESCRT-independent pathways.

1. Canonical ESCRT-dependent (sorting complexes required for transport) pathway: This pathway has four main steps: Step 1-Attachment of ESCRT-0: ESCRT-0 is acquired by attaching to phosphatidylinositol-3- phosphate (PtdIns3P- a lipid in endosomal membranes) from its HRS subunit. Step 2-Attachment of ESCRT-I: ESCRT-I is acquired by attaching to HRS from TSG101 subunit of ESCRT-1. If the ESCRT-0 does not interact with HRS, the HRS cannot interact with the TSG101 subunit of ESCRT-1. Step 3-Attachment of ESCRT-II: ESCRT-II is acquired by directing the interaction of ESCRT-II with ESCRT-I. ESCRT-I and ESCRT-II are believed to play a role in the invagination of endosomal membranes. Step 4-Attachment of ESCRT-III: ESCRT-III

is acquired by binding the CHMP6 subunit of ESCRT-III to the EAP20 subunit of ESCRT-II. It is hypothesized that the ESCRT-III plays a role in ILV scission into the MVB lumen. The scission procedure is carried out using VPS4 protein.

2. Non-canonical ESCRT-dependent: Four different pathways have been proposed for mammalian cells. In these pathways, the ESCRT-III engagement for ILV scission is required. For example, in the syndecan-syntenin- ALIX pathway (one of the non-canonical ESCRT-dependent pathways), first, Syntenin is acquired by interacting with Syndecan (an endosomal transmembrane protein), then, ALIX is acquired by interacting with captured Syntenin, and finally, the ESCRT-III is acquired by direct interacting with ALIX. In fact, the existence of ALIX bypasses the requirement of other ESCRT components (ESCRT-0, ESCRT-I, ESCRT-II). The pathway axis is modulated with heparinase, phospholipase D2 (PLD2), and cytosolic tyrosine kinase (SRC). In other non-canonical ESCRT-dependent pathways, the ALIX can directly interact with endosomal components such as protease-activated receptor 1 (PAR1) or lysobisphosphatidic acid (LBPA).
3. ESCRT-independent pathways: ESCRT complexes inhabitation does not block the MVB formation; therefore, MVB must be formed with some ESCRT-independent pathways as well. One proposed ESCRT-independent pathway is a ceramide-base invagination of endosomes membrane by transformation of sphingomyelin (a type of sphingolipid on endosomes membrane) to ceramide by neutral sphingomyelinase 2 (nSMase 2). Also, the MVB can be formed by the direct influence of tetraspanins CD63 protein (an endosome surface protein) without the requirement of ESCRT complex or ceramide.

**Microvesicles biogenesis:** The biogenesis of microvesicles is less well characterized. The mechanism of microvesicles formation should be similar to the mechanism used for ILVs formation inside MVBs. Therefore, one proposed biogenesis pathway for microvesicles is based on ESCRT machinery. Also, some modifications might be specifically used

for microvesicle formation. For example, the TSG101 and VPS4 subunits can be recruited by adaptor protein arrestin domain-containing protein 1 (ARRDC1). Furthermore, microvesicles might be formed by the activation of small GTPase proteins such as ADP-ribosylation factors 1 and 6 (ARF1 and ARF6) and Ras homolog family member A (RhoA). Again, similar to the IVLs formation, the ceramide generation with acid sphingomyelinase (A-SMase) activation can trigger microvesicles release.

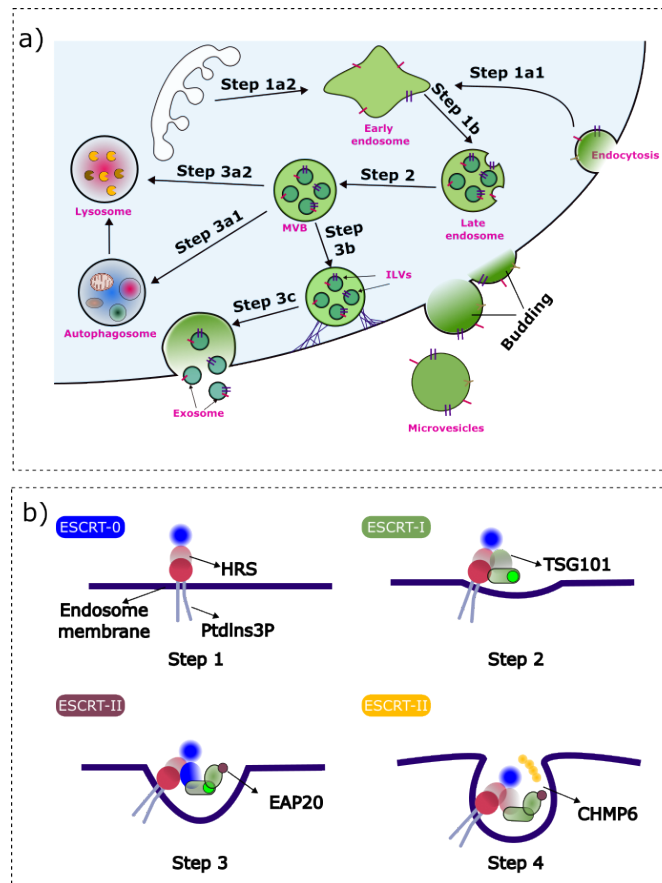


**Figure 2.2:** a) EVs biogenesis. EVs can be formed through Intra-Luminal Vesicles (ILVs) pathway which has three main steps: Step 1- Endocytosis; Step 2- MVB formation; Step 3- EVs release. EVs can be also formed through direct budding out from cells plasma membrane. b) (ESCRT) machinery is one of the main pathways for MBVs formation which has four main steps. In each step, one of the ESCRT components including ESCRT-0, ESCRT-I, ESCRT-II, and ESCRT-III attaches to the ESCRT complex.

## 2.4 General definitions for EVs analysis

EVs analysis studies can be divided into three main categories: 1- understanding EV biology; for example, which molecular factors make the cells generate more EVs, what factors affect cargo sorting into EVs, or how EVs are targeted to a specific recipient cell (e.g., how some EVs secreted by cancer cells are uptaken by T-cells) [22, 234, 235] 2- using EVs as drug-delivery systems [41, 50, 76]; 3- and using EVs for disease detection biomarker and technologies for using EVs as a disease biomarkers. New findings on EV biology or insights regarding EVs chemistry can help researchers to develop novel technologies for EV detection. Here, we focus on the technologies that have been proposed to detect EVs biomarkers. For EVs detection, researchers have two main aims: 1- isolation and purification of EVs from body fluids; 2- developing new methods and approaches for EVs analysis to increase the detection sensitivity and specificity. Sensitivity refers to a technology's capacity to **detect** the portion of EVs that carry target biomarkers (true positive) among **all** EVs in the sample that carry the target biomarkers. In other words, a highly sensitive technology has low false negatives (the EVs that carry the target biomarkers but are not detected). On the other hand, specificity refers to a technology's capacity to detect the portion of EVs that do not carry the target biomarkers among all EVs that do not carry the target biomarkers in a sample. In fact, a technology with high specificity has low false positives; in other words, the technology rarely detects EVs as a carrier of target biomarkers that they are not carrying.

Ultracentrifugation (UC) [157], chromatography (SEC) [7], ultrafiltration, and microfluidic-based methods (e.g., acoustic modulation [118], nano deterministic lateral displacement (nano-DLD) [206], and asymmetric field flow fractionation (a [204]) are well-known methods for EVs isolation from other biomolecules (e.g., proteins, ctDNA, cells). Two main features are desired for an optimum EV isolation procedure: 1- High final solution purity (low contamination) and 2- achieving the maximum number of extracted EVs with minimum EV loss (high yield). Among the aforementioned methods, UC is viewed as the gold

standard method for EVs isolation [4]. The sample is spun at high speeds ( $\approx 100,000g$ ) to separate EVs from other particles in the sample based on their density. However, recent studies show that the UC yield is low in comparison to other methods and also can damage the EVs structure [113,271]. The next most utilized method for EV analysis is SEC. In this method, the particles are separated based on their size. A sample of body fluid is loaded in a column filled with porous gel beads so that small particles such as protein can be absorbed inside. The absorption restricts the movement of the small particles; however, larger particles (EVs) can move between the beads and can exit the column faster. Commercial SEC columns are provided by IZON company (qEV columns). With this 80% of EVs can be isolated with less than 0.5% of dilution of proteins' initial concentration.

Detection technologies for EVs can be classified into two categories: diagnostic and distinguishing. Diagnostic methods enable us to accurately identify the type of molecules that EVs contain. On the other hand, distinguishing methods allow us to differentiate between samples by utilizing a unique characteristic or signature of the sample (such as EV size, surface charge, Raman spectra, and stiffness) as a type of fingerprint. While distinguishing methods may be useful for differentiating between samples, they cannot provide a definitive diagnosis of a specific disease. Consequently, many researchers are focusing on diagnostic-based methods that use molecular detection, such as polymerase chain reaction (PCR), hybridization, or next-generation sequencing. [20]).



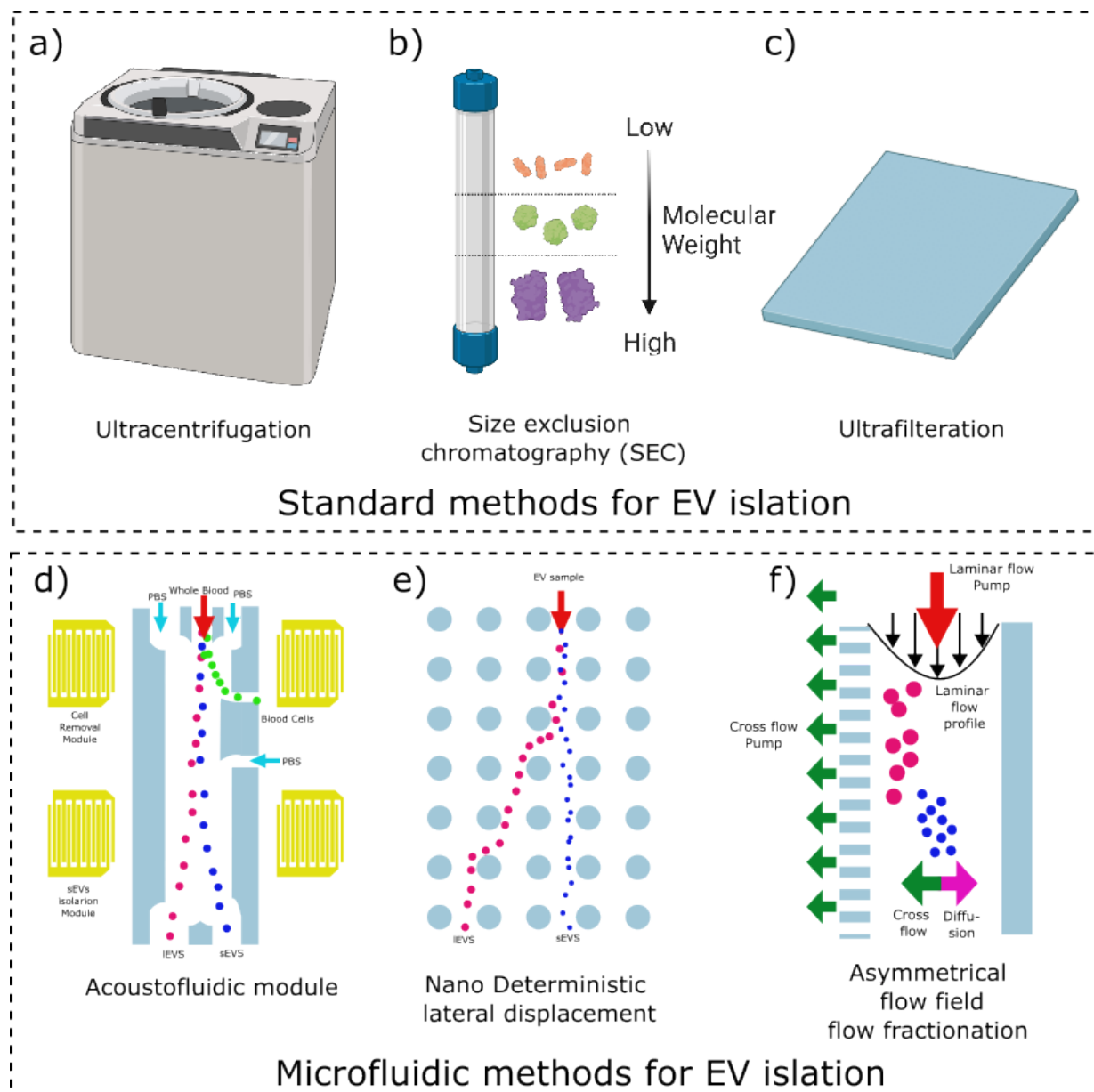


**Figure 2.3:** EV isolation methods. Three main standard methods exist including a) Ultracentrifugation, b) size exclusion chromatography, and c) ultrafiltration. Also, some microfluidic-base methods are

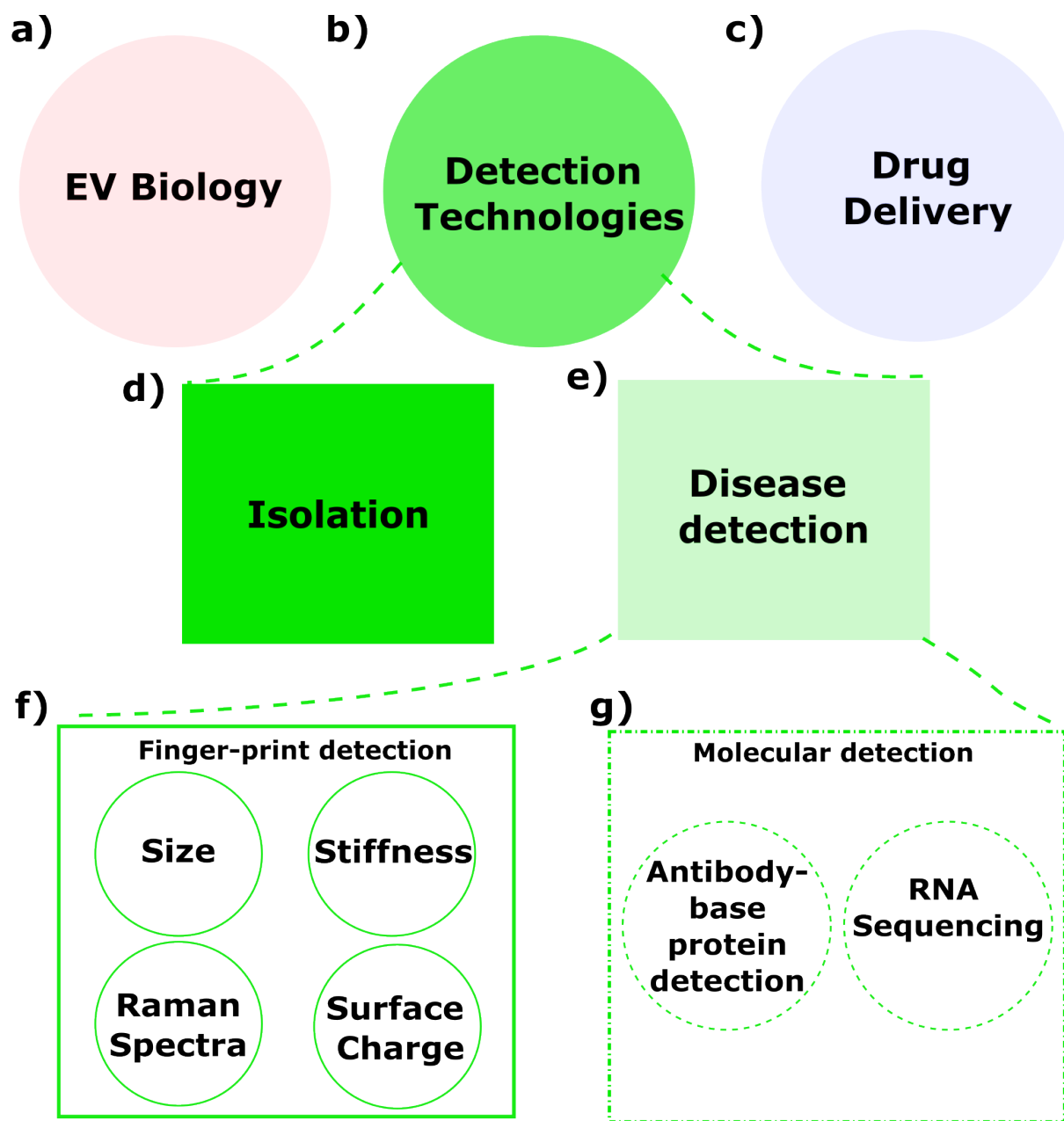


**Figure 2.4:** EV focused studies: the EVs studies methods can be divided into a) Studies of fundamental EV biology b) developing new detection technologies and c) harnessing EVs for drug delivery. The detection technologies can be sub-categorized into d) Isolation and e) developing new technologies. The new technologies proposed for EVs can be divided into two main categories: g) fingerprint methods based on different properties such as stiffness, Raman spectra, and surface charge, and h) molecular detection methods such as antibody-based protein identification, and RNA sequencing.

## 2.5 Why there is a need for high throughput multi-dimensional analysis of single EVs

**EV heterogeneity** is the principal reason why single EV technologies are needed. The heterogeneity is rooted in different sources and each of these brings different challenges for EV-base disease detection.

### **Sources of EVs heterogeneity:**

1. In addition to the exosomes and microvesicles (MV), other types of EVs can be formed in body fluid samples including apoptotic bodies (ABs), and viruses.
2. EVs can carry different surface proteins based on their size. The proteomic analysis of exosomes in different size ranges (i.e., 60 – 80 nm small-Exo and 90 – 120 nm large-Exo) show different surface protein enrichment indicating that they originate from different pathways [265].
3. Each of the sub-categories of EVs (exosomes, MVs, ABs) might be formed by different pathways. For example, as mentioned in the section for EVs biogenesis, the endosomal sorting complex required for transport (ESCRT) is one of the main pathways for protein sorting and intraluminal vesicles (ILV) formation [175]. A study showed that 20% of EVs have CD63 and MHC II surface proteins secreted by ESCRT machinery [36]. Also, exosome biogenesis can be ESCRT-independent via a ceramide-dependent pathway which allows membrane subdomain formation [229] or by tetraspanins proteins [275].
4. The size of MVs (which are directly released by blebbing from the plasma membrane) is reported to be in the range of 50 nm to 1 $\mu$ m. Similar to exosomes, the biogenesis and release of MVs are complex and different pathways may be used for the formation of MVs. One possible formation mechanism is that an increase of cytosolic Ca<sup>2+</sup> concentration near cells' plasma membrane leads to altering the flippase,

translocase, and scramblase and consequently lipid bilayer distribution and membrane blebbing [82]. Activation of P2X receptors can also cause plasma membrane blebbing. By suppressing the P2X receptors the number of EVs is decreased [224]. Some EVs are formed by combining machinery specific to different subgroups.

Cancer can be detected via single EVs analysis if the analysis is performed at a high throughput and in a multidimensional fashion. A single EV contains a signature of its parental cells by carrying specific biomolecules. For example, EVs secreted from cancer-cell might carry TGF- $\beta$  to modulate the immune system. However, other cells can also generate EVs with TGF- $\beta$  to modulate the immune system (such as stromal cells). Furthermore, the TGF- $\beta$  can be involved in several other processes including cell growth or differentiation. Therefore, the analysis of one single biomarker of a single EV would not bring enough information for reliable cancer detection. The detection of different biomarkers from a large number of individually analyzed EVs is required. Both high-throughput and multi-dimensional analysis of single EVs is required to overcome the challenge of EV heterogeneity.

**Multiplexing:** Multiplexed analysis of individual EVs addresses some of the challenges arising from EVs heterogeneity. Multiplexing can be referred to as multidimensional analysis (several proteins or several nucleic acids for a single sample) or multi-omic analysis (e.g., proteomic, genomic, lipidomic and etc). Single EVs analysis may make it feasible to quantify multiple properties extracted from a single EV simultaneously, instead of obtaining the mean value of each property from an ensemble of EVs. By averaging from an ensemble of EVs, the correlation between the biomarkers (for example a set of proteins in specific signalling such as glycolysis signalling or IL-2/Stat5 signalling) will be lost. Also, a biomarker (e.g., proteins or nucleic acids) can be carried by EVs secreted from different originating cells or formed via different pathways, and consequently, the single biomarker might not be strong evidence of the EV's origin. However, a cohesive set of properties including size, surface charge, the specific profile of proteins, N-glycosylation, lipid, and nucleic acids might provide a clear guess about the EVs origin. For exam-

ple, proteomic profiling indicates for five different cancer cell lines that exosomes in the range of 60 – 80 nm (sExo) are mainly enriched with endosomes complexes, and multivesicular bodies associated proteins (e.g., VPS28, TSG101) [235]. However, exosomes in the range size of 90 – 120 nm (lExo) are enriched with IL-2/STAT5 signalling pathway-associated proteins (e.g., ANXA4, or MYO1C). Therefore, there is a correlation between size and protein enrichment. Each of the proteins might be in both size ranges (but with different levels of enrichment) or participate in different functions; however, analysis of several proteins and combining the proteomic analysis with the size measurement might converge to understanding the functionality of a single EV.

Tumour-derived EVs are critical players in the different processes involved in cancer proliferation, including angiogenesis, and metastasis. Consequently, EVs secreted by tumor cells carry specialized molecular cargo designed to facilitate these processes. For example, 896 different proteins have been found in EVs samples from five different glioblastoma cell lines, in which, 133 of the proteins were found in all of the cell lines. Each of the proteins plays different roles including but not limited to cellular process, biological regulation and metabolic process [154]. For example, Annexin A2 (ANXA2) is a calcium-dependent protein involved in different functions such as invasion, metastasis, angiogenesis, proliferation, inflammation, and host defence [39,264]. Or, CD44 is a found GBMs derived EVs protein that interacts with hyaluronic acid and other ligands (such as osteopontin, and collagens) and plays a role in malignant processes including cell motility, tumor growth, and angiogenesis [172]. Tenascin-C (TENA) is another protein of GBM-derived EVs that functions in cell migration, inhibits focal contact formation, and promotes angiogenesis [119]. Furthermore, EGFRvIII is involved in GBM processes such as cell invasion, angiogenesis and modulation of the tumor microenvironment [32]. It is expected that the coexistence of these biomarkers with other proteins converges the EV functionality to one of certain roles. Therefore, by multiplexing the detection, we might be able to decipher the co-existence of the proteins for each single EVs and finally understand cancer cells' different activities.

The multidimensional analysis can be expanded to multiomic analysis (genomics or lipidomics as well as proteomics). It is hypothesized that there should be a correlation between the proteins and the lipid and nucleic acids that a single EV carries and the coexistence of the biomolecules defines the determined EVs fate. For example, ALIX or PDCD6IP (programmed cell death 6-interacting protein) inhibits the Ca<sup>2+</sup>-dependent program apoptosis of cancer cells [28]. In parallel, miR-21 (microRNA) can suppress cell apoptosis [54]. Also, the existence of some proteins influences the loading of miRNAs. For example, ALIX protein increases the packing and enrichment of miRNAs such as miR-21 [83].

Furthermore, a single biomarker may not provide sufficient diagnostic information. For example, KRAS mutation is reported in ovarian cancer [8,212], colorectal cancer [207], endometrial cancer [202], pancreatic cancer [18,19,51,244], and lung cancer [182,246]. By multiplexing and simultaneous detection of other biomolecules (such as proteins), the diagnostic information might converge to a specific disease. For example, the enrichment of EVs ADAM8 protein has been proposed for pancreatic cancer detection. Therefore, the coexistence of ADAM8 protein and KRAS mRNA in EVs might converge in the detection of pancreatic cancer.

**High throughput:** High throughput analysis of EVs using single EV methods addresses other challenges raised by EVs heterogeneity. High throughput analysis is required to obtain sensitive detection for three main reasons: 1- The bio-contents of EVs vary from one EV to another (each EV carry specific proteins, RNAs, and lipids, based on their functionality) [16] 2- Given the small size of EVs, the number of biomarkers carried by EVs are limited; therefore, high sensitivity is required to avoid missing the scarce markers. [56] 3- The normal cells are generating EVs as well as tumour-derived EVs; therefore, tumour-derived EVs are diluted in a body fluid relative to healthy cells-derived EVs.

Also, it should be mentioned that even low concentrations of cancer biomarkers can be also found in healthy samples. As a result, simultaneous analysis of many EVs is required for accurate and specific diagnosis and prognosis [260].

One of the most critical challenges in EV studies is that the ratio of cancerous EVs to the total number of vesicles in a sample is not yet well known [81]. One of the possible solutions for this issue is to quantify the mutated RNA or DNA encapsulated inside the EVs; however, this quantification is impossible unless quantitative analysis can be performed on a large number of EVs. [256].

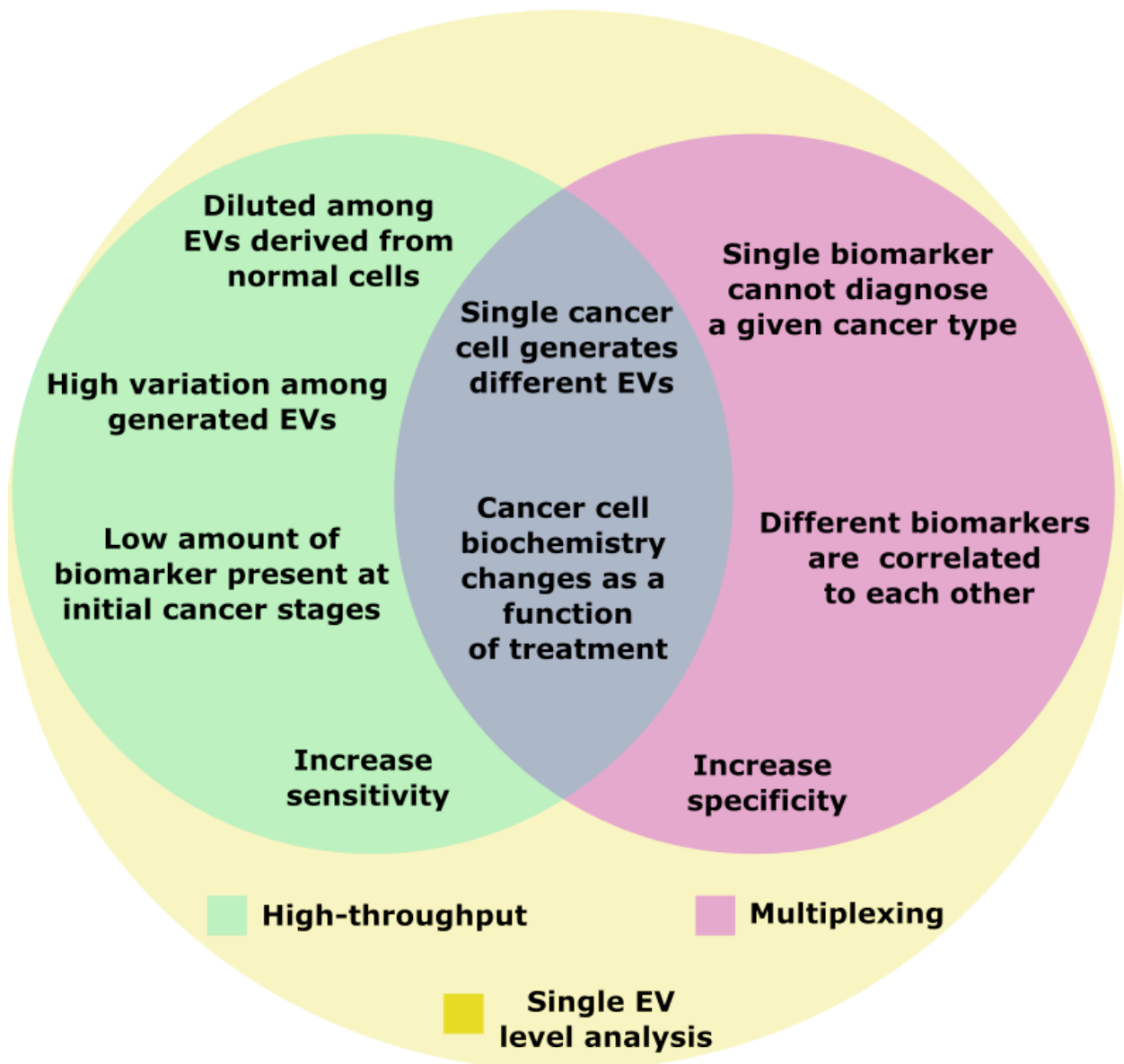


**Figure 2.5:** Single EV analysis enhances the potential use of EV-derived biomarkers for cancer diagnosis and monitoring. These capabilities can be obtained by high-throughput and multiplexed detection.



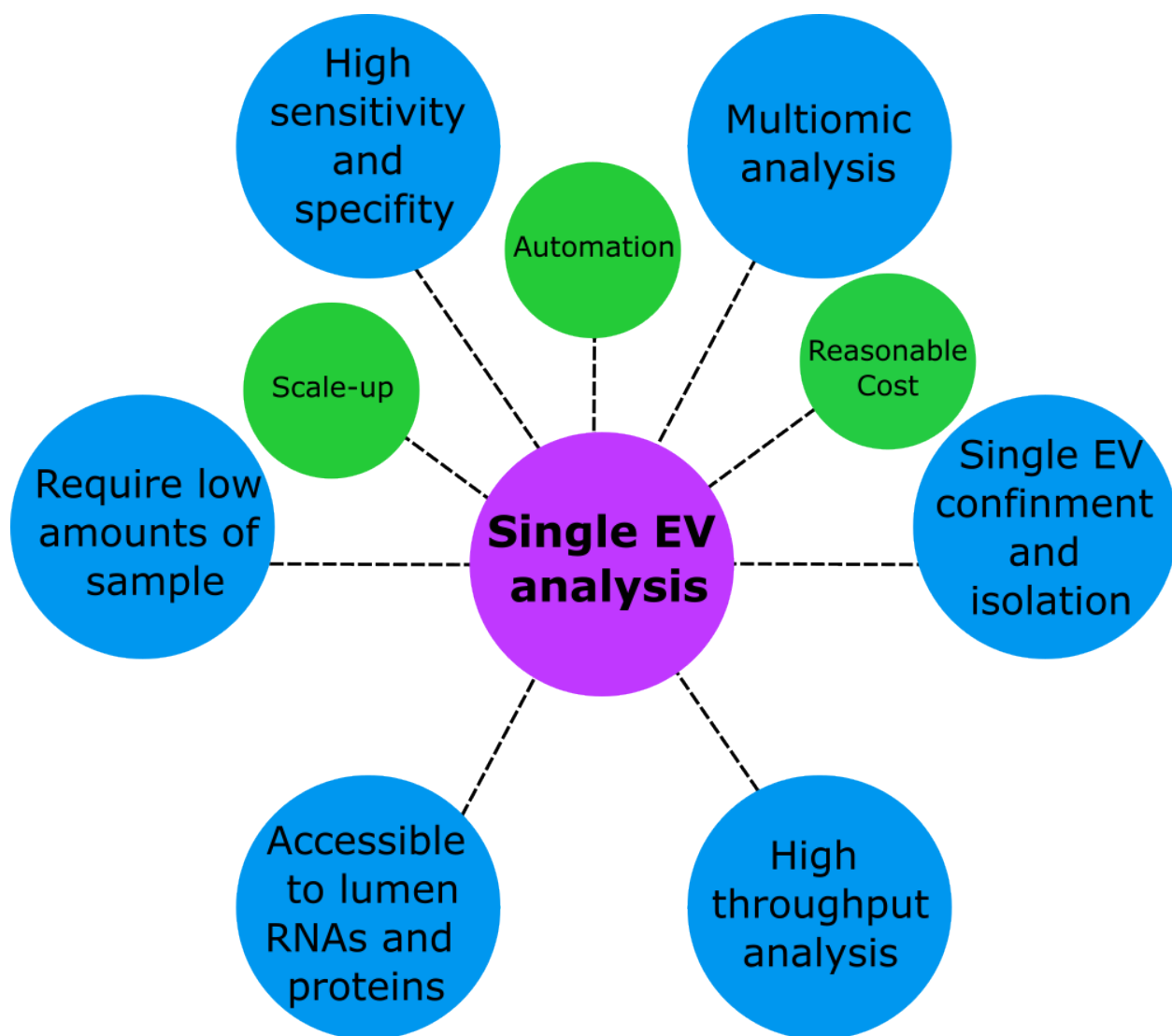


**Figure 2.6:** An ideal single EV analysis approach should be able to confine and isolate individual EVs, detect EVs molecular cargo, perform high-throughout analysis, perform multi-omic analysis, detect EVs and EV encapsulated biomarkers with high sensitivity and specificity, and work with a low amount of sample. Also, industrial scalability, automatic operation with minimum labor input and reasonable cost are desirable.

## 2.6 Characteristics of ideal single EV analysis approach

**Single EVs confinement and isolation:** Single EVs have been analyzed in confined and non-confined status. For example, in the flow cytometry method [198], the EV cargo is

targeted, and labeled fluorescently. The labeled EVs are passed through a laser beam and the emitted light is detected by a fluorescent detection camera. Although these methods provide fast and minimum background noise (as discussed "current single EVs analysis methods" section) from other particles, the analyzed EVs cannot be tracked after analysis since they are not confined and analysis of each EV will be limited to 4-6 biomolecules due to fluorescent spectra overlap existing for available fluorescent dyes. Therefore, analysis approaches that require multi-steps to target multiple cargo molecules on single EVs are challenging using methods that do not rely on confinement. Confinement of EVs provides the opportunity to track an analyzed EV for several sequential analyses. Therefore, the first step of multiplex analysis of single EV is isolation and confinement of individual EVs. Given the high EV heterogeneity, the confinement and isolation method should be able to capture all types of EVs regardless of their cargo. For example, most isolation methods utilize EVs surface proteins as an anchor via capturing antibodies and, therefore, the information obtained is limited to EVs carrying surface proteins recognized by the given capturing antibodies [47, 117, 245]. Furthermore, the isolation method should not hinder the accessibility of the detection reagents to the EVs. Some methods for single molecule analysis (e.g., droplet generation method) completely cut-off the access of other reagents to the confined EVs [99, 261]. Also, the isolation should be sufficiently strong to inhibit EV escape from their confined area. In single EV level analysis, the information from the isolated EVs can be lost or create artifacts if they can escape their confined area. Therefore, an ideal method for the EVs isolation should be all-inclusive, fully confined and simultaneously accessible by detection reagents.

**Access to encapsulated molecular cargo:** One important characteristic of an ideal single EV analysis approach is the ability to access molecular cargo encapsulated inside EVs, especially information contained in encapsulated nucleic acids. Although the phospholipid bilayer of EVs protects their cargoes (including different types of RNAs, and inner proteins) from degradation, the phospholipid bilayer hinders the accessibility of detection reagents to the capsulated cargoes. Therefore, an ideal method should be able to detect

**Table 2.2:** Throughput of well-known methods for EVs analysis

Methods	Throughput (per min)	Reference
NTA	$\approx 280\text{-}400$	[9]
Flow cytometry	$\approx 1000$	[198]
Digital Methods	$\approx 1$	[251]
Raman Spectroscopy	120	[214]
Nanoplasmonic pillars	12	[167]
Resistance pulse	2000	[238]
TIRF	$\approx 83$	[74]
DNA-Paint	$\approx 1$	[29]

the EVs encapsulated cargo as well as their surface molecules. The easiest way to access the encapsulated cargo is via lysing the EVs membrane; however, the contents can be dispersed out from the confined space and mixed with the contents of other isolated EVs. Some studies perform cross-linking (e.g., via formaldehyde) of the inner contents of EVs before permeabilizing the EVs [138, 142]. However, using a crosslinker reduces the detection sensitivity by creating a physical steric hindrance between the detection reagents and the target molecules [142]. Although cross-linking might be applicable for protein detection; using this approach dramatically decreases the interaction of polymerase with RNA/DNA molecules for further molecular amplification detection methods [75].

**High throughput analysis:** Given high EV heterogeneity, a large number of EVs are required for analysis. One study showed, in a plasma sample of pancreatic ductal adenocarcinoma (PDAC) patients in stages three and four, only 3% of EVs carry PDAC cancer biomarkers. And at lower stages, only 0.01 – 0.05% of EVs contain the known biomarker (KRASG12D) [56]. Therefore, a large number of EVs must be analyzed to find a cancer biomarker against a large background of healthy cells. The throughput of several well-known methods for EVs analysis is listed in Tab. 2.2.

A method's throughput is limited by three factors: the number of EVs that can be analyzed simultaneously, the processing time required for each measurement, and the capability of sequential analysis. The processing time mentioned in Tab.2.2 might not include the sample preparation time (i.e., the sample should be incubated with some reagents for

confinement or detection steps). Although standard versions of some methods such as flow cytometry or resistance pulse sensing [90,198] provide a very short processing time, these might not be useful for multidimensional analysis of single EVs due to single EV loss following measurement. Array confinement provides the opportunity to have a multidimensional analysis by tracking the confined EVs and having sequential steps of analysis. Detection methods such as fluorescent microscopy [117], Raman microscopy [37] that can detect several EVs simultaneously are limited to a certain number of EVs that can be detected in one step. For example, in the most compact field of view, the detection is limited to 160 thousand EVs in each step. The solution for extending the throughput is sequential measurements to increase the total number of EVs that can be measured in a solution.

**High sensitivity and specificity:** The ideal method should thus analyze the EVs with high sensitivity and specificity. The main parameter that affects the required sensitivity is the concentration of target EVs in the body fluid sample. Extensive work exists regarding EV concentration and how EV concentration is increased during cancer progression. [55]. In summary, EVs concentration is correlated to the tumor size and the type of cancer. An increase in the tumor size or stage of cancer results in a higher concentration of tumor-secreted EVs, and consequently, lower sensitivity is required. However, the survival rate decreases by increasing the tumor size and stage of cancer [153,218]. Therefore, to enhance the cancer survival rate, a higher sensitivity is required to detect EVs present at lower concentrations in early disease stages. In Tab. 2.4, the sensitivity of different EVs methods is discussed.

Regarding specificity, a proper biomarker or combination of different biomarkers (signatures) is required to distinguish tumor-derived EVs from the EVs generated from host cells. There is still no strong evidence of how many EVs in different body fluids carry tumor biomarkers tEVs<sup>+</sup>. When we look at a sample of body fluid, the total EVs (bEVs) contain the EVs generated from healthy cells (hEVs) and the EVs generated from tumor

**Table 2.3:** Sensitivity of well-known methods for EVs analysis

Methods	Sensitivity (per ml)	Reference
SPIRIS	3.94 – 5.07e9	[38]
LFIA	8.54e8	[161]
Colorimetric aptasensor	5.2e8	[254]
Electrochemical Method	4.7e8	[257]
Western Blot	1e8	[193]
SERS	1.2e6	[276]
ELISA	$\approx 1e6$	[55]
Aptasensor for Electrochemical	1e6	[272]
Electrochemical Sandwich Immuno-sensing	2e5	[46]
iMEX	$\approx e5$	[89]
Immuno-capture on GO/PDA nano-interface	5e4	[267]
SiMoA	3.4e4	[245]
Aptasensor with Expanded Nucleotide	2.09 – 3.96e4	[243]
ExoELISA	1e4	[125]
Micro-Nuclear Magnetic Resonance	$\approx 1e4$	[193]
iMER	$\approx 1e4$	[56]
DEVA	9e3	[261]
nPLEX	1e3	[86,194]
SEA	1	[117]

cells that do not carry tumor markers ( $tEVs^-$ ) as well as  $tEVs^+$  (Figure 2.4). Therefore, the concentration of EVs that carry the tumor marker  $C_{tEVs^+}$  can be expressed as:

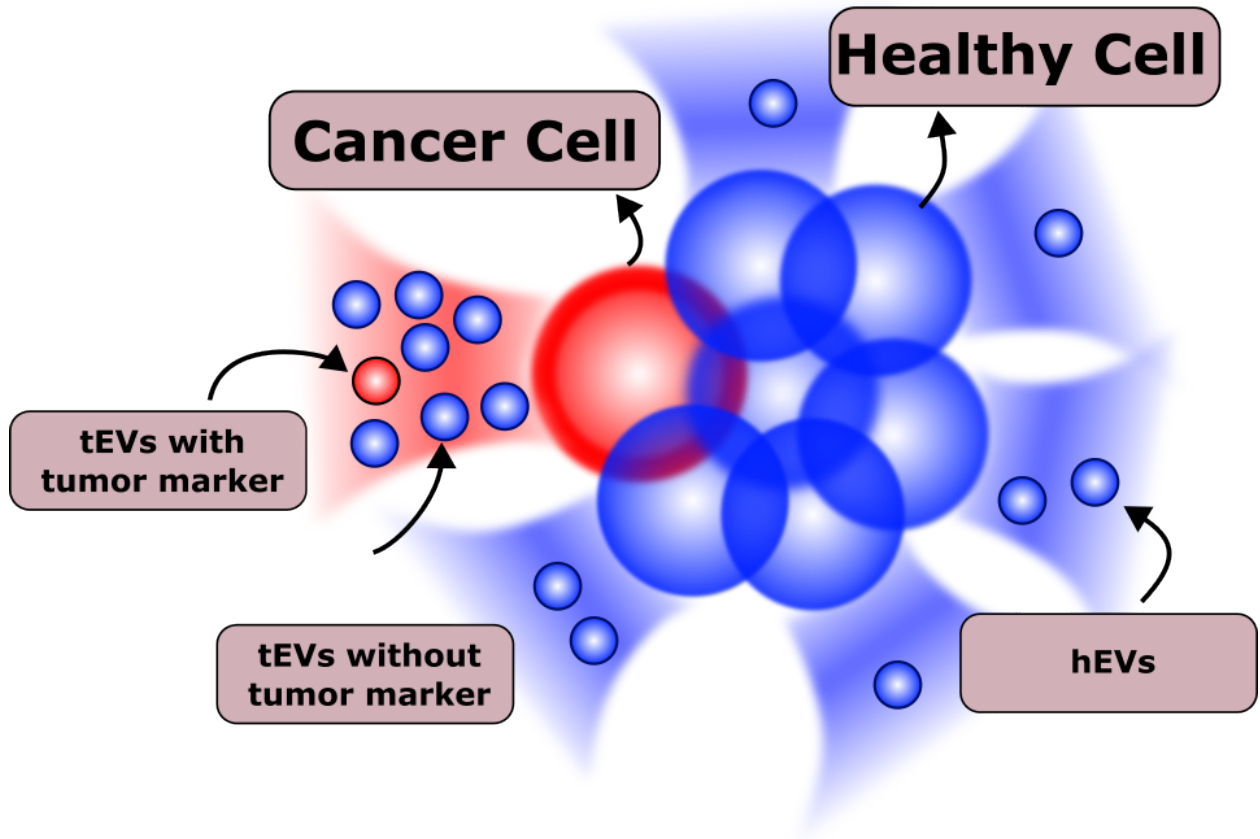


**Figure 2.7:** Cancer cells secrete EVs at a higher rate than normal cells. However, a portion of EVs released by cancer cells carry detectable cancerous markers.

$$\underbrace{C_{\text{tEV}^+}}_{\substack{\text{concentration of} \\ \text{tumor EVs} \\ \text{with cancer markers}}} = \underbrace{C}_{\substack{\text{concentration of} \\ \text{total EVs}}} \times \underbrace{\frac{V_{\text{tumor}}}{V_{\text{all}}}}_{\substack{\text{ratio of} \\ \text{tumor to} \\ \text{total body} \\ \text{tissue volume}}} \times \underbrace{\frac{R_{\text{cancer}}}{R_{\text{healthy}}}}_{\substack{\text{ratio of} \\ \text{EVs secreted} \\ \text{from cancerous} \\ \text{cells relative to} \\ \text{healthy cells}}} \times \underbrace{\frac{N_{\text{tEV}^+}}{N_{\text{tEV}}}}_{\substack{\text{ratio of tumor EVs} \\ \text{with cancer markers} \\ \text{relative to the total} \\ \text{number of tumor EVs}}}$$

(2.1)

A study does not exist predicting the concentration of EVs which carry cancer markers. However, different studies are conducted to predict each part on the right side of the equation 2.1. The concentration of EVs in a plasma sample lies in the range of  $1e7 - 1e12$  per millilitre [232]. This much variance likely arises from the different separation methods used. The degree of particle loss and separation purity varies greatly among EV separation methods [268]. Tumor tissue volume can be as small as one cubic millimetre ( $1\text{mm}^3$ ) to up to several hundreds of cubic centimetres ( $100\text{cm}^3$ ). Many studies have shown that cancer cells secrete EVs at a higher rate than normal cells. The shedding rate varies depending on the cancer type and stage.. Using modelling, the EV shedding rate of human tumor cells is obtained from experimental results in mice. The shedding rate can be  $23 \frac{\text{EVs}}{\text{ml}}$  to up to  $1900 \frac{\text{EVs}}{\text{ml}}$ . [55]. Finally, all EVs secreted from cancer cells do not carry detectable cancerous markers. Only 0.1 – 10% of EVs secreted from cancerous cells can be distinguished from EVs secreted from host cells [55].

**Multimic analysis:** EVs carry different types of biomarkers including proteins, nucleic acid fragments, and lipid structures. Also, a single EVs might contain multiple proteins or nucleic acids. In one study in which 11 surface proteins are studied on single EVs, it was found that about 60% of EVs carry more than the 11 proteins [117]. Due to the absence of technology that can perform for multidimensional analysis of single EVs, the correlation between the components of EVs is not yet well studied. However, it is hypothesized that the multidimensional analysis sheds light on the interdependency of different cell functionalities such as differentiation status, local environment, also phenotyping.

**Require a low amount of sample:** The ideal EVs analysis method should be able to work with an optimum amount of sample which depends on the type of sample (e.g., urine, blood, saliva, CSF, etc) to minimize the loss of tumour marker containing EVs. Given the scarcity of markers in the body fluids, losing the EVs in the sample (in isolation or detection steps) results in reducing the sensitivity of detection.

**Low cost, automated, industrial scalability:** Similar to any other biomarker detection devices, the EVs analysis method should be cost-effective so it can be used repeatedly dur-

ing cancer monitoring. Also, the method should be able to be automated to be extended to the Point-Of-Care (POC) to be used by a layperson as well as reduce the errors raised from a user action. In addition, the detection platform should be compact and industrially scalable so it can be mass-produced. Some methods like Raman Spectroscopy [116] or AFM-PS [239] usually need bulky detectors which limits scalability.

## 2.7 Current single EVs analysis methods

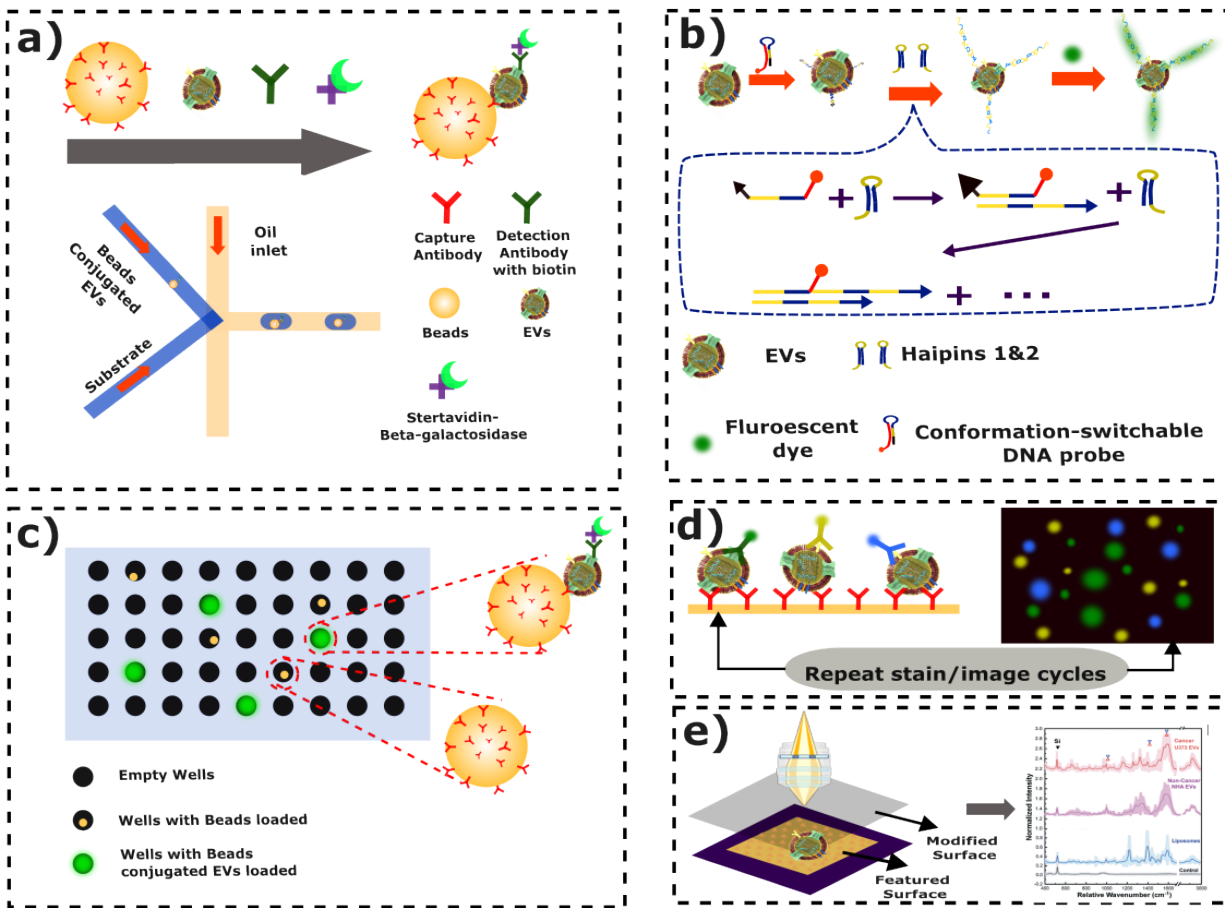


**Figure 2.8:** Current Single EVs analysis methods. a) Droplet generation method for EVs digitization [125] b) Increasing the sensitivity of flow cytometry [198] c) Single-molecule analysis method for EV isolation in microwells. (SiMoA) [252] d) EV surface immobilization [117] e) Surface-enhanced Raman spectroscopy [259].



**Droplet generation:** The droplet generation method is a well-known technology for single particle analysis. Many small and uniform droplets are generated each containing the target molecules and detection reagents including fluorescent dyes or probes which can be imaged after droplet encapsulation (Figure 2.8-a). Microfluidics provide accurate control over the size and contents of each droplet. Two immiscible fluids intersect with each other at a junction and form droplets. In the first attempt, Lie Zheng's group developed a platform called ExoELISA [261]. The number of EVs that can bond to a bead follows the Poisson distribution [67]

$$P(X = x) = \frac{\lambda_{eb}^x}{x!} e^{(-\lambda_{eb})} \quad (2.2)$$

where  $x$  is the number of EVs attached to the beads and  $\lambda_{eb}$  is the ratio of the number of EVs per bead (i.e., the average number of EVs that can bind to a bead). The probability of having 2 or more EVs on a bead will be equal to unity minus the probability of having one or zero EVs per bead which is:

$$P(X > 1) = 1 - (P(X = 0) + P(X = 1)) = 1 - (1 + \lambda_{eb})e^{(-\lambda_{eb})} \quad (2.3)$$

Therefore, if  $\lambda_{eb} = 0.1$  (10 beads per each EV), the probability of 2 or more EVs on a bead will be less than 0.5 percent. The sensitivity of the ExoELISA platform is defined relative to the background signal plus 3 times of standard deviation. Before encapsulation, the EVs are bonded to microbeads by antibodies against EV surface proteins, then each bead is placed in droplets with a ratio of 10 droplets per bead. Using the droplet method, the sensitivity is enhanced up to 10 EVs/microliter. In a recent study, EVs are encapsulated inside droplets and their surface proteins are analyzed using a platform called droplet-based extracellular vesicle analysis (DEVA) [261]. Capturing of EVs on the microbeads provides high specificity of detection ( $< 0.03\%$ ). This high specificity is obtained by the high ratio of the number of beads over the number of EVs (the optimum  $4e3$ ) and the high ratio of the number of droplets over the number of beads (the optimum 20). Using DEVA, 20 million droplets per minute can be analyzed, equal to 1 million beads per min.

The high throughput and the high ratio of beads per EVs provide a high sensitivity of up to 9 EVs per microliter. The droplets are also used to compartmentalize a detection reaction of EVs surface proteins as well as imaging of single EVs. In one study conducted by Ralph Weissleder's group, the EVs and detection molecules are encapsulated inside droplets [99]. The detection molecules are used for the barcoding of proteins. First EVs are conjugated with specific oligos coupled with antibodies to EVs surface proteins. The oligo sequences are chosen specifically for each protein. In parallel, some barcoded beads are used to increase the specificity of detection by removing the possibility of cross-talk. The barcoded beads, DNA conjugated EVs, and the master mix for amplification are loaded inside the droplet using a microfluidic device. After amplification inside the droplets, the results are sequenced using the Sanger sequencing method. The droplets, in fact, provide confined spaces to speed up the reaction as well as enhance the sensitivity. The barcoding provides the multiplexing (i.e., detection of different proteins) unlimitedly while using fluorescent imaging is limited to 4-6 dyes due to spectral overlapping.

**Cavity deposition:** Tian et al. proposed an approach for the detection of individual EVs using digital cavities [226]. The authors claim that, after checking the EVs concentration using nano tracking analysis (NTA), they can isolate single EVs by diluting solution up to one or fewer EVs per cavity according to Poisson-distribution probability. According to Poisson-distribution the probability of filling cavities will be:

$$P(n, \lambda) = \frac{\lambda^n}{n!} e^{(-\lambda)} \quad (2.4)$$

Where  $\lambda$  is the average of EVs per cavity and  $n$  is the number of EVs in a cavity and  $P$  is the probability of filling cavities with  $n$  particles while the solution contains  $\lambda$  number of EVs per cavity. It is clear that, by dilution of the sample (i.e., reducing the  $\lambda$  value), the probability of filling a cavity with more than one particle decreases. After isolation of single particles, the EVs proteins are detected using a method called Rapid Isothermal nucleic acid Detection Assay (RIDA), which increases the detection sensitivity. First, an

antibody-conjugated DNA labels the surface proteins of EVs, then, a probe attaches to the free opening of the DNA at 55°C. The probe has a fluorophore at one end and a quencher at the other end which quenches the fluorophore. A nick enzyme (N.BstNBI) that only attaches to the formed double-stranded DNAs cut the probe (separates the quencher and fluorophore) and simultaneously drops the melting temperature of the probe to room temperature or below which causes the detachment of the probe from the target DNA (the antibody-DNA which is attached to the surface protein of EVs). The separation of fluorophore from the quencher generates a fluorescent signal. The procedure of attachment of probe, detachment of nicked probe, and increasing the signal continues incessantly at isothermal temperature (55°C).

**Flow cytometry:** Xiaomei Yan's group proposed a flow cytometry device with high sensitivity for single particle analysis called High Sensitivity Flow Cytometry (HSFC) in 2014 [274] and extended the technology for the analysis of viruses in 2016 [135] and then extracellular vesicles in 2018 [127]. In the flow cytometry technique, the signal intensity depends on the diameter of particles with six-power based on the Rayleigh scattering theory:

$$\sigma_{\text{scatt}} = \frac{(2\pi^5 d^6 n_{\text{medium}}^4)}{(3\lambda^3)} \left| \frac{(m^2 - 1)}{(m^2 + 2)} \right|^2 \quad (2.5)$$

Where  $d$  is the diameter,  $\lambda$  is the wavelength of the incident light,  $n_{\text{medium}}$  is the refractive index of the medium around the particle, and the  $m$  is the ratio of the refractive index of the particle and the medium ( $m = \frac{n_{\text{particle}}}{n_{\text{medium}}}$ ). Therefore, the detection of particles with a diameter of less than 100 nm will be challenging due to the lower scattering intensity. The authors applied four main modifications to enhance the intensity: 1- using a narrow channel to bring the particles' stream concentrated in the middle of the laser beam to reduce the background noise; 2- particles flow rate is decreased to increase the laser incident time; 3- the laser beam intensity is increased to collect more photons; 4- avalanche Photo-Diode (APD) detector is used to increase the photon quantum efficiency. The technique is used to analyze EV encapsulated DNA as well as EVs surface proteins (Figure

2.8-a). They find that 30 – 80% of EVs carry dsDNA some of them simply bonded to the surface of EVs (external DNAs) and some of them are encapsulated inside the EVs (encapsulated DNAs). In other studies, instead of improving the quality of FCM machine, the sample is modified to increase the fluorescent intensity from the target molecule. In one study [198], the hybridization chain reaction (HCR) is used to increase the size of EVs up to 500 nm as well as enhance the fluorescent signal (Figure 2.8-b). In the HCR used method, three main components are used: 1-a conformation-switchable probe (T1) 2-first hairpins (H1) 3-second hairpins (H2). The first and second hairpins (H1, and H2) carry fluorescent tags. First, T1 binds to the target protein by anti-target protein aptamer sequences of the probe. The probe is opened by attaching to the target protein and provides the initiator sequences of the HCR amplification. Next, H1 is opened by finding the initiator and consequently opens up the second hairpin (H2). The opened H2 hairpin again opens another H1, and this procedure sequentially continues. The sequential attachment of the hairpins increases the fluorescent tags' hybridization to the target molecule and consequently enhances the fluorescent intensity. The authors detected the human epidermal growth factor receptor 2 (HER2) and CD63 on extracellular vesicles and observed the heterogeneity of EVs in different breast cancer cell lines Figure 2.5-b.

**Raman Spectroscopy:** If a material is illuminated with a light, a portion of the light will be scattered with a different frequency than the illuminated light; this is known as Raman Scattering (RS). By measuring the intensity and frequency of the scattered light, the vibrational modes of the sample can be determined (Figure 2.8-e). The vibrational modes of molecules are correlated to the atoms and bonds within the molecule. For example, the stretching and bending of chemical bonds vibrate the molecule at specific frequencies. Therefore, by performing a RS analysis, we can get information about the chemical bonds that exist in the sample. For example, it is discovered that the scattered light from a biological sample at Raman shifts (1466, 1440, 1378, 1256, 1050)  $\text{cm}^{-1}$  represents the origin of lipid structures in the sample [116]. For the first time, I. Tatischeff et. al. [220] used RS for the EVs analysis of in human urine sample. The first RS approaches suffered from three

limitations: 1- low throughput 2- low sensitivity, 3- immobilization limitation. The sensitivity of RS is enhanced using optical resonance phenomena called Surface-Enhanced Raman Spectroscopy (SERS) by creating geometrical features in the range of incident light wavelength length (300 – 700 nm). L. Tirinato et al. [227] used SERS for the detection of EVs by creating super-hydrophobic pillars in which EVs accumulate on top of the pillars. After that, different geometries have been applied to create the optical resonance including gold nanoparticles [97], an array of nano-bowls [116], an array of pyramids [259], macroporous inverse opal (MIO) [48], nano-wire [47], and an array of nanocavities [37]. These nanofeatures increase the sensitivity and enable single EV capture and immobilization. In one approach, a single particle automated Raman trapping analysis (SPARTA) platform is developed to increase the throughput of the measurement [166]. The SPARTA system works based on a featured confocal Raman spectroscopy in which the laser, camera and spectroscope are controlled using MATLAB scripts simultaneously [167].

**Single Molecule Assay (SiMoA):** SiMoA is a technology used to analyze single EVs released by different cancer types [121, 149, 222, 245]. SiMoA technology was first developed for the detection of low protein concentrations with high sensitivity Figure 2.8-c. The high sensitivity is achieved by capturing target proteins on the surface of immuno-magnetic beads and digitalization of the beads inside an array of cavities. The method is commercialized by Quanterix. By capturing proteins in a single level, the sensitivity is increased 900 times (i.e., the LOD improved to  $0.01 \frac{\text{pg}}{\text{ml}}$  of protein) [183]. In this method, the paramagnetic beads labelled with target antibodies are added to the body fluid sample (e.g., urine, saliva, CSF, etc.). Then, the captured molecule is detected with a second antibody coated with biotin and fluorescent tags conjugated with streptavidin. Usually, a higher number of beads are added to the sample (e.g., 500,000 beads in 60, 000 target molecules in 100 $\mu$ L of the sample); therefore, a large portion of the beads do not contain bound the target proteins. Then, the beads are loaded on a platform which contains 239,000 wells with 4 $\mu$ m diameter and 3 $\mu$ m depth using gravity and sealed by oil. The platform has the ca-

**Table 2.4:** Throughput of well-known methods for EVs analysis

Target molecules	Conclusion	Reference
PD-L1+ EVs in Lymphoma patients	PD-L1+ EVs are rich in the plasma of diffuse large B-cell lymphoma patients	[120]
CD9+/CD63+ EVs in breast cancer patients	The concentration of CD9+/CD63+ EVs is about two times higher in Breast cancer patients	[149]
CD9-CD63 +EVs and Epcam-CD63 +EVs in 5 different cancer	AUC of 0.96 and 0.90 for CD9-CD63+ and Epcam-CD63+ EVs	[245]
CD9/CD63/CD81 in healthy plasma and CSF	The optimized method for isolation of EVs	[222]
Epcam-PD-L1 +EVs in lung cancer patients	The quantification of PD-L1+EVs can predict the lung cancer tumor proportion score (TPS)	[252]
L1CAM+ EVs in healthy plasma and CSF	L1CAM is not associated with neuron-derived EVs	[158]

pability to detect four fluorescent dyes simultaneously. Researchers have found different interesting properties of EVs using SiMoA technology discussed in table 2.4:

**Single EVs Analysis (SEA):** One of the best well-known methods for single EVs analysis is the immobilization of EVs on a substrate using capture antibodies followed by assessment of EV surface protein content via adding fluorescently tagged antibodies (Figure 2.8-d). The immobilization of particles on a surface increases the signal to noise ratio (SNR) in comparison to when the particle is suspended in a solution [98]. This approach can enhance the sensitivity of the detection up to 1 EVs per microliter [117]. First EVs are biotinylated for immobilization on the substrate surface then fluorescently tagged antibodies are loaded above the sample. The main feature of this technology is the unlimited multiplexing assessment of single EVs. The multiplexing is achieved by serial staining and quenching rounds. In each round, three surface proteins are targeted with three fluorescent dyes and then quenched to be ready for the second round by injecting an oxidation buffer. Using the method, 11 surface proteins on EVs secreted from a glioblastoma cell line are assessed. The multiplex measurement provides information about the interde-

pendency of different cell states and functionalities including differentiation status, local environment, also phenotyping. This type of information is missed by ensemble-level analysis.

**EVs mechanical properties:** are correlated with different cellular functionalities including cell adhesion, the uptake of cells, and mechanosensing [262]. Force Spectroscopy (FS) analysis implemented via an Atomic Force Microscope (AFM-FS) was first applied to study the mechanical properties of liposomes [239]; this approach was then extended to EVs [240]. The mechanical properties of EVs depend on two main components 1: lipid bilayer structure and 2- intraluminal proteins. In the first study, EVs in the blood sample of hereditary spherocytosis (HS) patients were compared with healthy individuals. They observed that although the red blood cells of HS patients have higher stiffness than healthy ones, the EVs of HS patients are softer than healthy individuals. In the first attempt, the measurements were obtained using FS which required long analysis times since in the FS method the AFM tip approaches and then is required to probe a single target point. Francesco Valle's group, instead of using AFM-FS, used standard AFM. In the standard AFM method, by raster scan of the substrate instead of poking a target point used in AFM-FS, the topography and size of EVs as well as their mechanical properties can be measured. Although this method provides "semi-quantitative" information, several hundred single EVs can be analyzed in one hour. The EVs from three different sources were distinguished using the regular AFM method, and the EVs can be discriminated from sample contamination (e.g., proteins) left over from the EV isolation step [181].

# Connection between Chapter 2 and 3

In this chapter, we discuss the fundamental knowledge and background information used in both manuscripts in chapters 4 and 5. First, the electrostatic energy minimum between two parallel charged plates is discussed and modelled via the Poisson-Boltzmann equation. Next, we elaborate on the use of Langevin Eq. and Kramer's theory to model particle Brownian motion and thermal escape from nanowells. We also discuss the design and fabrication of pneumatically actuated membrane devices. Next, the EVs separation method used in this thesis will be illustrated and a short background of the field of EVs isolation is provided. Finally, a short discussion on the working principle of the two isothermal amplification methods (LAMP and RCA) used in the second manuscript is provided.



## Chapter 3

# Background

### 3.1 Nanoparticle Confinement in Electrostatic Energy Wells

**Electric double layer:** A charged surface in contact with an ionic solution induces a gradient of electrostatic potential inside the solution. Counter ions, ions opposite in charge to that of the surface, adsorb directly at the surface and form a layer with a thickness on the order of the ion size; this is called the Stern layer [165]. Beyond the Stern layer, the mobile ions in solution are attracted by the charged surface. The concentration of counterions is elevated near the surface and the concentrations of coions decreased, with electroneutrality holding in bulk solution far from the surface. Within the diffuse layer, the electric potential decays exponentially with distance from the surface. The diffuse layer thickness is defined as the distance from the surface where the electrical potential decays to  $1/e$  (0.37) of its maximum value at the surface (technically, surface of shear).

The model used for electrostatic potential estimation is the Poisson-Boltzmann (PB) equation. PB equation is derived from the Poisson equation, which describes the electrostatic potential created by a distribution of charges, and the Boltzmann distribution, which describes the probability of finding a particle in a given energy state at a given temperature. The general Poisson equation is:

$$\nabla^2 \Psi(r) = -\frac{\rho_e}{\epsilon_r \epsilon_0} \quad (3.1)$$

where  $\Psi(r)$  is the electrical potential,  $\rho_e$  is local electric charge density,  $\epsilon_0$  is vacuum permittivity constant ( $8.8542 \times 10^{-12} \text{F/m}$ ) and  $\epsilon_r$  is the permittivity of solution (for water equal to 80). local electric charge density  $\rho_e$  is given by:

$$\rho_e = e(c^+ - c^-) \quad (3.2)$$

where  $c^+$  and  $c^-$  are the concentrations of cations and anions, respectively, and  $e$  is the elementary charge ( $1.6 \times 10^{-19} \text{[C]}$ ). Using Boltzmann's equation, the ion concentration is calculated by:

$$c_i = c_i^0 e^{\frac{-W_i}{k_B T}} \quad (3.3)$$

where  $c_i^0$  is the ion concentration in bulk solution,  $W_i$  is the work needed to bring an ion closer to the surface from an infinity,  $k_B$  is the Boltzmann constant ( $1.38 \times 10^{-23} \text{J/K}$ ) and  $T$  is the temperature (assuming room temperature  $T = 298 \text{K}$ ). For the electric double-layer phenomenon, electrical work can be considered as the only source of  $W_i$ :  $W_i = \pm e\Psi$  where  $W_i$  is correlated with the positive and negative sign of the electrical potential for cations and anions, respectively. By substituting the work in Boltzmann equation:  $c^+ = c^{0+} e^{\frac{-e\Psi}{k_B T}}$ , and  $c^- = c^{0-} e^{\frac{e\Psi}{k_B T}}$ . If we hypothesize that the solution is composed of 1:1 salts (i.e., constituent salt consists of two types of ions in equal proportions):  $c^{0-} = c^{0+} = c_0$ , then the local electric charge density ( $\rho_e$ ) can be written as:

$$\rho_e = c_0 e \left[ e^{\frac{-e\Psi}{k_B T}} - e^{\frac{e\Psi}{k_B T}} \right] \quad (3.4)$$

By substituting the electric charge density in Eq. 3.1, the Poisson-Boltzmann equation is given by:

$$\nabla^2 \Psi(r) = \kappa^2 \sinh(\Psi(r)) \quad (3.5)$$

$\kappa$  is the inverse Debye length. The inverse of Debye length is correlated to the solution ion concentration using the equation:

$$\kappa = \sqrt{\frac{2c_0 e^2}{\epsilon_0 \epsilon k_B T}} \quad (3.6)$$

As can be seen, the Debye length is proportional to the inverse square of ion concentration ( $\frac{1}{\sqrt{C}}$ ) and the Debye length decreases when ion concentration increases.

**Poisson-Boltzmann equation:** One of the best methods for solving the Poisson-Boltzmann is via Finite Elements. In this numerical method, the geometry is discretized to finite elements (meshing) and the Poisson-Boltzmann equation is solved along the mesh. Using the available commercial Finite Element packages (e.g., COMSOL Multiphysics), complex geometries can be meshed by the packages' graphical user interfaces. Here, the Poisson-Boltzmann equation is solved using COMSOL Multiphysics package with the PDE solver module used to calculate the electrical potential distribution induced by a surface charge. The boundary condition in this simulation is a Dirichlet boundary condition (i.e., the electrical potential is specified as a known value at the solution-surface interface and very far from the surface considering infinite boundary conditions which can be applied in COMSOL multiphysics). The results shown here use  $C = 0.5 \text{ mol/m}^3$ . As mentioned, the Debye length is the distance from the surface that the electrical potential reduces to  $1/e$  of its maximum value which in this calculation agrees with the value obtained from Eq. 3.6 and is equal to 13.7 nm (red point in Figure 3.1-b).

In the limit of low surface potential the PB equation can be linearized and has an exact exponential solution. Considering the case of low potential ( $e\Psi \ll k_B T$ , or  $\frac{e\Psi}{k_B T} \ll 1$ ), by writing the Maclaurin series of exponential function and neglecting the higher order terms (i.e.,  $e^{-x} = 1 - x$  when  $x \ll 1$ ), the Boltzmann equation (Eq. 3.4) can be approximated by:

$$c_i = c_i^0 \left[ 1 - \frac{W_i}{k_B T} \right] \quad (3.7)$$

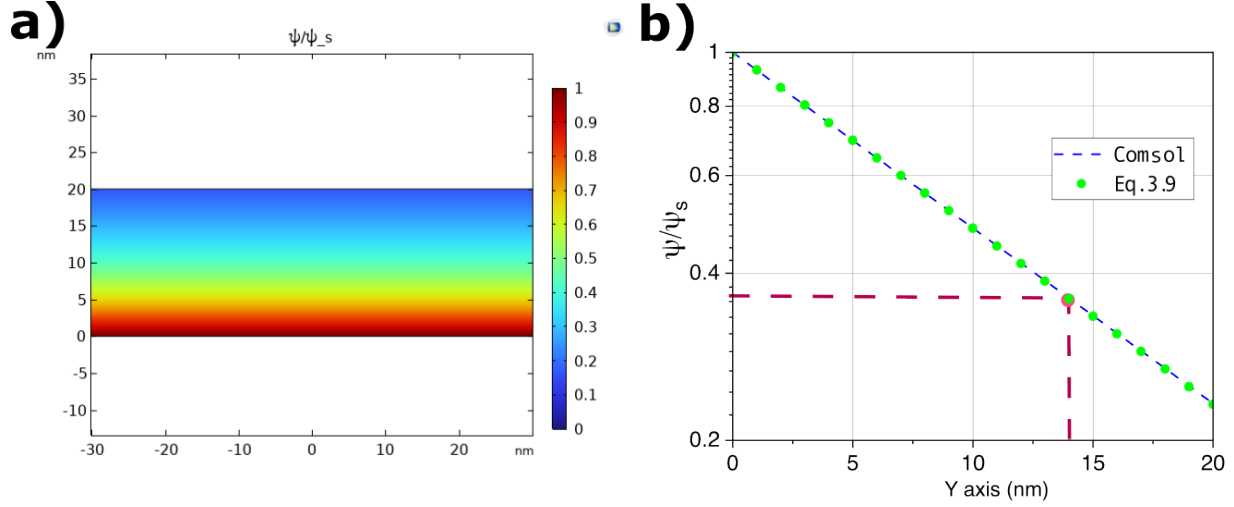


**Figure 3.1:** Finite element calculation of an electrical potential distribution at the interface of a charged surface with an ionic solution obtained by solving the Poisson-Boltzmann equation. a) Color map of electrical potential normalized to the electrical potential at the surface. b) Electrical potential versus distance away from surface.

Therefore, the nonlinear PB equation (Eq. 3.4) will be simplified to the linear PB equation as:

$$\nabla^2 \Psi(r) = \kappa^2 \Psi \quad (3.8)$$

In case of a planer surface (i.e., 1D modeling), two boundary conditions can be considered as  $\Psi(x = 0) = \Psi_s$  and the  $\Psi(x = \infty) = 0$ , and the Eq. 3.8 has a exact solution as:

$$\Psi = \Psi_s e^{-\kappa z} \quad (3.9)$$

Where  $z$  is the vertical distance from the surface and the  $\Psi_s$  is the surface electrical potential. In Figure 3.1-b, the blue line is the electrical potential obtained from Eq. 3.9 which is very close to the results of the Poisson-Boltzmann equation. If the assumption  $e\Psi \ll k_B T$  is not valid, the solution for linearized PB equation (Eq. 3.9) is still valid for electric potential at sufficiently far from the surface. In the general solution of PB equation for a plane surface and 1:1 solution, the exponential prefactor in Eq. 3.9 is a complex function of var-

ious parameters, including surface electrical potential [15]; the prefactor will converge to  $\Psi_s$  if  $z \rightarrow \infty$ .

### Minimum energy between two parallel like-charged plates:

If two like-charged surfaces are placed in proximity, the electrical potential is maximum at both surfaces and there will be a minimum value in the middle of the two surfaces (Figure 3.2-a). If the gap (the distance between two plates) is 40 nm ( $2h=40$  nm, in which the  $h$  is half of the gap between the plates), the minimum electrical potential will lie at 20 nm distance from each plate. In this case, if a like-charged particle is placed between the plates and interacts with the electrical potential, it will come to an equilibrium position at the midplane between the plates. (Figure 3.2-b). The electrical potential of the

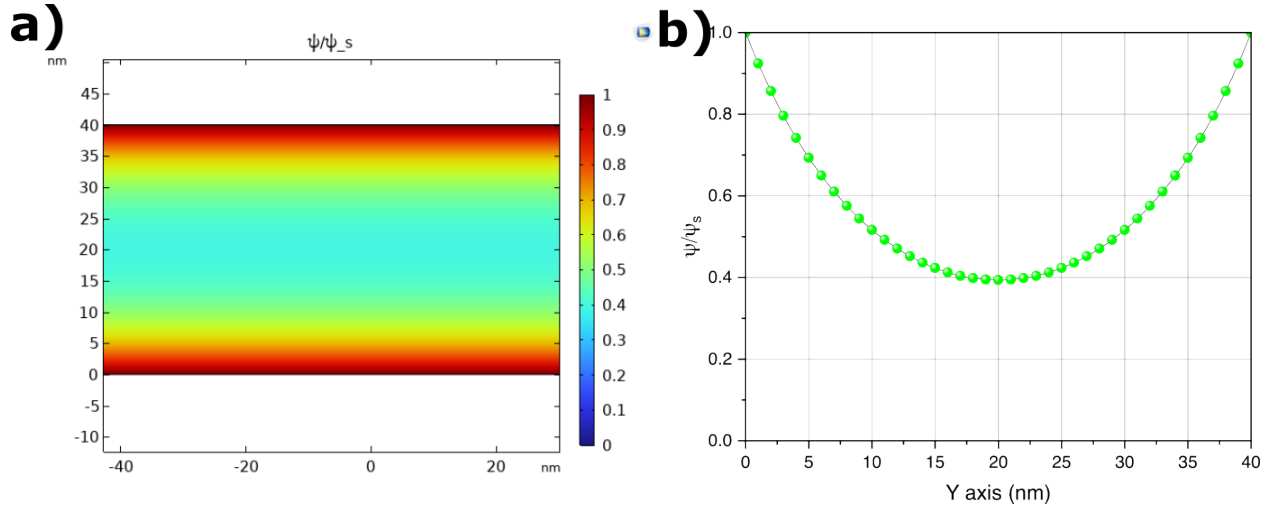


**Figure 3.2:** Electrical potential between two parallel like-charged plates. a) Colormap corresponding to the electrical potential of two plates at a 40nm separation. b) The electrical potential normalized to surface potential plotted along the vertical axis from the lower plate.

two parallel like-charged plates can be obtained from the superposition of the electrical potential of each plate, if the plates are far enough, as:

$$\Psi = \Psi_s(e^{-\kappa z} + e^{-\kappa(2h-z)}) \quad (3.10)$$

The quantity  $h$  is half of the gap between the plates. The value of the minimum energy between the plates is related to the gap value. By increasing the gap distance, the electrical potential will have more chance to be dropped and consequently, the electrical potential at the minimum position will be lower (Figure 3.3). The dependence of the electric poten-

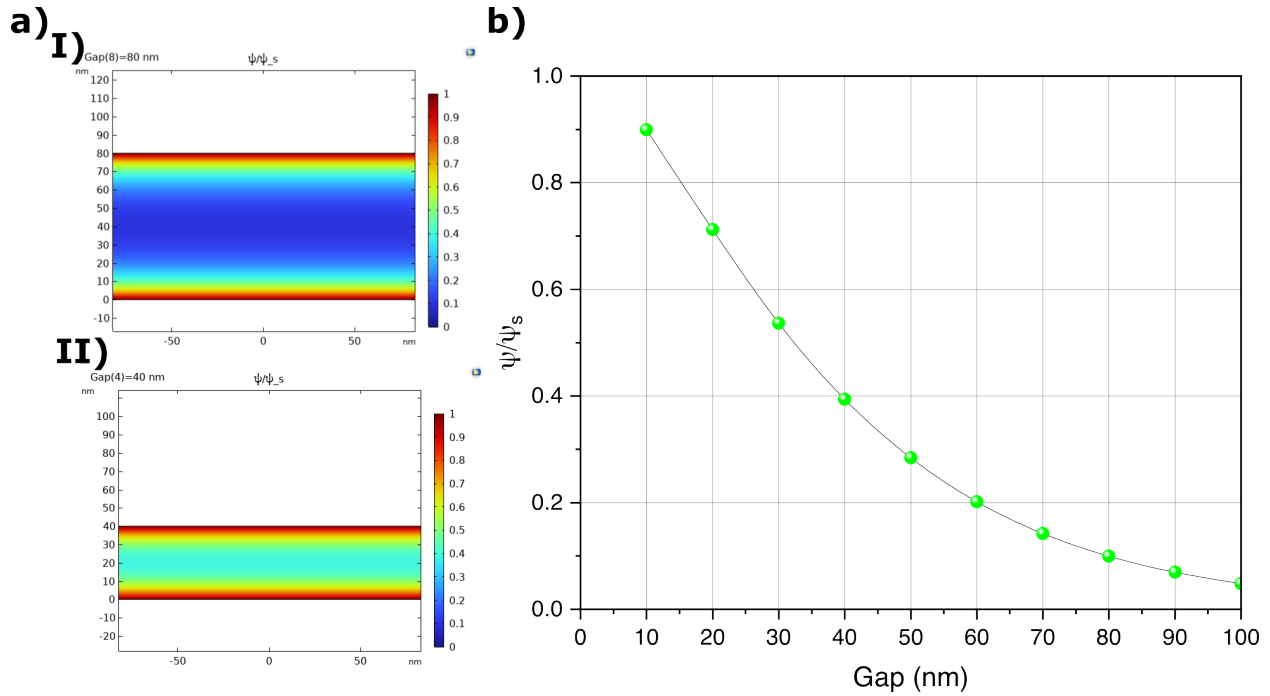


**Figure 3.3:** the electrical potential between two like-charged plates as a function of gap height. a) colormap of the electrical potential at I) 80 and II) 40 nm slit heights. b) The minimum electrical potential normalized to surface potential versus different slit height values.

tial minimum on the gap height implies that the potential experienced by a like-charged particle can be tuned by modulating the slit height. This might be accomplished, for example, by etching structures in the slit, say local cavities where the gap height is greater. If a like-charged particle is placed between the two plates, the particle will tend to jump into the deeper cavity due to the cavities lower electrical potential, so the cavity will act as a local electrical potential well for the particle \*see Figure 3.4). As the minimum energy inside the cavities is almost negligible in comparison to the minimum potential outside the cavities (Figure 3.6), the depth of the potential well can be considered equal to the

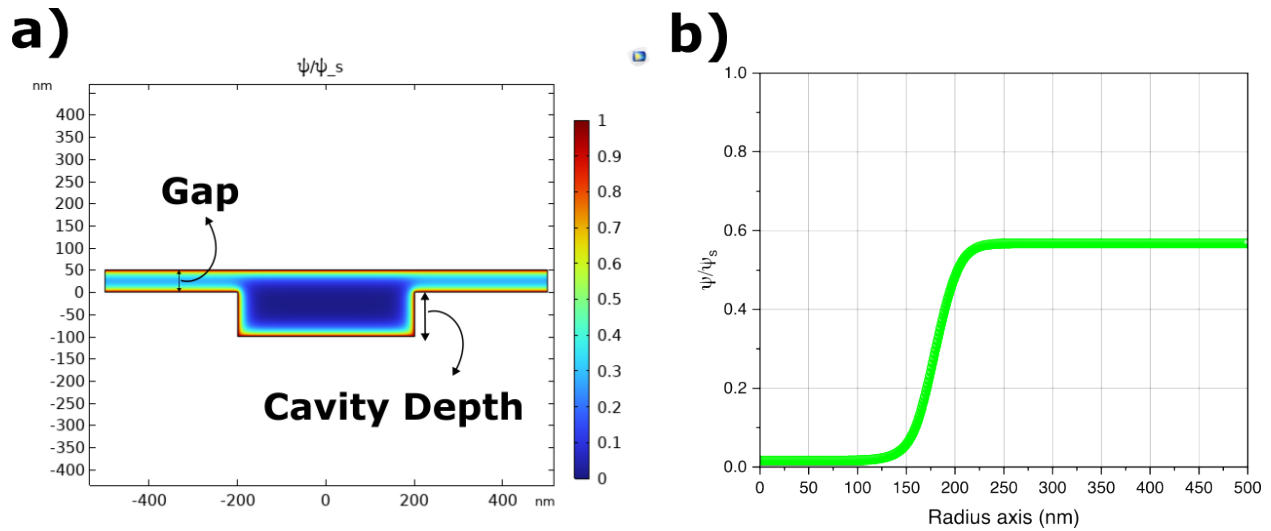


**Figure 3.4:** local minimum energy induced by creating nanocavities embedded in the slit. a) colormap of minimum energy b) minimum energy along the cavity radius. In this simulation, the depth of the cavity is 100 nm, and the gap is 50 nm.

minimum energy in the slit surrounding the cavities. The potential well depth is therefore decreased by increasing the gap height (Figure 3.6)

## 3.2 Brownian motion of nanoparticles

Nanoparticles experience thermal fluctuations due to their interaction with the solvent molecules. These fluctuations cause the nanoparticles to undergo Brownian motion which can be simulated using the Langevin equation.

**Langevin Equation:** The Langevin equation given by:

$$m \frac{dv}{dt} = F_D + F_E + F_T(t) \quad (3.11)$$

Here  $F_D$  is the drag force that the particle experience when moving in solution,  $F_E$  is the force generated by external sources (e.g., the electrostatic fields) which is given by the electric potential gradient and  $F_T$  is the random force generated by thermal fluctuations. In low Reynolds number flow, the drag force that a nanoparticle experiences is given by

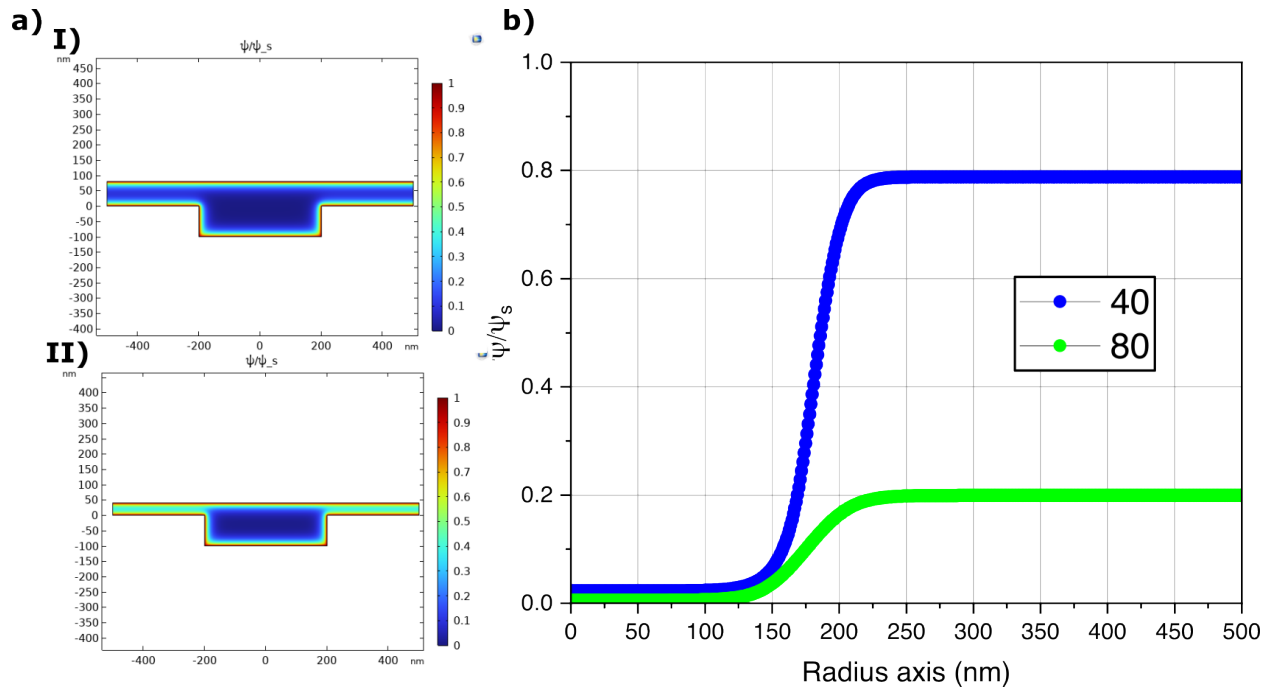


**Figure 3.5:** The electrical potential between two like-charged parallel plates with embedded nanocavities with different gap heights. a) Colormap of electrical potential for plates with I) 40 and II) 80 nm gap and b) minimum electric potential versus radial coordinate from the center of cavities for the two gap heights.

Stoke's law:

$$F_D = -\gamma v \quad (3.12)$$

with  $v$  is the particle velocity and  $\gamma$  is the friction coefficient. The reason that the drag force has a negative sign is that every time the particle moves in the + direction, the drag force applies in the – direction, and vice versa; in other words, the friction force always points in the direction opposite to that which the particle is moving. The friction coefficient is dependent on the particle geometry. For a hard spherical particle, the friction coefficient is:

$$\gamma = 6\pi\eta R \quad (3.13)$$

where  $\eta$  is the viscosity coefficient of the solution that the particle is suspended in, and  $R$  is the radius of the spherical particle.



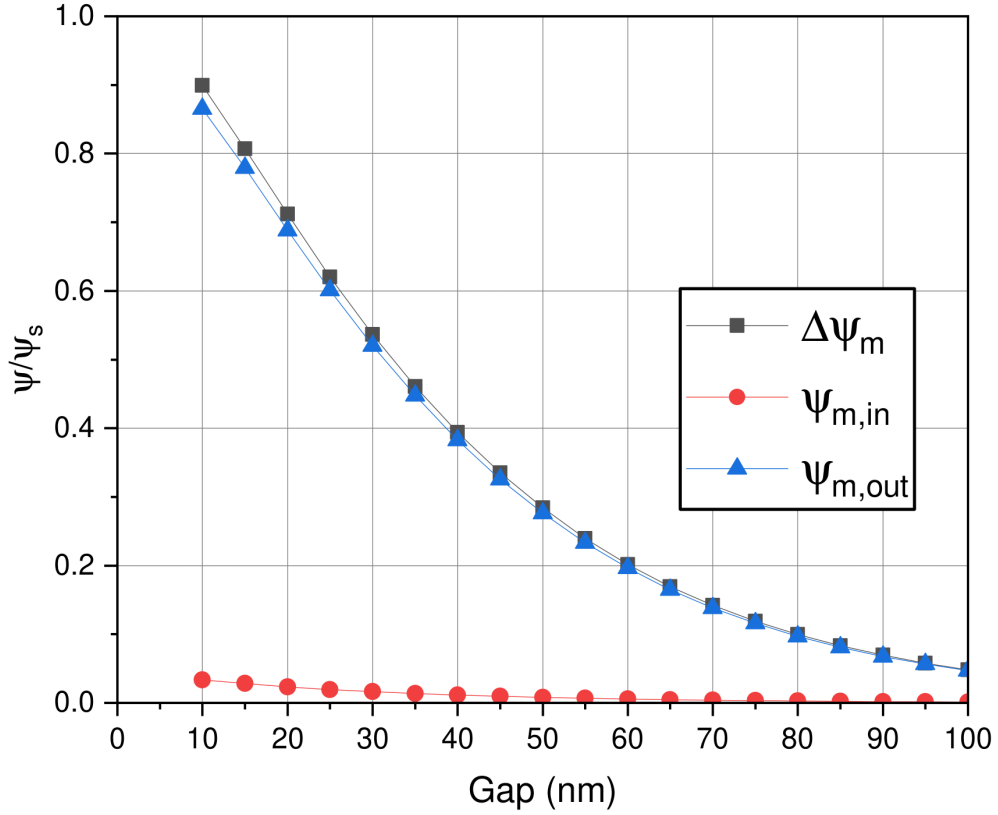


**Figure 3.6:** Electrical potential inside and outside of the cavity and the depth of potential well induced by the cavity.

Since, in equilibrium, the particle motion is purely Brownian, the probability of particle movement in the positive direction is the same as in the negative direction, and the average of the force must be zero:

$$\langle F(t) \rangle = 0 \quad (3.14)$$

The thermal fluctuations at a given time must be independent of their value at times before and after. This property is quantified via the time-correlation function:  $\langle F(t)F(t') \rangle$ . The time correlation function shows how fast the function forgets its value at time  $t$ . When the time step  $(t' - t)$  is much shorter than the correlation time, the function value will remain almost unchanged; in other words:  $\langle F(t)F(t') \rangle = \langle [F(t)]^2 \rangle$ . But, when the time step

is much greater than the correlation time, the function completely forgets its value at time  $t$ , and  $F(t')$  is uncorrelated with  $F(t)$ . This means the probability that the  $F(t)F(t')$  is positive is the same as the negative; consequently,  $\langle F(t)F(t') \rangle = 0$ . The question is that what is the value of  $\langle [F(t)]^2 \rangle$  [94]. To answer this question, we can simplify the Langevin equation to a first-order differential equation by ignoring the external source:

$$\dot{v} = -\gamma v + F(t) \quad (3.15)$$

By considering the initial condition as:  $v(0) = v_0$ , the answer is:

$$v(t) = v_0 e^{-\gamma t} + e^{-\gamma t} \int_0^t F(t') e^{\gamma t'} dt' \quad (3.16)$$

Considering the fact that  $v_0$  is independent of  $F(t')$  and  $\langle F(t) \rangle = 0$ , by squaring the equation we can get:

$$\langle v(t)^2 \rangle = v_0^2 e^{-2\gamma t} + \frac{F(t')^2}{2\gamma} (1 - e^{-2\gamma t}) \quad (3.17)$$

Based on the kinetic theory, the mean square velocity is equal to  $k_B T$ , and:

$$\langle F(t)^2 \rangle = 2\gamma k_B T \quad (3.18)$$

In conclusion, the  $F(t)$  can be written as:

$$F(t) = \sqrt{2\gamma k_B T} w^*(t) \quad (3.19)$$

Which  $w^*$  is the noise function satisfying two criteria:

$$\langle w^*(t) \rangle = 0 \quad (3.20)$$

$$\langle w^*(t) w^*(t') \rangle = \delta(t - t') \quad (3.21)$$

Regarding the dimension of the noise function, the units of  $\sqrt{2\gamma k_B T}$  are  $\text{kgm/s}^{3/2}$ ; therefore, the unit of  $w^*(t)$  must be  $1/\text{s}^{(1/2)}$  to satisfy dimensions on both sides of the equation.

If there is a gradient of potential energy, the particle experiences a net force. The is given by:

$$F_E(x) = -\nabla W(x) \quad (3.22)$$

where  $W$  is the potential energy. In this thesis, the most dominant potential energy comes from the electrical potential field induced by charged surfaces. The energy is related to the particle surface charge (which is an intrinsic property of the particle – not induced) as well as the electrical potential. The potential energy induced by the electrical potential is given by:

$$W(x) = q_{\text{eff}}\psi_m(x(t)) \quad (3.23)$$

In most cases, the acceleration damps very fast (overdamped condition) and the applied force and the drag force reach an equilibrium condition in nanoseconds. Therefore,  $\frac{dv}{dt} = 0$ , and, by bringing the drag force right side of the equation to the left side, we reach the following overdamped version of the Langevin equation:

$$-F_D = F_E + \sqrt{2\gamma k_B T} w^* \quad (3.24)$$

For the numerical solution of the Langevin equation, although the terms on the left-hand side of Eq. 3.24 are deterministic functions, the last force caused by thermal fluctuation is a stochastic function [139]. Therefore, the numerical solution requires the use of a discretization scheme, such as the Euler-Maruyama or Milstein methods. Usually, the noise function ( $w$ ) is given by the Gaussian white noise function with a variance proportional to the time step  $\delta t$  and the standard deviation  $\sqrt{\delta t}$ . Using  $\sqrt{\delta t}$  instead of  $\delta t$  in the discretization of the thermal fluctuation term ensures that the amplitude of the random fluctuations is correctly scaled with the time step and can help to avoid numerical artifacts in the simulation. The Langevin equation can be rewritten in the stochastic differential

equation by Euler-Maruyama method as:

$$x(t + \delta t) = x(t) - \frac{\delta t}{\gamma} \nabla W + \sqrt{2 \frac{k_B T}{\gamma}} \delta t w(t) \quad (3.25)$$

In this equation,  $w(t)$  is gaussian white noise  $\langle w(t) \rangle = 0$  and  $\langle w(t)w(t') \rangle = I$  if  $|t - t'| < \delta t$ , 0 otherwise.

**Kramer's theory:** Kramer's theory is a theoretical framework used to estimate the rate at a given thermodynamic process like a chemical reaction can proceed over a potential energy barrier [106]. It was developed by Dutch physicist Hendrik Kramers in the early 1940s and is based on the idea of an activated complex, an intermediate state that occurs during a chemical reaction when the reactants are in the process of forming products. According to Kramer's theory, the rate of a chemical reaction is proportional to the exponential of the negative energy barrier divided by the thermal energy of the system. That is, the rate of a reaction increases exponentially as the temperature of the system increases or as the height of the energy barrier decreases [6]:

$$t_{\text{esc}} = t_r e^{\frac{W}{k_B T}} \quad (3.26)$$

Where  $t_r$  is called the molecule relaxation time and has units of sec. The relaxation time parameter depends on the particle diffusion coefficient as well as curvature at energy landscape maxima and minima.

Kramer's theory is valid only when the potential well is larger than  $5k_B T$ . The reason for this is that when the potential well is too shallow, the energy of the activated complex is comparable to or less than the thermal energy of the system. In this case, the assumption of the energy barrier is no longer valid, and other mechanisms, such as diffusion, become dominant in determining the rate of the reaction. Kramer's theory also can be used to analyze the mean-time escape of nanoparticles from electrostatic potential barriers [184].

### 3.3 Pneumatic nanofluidic devices

Nanoparticles in solution constantly experience Brownian motion [34,35]. In addition, the particles can also easily move due to a small amount of fluid flow. Therefore, long-time nanoparticle confinement is a challenge in biophysics research [205]. Also, most studies including single EVs analysis require confinement to track the particles' movement over long times, so that the particle does not leave the microscope's field of view. Nano/microfluidic devices have shown promising capability for extended-time confinement of nanoparticles [49]. Such nanofluidic devices have been implemented in single particle confinement (e.g., DNA confinement [144,169,236,242], lipid vesicles [52,57,60,69,146,253], and proteins [42,59,184,258]). Confinement can be achieved using external actuators such as electrophoresis [73], dielectrophoresis (DEP) [137], fluid flow [219], or optical trapping [140]. One of the methods for the confinement of micro/nanoparticles is the deformation of nano/microchannels using external force. Unger et al. developed a pneumatically actuated multilayer PDMS system that operates as valves, and pumps and is designed to regulate fluid flow [230]. In this system, thin PDMS membranes are deflected and induce a pressure flow gradient while separating the fluid channel and control channel (Figure 3.7-a). The fluid flow can be halted by applying pneumatic pressure to the control channel, causing the PDMS membrane to flex downwards and seal off the fluid channel. Also, M. Shon and A. Cohen proposed a device with an array of nanocavities (the authors called them "dimples") on a fused silica coverslip which is covered with a PDMS lid. In their method, instead of pushing the lid down, suction is applied to the inlets and the elastomer lid is actuated by the negative pressure in the side-channel. They used the method to capture single molecules in cavities and they could load a new sample and capture fresh molecules sequentially [200]. Similar to A. Cohen's work, M.A. Gerspach et al. proposed a nanofluidic device coupled with a flexible PDMS lid to capture nanoparticles. This work analyzes the effect of minimum electrostatic potential induced by the nanocavities patterned on charged SiO<sub>2</sub> substrate on particle confinement.

With this feature, the authors were able to change the level of confinement by changing the height between the PDMS flexible lid and the SiO<sub>2</sub> substrate [61,64]. Although the method of using elastomers as a flexible lid is cheap and easy-to-fabricate, precise and reproducible confinement seems to not be possible due to channel collapse or hysteresis effect of PDMS after several deformations. The flexible membrane can also be formed from using a coverslip which is pushed by a modified lens (called CLiC) [14,195]. In this method, the actuator for pushing the flexible glass is based on a piezoelectric automated stage; particle confinement is observed using an inverted objective. This method has been used for several applications including the linearization of DNA [14], diffusion of particles in condensates based on different particles including PEG/dextran [195], and the interaction of drugs on cell properties. Our team has developed a nanofluidic device coupled with a thin silicon nitride membrane that can be deflected by pneumatic pressure. We used different thicknesses of membranes including 100, 200, and 400 nm membranes that are deflected in different ranges by the applied pressure based on the membrane size and the gap between the membrane and the bottom of the channel. The device is fabricated in two parallel steps: 1- a borosilicate glass substrate containing a microfluidic channel and nanocavities, 2- a silicon wafer substrate coated on both sides with silicon nitride membrane using LPCVD. These layers are bonded together using anodic bonding, and a central 100 $\mu$ m  $\times$  100 $\mu$ m, or 170 $\mu$ m  $\times$  170 $\mu$ m window is opened on the silicon wafer through a KOH etching process. The exposed free-standing nitride film serves as a flexible lid. A schematic of the device is depicted in Figure 3.15.

## 3.4 Experimental Steps

### 3.4.1 Nanofluidic fabrication

The process is illustrated in detail in Figure 3.9.

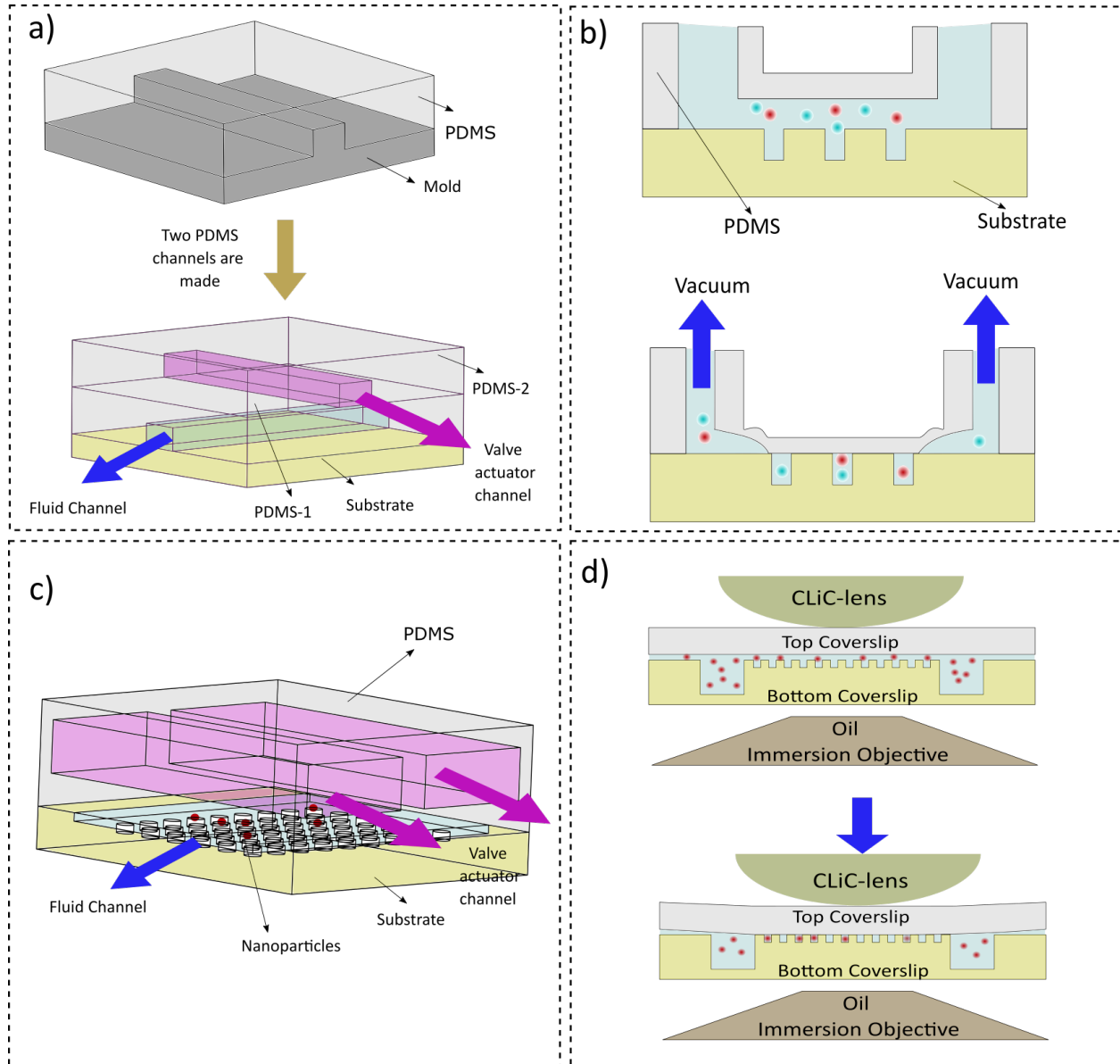


**Figure 3.7:** Pneumatically actuated micro/nanofluidic devices. a) PDMS based device for adjusting the height of a channel via pneumatic pressure [230] b) The device called dimple machine which has trapping and refreshing states [200] c) PDMS base device for contact-free trapping and manipulation of nanoparticles [61] d) Convex lens-induced confinement (CLiC) [195].

1. Cleaning: A borosilicate glass substrate is cleaned using acetone/IPA or nanostrip cleaning procedure followed by a plasma Asher cleaning step to remove inorganic residues from the surface.

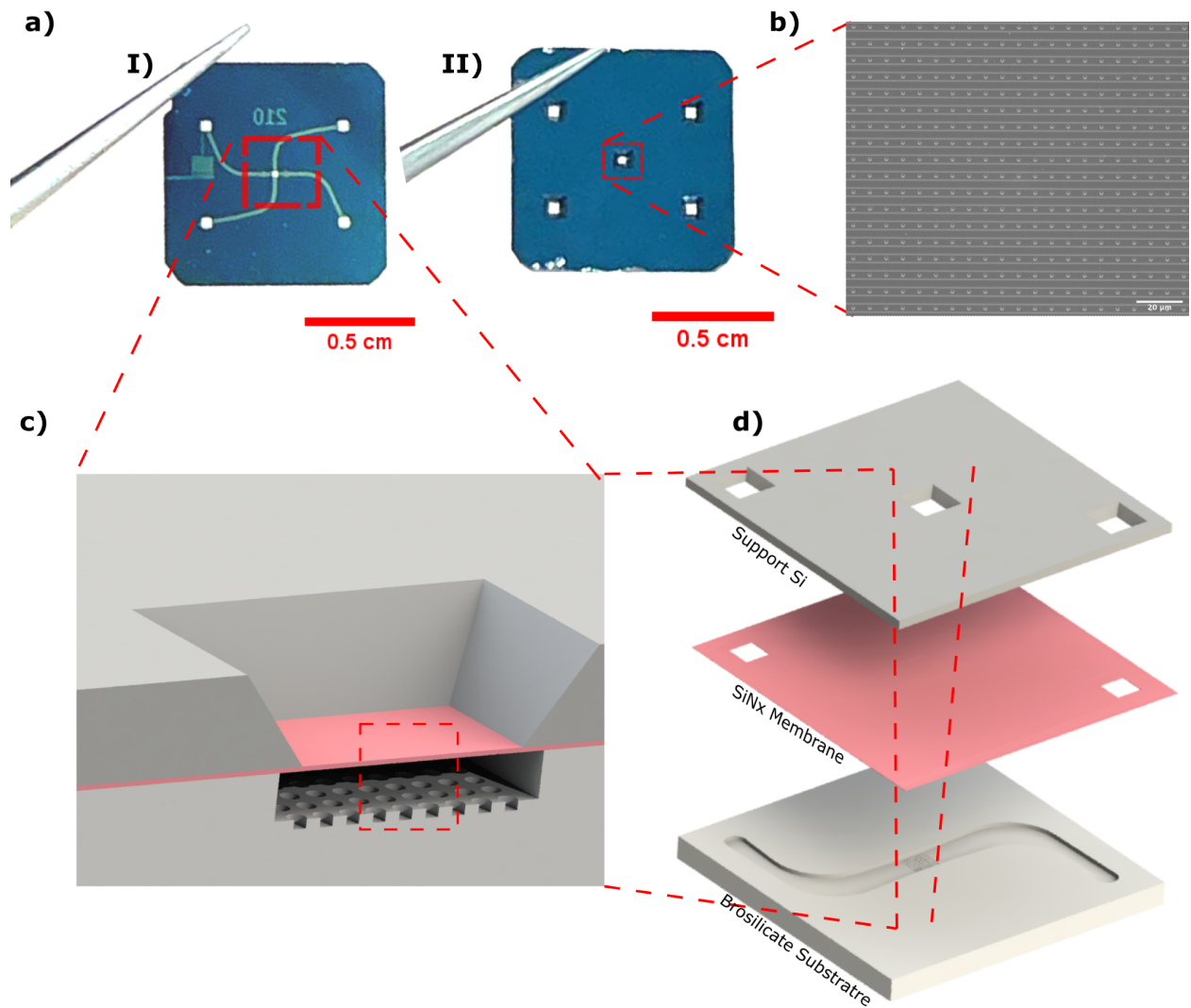


**Figure 3.8:** Overall image of the nanofluidic device representative of its compartments. a) the camera image of the I) front and II) back of the nanofluidic device. b) SEM image of the central area of the nanofluidic device including the nanocavities and nanochannels. c) schematic image of the membrane area of the device d) schematic image of the nanofluidic device and its different layers.

2. Alignment marks: Gold markers are made by photolithography/E-beam evaporation/Lift-off procedure. The gold markers are used as alignment marks for the following E-beam patterning.
3. Nano-features fabrication: E-beam patterning is used to create the nanocavities and nanochannels. For E-beam patterning, the wafer patterned with gold marks coated



with ZEP520A resist. Then, the wafer is exposed in an E-beam lithography (Vistec VB6 UHR EWF). The nanochannels and the nanocavities are designed using L-edit software. The ZEP520A is used as a mask and the nanofeature pattern is etched through the wafer using inductively coupled plasma reactive ion etching (ICP-RIE) to etch borosilicate glass up to 200-300 nm deep with a smooth surface and less than 1-2 nm surface roughness Ra.

4. Micro-features fabrication: Finally, the microfluidic channels (100-200  $\mu\text{m}$  width with 400-500 nm depth) are created using standard UV photolithography with coated S1818 resist on the glass wafer followed by another ICP-RIE procedure.
5. Bonding with SiNx coated silicon wafer: In parallel, a silicon wafer coated with SiNx on both sides is obtained. A Piranha cleaning step is performed on both wafers (borosilicate glass wafer, and silicon wafer) before bonding. The two wafers are bonded together using the anodic bonding method (gradually heated and applied high-voltage pulses).
6. Window opening: For opening the membrane area, another photolithography is performed to pattern the opening windows and etch through the SiNx layer using RIE to expose the opening windows. The opening windows are used for the membrane area as well as the inlets and outlets of the microfluidic channels.
7. Silicon etching by chemical etching: The exposed windows of silicon are etched all the way through using 30% KOH wet etching process at 75°C after dicing the wafer into small devices. Then the device is wetted by breaking membranes at inlets and adding TE buffer.

### **3.4.2 3D printed chuck:**

For applying pressure to the membrane and also applying back-flow pressure for running the reagents and buffer in microchannels, the nanofluidics device is mounted on a

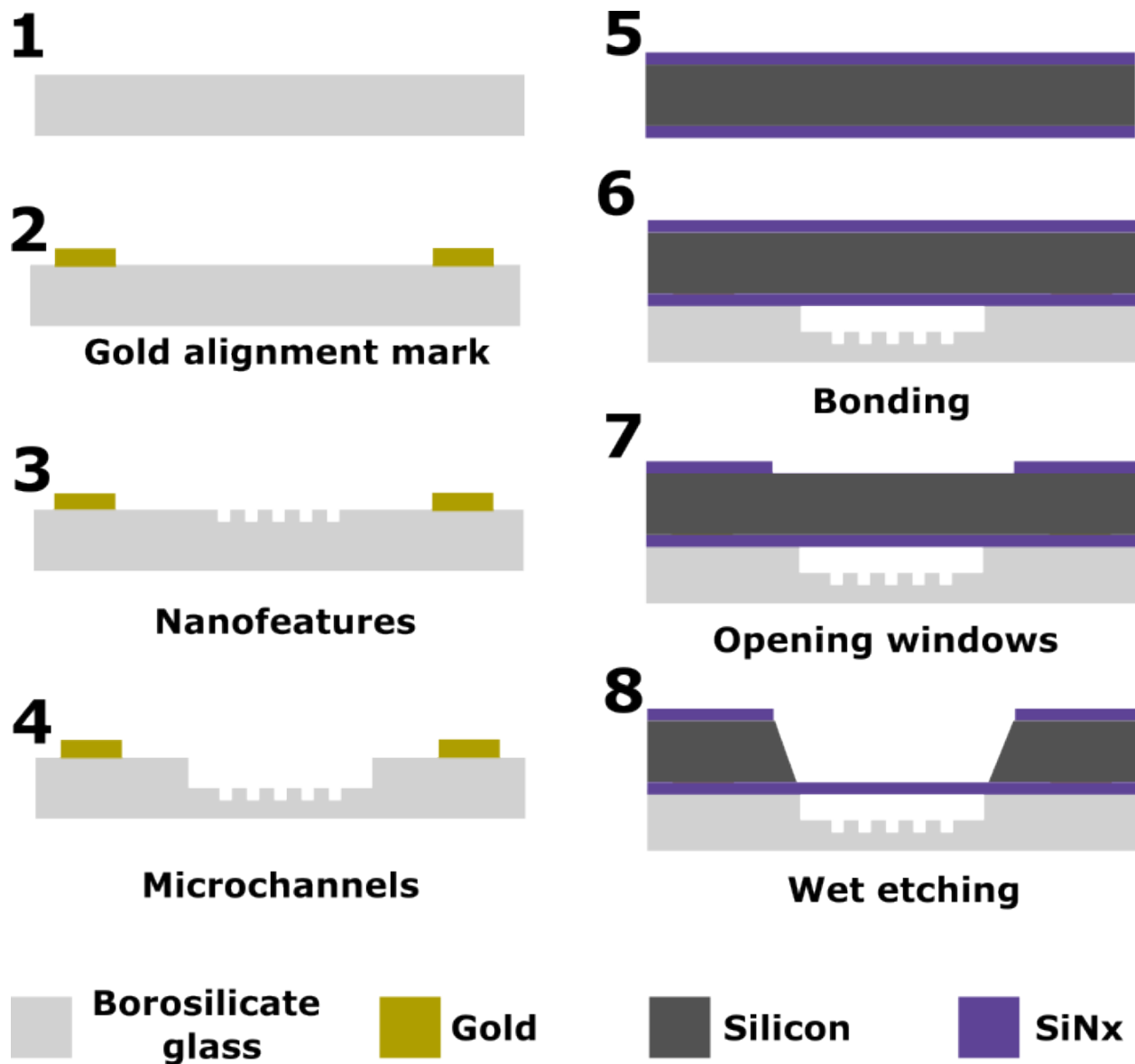


**Figure 3.9:** The fabrication procedure: 1- Cleaning the borosilicate glass. 2- Adding the gold alignment marks. 3- Creating the nanofeatures including the nanocavities and nanochannels using E-beam lithography. 4- creating the microchannels using photolithography following RIE. 5- Obtaining the silicon wafer double-sided coated with SiNx. 6- Bonding the nitride-coated silicon wafer to the prepared glass wafer. 7- opening the windows on SiNx layer. 8- KOH wet etching of the wafer.

3D-printed chuck. The chuck is designed in SolidWorks and printed using FormLab3 stereolithography 3D printer using clear resin. The chuck is washed using IPA solution for 30 min to remove the extra non-cured resins. Then the chuck is placed in a UV-heat

curing chamber for 30 min at 60°C to make sure that all the resins are cured and the IPA is evaporated. Finally, the chuck is sonicated in hot water to remove possible small dust particles. The threads are created using a tap to connect luer lock tubes to the chuck and close the inlets using plastic screws. The nanofluidic devices are secured using a metal retainer plate with screws and the inlets are sealed using O-rings which are placed near the inlets. The chuck is mounted on an inverted microscope and observed using 60X and 100X objectives. The camera is Prime 95B Scientific CMOS (sCMOS). Before the experiment, first, the channels are washed with 1X TE buffer, then, the device is incubated by flowing 8%  $\frac{W}{V}$  polyvinylpyrrolidone (PVP) inside the device overnight at 4°C.

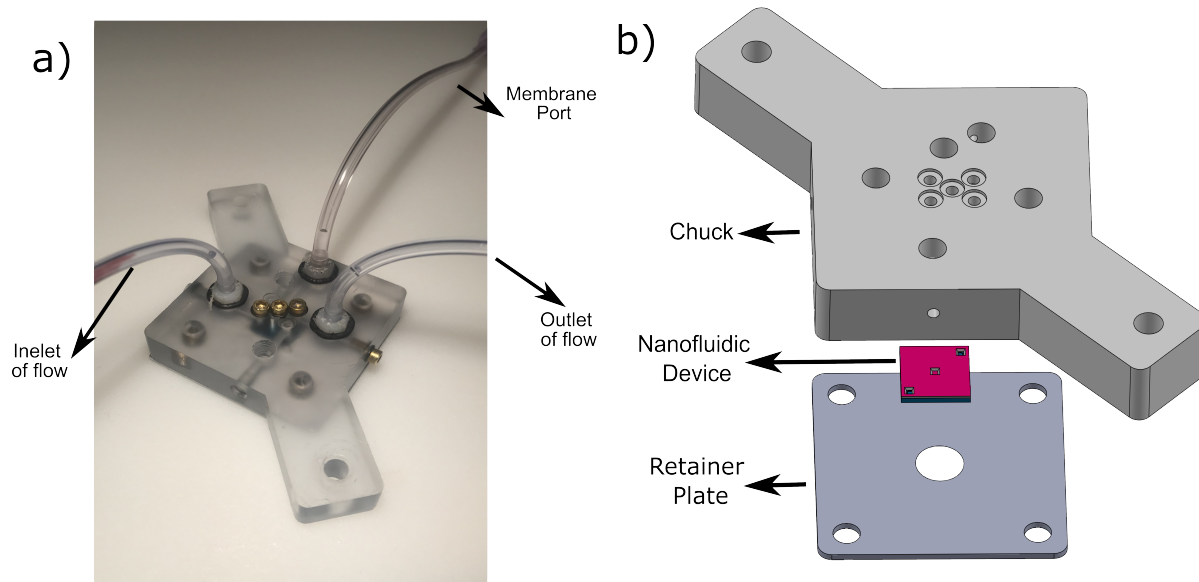


**Figure 3.10:** 3D printed chuck a) the camera image of the 3D printed chuck connected to the luer tubes. b) the schematic image of the 3D chuck and the retainer plate holding the nanofluidic device against the chuck.

### 3.4.3 Nucleic Acid Amplification

We have used two isothermal amplification methods: Loop-mediated isothermal Amplification (LAMP) and Rolling Circle Amplification (RCA). Non-isothermal amplification methods require a thermal cycle due to the denaturation steps. The denaturation step (which usually happens at 95C) separates the DNA into two single-stranded chains which provide an opportunity for primers to attach to the two single-stranded DNAs. Isothermal amplification methods do not require thermal cycling which makes them easier to implement in a micro/nano device. Let us first look at LAMP. The key novelty of LAMP method is creating loop structures (dumbbell-like) (Figure 3.11-a) which provide open single-stranded sequences at low temperature (below the denaturation temperature) with which primers can easily hybridize. The loop structure is created using two primers. 1- FIP primer attaches to the target DNA. FIC primer has two main sequences: 1- F2 sequences which are complementary to the main target DNA sequences (F2C), 2: F1C sequences which are placed before F2 and are the same as the main DNA sequences placed after the F1C (therefore these sequences do not bind with the target DNA). When the polymerase (which is usually BST 2.0) starts to synthesize along the primer it creates sequences that are complementary to the F1C (polymerase great the F1 sequence). Therefore, the synthesized strand has F1C-F2-F1 sequences in which the F1C and F1 transform the end of the synthesized strand into a loop. 2- F3 prime connects the sequences placed before the F1C sequences on the main target DNA. By attachment and strand displacement of the polymerase, the synthesized strand along the FIC primer is detached which lets the F1C part of the strand attach F1 (complementary part in the synthesized strand). 3- LF primer starts the amplification of the formed amplicon which contains the loop structure. Although FIP can also initiate amplification, it might not have the highest possible stability. The option of choosing the right place for forming the loop structure is limited to the F1 affinity as well as the FIP affinity. Therefore, the FIP (which contains the F2 and its complementary sequences placed between the loop) might not have the optimum stability between F2 and F2C sequences. In conclusion, some LAMP primer

designs have suggested using the LF primer which has a stronger attachment with its complementary located between the loop. However, it is not mandatory and is just used to increase the efficiency of the attachment.

In the RCA method, the target molecule is a circular string of DNA. When a primer attaches to the target molecule, the polymerase (usually Phi29) starts to complete the circle. At the time, the polymerase completes a circle (the 5' end of the primer), the polymerase opens up the synthesized circle and continues to synthesize DNA complementary to the target. This procedure continues until the polymerase reaches its processivity limit. Each polymerase is disassociated from the target after several polymerizations of nucleotides into the growing strand of DNA or RNA, which is called processivity. The processivity of the Phi29 polymerase is around 70kbp [95]. If the target molecule is not circular DNA, a method called Pad Lock Probe is used to create the circle. First, the two ends of the PLP (usually 90-110 bp) are complementary to the target molecule. By attachment of the PLP to the target molecule, the two ends of the probe are placed adjacent together. Then the two ends are filled by another polymerase (usually T4 Polymerase). The polymerase attaches to the 3' end of PLP and by 5' to 3' exonuclease activity bonds the two end-arms of the PLP together, and finally forms the circular RCA template for amplification. The PLP method provides the opportunity for barcoding as well as amplification of non-circular DNAs by choosing specific sequences between the two end arms of PLP. In the LAMP method, the result of the amplification of a single DNA molecule is multiple molecules with different sizes from several base pairs (< 70-80 pb) up to kilobase pares (> 20,000 bp). However, in the RCA method, the final result of a single molecule amplification will be a single with very long DNA ( < 50,000 bp). The subtle point is that the produced amplicons can be smaller than the target molecule in the LAMP method; though, the product of RCA is always bigger than the target molecule. In the modified versions of RCA such as hyperbranched RCA, the amplification products can be smaller than the target molecule.

### 3.4.4 Extracellular Vesicles Isolation

Cell Culture media preparation: GFRvIII expressing a variant of U373 (human astrocytoma) and NHA (normal human astrocytoma) are grown in Dulbecco's modified essential medium (DMEM; Wisent, Canada) supplemented with 10% heat-inactivated fetal bovine serum (FBS) (Wisent) and 1% penicillin-streptomycin (Gibco-Life Technologies, Grand Island, NY) at 37 in 5% CO<sub>2</sub>. The conditioned medium (CM) was collected from cells grown for 72 hour in culture media containing 10% of Extracellular Vesicle (EV) depleted FBS (generated by centrifugation at  $150,000 \times g$  for 18 hours at 4).

The CM is centrifuged one time at  $400 \times g$  for 15 min in a filter tube (Merck™ UFC900324) to concentrate the particles. Finally, the EVs are separated using size exclusion chromatography columns (IZON Science Ltd, United States) in 1mM Tris with 0.4 mM NaCl solution. For size distribution analysis of EVs, nanoparticle tracking analysis (NTA) was carried out with each collected iodixanol fraction using NanoSight NS500 instrument (NanoSight Ltd., UK). Three recordings of 30 s at 37°C were obtained and processed using NTA software (version 3.0).

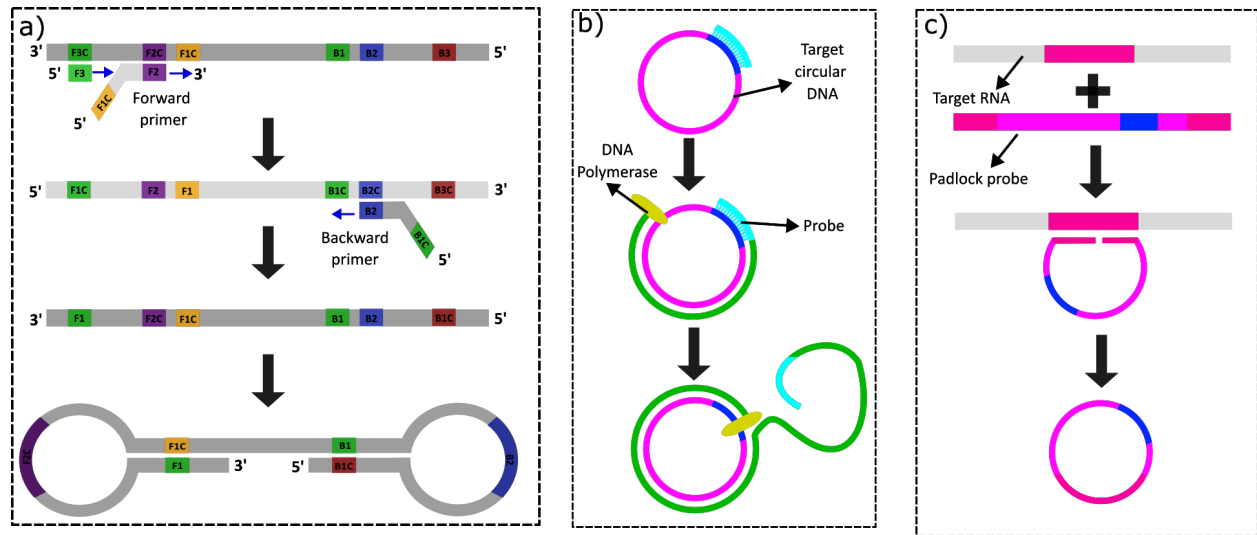


**Figure 3.11:** Isothermal amplification method. a) Loop-mediated isothermal amplification [165]. b) Rolling circle amplification [115] c) PLP method for RCA amplification of targets which are circularized [115].

# Connection between Chapter 3 and 4

After providing the motivation and objective of the project in Chapter 1, the importance of single EVs analysis in Chapter 2, and background knowledge and technologies used in this thesis in this Chapter 3, the first published manuscript conducted to fulfil the first objective of the thesis is presented here. The nanofluidic coupled membrane device is used to confine single molecules in nanocavities. The level of confinement (escape time, the time it takes that a confined particle leaves the nanocavity due to its thermal fluctuation) is related to the height of the nanochannel. In our preliminary study, we observed that the escape time could be modulated in real-time by controlling the membrane deflection. The level of confinement is correlated to the net surface charge of particles. Therefore, first, the system is calibrated using DNA plasmid vectors (pBR322) with determined sequences. Next, the method is used to measure the surface charge of controlled lipid vesicles (liposomes) and then the EVs surface charge is estimated by measuring the escape time in the calibrated device. EVs secreted from two brain cell lines are analyzed using the nanofluidic device. The surface charge analysis provides information about the heterogeneity of EVs in a sample and may serve as a fingerprint marker for the differentiation of the two EV samples.

## Chapter 4

# Nanofluidics for Simultaneous Size and Charge Profiling of Extracellular Vesicles

### 4.1 Abstract

Extra-cellular vesicles (EV's) are cell-derived membrane structures that circulate in body fluids and show considerable potential for non-invasive diagnosis. EVs possess surface chemistries and encapsulated molecular cargo that reflect the physiological state of cells from which they originate, including the presence of disease. In order to fully harness the diagnostic potential of EVs, there is a critical need for technologies that can profile large EV populations without sacrificing single EV level detail by averaging over multiple EVs. Here we use a nanofluidic device with tunable confinement to trap EVs in a free energy landscape that modulates vesicle dynamics in a manner dependent on EV size and charge. As proof-of-principle, we perform size and charge profiling of a population of EVs extracted from human glioblastoma astrocytoma (U373) and normal human astrocytoma (NHA) cell-lines.



## 4.2 Introduction

Cells continuously secrete membrane vesicles into the extracellular environment. These vesicles, known as extra-cellular vesicles (EV's), transport a broad range of molecular cargoes, including proteins and nucleic acids, enabling intra-cellular exchange of molecular components. [231, 233] EV driven exchange plays an important role in maintaining normal bodily homeostasis; [210] EV cargo may also contain markers indicating the presence of disease in the originating cells, [231] such as cancer. [152] As EVs circulate in the blood, they can be sampled without need for invasive tissue biopsy, [203] offering hope for a rapid, risk-free diagnosis or real-time monitoring of a known disease. [152]

EV based diagnostics face substantial challenges due to the small size of EVs and their biochemical complexity; an additional challenge is the extreme heterogeneity of EV populations. [27] Circulating EV's derive from a wide-range of cell-types, including cells that do not exhibit any underlying pathology. [210] Circulating EVs also arise from distinct biogenesis processes. [231, 233] One class of EVs, known as exosomes (50-100 nm in diameter), are formed when multi-vesicle endosomes (MVE's) fuse to the cell membrane and release their intraluminal vesicles into the extra-cellular environment. A second class of EVs, known as microvesicles (50-1000 nm in diameter), arise from outward budding and fission of the cell plasma membrane (blebbing). Both exosomes and microvesicles have diagnostic significance in cancer, with physical properties and co-expressed oncogenic mutations that reflect a single originating tumor cell. Heterogeneity is also observed within each subgroup. Exosomes may be formed via different mechanisms, including Endosomal Sorting Complex Required for Transport (ESCRT) [175], ESCRT- independent machineries [229] and tetraspanin proteins, [275] with each distinct mechanism leading to different molecular cargo. Exosomal content may also be size dependent. [265] Microvesicles are also formed via different blebbing mechanisms, e.g. increases in cytosolic  $\text{Ca}_2^+$  levels on plasma membrane, [82] or activation of P2X receptors. [224]

Tumorigenesis and consequent treatment regimes may also influence EV heterogeneity. Cancer's incredible molecular complexity arises through selection pressures operating in the spatially complex and dynamic tumor microenvironment. [40, 87, 191] When a tumor cell acquires a specific driver mutation conferring a fitness advantage, the cell will proliferate rapidly giving rise to a clonal population containing the initial driver. These clonal populations will then undergo successive sub-differentiation as cells interact with/reorganize their surroundings, undergo metastasis to colonize far-flung regions of the body and acquire mutations to overcome drug therapy. Sampled EV populations may contain molecular signatures of this underlying dynamics, [40, 88] which in turn may have crucial implications for treatment (e.g. providing early warning of the emergence of resistant tumor cell sub-populations [191]).

Standard molecular analyses of bulk EVs by polymerase chain reaction (PCR) and other methods require 'averaging' of diagnostic signals. Averaging implies that the diagnostically crucial single-cell level information carried by each EV is lost against high backgrounds of irrelevant and/or normal cells. For example, classical bench-top EV analysis protocols typically use  $\mu\text{L}$  to  $\text{mL}$  of sample (containing  $10^5 - 10^8$  of exosomes [190]). Microfluidic approaches for EV isolation/analysis reduce sample size requirements. [123] Yet these platforms, which typically use immunoaffinity to capture EVs with pre-selected markers, still average over many EVs, in particular requiring the binding of multiple EV's to microbeads [270] or device surfaces [85] (the best platforms average over  $> 10$  EV's [270]).

In order to fully harness the potential of EV based diagnostics, there is need to develop platforms that can output multiple interrelated disease markers from a single EV. The ability to output multiple disease markers on a single EV basis can not only increase the level of biomedically relevant detail, for example for improved prognosis and prediction, but also increase the number of diagnostically significant marker combinations available, thereby increasing the chances of disease detection. Here we harness a nanofluidic system incorporating tunable confinement to output the size and charge of individual

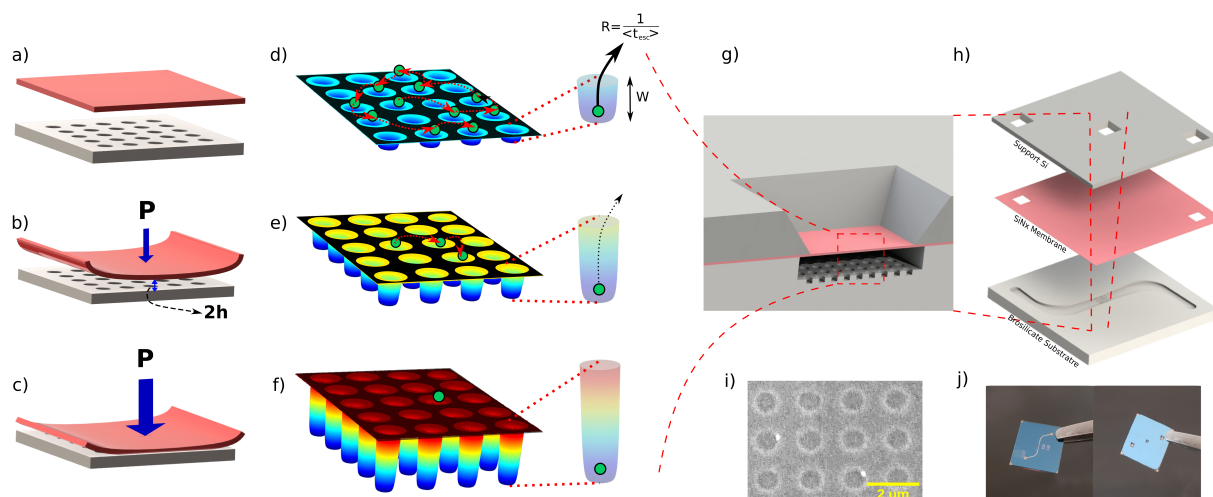


**Figure 4.1:** (a) The device consists of a lattice of circular nanocavities bonded to a flexible membrane lid. (b) When pneumatic pressure  $P$  is applied to the lid, the lid is deflected downwards, increasing the degree of vertical confinement experienced by the particles. At maximum deflection (c), the confinement is complete and the particles cannot escape from the cavities. (d-f) The imposed confinement alters the electrostatic free energy landscape experienced by the particle, increasing the potential well depth  $W$  for a particle confined in a cavity, which in turn decreases the particle escape rate  $R$ . (g-h) The device consists of a nanoslit with embedded cavity lattice etched into a borosilicate substrate. A flexible nanoscale nitride lid is exposed at the device center and suspended over the cavity lattice. The nanoslit is interfaced to two loading ports for introducing particle containing solution. (i) SEM of cavities taken through the nanoscale lid. (j) photograph of  $1 \times 1$  cm device.

EVs analyzed in parallel over an array of nanofluidic traps. EV charge arises from surface associated molecules (e.g. proteins [233], glycans [248] and cholesterol [171]) that are incorporated during biogenesis. EV charge is one of the predominant factors to uptake by the receiving cell [150].

Moreover, EVs from prostate cancer cells have a higher charge (PC3) than normal prostate epithelial cells (PNT2) possibly due to their higher concentration of sialic acids [3], and therefore EV charge is a potential cancer biomarker.

Our device consists of an array of nanocavities embedded in a nanoslit (Figure 4.1-a). A flexible nanoscale lid is deflected downwards by pneumatic pressure (Figure 4.1-

b), [12, 25] varying the degree of vertical confinement experienced by vesicles in the nanoslit. At the highest membrane deflection, the cavities are closed-off from the surrounding slit, isolating single vesicles in the cavities (Figure 4.1-c). This and closely related approaches [2, 13, 14, 62, 63, 136, 137, 195, 196, 201, 223] have been applied to a range of trapping/physical confinement applications, including trapping of single nanoparticle's [62, 63, 195, 223], ds/ss DNA [12, 13, 25, 201] and chromatin. [196] Here we exploit the capability of such devices to directly vary the escape rate ( $R_{\text{esc}}$ ) of vesicles from the well by varying the surrounding confinement. The escape rate, equivalent to the inverse average time of escape of a vesicle from a cavity ( $\langle t_{\text{esc}} \rangle$ ), is determined by the depth of the free energy well experienced by a confined vesicle (Figure 4.1-d-f). [58, 147, 186] In low ionic strength buffer, this potential well depth (DPW, or Depth of Potential Well,  $W$ ), has a strong dependence on electrostatics, so that measurement of the escape rate can access both the size and charge of single vesicles, an approach termed single-molecule electrometry. [58, 185] By combining the single-molecule electrometry with tunable confinement, we gain the ability to make precision measurements of charge on a single-vesicle basis, due to the ability to perform multiple measurements of escape rate of a single vesicle for different degrees of confinement. Critically, our flexible lid constructed from a nanoscale silicon nitride membrane is sufficiently rigid so that the DPW is constant over a number of cavities (Figure 4.1-d-f), enabling acquisition of sufficient statistics on particle trajectories to make precise measurements of escape-rate. As our approach can also access Brownian diffusion of vesicles in the slit between cavities, we can also measure vesicle size, comparable to Nanoparticle Tracking Analysis (NTA). Note that NTA yields only particle size, while our approach yields both size and charge for each vesicle. As proof-of-principle, we probe both the size and charge of EVs extracted from a human glioblastoma astrocytoma cell-line (U373) and benchmark these results against equivalent measurements taken from the healthy counterpart cell line (normal human astrocytoma, NHA).

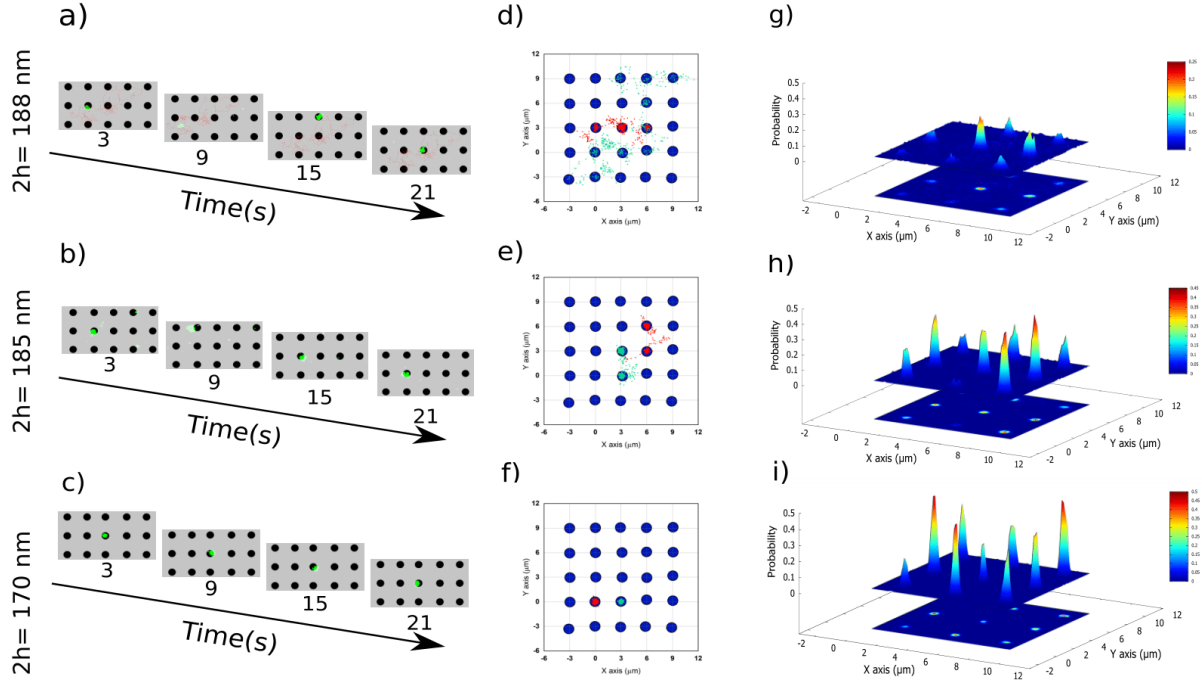


**Figure 4.2:** (a-c) Sequence of fluorescence micrographs of plasmids diffusing in cavity lattice for (a) weak, (b) moderate and (c) strong confinement. The cavity positions are indicated in gray. (d-f) Corresponding trajectories for three example plasmids for (d) weak, (e) moderate and (f) strong confinement. (g-i) The probability of finding the plasmid at a point in the cavity lattice, for (g) weak, (h) moderate and (i) strong confinement. At higher confinement the plasmids remain in the cavities longer relative to the slit, resulting in a higher probability for a plasmid to be found in a cavity.

### 4.3 Material and Methods

Our tunable confinement device is fabricated using the approach outlined in Capaldi *et al.* [25]. In detail, the device consists of a borosilicate substrate containing a lattice of circular nanocavities (radius  $R_c = 500 \text{ nm}$ ), embedded 200 nm deep in a 400-500 nm deep nanoslit connected to two loading reservoirs (Figure 4.1-g, h), see Sup. Mat. I). A free-standing 100 nm thick silicon nitride membrane is exposed in the device center, forming a flexible lid over the nanoslit. The device is secured to a 3D printed chuck via a membrane gasket. The chuck contains access ports for injecting particle containing buffer solution

as well as application of pneumatic pressure to depress the membrane. Prior to operating the device, the nanoslit is incubated in PVP solution to prevent vesicle adhesion. The chuck is mounted in a fluorescence microscopy setup with LED-based multi-wavelength illumination. When the membrane is deflected by applied pneumatic pressure, the vertical gap (slit height) is decreased. We calibrate the slit height as a function of pressure by measuring the intensity of fluorescent dye in the nanoslit (see Sup. Mat. II). Note that the gap height varies across the membrane (see Figure 5.4-b,c); we perform measurements only over the portion of the membrane with a gap height varying less than a fixed threshold  $2\delta h_{\max}$ , which we call the plateau region (see inset to Figure S8 in Sup. Mat. XII for definition of plateau region). Experiments were primarily performed in devices with  $\delta h_{\max} = 0.8 \text{ nm}$ , with a corresponding 'plateau region no smaller than the  $6 \times 5$  array of cavities in the device center (the total membrane area was  $160 \times 200 \mu\text{m}^2$  and the slit was  $500 \text{ nm}$  deep). A second device class used a larger  $\delta h_{\max} = 10 \text{ nm}$  (plateau region corresponded to  $6 \times 6$  array of cavities in the device center, total membrane area was  $100 \times 100 \mu\text{m}^2$  and slit depth was  $400 \text{ nm}$ ). Height measurements are determined as an average over the gap heights in the plateau region.

We choose low ionic strength buffer conditions to ensure that the confining free energy well at each lattice site is determined by electrostatics (we use  $1 \text{ mM}$  Tris with  $0.4 \text{ mM}$  NaCl solution, yielding an ionic strength  $I = 0.7 \text{ mM}$  and a Debye length of  $11.5 \text{ nm}$ , see Sup. Mat. III). A charged particle confined between two parallel like-charged confining surfaces has an equilibrium position, or potential energy minima, lying at the mid-point between the two surfaces. [109,185] At the position of an embedded cavity, this mid-point potential energy minima will lie inside the cavity and be lower than the mid-point potential minima in the surrounding slit. Consequently, an energy barrier will exist preventing particle escape from the well, given by the potential difference between the inside and outside of the cavity; this is the potential well depth (DPW,  $W$ ). The DPW can be computed by solving the Poisson-Boltzmann equation for the circular cavity geometry [107], and depends in detail on the buffer ionic strength, zeta potential of confining surfaces

( $\psi_s$ ), and the device geometry, including the cavity radius ( $R_c$ ), cavity depth ( $d$ ), and the slit height ( $2h$ ). By varying the slit height via our tunable confinement capability, we directly modulate the DPW, and therefore modulate the particle residency time in the cavity traps (see Figure 4.1-d-f) for examples of the electrostatic potential landscape for different gap heights computed from the PB equation).

We use fluorescently labeled plasmids (pBR322g, New England Biosciences) to benchmark and calibrate the tunable confinement device for single vesicle electrometry. The plasmids, all possessing the same sequence, have a uniform chemistry, so differences in behavior between individual plasmids arise necessarily from Brownian dynamics and not intrinsic chemical heterogeneity. We find that, as expected, plasmid diffusive dynamics in the cavity lattice depends strongly on the degree of imposed confinement (Figure 4.2, also see supplementary movie). When confinement is weak, particles transit rapidly between many cavities over the minute long movie (Figure 4.2-a, d) with a low residency time in each cavity (Figure 4.2-g). In this case the DPW is low and it is highly probable that a thermal fluctuation will drive the plasmid out of a well at any given instant. Once a plasmid escapes from the well, the plasmid diffuses in the nanoslit until it reaches the next local energy minimum. At an intermediate degree of confinement, the DPW is higher and particles can explore only a limited number of wells over the course of the movie (Figure 4.2-b, e), with a higher residency time in each well (Figure 4.2-h). Finally, at the highest confinement, the plasmids are trapped in a single well over the entire movie (Figure 4.2-c, f, i).

## 4.4 Results and Discussion

By quantifying the plasmid trajectories in the cavity lattice we can deduce the distribution of plasmid escape times from the well  $t_{\text{esc}}$  for each confinement condition (Sup Mat. IV). The escape times follow an exponential distribution (Figure 4.3-a-c), as expected for a Poisson process. The average escape time  $\langle t_{\text{esc}} \rangle$  is obtained from fitting an exponential

model to the escape time distributions:  $P(\Delta t) = A/\langle t_{\text{esc}} \rangle \exp(-\Delta t/\langle t_{\text{esc}} \rangle)$ . The quantity  $\langle t_{\text{esc}} \rangle$  increases strongly with increasing confinement (decreasing slit height  $2h$ , Figure 4.3-d). Note that Figure 4.3-d includes measurements of  $\langle t_{\text{esc}} \rangle$  versus slit height for devices with well controlled height variation ( $\delta h_{\text{max}} = 0.8 \text{ nm}$ , device class 1) and less well controlled height variation ( $\delta h_{\text{max}} = 10 \text{ nm}$ , device class 2); measurements taken for both device classes agree well. The relationship in Figure 4.3-d can be used to calibrate our tunable confinement system: calibration entails linking a given measurement of  $\langle t_{\text{esc}} \rangle$  to a corresponding charge value.

Calibration has two parts: firstly the DPW is linked to charge via [109, 185]

$$W = \delta\psi_m q_{\text{eff}}. \quad (4.1)$$

The quantity  $\delta\psi_m$  is the difference in electric potential, averaged over the particle's surface, between the inside and outside of the well evaluated at the mid-point between the parallel device surfaces;  $\delta\psi_m$  can be obtained from the Poisson-Boltzmann equation for known cavity geometry, effective and particle size (see Sup. Mat. V). The quantity  $q_{\text{eff}}$  is the particle's effective charge, the charge of the particle observed in a far field regime several Debye lengths away from the particle. [109] Secondly, Brownian Dynamics (BD) simulations are used to link  $\langle t_{\text{esc}} \rangle$  to the DPW. For this calibration, the plasmid's effective charge  $\sigma$  is obtained independently from electrophoresis ( $q_{\text{eff}} = -152 \pm 4e$ ). The plasmid's hydrodynamic radius  $r_H$  is fixed using the value from Newman *et al* (65 nm). [155] The missing parameter, the zeta potential of the confining surfaces  $\psi_s$ , is determined by finding the  $\psi_s$  value that brings the  $\langle t_{\text{esc}} \rangle$  values obtained from BD simulation into agreement with experiment (see Sup. Mat. VI). Figure 4.3-d shows the final calibration curve obtained from Langevin simulations against  $2h$  and  $\psi$  for  $q_{\text{eff}}$ ,  $r_H$ . The dependence of  $\langle t_{\text{esc}} \rangle$  on  $\delta\psi_m$  follows an exponential (Figure 4.3-d, inset), in accordance with the Kramer relation:

$$\langle t_{\text{esc}} \rangle = t_r \exp\left(\frac{q_{\text{eff}} \delta\psi_m}{k_B T}\right) \quad (4.2)$$



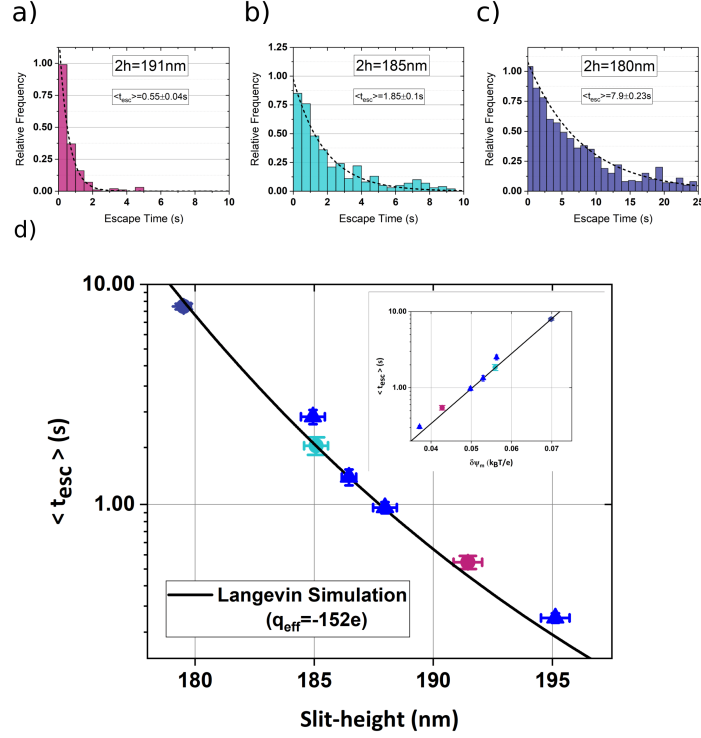


**Figure 4.3:** Normalized histogram of measured plasmid escape times for (a) slit height of 191 nm with 25 particles and 195 hopping events; (b) slit height of 185 nm with 42 particles and 351 hopping events; and (c) slit height of 180 nm with 74 particles and 295 hopping events. (e) Comparison of experimentally measured averaged escape times for different slit heights with Langevin simulation results. The inset gives the measured average escape time for different DPW on a log-linear scale with an exponential fit to the simulation results. Data points from device class 1 ( $\delta h_{max} = 0.8$  nm) are shown as circles with colors that match the corresponding histograms in (a), (b) and (c). Data points from device class 2 ( $\delta h_{max} = 10$  nm) are shown as blue triangles.

with  $t_r$  a pre-exponential factor with dimension of time corresponding to a positional relaxation time (see Sup. Mat. IV).

Next we use our calibrated system to perform simultaneous size and charge measurements on single confined vesicles (Figure 5.4). Our EVs are obtained from the human glioblastoma astrocytoma (U373) and normal human astrocytoma (NHA) cell-lines, fluorescently labeled (with Dil) and suspended in 1mM Tris with 0.4 mM NaCl solution (see

supporting information for details on EV isolation and preparation). Prior to introducing the EVs into our device, the EV size and charge were characterized respectively via Nanoparticle Tracking Analysis (NTA) and electrophoretic mobility. In addition, as a control, we investigated vesicles with a relatively more controlled, uniform chemistry: liposomes based on the phospholipid combination DOPC/Chol with incorporated Rhodamine DHPE dye (FormuMax Scientific Inc, US). Vesicle samples were introduced into our system and sufficient confinement was applied to fully isolate vesicles within individual cavities, completely preventing their escape. Then the confinement was reduced in  $\approx 5$  nm increments, with a 10 s hold after each confinement increment to observe if particle escape occurred. When particle escape was observed, the critical height was recorded and particle dynamics were integrated for 60 s. Note that the critical height depends on the size and charge of particles. For the liposome sample, almost all particles escaped from the cavities at  $2h = 291$  nm; however, for the EV sample, the critical confinement varied between 120 and 320 nm, hinting at the greater heterogeneity present in the EV sample. The  $t_{\text{esc}}$  can be obtained from analysis of single particle trajectories (Figure 4.4-a), with the measured  $\langle t_{\text{esc}} \rangle$  the average of the escape times for each trapping event. We have never observed occupancy of a single cavity by more than one vesicle, likely due to a self-exclusion effect arising from the vesicle's charge, i.e. the free energy of cavity occupancy of a charged vesicle is increased in the presence of a second like-charge vesicle due to strong repulsive electrostatic interactions between the vesicles. In order to obtain the vesicle hydrodynamic radius  $r_H$ , the vesicle mean square displacement (MSD,  $\langle r^2 \rangle$ ) is obtained for the portion of the particle trajectory that is outside of the cavity, e.g. takes place completely in the surrounding slit (Figure 4.4-b,  $\langle r_{\text{slit}}^2 \rangle$ ). The diffusion constant and particle size is then inferred via  $\langle r_{\text{slit}}^2 \rangle = 4Dt$  and the Einstein relation  $D = k_B T / \zeta_{\text{eff}}$ . The quantity  $\zeta_{\text{eff}}$  is a friction factor that takes hydrodynamic coupling between the particle and device surfaces into account using Faxén's approximation (see Sup. Mat. VII).

While measurements of  $\langle t_{\text{esc}} \rangle$  at a single confinement value can be used to deduce  $q_{\text{eff}}$ , this approach requires using Langevin simulations to deduce the exponential pre-factor

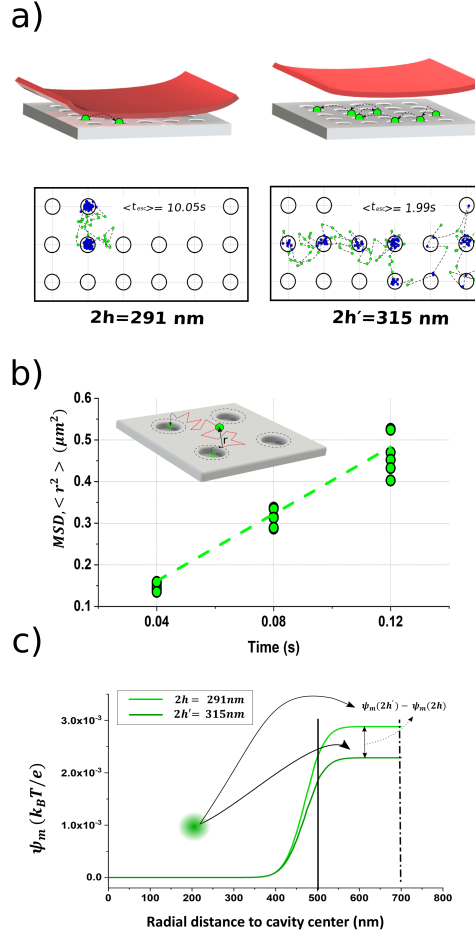


**Figure 4.4:** Methodology for measuring size and charge of single vesicles. (a) A sample trajectory of a liposome particle at two different slit heights ( $2h = 291\text{ nm}$  and  $2h' = 315\text{ nm}$ ) and resulting  $\langle t_{esc} \rangle$ . (b) Mean square displacement in slit of 5 vesicles of similar size at the two different slit heights. The inset indicates the definition of the displacement vector  $\mathbf{r}$  for a vesicle undergoing Brownian motion in the slit between cavities. (c) Mid-point potential measured for the two different slit heights.

$t_r$ . Instead, using our ability to vary confinement experienced by a single vesicle, we reduce the confinement after the first measurement and perform a second integration over the dynamics to obtain  $\langle t_{esc} \rangle$  for an additional slit height  $2h'$  (Figure 4.4-c). This second slit height was chosen by finding the minimum increment in  $2h$  that yielded an appreciably lower  $\langle t'_{esc} \rangle$  (specifically,  $\langle t'_{esc} \rangle$  is 2-3 times smaller than  $\langle t_{esc} \rangle$  which is correlated to a 1-2  $k_B T$  lower DPW).

For the liposome sample,  $2h' = 315$  nm. For the EV samples, we observed that  $2h'$  was typically 20-50 nm greater than  $2h$  ( $2h' = 145$ -360 nm). By taking the ratio of the two average escape time measurements, from Eq. 4.2 we can deduce  $q_{eff}$  without knowledge of the exponential pre-factor:

$$q_{eff} = \frac{1}{\psi_m(2h) - \psi_m(2h')} \log \frac{\langle t_{esc} \rangle}{\langle t'_{esc} \rangle}. \quad (4.3)$$

We used our device to characterize 30 liposome and 100 EVs for each of the EV samples (Figure 4.5). Our results for both EV size (Figure 4.5-a) and zeta potential (Figure 4.5-b) are consistent with bulk approaches (i.e. electrophoresis and NTA), but our approach yields a correlated size and charge value for a single vesicle (Figure 4.5-c). To compare with electrophoresis measurements, our measured charge was converted to zeta-potential using a result derived from Poisson Boltzmann theory for spherical colloids [110, 131] (see Sup. Mat. VIII). Note that, as expected, the EV samples have a considerably broader and more heterogeneous size and effective charge than the liposome sample. As the liposome sample are more chemically uniform than the EVs with a more tightly controlled diameter, the spread of the liposome measurements about the mean gives a measure of the expected error in a single vesicle measurement (technically, an upper limit in the single vesicle error as the liposomes are not completely mono-disperse). The measured mean  $\pm$  standard deviation for liposome diameter and zeta potential are respectively  $239 \pm 8$  nm and  $38 \pm 2$  mV, corresponding to one-sigma errors in vesicle diameter and zeta potential of respectively 3% and 5% (for comparison, the respective values from NTA and electrophoresis are

236±10 nm and 38.1±1.5 mV.) The liposome measurements were performed entirely with class 1 devices with well-controlled height ( $\delta h_{\max} = 0.8$  nm). For the EV measurements, measurements were performed in both device classes, but predominantly in class 1. Measurements in both device type yielded equivalent means and distribution spreads (see Table S1 in Sup. Mat XI). The diameter dependence of the effective charge appears to roughly reflect a scaling  $q_{\text{eff}} \sim \zeta R^2$ , with  $R$  the EV radius (see the inset to Figure 4.5-c which suggests that  $q_{\text{eff}}$  normalized to the EV surface area  $4\pi R^2$ , or equivalently zeta potential, is independent of diameter). The absence of particles below 60 nm in our sample is likely due to our use of a lipophilic stain; particles below 60 nm likely do not contain a lipid component. [265]

In addition, comparing the NHA and U373 secreted EVs shows that while the NHA and U373 EVs have a comparable size distribution (Figure 4.5), the NHA EVs are more highly charged (by about 18%, Figure 4.5-b). This difference is significant: the U373 EVs have a mean zeta potential of 41.3±0.6 mV, the NHA EVs have a mean zeta potential of 48.6±0.6 mV, with errors quoted corresponding to standard-deviation on the mean. Regarding the possible biological significance of this difference, it is well known that profound changes in membrane glycosylation occur in cancer. Although these changes usually lead to more sialylation and consequently more negatively charged EVs, [3] there are complicating effects, for example variability in negatively charged lipids like phosphatidyl serine [23] or changes in carbohydrate (HSPG) content of cellular membranes that spill over to EVs. [23,143] Also, the protein repertoire of EV surfaces is very different in cells that have undergone transformation, where hundreds of proteins appear or disappear as the cell acquire aggressive traits. [31] Lastly, different pathways of EV formation may be activated in cancer cells. [208]

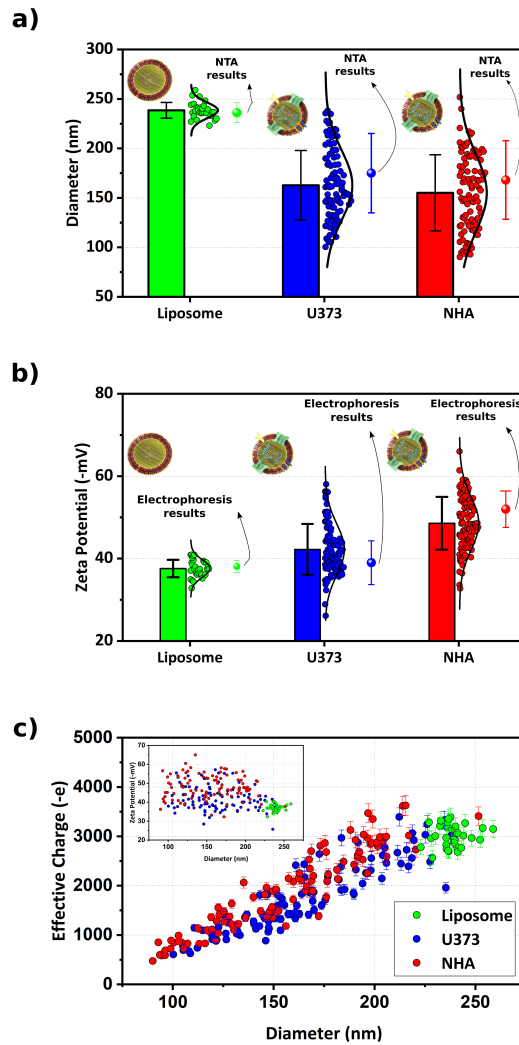


**Figure 4.5:** Size and charge measurement of 100 NHA (red) and 100 U373 (blue) EVs and 30 liposomes (green). (a) Distribution of diameter characterized in device. The small dots give results for individual vesicles measured in device, the bar gives the average over the individual vesicle measurements (with error-bar based on standard-deviation) and the large point to the right of the distributions gives the NTA result for comparison (with error-bar based on standard-deviation). (b) The zeta potential analysis for the same vesicles as in (a). The small dots give results for individual vesicles measured in device, the bar gives the average over the individual vesicle measurements (with error-bar based on standard-deviation) and the large point to the right of the distributions gives the electrophoresis result for comparison (with error-bar based on standard-deviation). (c) Scatter plot of effective charge versus diameter for the vesicles. Inset gives zeta potential versus diameter

## 4.5 Conclusion

In summary, we use tunable electrostatic confinement combined with single-molecule electrometry to characterize simultaneously the size and charge of EVs. Our configuration allows the confining potential to be varied over two orders of magnitude ( $\sim 0.1 - 10 \text{ k}_\text{B}\text{T}$ ), allowing tuning of the particle escape rate from the wells. This tunable escape rate makes possible the extraction of the size/effective charge of single vesicles of differing size and charge measured in the array. While our current devices have a relatively small plateau region and hence throughput, increasing the total membrane area should be straightforward and then simple scaling suggests that we should be able to achieve throughputs  $\sim 500$  EV measurements per minute, with throughputs  $\sim 1000$  EV measurements per minute feasible with more concentrated samples that can ensure increased array occupancy (see Sup. Mat. XII). In addition, by fully deflecting the membrane lid, we can fully confine a vesicle in a single well. The tunable device, after extracting the charge and size of a single vesicle, might then potentially be able to isolate the vesicle in a single cavity where repeated chemical exchanges could lyse the EV, release the molecular cargo and then target the encapsulated RNA's and proteins for more detailed analysis. In particular, the ability to correlate the molecular repertoires of individual EVs with their size and charge, might give rise to new approaches for EV classification, complementary to isolation of EV subsets via flow-differentials. [265] Alternatively, we might stain EVs with fluorescent antibody conjugates specific to certain surface markers, and then use our approach to observe if these populations differ in their physical properties.

## 4.6 Supplementary Information

### 4.6.1 Device Fabrication and Operation

The device is fabricated with the process outlined in Capaldi *et al.* [26] Briefly, a 400-500 nm deep nanoslit is fabricated in borofloat glass with UV lithography followed by

a CHF<sub>3</sub>: CF<sub>4</sub> etch step. Then, circular nanocavities with a radius of 500 nm are defined lithographically and etched 200 nm deep with RIE. Next, the substrate is bonded to a silicon wafer coated on both sides with 50 nm silicon nitride (Cornell, NanoScale Facility, silicon wafers 400  $\mu$ m thick). A lithography/RIE step is performed on the wafer top-side to open up a window for KOH etching. Final, KOH etching is performed to expose the free-standing nitride membrane over the nanocavity region. Our device is incubated with PVP (polyvinylpyrrolidone) 8%. The fabricated device is mounted on a 3D printed chuck and plasmid or vesicle containing solution is introduced in the device inlet (Figure S4.6). Pneumatic pressure applied to the device inlet is then used to drive plasmids or vesicles to the nanocavity region below the free-standing membrane.

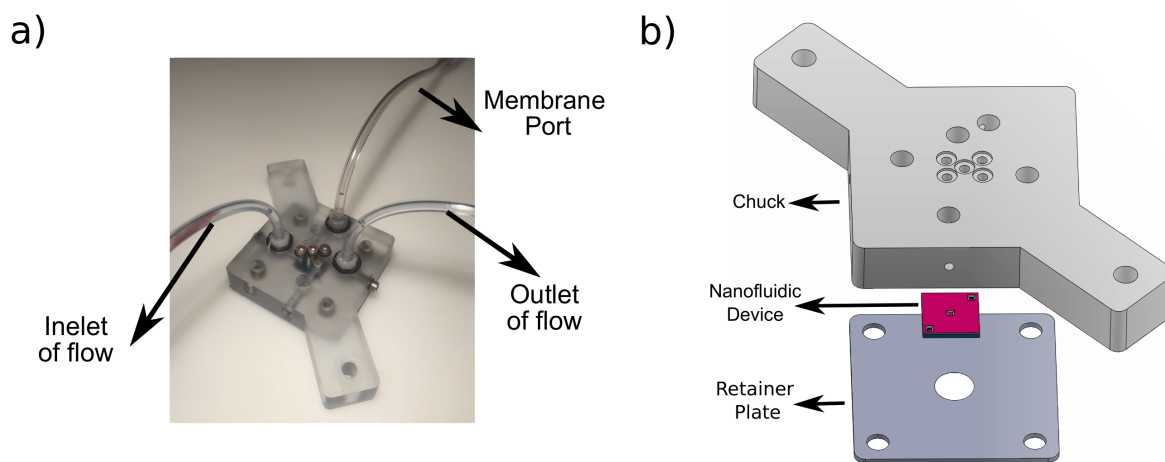


**Figure 4.6:** (a) Photograph of 3D printed chuck interfaced to luer tubing for applying pneumatic pressure to deflect membrane lid and transport solution through flow-cell. (b) Schematic showing chuck/nanofluidic device assembly.

#### 4.6.2 Slit Height Calibration

In order to find the relation between the pressure used to deflect the membrane lid and the slit height ( $2h$ ), we introduce fluorescent dye into the device. The variation of fluorescent dye intensity with pressure applied to the membrane lid can then be used to deduce the



variation of the slit height with pressure. Consider a fluid volume  $2hA$  enclosed between the membrane lid and the device bottom surface in a region of the device of area  $A$ . The fluorescent intensity arising from dye molecules present in this volume is: [78]

$$I_F = I_e \varepsilon(\lambda) \Phi C(2hA) \quad (4.4)$$

with  $I_e$  is the light source intensity,  $\varepsilon$  the molar absorptivity (a function of light source wavelength  $\lambda$ ),  $C$  the dye concentration and  $\Phi$  the quantum efficiency of the dye. The slit height at zero applied pressure  $2h_0$  corresponds to a measured fluorescent intensity  $I_{F0}$ . From the linearity of Eq. 4.4, the slit height corresponding to a measured intensity  $I_F$  is then  $h = (I_F/I_{F0})h_0$ . Figure S4.7 gives the resulting slit height as a function of pressure applied to the membrane lid. Specifically, the reported height measurements are obtained by averaging the fluorescent dye intensity over the central portion of the membrane with a gap height varying less than  $2\delta h_{\max}$  (termed “plateau region,” see inset of Figure S4.7 inset). Experiments were primarily performed in devices with  $\delta h_{\max} = 0.8 \text{ nm}$ , with a corresponding ‘plateau region no smaller than the  $6 \times 5$  array of cavities in the device center (the total membrane area was  $160 \times 200 \mu\text{m}^2$  and the slit depth  $h_0 = 500 \text{ nm}$ ). A second device class used a larger  $\delta h_{\max} = 10 \text{ nm}$  (plateau region corresponded to  $6 \times 6$  array of cavities in the device center, total membrane area was  $100 \times 100 \mu\text{m}^2$  and the slit depth  $h_0 = 400 \text{ nm}$ ).

### 4.6.3 Measurement of Solution Ionic Concentration

The electrolyte solution used is 1 mM Tris with 0.4 mM NaCl in DI water. To find the solution ionic concentration, we measured the solution conductivity and then converted conductivity to ionic concentration. First a conductivity calibration curve is obtained using a pure NaCl concentration standard (i.e. conductivity of a solution of DI water and NaCl measured for different NaCl concentrations). Then, the conductivity of our experimental solution is measured and the ionic concentration obtained by comparison

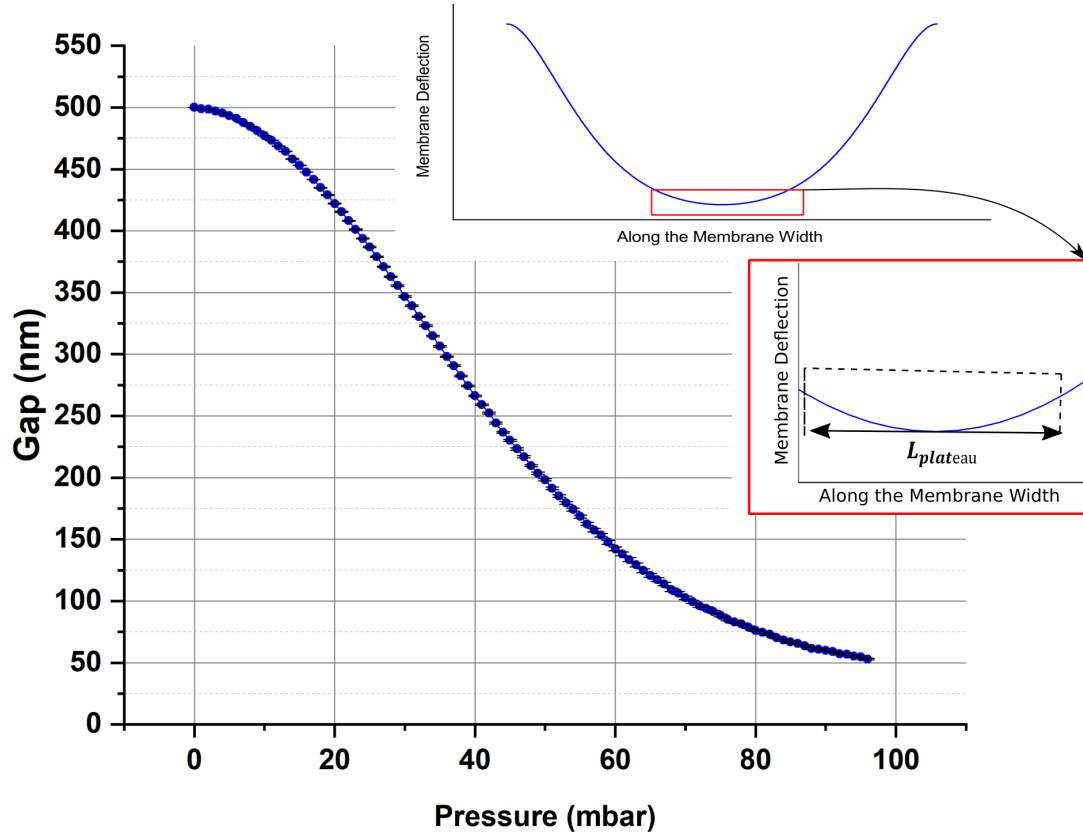


**Figure 4.7:** Relation between slit height and applied pressure used to deflect the membrane lid. The error bars show the variation of slid height in plateau region. The inset shows the plateau region definition. This curve was taken for device class 1.

with the calibration curve (see Figure S4.8). The conductivity of the experimental solution is  $63 \frac{\mu S}{m}$  and the corresponding ionic concentration is 0.7 mM.

#### 4.6.4 Calculation of Particle Escape Time

According to Kramers' theory, for the regime  $W > 6k_B T$ , the average escape time  $\langle t_{esc} \rangle$  of a particle from a potential well is given by:

$$\langle t_{esc} \rangle = t_r \exp \left( \frac{W}{k_B T} \right) \quad (4.5)$$

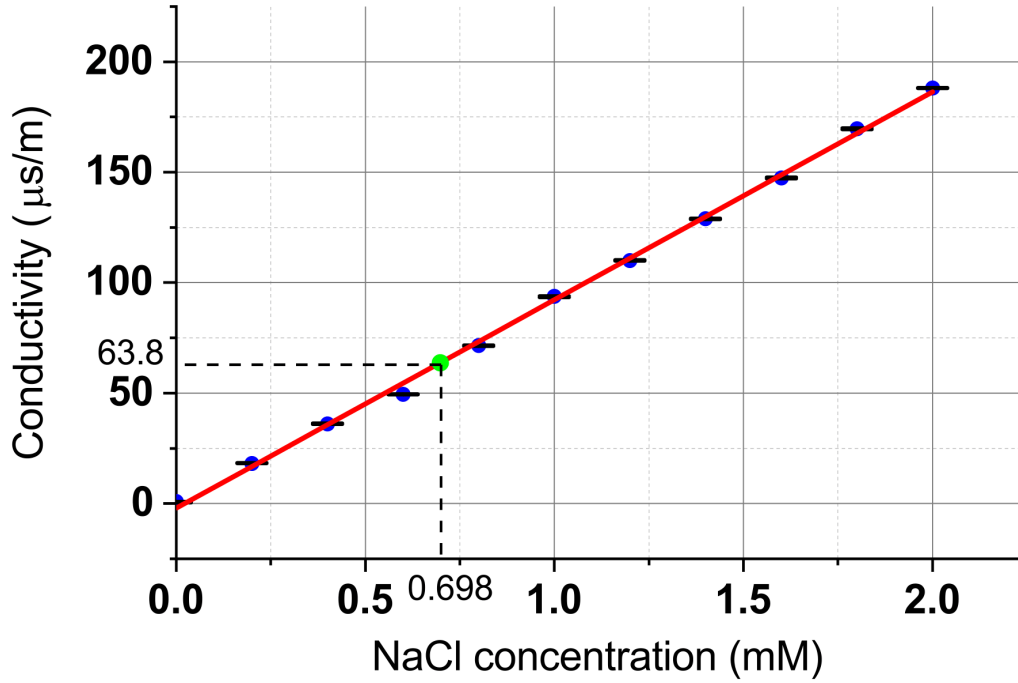


**Figure 4.8:** Solution conductivity versus ionic concentration. The error bars are smaller than the symbols and the maximum error is less than 0.1 %.

in which  $k_B$  is Boltzmann constant,  $T$  is temperature considered as 298K. The quantity  $t_r$  is the particle positional relaxation time and  $W$  is the potential well depth (see Figure S4.9). Note that  $t_r$  depends on the particle diffusion coefficient ( $D$ ) and the well geometry. In particular,  $t_r = \frac{L^2}{4D}$ , with  $L$  a length scale that depends on the cavity depth ( $d$ ) and cavity radius ( $R_c$ ). We find that in our system  $L \sim 100$  nm; the cavity depth and cavity radius are 200 nm and 500 nm, respectively. To correctly relate the experimentally measured time scale ( $\langle t_{\text{esc}} \rangle$ ) to simulation results, we introduce an “escape boundary” consisting of a radial contour at  $r_{\text{esc}}$  centered on the cavity ( $r_{\text{esc}} > R_c$ ). The use of an escape boundary larger than the cavity radius ensures that particle escape from a well always results in the particle transitioning to a neighboring well. For analysis of both experimental results and simulation,  $r_{\text{esc}} = 750$  nm (Figure S4.9a). The particle is considered to have entered the cavity when the particle radial coordinate  $r \leq r_{\text{esc}}$  (occurring at time  $t_1$ ). The particle

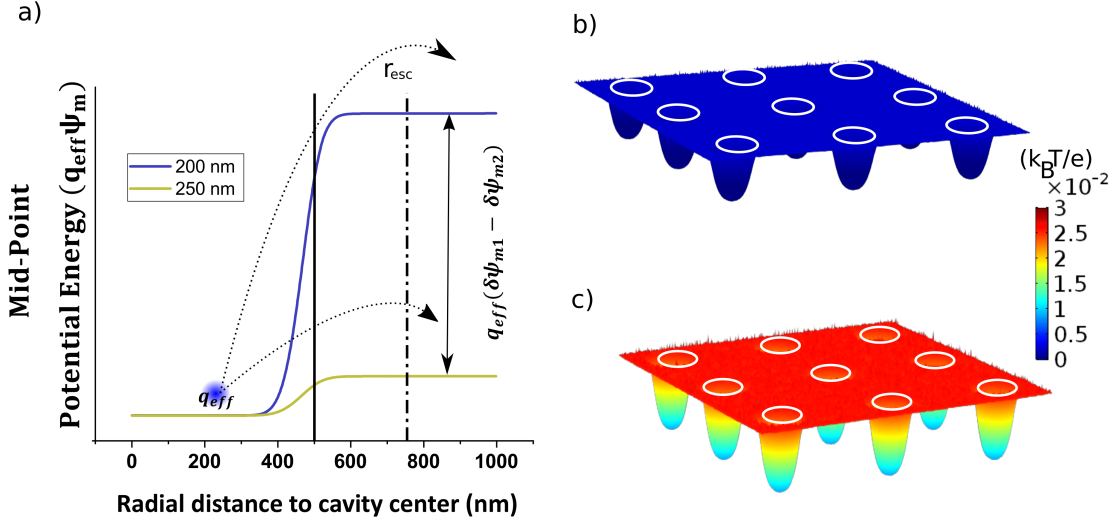


**Figure 4.9:** (a) The mid-point potential Energy as a function of radial distance from the cavity center for a slit height of 200 nm and 250 nm. By decreasing the slit height, the energy barrier increases and the average of escape time increases. The quantity  $r_{\text{esc}}$  gives the boundary a particle should pass to be considered as having escaped from the well. The mid-point potential corresponding to a  $3 \times 3$  cavity lattice for a slit height of (b) 250 nm and (c) 200 nm.

is considered to have left the cavity when its radial coordinate  $r > r_{\text{esc}}$  (occurring at time  $t_2 > t_1$ ). The escape time  $t_{\text{esc}} = t_2 - t_1$ .

In the case that the well geometry ( $R_c$ ,  $d$ ) and particle chemistry remain unchanged (i.e.  $q_{\text{eff}}$  is constant),  $\langle t_{\text{esc}} \rangle$  depends only on the potential well depth ( $W$ ). We can use the dependence of  $\langle t_{\text{esc}} \rangle$  on  $W$  to measure the particle effective charge. The potential well depth,  $W$ , depends on the particle effective charge  $q_{\text{eff}}$  via  $W = q_{\text{eff}}\delta\psi_m$ , where  $\delta\psi_m$  is the difference of the value of the electrical potential averaged over the particle surface inside and outside of the cavity. Therefore, when the average escape time is measured for two differing degrees of confinement ( $\langle t_{\text{esc},1} \rangle$  and  $\langle t_{\text{esc},2} \rangle$ ), Eq. 4.5 can be rewritten:

$$q_{\text{eff}} = \frac{\ln \left( \frac{\langle t_{\text{esc},1} \rangle}{\langle t_{\text{esc},2} \rangle} \right)}{\psi_{m1} - \psi_{m2}} \quad (4.6)$$

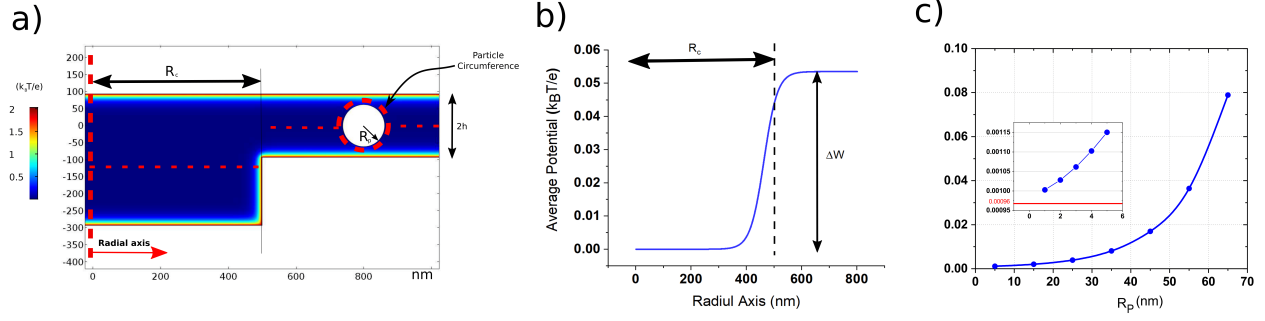


**Figure 4.10:** Electrostatic potential obtained from COMSOL simulation. (a) Electrostatic potential contours inside the chamber; (b) surface-averaged value of electrostatic potential at mid-plane  $\psi_m$  versus the radial distance from cavity center; (c) surface-averaged value of electrostatic potential versus particle radius.

#### 4.6.5 Solution for Electrostatic Potential

The electrostatic potential in the device is obtained from solution of the Poisson-Boltzmann equation:

$$\nabla^2 \psi = \kappa^2 \sinh \psi \quad (4.7)$$

here  $\kappa$  is the inverse Debye length, given by  $\kappa = \sqrt{\frac{2cN_A e^2}{\epsilon_m \epsilon_0 k_B T}}$  with  $N_A$  the Avagadro number,  $e$  the elementary charge,  $\epsilon_0$  the permittivity of free space,  $\epsilon_m$  the relative permittivity of our medium (taken to have a value of 78 for water at a temperature 298 K) and  $c$  the medium ionic concentration. Eq. 4.7 is solved by simulation in COMSOL Multi-physics using axisymmetric cylindrical coordinates  $(r, z)$  according to M. Krishnan. [108] (Figure S4.10-a,b). The particles will tend to occupy the position of minimum electrostatic potential, which occurs at mid-plane (e.g. position equidistant between membrane lid and substrate). Since the particle's size is comparable to the slit height, we need to take into account the variation of the potential around the particle. This is accomplished by computing the average of the potential over the particle's surface. [108] Figure S4.10-c gives the dependence of the surface-averaged value of the electrostatic potential at mid-plane  $\psi_m$  on particle radius for a slit height of 200 nm. Note that the surface-averaged value of the electrostatic potential increases exponentially with particle radius.

#### 4.6.6 Determining Zeta-Potential of Device Surfaces

Solution of the electrostatic potential via Eq. 4.7 requires knowledge of the electrostatic potential (zeta-potential) on the membrane lid and substrate ( $\psi_s$ ). In order to measure  $\psi_s$ , we use YOYO-1 labeled pBR322 Vector as a calibration particle with known size and effective charge. The advantage of using this plasmid vector is that the plasmids, each having the same sequence, are chemically uniform. First, the average escape time of the plasmid from an electrostatic well is measured in our nanofluidic device at a specific slit height  $2h$  (specifically, for a slit height  $2h = 185$  nm, the averaged plasmid escape time over 351 escape events is 1.85 s, Figure S4.11-a). Then, using simulation, the average escape time is obtained for different  $\psi_s$  values for a particle with the same size and effective charge as the plasmid at the same fixed slit height. Note that the plasmid hydrodynamic radius is reported as 65 nm [155] and the particle's effective charge is evaluated using electrophoresis as  $-152 \pm 4e$ . Finally, by correlating our experimental and simulation results, the  $\psi_s$  value yielding the same average simulated escape time as experiment is obtained. This value of  $\psi_s$  corresponds to the device zeta-potential.

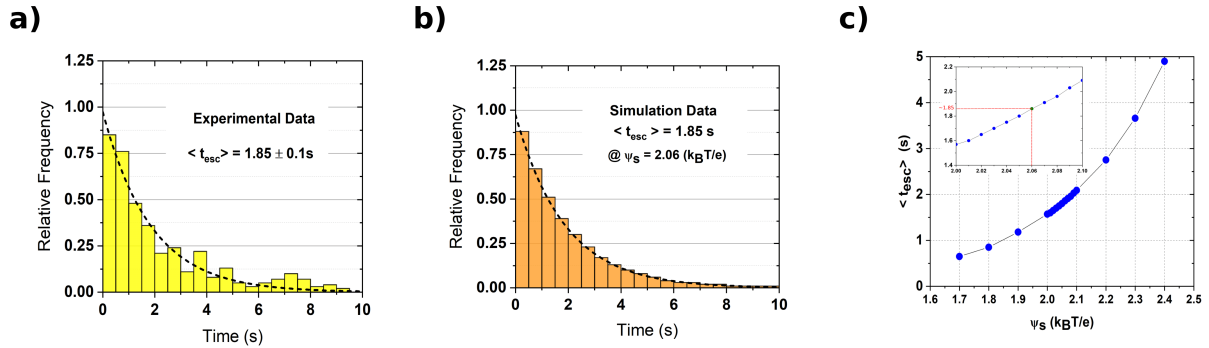


**Figure 4.11:** (a) Histogram of 351 experimentally measured escape times for pBR322 Vector with a hydrodynamic radius of 65 nm and a slit height of 187 nm. (b) Histogram of 10000 simulated escape times using BD simulation for a particle with the same size, charge and the same slit height as experiment. Setting  $\psi \sim 2.06(\frac{k_B T}{e})$  yields an average escape time in agreement with experiment. (c) Average escape time versus surface electrostatic potential using BD simulation.

The simulated escape times are found from solving the Langevin equation:

$$\mathbf{x}(t + \delta t) = \mathbf{x}(t) - \mu \nabla \bar{W} + \sqrt{2D\delta t} \mathbf{w}(t), \quad (4.8)$$

Here,  $D$  is the diffusion coefficient calculated in the next section 4.6.7. The quantity  $\mathbf{w}(t)$  is a random displacement arising from Gaussian distributed thermal fluctuations:  $\langle \mathbf{w}(t) \rangle = 0$  and  $\langle \mathbf{w}(t) \mathbf{w}^T(t') \rangle = \mathbf{I}$  if  $|t - t'| < \delta t$ ,  $\mathbf{0}$  otherwise. The quantity  $\mu = \frac{\delta t}{6\pi\eta R}$ . For good convergence, the simulation time step ( $\delta t$ ) is set at  $10 \mu\text{s}$ . The quantity  $\bar{W}(\mathbf{x}(t))$  is a potential energy given by  $\bar{W} = q_{\text{eff}}\psi_m(\mathbf{x}(t))$ .

The simulations are performed with the particle initially located at the cavity center. Escape occurs when the particle's radial position exceeds  $r_{\text{esc}}$ . Equivalent escape simulations are performed 10000 times, giving rise to a distribution of simulated escape times. To obtain the average simulated escape time, the histogrammed escape times are fitted to the same exponential model as experiment:  $P(\Delta t) = A/\langle t_{\text{esc}} \rangle \exp(-\Delta t/\langle t_{\text{esc}} \rangle)$  (Figure S4.11-b). We performed this simulation for different surface electrostatic potential values, and the average escape time as a function of  $\psi_s$  is shown in Figure S4.11-c.

We found that when  $\psi \sim 2.06(\frac{k_B T}{e})$ , there is less than a 1% deviation between the experimental and simulated escape times. The results show that the PVP incubated surfaces of our nanofluidic device have slightly lower surface electrostatic potential values in comparison to the previously reported silica-water surface electrostatic potential ( $2.8\frac{k_B T}{e}$ ) . [184]

#### 4.6.7 Effect of hydrodynamic coupling between particle and device surfaces

When a particle moves between parallel surfaces, there is a non-negligible hydrodynamic coupling between the particle and the surfaces that results in an increased friction. Consider a spherical particle of radius  $R$  moving at the mid-point position between two parallel surfaces positioned a distance  $2h$  away. Faxén showed that hydrodynamic coupling

between the particle and surface leads to a friction factor given by: [72]

$$\zeta_{\text{eff}} = \frac{\zeta_0}{1 - 1.004(R/h) + 0.418(R/h)^3 + 0.21(R/h)^4 - 0.169(R/h)^5} \quad (4.9)$$

with  $\zeta_0 = 6\pi\eta R$ , the friction factor in bulk solution (i.e. far away from the surface). The quantity  $\eta$  is the solution viscosity ( $= 8.90\text{e}^{-4}$  Pa.s, i.e. viscosity of water at temperature 298K). The diffusion coefficient is given by  $D = k_B T / \zeta_{\text{eff}}$ .

#### 4.6.8 Relationship Between Zeta Potential and Charge

Once the size and charge of the spherical particles is known, the particle zeta potential  $\zeta$  can be calculated from the below equation: [110,131]

$$q_{\text{eff}} = -\epsilon_m \epsilon_0 \kappa 4\pi R^2 \left( \frac{k_B T}{e} \right) \left[ 2 \sinh \left( \frac{y}{2} \right) + \left( \frac{4}{\kappa R} \right) \tanh \left( \frac{y}{4} \right) \right] \quad (4.10)$$

where  $y = \frac{e\zeta}{k_B T}$  is the dimensionless zeta potential and  $R$  is the particle radius. We numerically invert the equation to access  $\zeta$  from knowledge of  $R$  and  $q_{\text{eff}}$ .

#### 4.6.9 Automation

We automated the measurement approach using a custom Python code to control lid-deflection, camera and LED operation (Figure S4.12). First, new particles are pumped into the array (5 s). Then the membrane is deflected by high pressure and the particles are maintained in a state of high confinement. After holding 2 s to ensure the membrane stabilizes, the applied pressure is decreased to reduce the potential well depth to  $\text{DPW}_1$ . After holding another 2 s to ensure the membrane stabilizes, the microscope camera and LED illumination are turned on and the particle trajectory is recorded for 1 min. Subsequently, the pressure controller reduces the pressure to lower the potential well depth to  $\text{DPW}_2$ . Again, after holding 2 s to ensure the membrane stabilizes, the microscope cam-



era records the particle trajectory for 1 min. Acquisition is then halted and the trajectory saved.

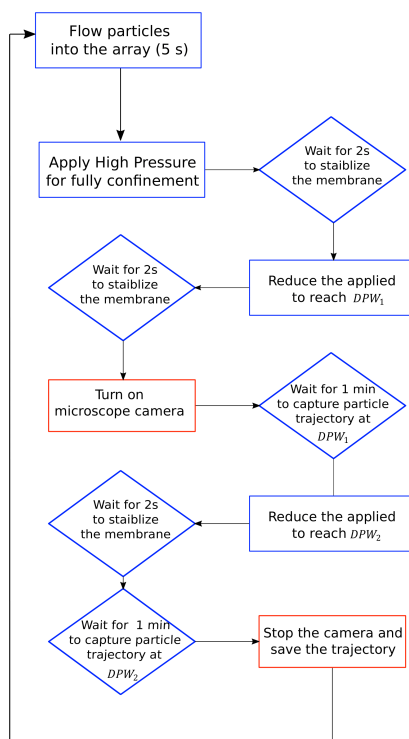


**Figure 4.12:** Flow Chart of python code for syncing microscope camera and LED and pressure controller.

#### 4.6.10 Preparation of Extracellular Vesicles

EGFRvIII expressing variant of U373 (human astrocytoma) and NHA (normal human astrocytoma) are grown in Dulbecco's modified essential medium (DMEM; Wisent, Canada) supplemented with 10% heat-inactivated fetal bovine serum (FBS) (Wisent) and 1% penicillin-streptomycin (Gibco-Life Technologies, Grand Island, NY) at 37 in 5% CO<sub>2</sub>. The conditioned medium (CM) was collected from cells grown for 72 hour in culture media containing 10% of Extracellular Vesicle (EV) depleted FBS (generated by centrifugation at  $150,000 \times g$  for 18 hour at 4). The CM is centrifuged one time at  $400 \times g$  for 15 min in a filter tube (Merck™ UFC900324) to concentrate the particles. Finally, the EVs are sepa-

rated using Size Exclusion Chromatography columns (IZON Science Ltd, United States) in 1mM Tris with 0.4 mM NaCl solution. For size distribution analysis of EVs, nanoparticle tracking analysis (NTA) was carried out with each collected iodixanol fraction using NanoSight NS500 instrument (NanoSight Ltd., UK). Three recordings of 30 s at 37°C were obtained and processed using NTA software (version 3.0). All experiments were carried out in three biological replicates.

#### 4.6.11 Data Table for Vesicle Measurements

Table 4.1 gives the mean values and accompanying standard deviations for the three vesicle populations measured in the device. Note that the observed difference in values between device class 1 and 2 is not significant.

**Table 4.1:** The mean diameter, charge and zeta potential for vesicles measured in the device along with their accompanying standard-deviation ( $\sigma$ ). In total, 30 liposomes were measured (device class 1) and 100 U373 and NHA EVs each (70% of EVs in device class 1 for both U373 and NHA, 30% in device class 2). Each mean value is given an error bar determined from the standard-deviation of the mean.

Vesicle	$\langle d \rangle$ (nm)	$\sigma_d$ (nm)	$\langle q \rangle$ (e)	$\sigma_q$ (e)	$\langle \zeta \rangle$ (mV)	$\sigma_\zeta$ (mV)
Liposomes	239 $\pm$ 2	8	3010 $\pm$ 40	230	37.6 $\pm$ 0.4	2
U373 (all)	163 $\pm$ 4	35	1719 $\pm$ 70	701	41.3 $\pm$ 0.6	6.0
NHA (all)	155 $\pm$ 4	39	1883 $\pm$ 84	835	48.6 $\pm$ 0.6	6.4
U373 (device class 1)	164 $\pm$ 4	34	1706 $\pm$ 83	691	41.5 $\pm$ 0.7	5.5
U373 (device class 2)	161 $\pm$ 7	38	1749 $\pm$ 135	738	43.9 $\pm$ 1.4	7.5
NHA (device class 1)	158 $\pm$ 5	40	1960 $\pm$ 103	863	48.7 $\pm$ 0.7	5.9
NHA (device class 2)	148 $\pm$ 6	34	1705 $\pm$ 137	748	48.2 $\pm$ 1.4	7.5

#### 4.6.12 Discussion of Technology Scaling

The time  $t_N$  to measure  $N$  EVs is given by  $t_N = t_0(N/n)$  where  $t_0$  is the time required to measure EVs in one field of view and  $n$  is the number of EVs measured simultaneously in one-field of view. The time  $t_0$  is determined by the time to flow particles into the ar-

ray (5 s), the time of lid-lowering/raising plus stabilization (6 s) and the two trajectory integration steps required (each 1 min long). Thus,  $t_o = 131$  s. How many EVs can we measure simultaneously in a field of view? In order to measure the escape time, we need in principle only two adjacent cavities available for a single EV (one well for particle to leave, one well for a particle to enter). Thus, the maximum number of EVs we can fit in principle in array is half the total number of cavities (so the maximum occupancy is 50%). For cavities with a center-to-center separation of  $3\text{ }\mu\text{m}$  in a  $100\times 100\text{ }\mu\text{m}^2$  field of view, this gives  $n = 545$ , and suggests we can measure 1000 EVs in around 4 min ( $t_{N=1000} = 4$  min). Of course, this situation is idealized: we cannot assume the array will be so densely occupied. Yet, note that assuming an occupancy of only 10% still yields a practical measurement time of around 20 min for 1000 EV's ( $\sim 50$  EV/min). Note that multiple occupancy of a well by more than one EV, which might confound the trajectory of different particles, is not an issue: the EVs self-exclude strongly due to their high negative charge. We have never observed multiple occupancy of a well by more than one EV.

In order to increase throughput further we can increase the optical field of view and the corresponding array area, ensuring that a larger number of EVs are measured in parallel for a given acquisition sequence. Single-molecule imaging technology based on back-illuminated CMOS CCDs (such as the Photometrics Prime 95B 25MM and Photometrics Kinetix) routinely provide a  $170\times 170\text{ }\mu\text{m}^2$  and even  $200\times 200\text{ }\mu\text{m}^2$  field of view for a 100x objective. We can further increase the field of view by using a 60x objective, yielding a  $330\times 330\text{ }\mu\text{m}^2$  field of view. This increase in the field of view by a factor of 3.3 leads to a 11-fold increase in statistics yielding a  $t_{N=1000} \sim 1.8$  min ( $\sim 600$  EV/min).

Now, of course we cannot exploit the entire array area due to the membrane curvature; we wish to only perform measurements within the “plateau region” where the slit height variation is less than the prescribed value  $2\delta h_{\text{max}}$ . Thus, it is important to determine whether it is practical to increase the plateau region to extend across the field of view (i.e. to cover up to a  $330\times 330\text{ }\mu\text{m}^2$  area). Using a  $h_{\text{max}} = 0.8$  nm, Comsol simulation predicts that a  $L_{\text{plateau}} = 100\text{ }\mu\text{m}$  requires a membrane width of  $500\text{ }\mu\text{m}$  and a  $L_{\text{plateau}} = 330\text{ }\mu\text{m}$

will require a membrane width of around  $800\mu\text{m}$  (see Figure S4.13). While the current class 1 devices with a membrane area of  $160\times 200\mu\text{m}^2$  yield roughly a  $L_{\text{plateau}} = 15\mu\text{m}$ , we feel that it is quite practical in a next generation of devices to increase the membrane area to  $800\mu\text{m}$ , and even higher, as the  $100\text{ nm}$  thick nitride lids are extremely stable. Note that if membrane fragility were a problem, we could simply increase the membrane thickness. If, for some reason we could not make larger stable free standing membranes, than in principle the CLIC approach could be used as an alternative, which implements the confinement variation by deforming a coverslip via a piezo-controlled lens-pusher. [13]

Finally, our estimate of only a 10% array occupancy is quite conservative. We believe it may be feasible to increase array occupancy by increasing sample concentration. Concentration might be performed on-chip, for example, by running EV-containing buffer against a slit barrier with a gap that permits buffer to escape but traps EVs. Note that just a two-fold increase in occupancy (corresponding to only 20% of all cavities occupied in the array, which is still conservative) will yield a throughput  $\sim 1000\text{ EV/min}$ .

#### 4.6.13 Supporting Movie

The movie shows the motion of a single YOYO-1 labeled pBR322 vector at different levels of confinement including low confinement ( $2h = 188\text{ nm}$ ), medium confinement ( $2h = 185\text{ nm}$ ) and strong confinement ( $2h = 170\text{ nm}$ ). In all experiments, the cavity radius ( $R_c$ ) is  $500\text{ nm}$  (Figure 2, manuscript). The movement of the plasmid vector is captured using fluorescence microscopy and superimposed on graphical images of the nanocavities. The dashed circles depict the escape boundary ( $r_{\text{esc}} = 750\text{ nm}$ ). The right panels display the particle status (e.g. whether the particle is inside or outside of the cavities). If the degree of confinement is increased the particle will stay longer in the potential wells. At the highest level of confinement the particle will stay in a single cavity for the entire movie duration. The movie is sped-up by a factor of 2.4.

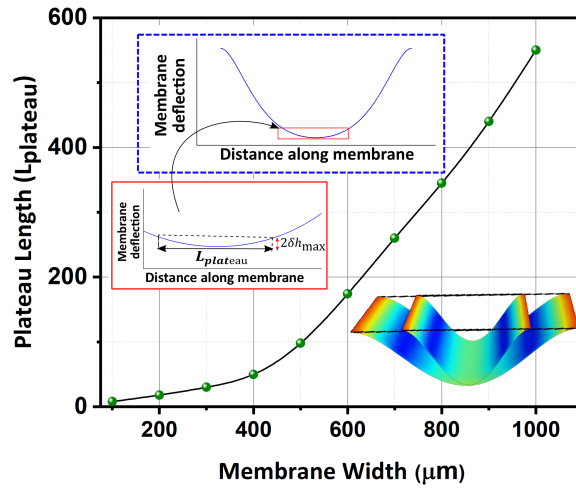


**Figure 4.13:** COMSOL simulation results for the plateau length  $L_{\text{plateau}}$  versus membrane width. The effective utilizable membrane area is given by  $L_{\text{plateau}} \times L_{\text{plateau}}$ . The total variation in slit height across the plateau region is given by  $2 \delta h_{\text{max}}$ . For these simulations  $\delta h_{\text{max}} = 0.8 \text{ nm}$ .

# Connection between Chapter 4 and 5

In the previous study, we observed two interesting facts about EVs confinement. 1- full confinement of particles (staying in a cavity for several hours) can be achieved while still there is a gap between the membrane and substrate. This barrier can be a physical barrier (the gap size is smaller than the particle's size) or an energy barrier raised from a differential electrostatic potential. 2- There is accurate control over the membrane deflection (about 5 nm) which let us meticulously tune the gap size. We came up with the idea to load detection reagents while a target molecule is fully confined in nanocavities. This is important for the EVs multidimensional analysis to be able to detect the target molecules after the isolation procedure. It is worth emphasizing that, EVs are not analyzed in the second manuscript and the progress in this manuscript can be expanded to the EVs analysis in future studies. We first examined the stability of DNA molecules inside the cavities while the tagged primers are diffused inside and washed from the cavities. Then, the control over diffusing of particles from the cavities is examined by testing the batch of tagged spherical gold nanoparticles with 15 nm and 50 nm mean diameters. Finally, to increase the specificity of detection, we used two isothermal amplification methods to detect the DNA molecule inside the cavities.

## Chapter 5

# Tunable nanofluidic device for digital nucleic acid analysis

### 5.1 Abstract

Nano/microfluidic-based nucleic acid tests have been proposed as a rapid and reliable diagnostic technology. The two key steps for many of these tests are target nucleic acid (NA) immobilization followed by an enzymatic reaction on the captured NAs to detect the presence of a disease-associated sequence. NA capture within a geometrically confined volume is an attractive alternative to NA surface immobilization that eliminates the need for sample pre-treatment (e.g. label-based methods such as lateral flow assays) or use of external actuators (e.g dielectrophoresis) that are required for most nano/microfluidic-based NA tests. However, geometrically confined spaces hinder sample loading while making it challenging to capture, subsequently, retain and simultaneously expose target NAs to required enzymes. Here, using a nanofluidic device that features real-time confinement control via pneumatic actuation of a thin membrane lid, we demonstrate the loading of digital nanocavities by target NAs and exposure of target NAs to required enzymes/co-factors while the NAs are retained. In particular, as proof of principle, we

amplified single-stranded DNAs (M13mp18 plasmid vector) in an array of nanocavities via two isothermal amplification approaches (loop-mediated isothermal amplification and rolling circle amplification).

## 5.2 Introduction

The Nucleic Acid Test (NAT) is a reliable method for early disease detection. For example, polymerase chain reaction (PCR) has been used to detect viral infections such as SARS-CoV-2 [247], and next-generation sequencing (NGS) has been used for whole genome sequencing (WGS) to detect single nucleotide variants (SNVs) that result in cancer [66]. In NA amplification, detection specificity can be significantly improved by using designed primers to enable the detection of single nucleotide variants [145]. In addition, partitioning the sample, i.e. dividing the sample into small volumes either in micro wells [197] or droplets [168], can increase detection specificity and sensitivity. Sample partitioning prior to amplification enhances the detection specificity by reducing cross-contamination between the samples in each partition [168]. Partitioning can also enhance detection sensitivity for low-abundant target molecule samples [77]. In this case, certain partitions may contain one or more target molecules, although many other partitions may be devoid of the target molecule. Consequently, detecting the target molecule is more probable within partitions enriched with the target molecule. Furthermore, there is a higher likelihood of detecting a response signal within each positive partition compared to traditional methods where the detection signal is diluted throughout the entire sample. Moreover, partitioning can provide accurate quantitative measurement of the target molecule concentration by mitigating quantitative biases found in traditional quantitative NAT methods. These include biases arising from target molecule properties (such as GC contents or secondary structures such as hairpins or stem-loops) or inhibiting effects (caused by DNA binding proteins or amplification contamination such as nucleases and salts) [168].



Digital PCR (dPCR) is the gold standard approach for partitioned NA amplification [100]. A key requirement of dPCR is thermal cycling which requires costly equipment. In thermal cycling the temperature is increased to  $\approx 95^{\circ}\text{C}$  for DNA denaturation, reduced to  $\approx 50^{\circ}\text{C}$  for primer annealing, and then increased to  $\approx 65^{\circ}\text{C}$  for synthesizing a new strand. Isothermal amplification methods have been proposed as alternatives to dPCR to eliminate the need for the complex setup required for thermal cycling in PCR and increase detection sensitivity and specificity. Loop-mediated isothermal AMPlificaiton (LAMP) method uses primers targeting multiple regions of the target molecule to decrease the non-specific amplification [11] at  $65^{\circ}\text{C}$ . Also, the polymerase used in LAMP (Bst 2.0) is a high-speed strand-displacing DNA polymerase with a higher tolerance to inhibitors. Digital LAMP has been proposed to further increase the sensitivity; however, the molecules are non-accessible after target molecule partitioning in small wells (Tan 2021 digital, Lin 2019 digital). Although LAMP has been reported as a powerful technique for point-of-care testing due to its robustness in DNA amplification and high selectivity via the use of three primer pairs, the high-temperature activity of Bst DNA polymerase ( $65^{\circ}\text{C}$ ) makes it challenging to couple LAMP with other platforms. Rolling Circle Amplification (RCA) is another isothermal amplification method that can work at room temperature due to the room-temperature activity of phi29 polymerase [255]. So far RCA has been integrated with microfluidic platforms [101], and combined with multiple read-outs including surface plasmon resonance (SPR) [199], and electrochemistry [53]. In addition, LAMP assays are likely to generate unwanted non-specific amplification products due to primer dimerization and mismatched hybridization, arising from the fact that in LAMP reactions about six primers at high concentrations ( $3.6\text{--}4.4\mu\text{M}$ ) are needed in comparison with RCA reactions where two primers at lower concentrations ( $0.4\text{--}1.0\mu\text{M}$ ) are employed [124,269].

Nanofluidic devices can be used for controlled digitization of NAT samples. Using nanofluidic devices, a larger number of partitions can be accommodated in one field of view, consequently enhancing the sensitivity and specificity of detection by mitigating the influence of quantitative biases and inhibitors. Also, the sample partitioning can be

done very accurately using nanofluidic devices, which reduces the biases raised by the sample loading inside the partitions. The primary step in the nanofluidic-base NAT is molecule capture. A number of approaches have been demonstrated for NA capture, including immunoaffinity [6,148], and external forces such as dielectrophoresis [137] and optical trapping [21].

Nucleic Acids can also be captured by confinement in nanofluidic compartments (e.g., nano-wells or nanochannels) without external forces or treatment of the nanofluidic device for immunoaffinity immobilization. In confinement-based capture, NAs are loaded in a narrow slit (with 50-1000 nm height) containing nanofluidic compartments implemented inside the slit. Although NA confinement eliminates the need for pretreatment or external actuation, it can hinder analyte accessibility for the next detection steps (i.e., incorporation of enzymes or fluorescent dye). One widely employed solution to ensure analyte accessibility to the embedded compartments is to leave a fixed nanoscale gap between the bonding lid and the compartments [170,187]. For example, Marie et al. confined lambda DNA in an array of nanopits and showed that phi29-driven amplification can be achieved while the DNA is immobilized in the nanopits with a slit gap [141]. Öz *et al.* stretched lambda DNAs in nanochannels and loaded nucleolytic enzyme DNase I to digest the stretched DNA while preserved in the nanochannels [163]. Two main obstacles exist in this approach. First, the target NA size must be significantly larger than the enzyme and primers; otherwise, the target NA can escape quickly. Fixing the slit height at a very narrow gap increases the residency time of captured NA in the confined space; however, loading the target molecule into the slit will be hindered in the narrow slit height. Secondly, the nanofluidic devices work with a limited range of NA sizes. At high slit heights, only large particles can be loaded and confined in the nanofluidic compartments, as small particles tend to escape quickly. Conversely, only small particles can be loaded and confined at narrow slit heights, while the loading of large particles is hindered by the narrowness of the slit.

One solution is to dynamically adjust the slit height so that the optimum degree of confinement can be achieved for a given assay step. Here we harness a coupled-membrane nanofluidic device featuring tunable confinement to confine and partition nucleic acids inside a matrix of nanocavities and amplify the target nucleic acids using isothermal amplification methods including the RCA and LAMP. In our previous work [26,80,130], we introduced a nanofluidic system that exploits pneumatic pressure applied to a flexible free-standing SiNx membrane lid to adjust in situ the degree of confinement experienced by nanoparticles and single molecule analytes in nanoconfined volumes. Pneumatic pressure applied from above deflects the lid downwards varying the degree of confinement; at the highest degree of deflection, the lid seals off nanocavity structures embedded in a nanoslit. Here we exploit and modify this approach with the objective of performing digital DNA amplification on target DNA confined inside the nanocavities. This requires performing biochemical processing steps on the confined nucleic acids, which in turn requires the capability of introducing chemical reagents into the nanocavities, such as DNA polymerase, amplification buffer and fluorescent dye, while the DNA targets are retained. This can be achieved using our ability to adjust the degree of membrane deflection with nm precision, creating gaps sufficiently small around the nanocavity to prevent the escape of target DNA while allowing the introduction of amplification reagents. Reagents are introduced via a set of parallel nanochannels located sufficiently close to the nanocavities for diffusive transport through the thin access gap to be efficient. The nanochannels are in turn interfaced with microchannels for reagent loading.

## 5.3 Experimental

### 5.3.1 Device design

Our adjustable confinement device is created using the procedure described in Capaldi *et al.* [25]. The device consists of a borosilicate substrate that incorporates two intersecting nanoslits, namely the target-loading channel and the reagent-loading channel (Figure 5.1-

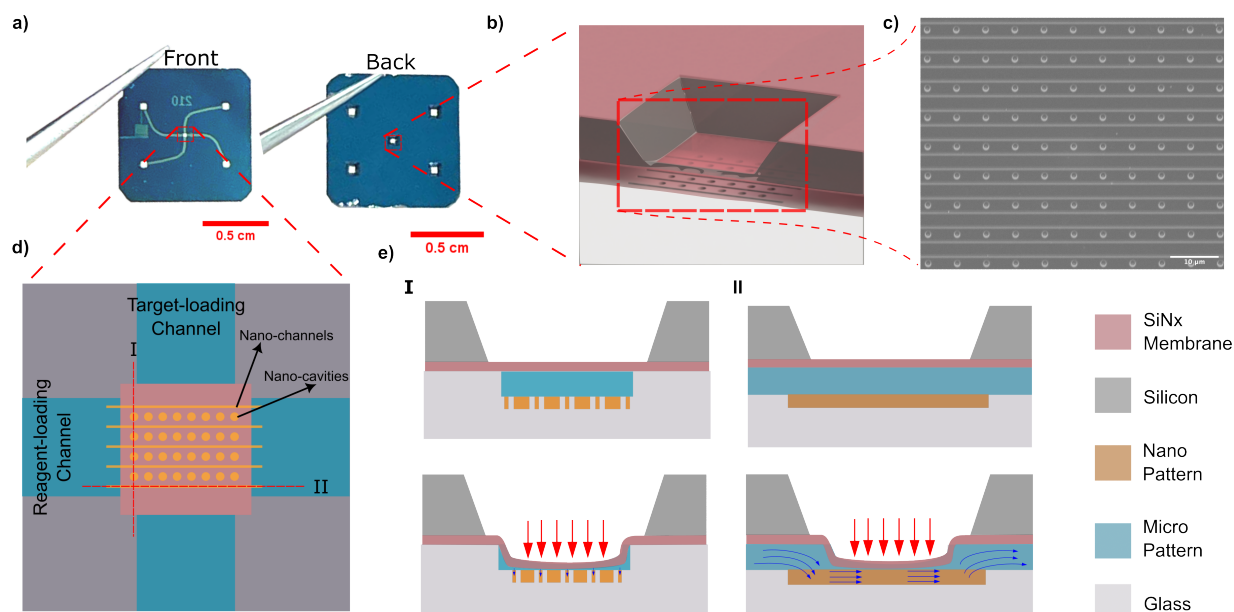


**Figure 5.1:** Nanofluidic device and its working principle a) Front and back views of the nanofluidic device b) 3D schematic of the deformable membrane. c) SEM of nanocavity array after the membrane is removed. d) The device has two crossed microchannels (target-loading channel and reagent-loading channel) which intersect at the membrane position. e I) Cut-out view of the nanofluidic device at the reagent-loading channel. When the membrane is pushed down, the membrane prevents the reagents from flowing from the nanochannels to the nanocavities. e II) Cut-out view of the nanofluidic device at the target loading channel. While the membrane is deflected, the reagents can enter the nanochannels as the nanochannels are connected to the reagent-loading channel external to the membrane area.

d). The nanoslit depth is 420 nm and each slit is connected to two loading reservoirs (refer to Figure 5.1-a, and Supporting Information section 5.9.1). A matrix of circular nanocavities (with a radius of  $R_c = 1000$  nm and 300 nm deep) and an array of nanochannels (with a width of 100 nm) are embedded at the intersection of the microchannels (Figure 5.1-b,c). The nanochannels are positioned a distance of 500 nm from the nanocavities so that they are in close proximity. Above the nanocavities, there is a flexible lid formed from a free-standing silicon nitride membrane (200 nm) thick. The device is mounted in a 3D-printed chuck enabling a solution to be introduced into the loading reservoirs and a pneumatic pressure applied to deflect the membrane (see Supporting Information section 5.9.1). The chuck is mounted on an inverted fluorescence microscope and imaged using an sCMOS Camera (PRIME 95 25MM) and 60X water immersion objective (Nikon).

### 5.3.2 Device operation

When pneumatic pressure is applied the membrane deflects, resulting in a reduction of the vertical gap (slit height). As we have previously shown [80], the slit height as a function of the applied pressure can be calibrated by measuring the intensity of fluorescent dye present in the nanoslit (see Supporting information 5.9.3).

Digital DNA amplification can be divided into two main steps. The first step is the confinement and concentration of DNA molecules in the nanocavities. The second step is DNA analysis, including removing the extra particles from the chamber by loading a washing buffer (e.g., 1X TE buffer), fluorescent staining, and DNA polymerization. In the first step, the DNA is loaded from the target-loading channel into the membrane region by constant pressure applied at the inlet (Figure 5.2-b-I). During the DNA loading into the membrane area, no pneumatic pressure is applied so the slit height is at its maximum value (420  $\mu$ m). The membrane is then deflected to push the DNA inside the cavities, reaching the maximum degree of deflection at which the nanocavities will be completely sealed (Figure 5.2-b-I).

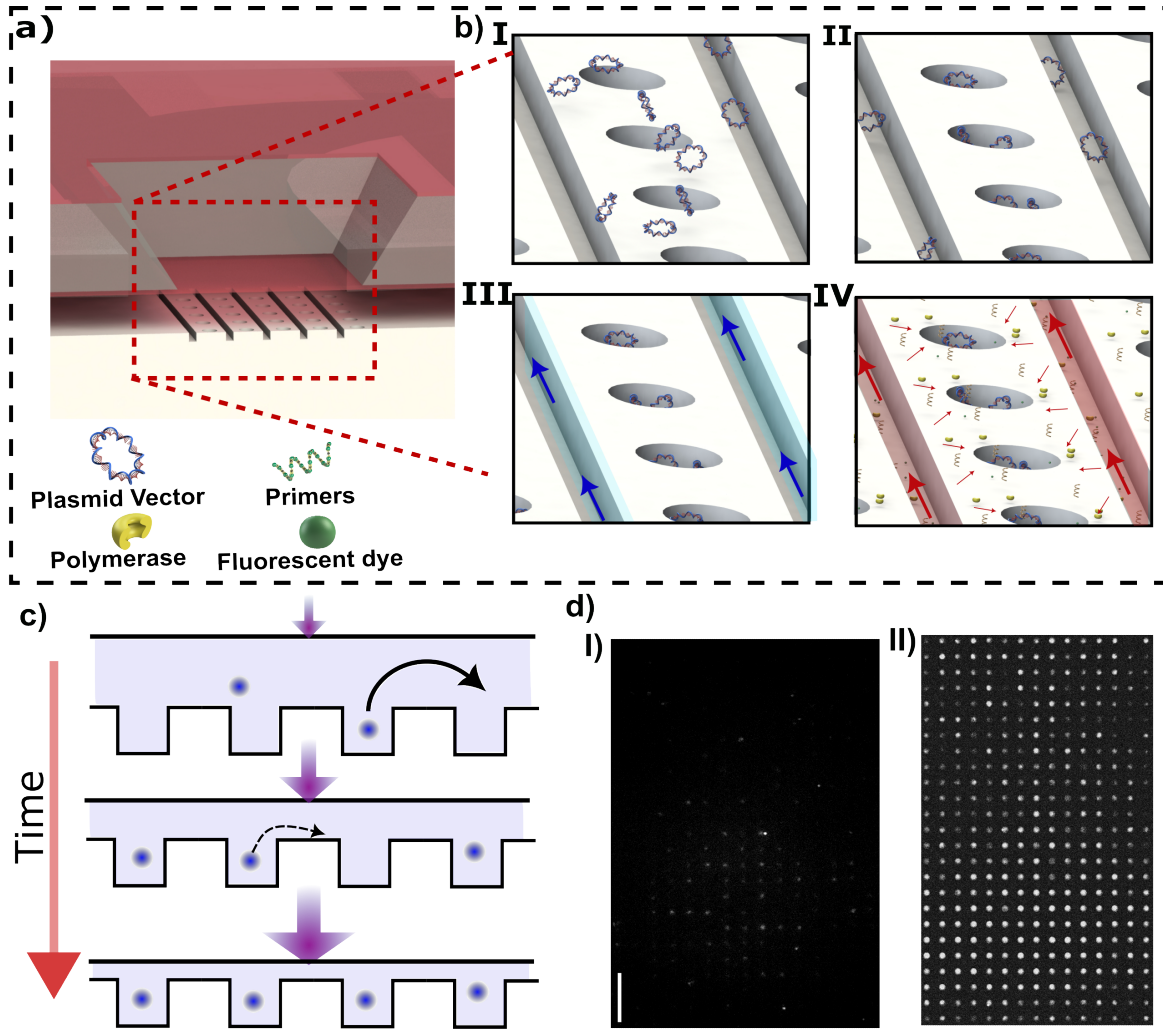


**Figure 5.2:** a) Schematic image of the membrane region. b) Loading and amplification steps of DNA inside cavities; bI) loading of target DNAs from target loading channel; bII) DNA confinement via membrane deflection; bIII) washing out extra DNAs in side nanochannels and reagent-loading channels; bIV) adding amplification reagents from nanochannels while the target DNAs remain confined in nanocavities. c) Cartoon showing molecule concentration in cavities as the membrane lid is lowered. d) Fluorescent images showing the confinement of YOYO-1 labelled-pBR322 plasmid vectors in nanocavities I) without and II) with the concentrating procedure.

In the second step, the detection reagents are loaded from the reagent-loading channel. First, NA molecules present in the side nanochannels are removed via a washing buffer introduced in the reagent-loading channel (Figure 5.2-b-III). Note that the membrane comes into contact with the bottom of the slit channel during the washing step. This contact prevents any particles from jumping or transferring from the nanochannel to the nanocavities. Then, the amplification reagents including polymerase, dNTPs, and fluorescent dyes are loaded from the reagent-loading channel (Figure 5.2-b-IV). The pneumatic pressure is reduced to create a narrow gap between the membrane and nanocavities which let the amplification reagents diffuse through the gap into the nanocavity while, given the large size of the NA, the target NA will stay confined in the nanocavities.

### **5.3.3 Nucleic Acid Concentration in Nanocavities**

While membrane deflection will confine molecules inside the nanocavities, confinement alone does not lead to DNA concentration (see Figure 5.2-d-I). Additional concentration can be necessary if the sample contains a low concentration of target NAs. Combined concentration and confinement can be achieved by a protocol combining membrane deflection with fluid flow. When target NA are driven over the embedded nanocavity array, the NAs will accumulate inside the cavities row by row [141]. This arises as induced flow, increasing the molecule throughput, increases the filling rate of cavities from molecules passing by in the slit that can then enter a cavity. At the same time, molecules that are captured in a cavity remain trapped, even in the presence of the flow, due to the high entropic barrier created by the slit. A high cavity filling rate combined with a very small escape rate leads to NA concentration within the cavities. As molecules are repelled from cavities that are already filled due to the strong excluded-volume interactions with molecules present in the filled cavities, cavity rows will tend to fill sequentially. Therefore, an intermediate flow should be adopted to obtain a high occupancy; however, a long waiting time is required to obtain full occupancy at an intermediate flow.

The entropic barrier can be increased by decreasing the slit height, allowing for using faster flow to achieve a high occupancy level in a shorter period of time. However, using a very thin slit height hinders the loading and washing of target NAs from cavities. The ability to adjust confinement in real time allows us to separate the particle loading and washing steps from the concentration step. Consequently, a narrow slit height can be employed specifically for the concentration step without any concerns regarding the loading and washing steps. Also, in our method, since the occupancy of one cavity is independent of the occupancy of all other cavities, a defect in one cavity does not affect the occupancy of other cavities, as in this case for pure flow-based loading without confinement modulation.

To demonstrate combined loading and concentration, YOYO-1 stained pBR322 vector plasmid with 1 ug/mL concentration is loaded into the membrane area with applied pressure in the reagents inlet the membrane is gradually depressed from an initial slit height of  $197 \pm 6$  nm (25mbar). The membrane is lowered in small increments, with 0.5 mbar pressure increase per increment each increment taking 5 s; the overall process takes 20 such steps and finally, the membrane reaches  $113 \pm 6$  nm (35mbar). We observed that more than 95 % of cavities are occupied with the vector plasmid in 120 seconds.

## **5.4 Result and Discussion**

### **5.4.1 DNA in-cavity retention during buffer exchange**

We demonstrate that pBR322 plasmid vectors can be retained while a staining buffer containing YOYO-1 dye is introduced. YOYO-1 is almost non-fluorescent in a solution; however, the fluorescent intensity increases by 1000-fold when it binds to double-stranded DNAs [188]. In the inlets of the target-loading channel and the reagent-loading channel, 5mg/ml of unlabeled pBR322 plasmid vectors and 10  $\mu$ M of YOYO1 are loaded, respectively. The pBR322 plasmid vectors are confined and concentrated in the nanocavities; this is performed by applying our previous protocol without observing the molecules.



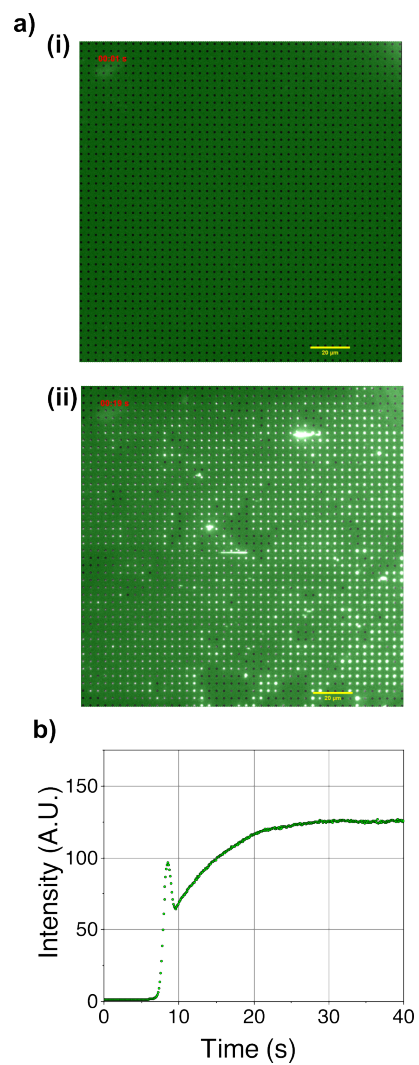


**Figure 5.3:** Labeling of pBR322 plasmid vector with YOYO-1 fluorescent dye in cavities. a) Fluorescent images before and after loading the fluorescent dye in nanochannels while pBR322 plasmid vectors are confined in nanocavities. b) Average fluorescent intensity variation over time.

After confinement, the YOYO1 solution is introduced into the reagent-loading channel from the reservoirs. A thin gap ( $< 5$  nm) is introduced between the membrane and substrate by membrane release; the YOYO-1 molecules can now diffuse through this gap from the nanochannels to reach the nanocavities (note the YOYO-1 has a molecular size below 1 nm, refer to size measurement section of Supplementary Information).

Once YOYO-1 dye reaches the nanocavities, the average fluorescent intensity abruptly increases and reaches a plateau value after about 25 seconds (Figure 5.3-b). This abrupt increase reveals the interaction of YOYO-1 dye with pBR322 plasmid vectors. Comparing the intensity inside the nanochannels (occupied with just YOYO-1 dye) and the intensity of the nanocavities (occupied with YOYO-1 labelled DNAs) shows about a 100-fold stronger signal in the intensity of the nanocavities. To explain the small jump at the beginning of the intensity increase, note that during the loading of DNA in the target-loading channel, the DNA will also migrate to the reagent-loading channel. The loaded fluorescent dye from the detergent-loading channel also interacts with the DNA molecules present in the reagent-loading channel. Just as the fluorescent dye reaches the nanocavities, the labelled DNA in the reagent loading channel will pass through the side nanochannel (It can be observed in Supporting Video III). The fluorescent signal emitted from the labelled DNA inside nanochannels influences the intensity collected from the nanocavities due to the Airy disk effect. According to our previous study [174] and the objective used in the measurement, we expect the Point-Spread Function (PSF) to have a  $0.9\mu\text{m}$  radius; this is sufficient for the intensity present in the nanochannels to affect the intensity measurement in the cavities (which are only  $0.5\mu\text{m}$  away) (see Supplementary Information).

### 5.4.2 Nanoparticle Retention in Nanocavities

To demonstrate our ability to retain small particles, we examined the retention of Cy3 labelled-gold nanoparticles with mean diameters of 15 and 50 nm (Nanocs inc.) at different slit heights. The particles are introduced from the target-loading channel and con-

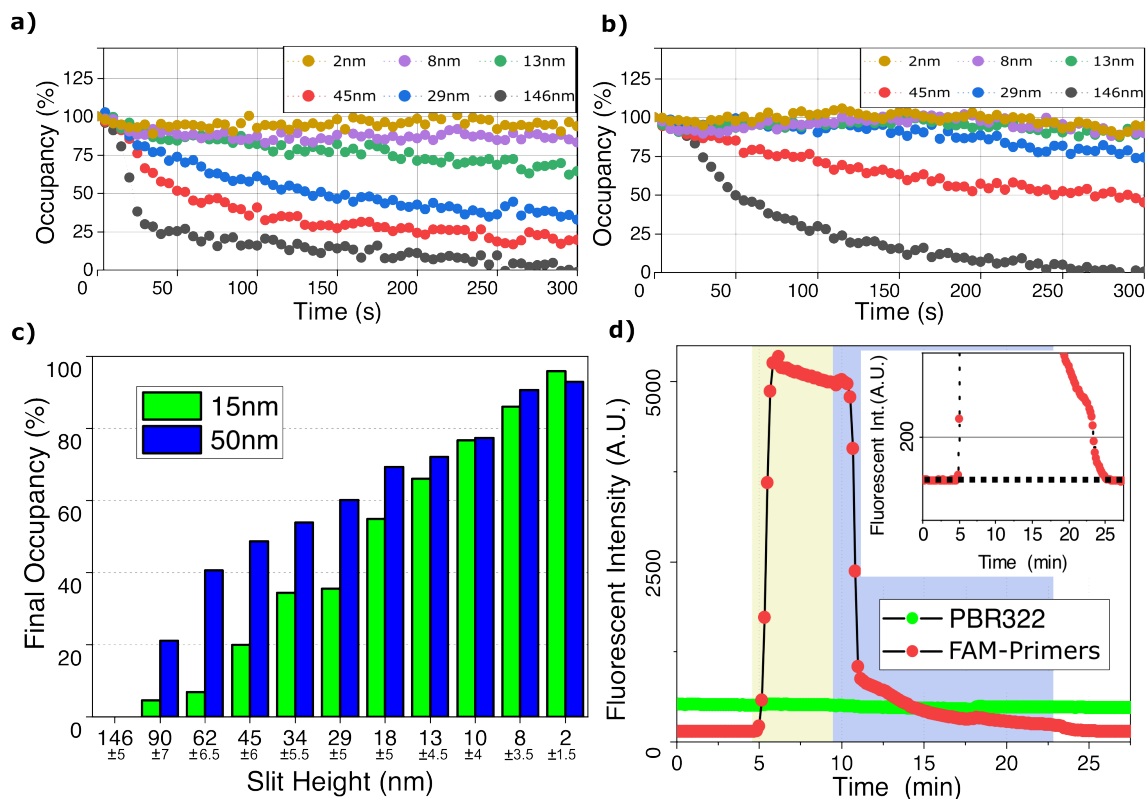


**Figure 5.4:** Variation of occupancy percentage of a) 15nm and b) 50 nm particles in nanocavities after waiting over 5 minutes at different slit heights. c) Comparison of final occupancy percentage of 15 and 50 nm nanoparticles for different slit heights after waiting 5min. d) Retention of YOYO-3 labelled-pBR322 plasmid vectors in nanocavities during the introduction of FAM-tagged primers

finned in the nanocavities by lowering the membrane to ensure complete sealing. Free fluorescent dye and extra gold nanoparticles in the side nanochannels are removed by introducing the washing buffer from the reagents channel. A very low flow (10  $\mu\text{m/s}$ ) is continuously applied from the reagent chamber to wash out the side channels. Then, the applied membrane pressure is decreased to create a gap between the membrane and cavities allowing nanoparticles to leave the cavities. The average fluorescent signal of six nanocavities in the middle of the membrane region is recorded for five minutes for a range of slit heights (Figure 5.4-a,b). Background intensity is removed by capturing a reference frame before nanoparticle loading. Linear photobleaching correction is applied to

the time-dependent fluorescent intensity by measuring the sample fluorescent depletion outside of the nanofluidic device.

When a small gap is introduced, the final fluorescent intensity decreases, indicating the depletion of nanoparticles from the nanocavities (Figure 5.4-a,b). By increasing the slit height still further, particle escape becomes more rapid and a lower concentration is reached. At a very high slit height ( $\approx 146 \pm 5$  nm), the gold nanoparticles escape rapidly and the intensity reaches zero in five minutes, while particles are retained for lower slit heights (Figure 5-5.4-c). Note the samples of gold nanoparticles exhibit a size distribution of 15% (Nanocs inc.), meaning that samples contain some nanoparticles which are smaller and larger than their mean value. For instance, in the case of the sample with 50 nm mean diameter, there are nanoparticles that can pass through a slit with a height below 50 nm because their diameter is smaller than 50 nm.

The nanoparticles with a mean diameter of 15 nm leave the nanocavities more rapidly compared to nanoparticles with a 50 nm mean diameter at the same slit height. Initially, the nanocavities are occupied with maximum concentration (100% occupancy) and are empty before loading (0% occupancy). Therefore, any signal between the maximum concentration and empty state is linearly correlated to the final occupancy. At very high slit heights ( $\approx 146 \pm 5$  nm) all particles exit the nanocavities. By reducing the slit height ( $\approx 45 \pm 6$  nm), although more than 50% of nanoparticles with 50 nm mean diameter remain confined, most of the nanoparticles ( $\approx 80\%$ ) with 15 nm mean diameter leave the nanocavities. Finally, at a very small gap height ( $\approx 2 \pm 1.5$  nm), a tiny reduction (less than 10%) in final occupancy is observed in both samples.

### 5.4.3 DNA retention in nanocavities

It is critical to ensure the retention of target DNAs in nanocavities during washing and reagent loading steps. To quantify the degree of retention, first, our confinement and concentration protocol was used to introduce YOYO-3 labeled pBR322 plasmid vectors into the nanocavity arrays with the lid maximally deflected to ensure complete nanocavity

sealing. Then, 20 bp primers tagged with FAM are loaded from the reagent channel. The primer's radius of gyration of the primer is estimated to be 1.9 nm (see Supporting Information section 5.9.6). After the primers reach the membrane region, a  $5.4 \pm 2.2$  nm gap is introduced so that the primers can enter the cavities. Primer loading in the nanocavities leads to an increase in a FAM-associated signal at the nanocavity location. While the FAM signal increases, the YOYO-3 signal associated with target DNAs stays stable. The observation suggests that we can keep the target NAs in a fully confined state while primers are loaded.

To perform sequential analysis, we need to remove from the nanocavities the molecules used in the previous round of analysis; their retention in subsequent analysis cycles might introduce noise or errors. For example, in sequential multiplex amplification, it is possible to quench fluorescent dye and perform another amplification round. However, the sequential amplification needs the reaction chamber to be emptied of the primers and reagents used in the previous analysis round. We demonstrate that we can remove the primers from the nanocavities while the target DNA molecules are stably retained. To achieve this, the reagent-loading inlet is flushed with the washing buffer which is then introduced inside the nanofluidic device. When the washing buffer reaches the membrane region, the FAM channel intensity drops indicating primers have been removed from the nanocavities. The relative intensity, the intensity is normalized to the intensity before loading primers, reaches zero signalling that the cavities are completely emptied of primers. (Figure 5.4-d-inset). During the washing step, the YOYO-3 channel remains constant indicating the retention of the target DNA inside the cavities.

#### **5.4.4 Amplification Results**

We performed amplification of single-stranded DNA (M13mp18 plasmid vector) in nanocavities using two isothermal amplification methods, namely LAMP and RCA. Once the cavities are loaded with target NAs the amplification assay can be implemented (Figure 5.2-b-IV). LAMP forms loop structures on the target NA, resembling dumbbells, containing

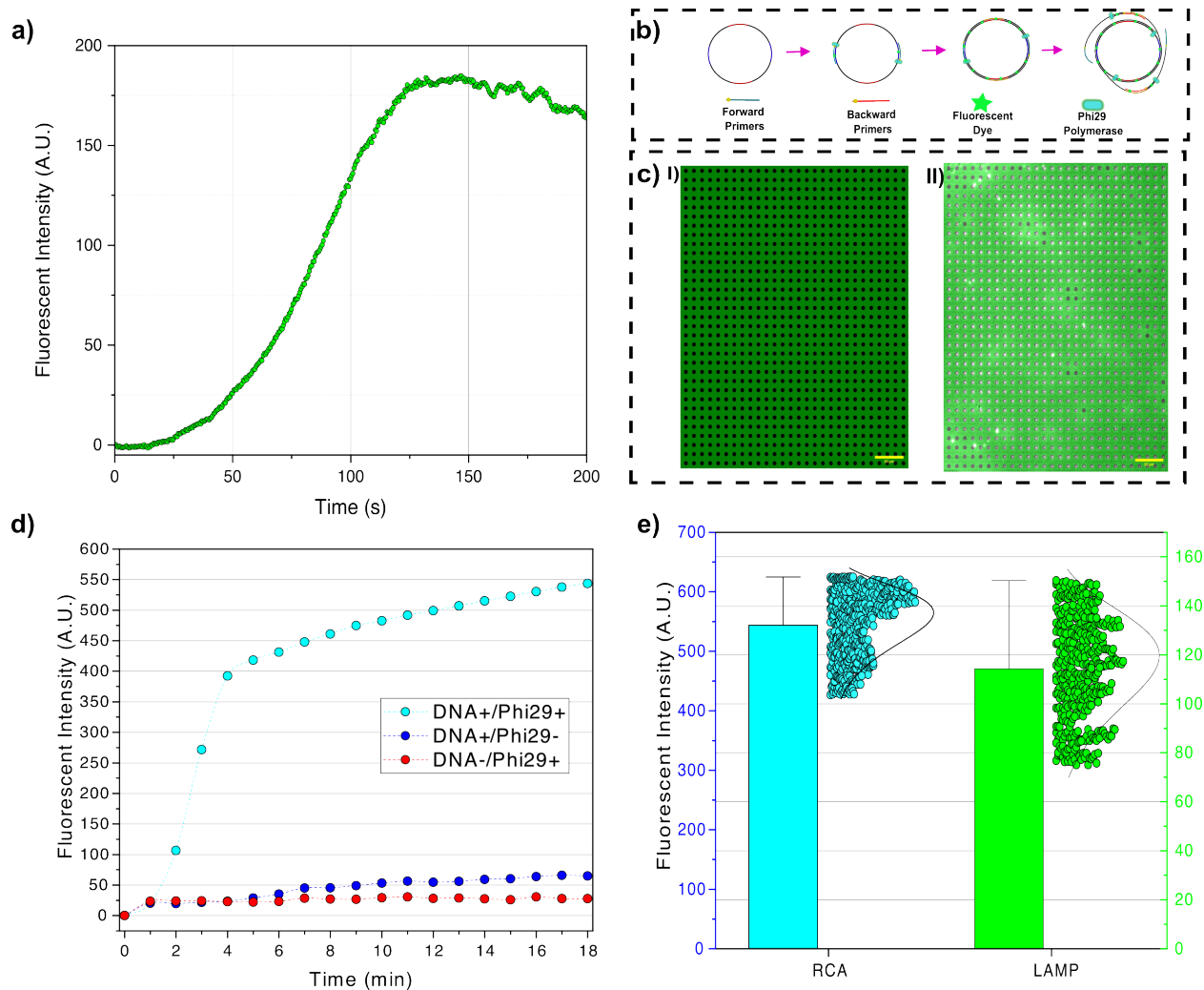


**Figure 5.5:** Digital amplification of M13mp18 in nanocavities. a) Real-time average fluorescent intensity measurement from nanocavities using the LAMP method. b) Four primer RCA amplification procedure. c) Fluorescent images before and 18 minutes after loading the RCA amplification reagents. d) Real-time average of fluorescent intensity measurement using the RCA method and comparison of results with the interaction of the fluorescent dye with target-ssDNA without amplification. e) Fluorescent intensity distribution over cavities for two used isothermal amplification methods.

open single-stranded sequences below the denaturation temperature. Primers can hybridize to the open single-stranded sequences without the need to increase the solution temperature up to the denaturation temperature (95°C). The formation of the loop structures involves two primers (Forward Inner Primer (FIP) and F3). FIP consists of two main sequences: F2 sequences which are complementary to the target DNA sequences F2C, and F1C sequence positioned before F2. F1C is identical to the target DNA sequences located after F2C. The polymerase (usually BST 2.0) in the amplification reagent (LAMP 1X Master Mix, NewEngland Biolabs) initiates synthesis along the FIP primer and generates F1C complementary sequences (F1). Consequently, the synthesized strand along the FIP primer contains F1C-F2-F1 sequences. Secondly, F3 primer binds to the complementary sequences in the target DNA (F3C) which is positioned before F2C. A new polymerase starts synthesizing along F3 primer and detaches the synthesized strand initiated by the FIP primer. Finally, the detached strand forms the loop structure by hybridization between F1C and F1 sequences. After loop formation, a Loop Forward (LF) primer hybridizes with the formed strand containing the open single-stranded sequences in the loop structure and initiates the amplification. While FIP can also trigger amplification (by attaching to the F2C sequences of the formed strand with F2 Sequences), it may not offer the highest stability due to limitations in choosing the optimal position for loop structure formation, dependent on F1 and F2 affinities. LAMP produces double-stranded amplicons that can be detected by an intercalating fluorescent dye (1X LAMP, NewEngland Biolabs). The LAMP primers sequences (ThermoFisher) are provided in the Supporting Information section 5.9.7.

In the RCA method, the target molecule is a circular DNA molecule. When a primer binds to the target molecule, the polymerase (typically Phi29, NewEngland Biolabs) initiates the synthesis from 3' of the attached primer. As the polymerase completes a whole circle and reaches the 5' end of the primer, it opens up the synthesized circle and continues synthesizing DNA. This process continues until the polymerase reaches its processivity limit, which is the number of nucleotide polymerizations it can perform before

dissociating from the target molecule. For Phi29 polymerase, the processivity is approximately 70 kilobase pairs (kbp) [95]. RCA primers (ThermoFisher) are discussed in the Supporting Information section 5.9.7. Similar to LAMP method, the RCA products are double-stranded DNA which are detected by intercalating fluorescent dye (1X LAMP, NewEngland Biolab).

In the LAMP experiment, the reagents are loaded at the reagent-loading inlet. The target DNAs are preserved from contamination by loading in a separate channel (reagent-loading channel). Therefore, several consecutive experiments can be performed in one device, i.e., after testing a batch of confined DNAs, the tested DNAs are released, washed away, and fresh intact DNA is loaded. The device is warmed up to 65°C using the method discussed in Supporting Information section 5.9.2. Then, the reagents are introduced inside the nanochannels. The largest reagent molecule is Bst 2.0 polymerase (WarmStart) with  $\approx 2.7$  nm radius of gyration, and primers with a maximum  $\approx 3.0$  nm radius of gyration (see Supporting Information section 5.9.6). Therefore, by creating about 5 – 10 nm gap between the membrane and nanocavities, the reagent molecules can diffuse from the side nanochannels into the nanocavities. The fluorescent dye (NEB LAMP fluorescent dye) has minimal interaction with the single-stranded M13mp18 and the signal only arises when the dye intercalates with the synthesized dsDNA (Figure 5.5-f). We observed an increase in fluorescent signal at  $\approx 120$  seconds at which the signal reaches its maximum value. In the LAMP method, the amplicons contain molecules with a large range of sizes, from oligonucleotide size ( $< 100$ bp) to very large molecules ( $> 10$ kbp) (see gel electrophoresis results in Supporting Information section 5.9.6). After saturation of cavities with amplicons, the small molecules can diffuse out from the cavities. The diffused DNAs to the nanochannels can react with the amplification reagents and, by producing very large amplicons in the nanochannels, the nanochannels can be clogged with a small defect that leads to particle accumulation. (see Supporting Video II)

In the LAMP method, a single amplicon generates several amplicons after forming looped. Polymerase can bind to the newly generated amplicons and perform several



amplifications in parallel (similar to PCR [156]). The parallel amplification and the high strand displacement rate of Bst 2.0 WarmStart polymerase give rise to a rapid increase in fluorescent signal. Amplicons generated using the LAMP method can migrate to other cavities which can cause contamination of other cavities and consequently give rise to false positives. In our digital amplification approach in which the confinement of particles depends on the size of the target molecules, the small amplicons can escape from their cavities. The migration of amplicons from one cavity to another has undesirable effects on applications like multiplexing which requires that targets should be kept isolated from other molecules. Therefore, a single-molecule amplification method in which the amplification product is one single large molecule instead several small amplicons like RCA is needed for digital amplification purposes.

In the RCA method, a single polymerase attaches to a DNA and synthesizes the complementary sequences. This gives rise to particles that will always be bigger than the target molecule (see Supporting Information section 5.9.5); therefore, no amplicon can leave the cavity. Given a single path of amplification (i.e., not being parallel like LAMP), the fluorescent signal increases slowly. To reduce the effect of a slow amplification rate, we used four primers (two forward and two reverse) instead of a single forward primer. The real-time PCR results for single primer and four primers amplification are presented in the Supporting Information section 5.9.6 which shows the effectiveness of the proposed four primers method. We also took images with longer exposure time (2s) and longer time-laps (1 min) to increase the signal and reduce bleaching, respectively. The two forward primers are placed on two opposite sides of the DNA, so, instead of one polymerase, two polymerases initiate the synthesis. The fluorescent intensity sharply increases in 2–3min. This sharp increase might represent the termination of one complete circle amplification. After the full circle completion, the polymerase opens up the synthesized double strand and generates ssDNA tails. The two backward primers which were placed on two opposite sides of the vector, attach to the ssDNA tails and another Phi29 polymerase starts to

synthesize the complementary part of the tails (Fig 5.5.c). The generated double-stranded tail results in an increase in fluorescent intensity with a lower slope (Figure 5.5-f).

We also compared the distribution of final fluorescent signals for both isothermal amplification methods. In the LAMP method, the final signal intensity correlates with the size of big particles generated during amplification (as the smaller particles leave the cavity). Given that the size distribution of generated particles is random, there is a relatively wide distribution in final fluorescent intensity (Figure 5.5-g). In the RCA method, we observed most cavities are in the same range of final intensity after 18 minutes which shows most DNAs follow the same amplification procedure (Figure 5.5-g). In RCA method, it is possible that only one of the forward primers continues the amplification. If the polymerase starts the amplification by one of the forward primers, and the second primer cannot find the target while the first polymerase synthesizes the half circle of M13mp18 vector (given the fast strand displacement speed of Phi29, 50-200 bases/s [218]), the second primer can no longer attach to the target; therefore, we expect a slower rate of fluorescent intensity increase.

## 5.5 Conclusions

In this study, we have introduced a novel nanofluidic coupled-membrane device designed for the digital amplification of nucleic acids (NA) within a nanocavity array. The device employs a flexible membrane that can be deflected to physically confine the NA within the nanocavities. By utilizing this membrane, we are able to retain the NA inside the nanocavities while allowing the loading of amplification reagents into the cavities through a narrow gap created between the membrane and nanocavities. For the amplification process, we employed two isothermal amplification methods: loop-mediated isothermal amplification (LAMP) and Rolling Circle Amplification (RCA). These methods facilitate the amplification of the NA directly within the confined nanocavities. By implementing this nanofluidic coupled-membrane device and utilizing LAMP and RCA tech-

niques, we successfully achieved the amplification of nucleic acids within the nanocavities, providing a platform for digital amplification in a controlled and confined environment.

In the future, we propose to extend the device to applications where amplification is multiplexed. Multiplexing can be achieved by designing padlock probes (commonly used for amplification barcoding [217]). Multiple DNA sequences can be detected by barcoding the padlock probe. Multiplexing digital amplification is important for single particle analysis such as single EV analysis. Following our previous study, in future, a single EV can be confined in nanocavities. We should be able to lyse and extract their mRNA using this nanofluidic device while the mRNA remains in the cavities and then detect mRNA-associated biomarkers via multiplexing and amplification.

## **5.6 Author Contributions**

IIH conceptualized the problem, performed the experiments, prepared the samples, performed the calibration tests, analyzed the results, discussed the results, prepared the figures and wrote the manuscript. SVH performed the experiments for control tests, provided technical and scientific advice on biological aspects, and advised on writing the manuscript. XC fabricated devices and provided technical and scientific advice for the fabrication of devices. ZL provided technical and scientific advice for the fabrication of devices. WR conceptualized the problem, provided technical and scientific advice, analyzed the results, discussed the results, wrote the manuscript, and provided resources and funding. SR conceptualized the problem, provided technical and scientific advice, analyzed the results, discussed the results, and provided resources and funding.

## **5.7 Conflicts of interest**

The authors declare no conflicts of interest.

## 5.8 Acknowledgements

The authors thank the Canadian Cancer Society (255878 CCSRI), Natural Science and Engineering Research Council of Canada (NSERC, G247765), New Frontiers for Research Fundexploration (250326 NFRFE) and Canada Foundation for Innovation (CFI, G248924) for financial support. The authors acknowledge Nanotools-Microfab at McGill University and INRS Varennes. I.I.M. acknowledge Faculty of Engineering at McGill University for MEDA award and CMC for the financial support.

## 5.9 Supporting Information

### 5.9.1 Device Fabrication and Operation

The nanofluidic device is fabricated with the following procedure discussed in Capaldi *et al.* [26] A 420 nm deep nanoslit is etched in 4-inch borofloat glass (500  $\mu\text{m}$ ) using UV lithography followed by a CHF<sub>3</sub>:CF<sub>4</sub> inductively coupled plasma (ICP)-Reactive Ion Etching (RIE). Circular nanocavities with a radius of 1  $\mu\text{m}$  and nanochannels with a width of 100 nm placed 500 nm away from the nanocavities are patterned using E-beam lithography and etched 200 nm deep with RIE. Next, the glass wafer is bonded to a silicon wafer coated on both sides with 200 nm silicon nitride (Cornell, NanoScale Facility, silicon wafers 400  $\mu\text{m}$  thick). Four windows for inlets and outlets of fluid and one window for membrane region sare opened using another lithography/etching steps for following KOH etching of silicon on the top side of SiN<sub>x</sub> wafer. Finally, KOH etching is performed through the opened windows to suspend the silicon nitride membrane above the nanocavities/nanochannels region. After dicing the wafer, the 1 cm  $\times$  1 cm nanofluidic device is placed in a 3D printed chuck (Formlabs Inc.) for introducing reagents in the nanofluidic device. (Fig. S5.6).

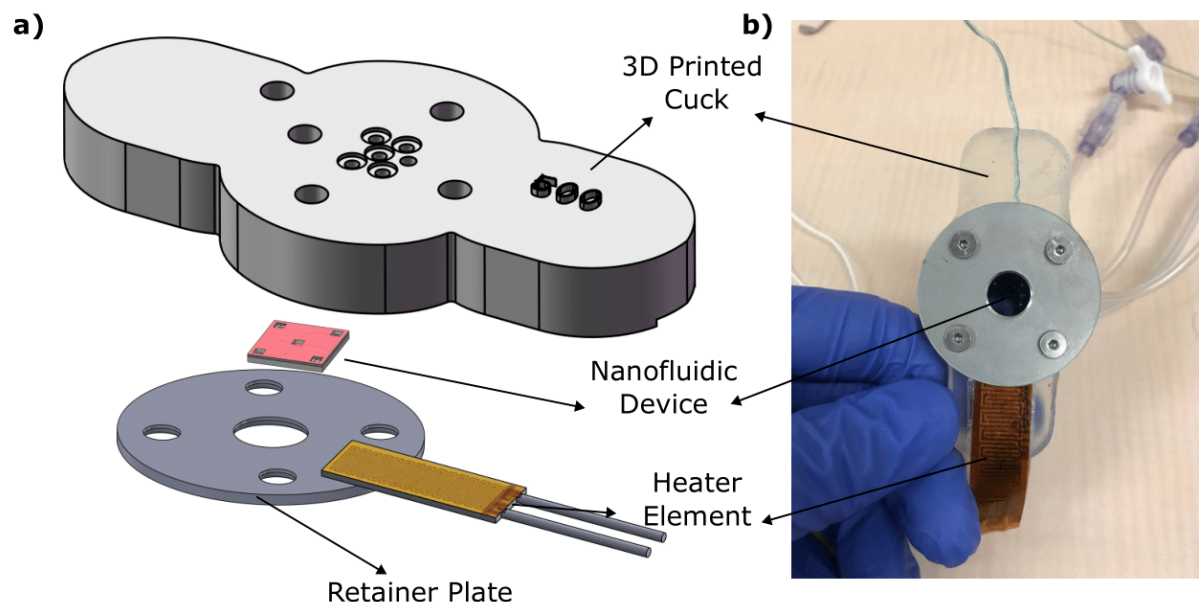


**Figure 5.6:** (a) Schematic image showing chuck/nanofluidic/heater device assembly. (b) Photograph of the assembled system which shows the opening that the microscope objective can image the nanocavity area through.

### 5.9.2 Temperature Controller

To control temperature, we used the Stage Top Incubator (Tokai Hit., Co, Ltd.) which can control the temperature accurately using PID controller. In the system, the temperature can be increased up to 50°C . The RCA method sets the temperature to 30 C, which is the optimum temperature for Phi29 polymerase performance (the rate of strand displacement). For the LAMP method, in which the optimum reaction temperature is 65 °C , we used an extra heater element (Omega Sensing Solutions ULC ) powered with DC power supply (Sky top power STP6005H) to increase the temperature of the retainer plate. The retainer plate uniformly transfers the heat to the nanofluidic device (Fig. S5.7b). To have real-time temperature control, a thermocouple is implemented in the 3d printed chuck which directly contacts with the nanofluidic device. The temperature measurement accuracy is validated using an infrared camera (Teledyne FLIR LLC).

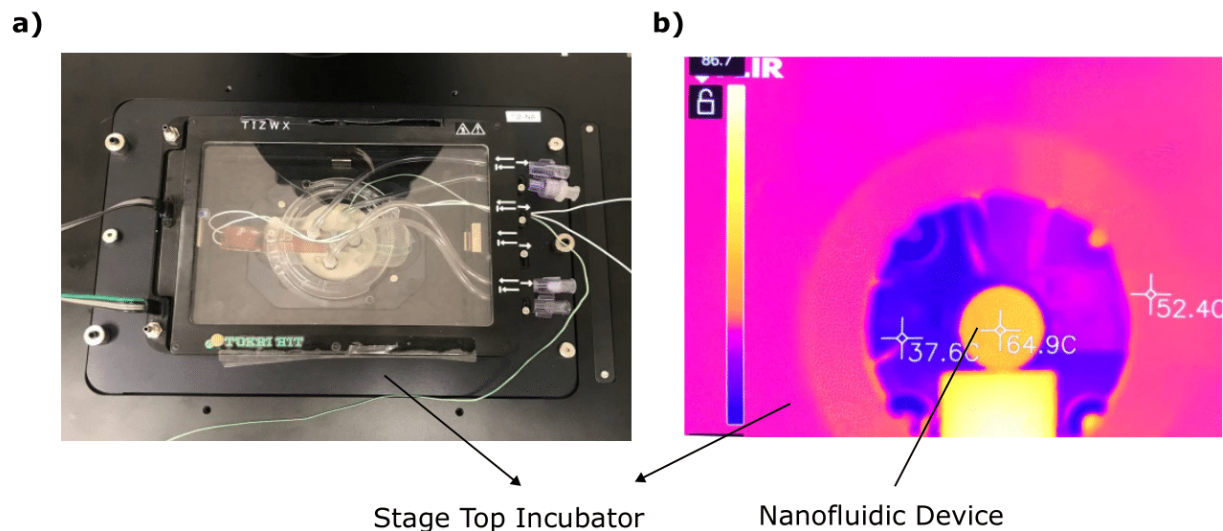


**Figure 5.7:** a) Photograph of the stage top incubator for applying homogenous heat up to 50°C. b) IR image taken using an infrared camera. The nanofluidic device temperature is increased to  $\approx 65^\circ\text{C}$  for loop-mediated isothermal amplification.

### 5.9.3 Slit Height Calibration

Following the procedure discussed in our previous study [80], the relation between slit height and applied pneumatic pressure to the membrane is measured using fluorescent intensity measurement between silicon nitride membrane and glass substrate. Shortly, a fluorescent dye is introduced to the nanocavity area. Fluorescent intensity is measured at different applied pressures to the membrane (and deflecting the membrane). Given the linear relation between fluorescent signals and slit height (i.e.,  $h = (I_F/I_{F0})h_0$  which  $h_0$  is the maximum slit height (420 nm),  $I_{F0}$  is the initial fluorescent signal,  $I_F$  is measured fluorescent signal at different slit height, and  $h$  is the slit height), the fluorescent signal is correlated to the slit height (Fig. S5.8).

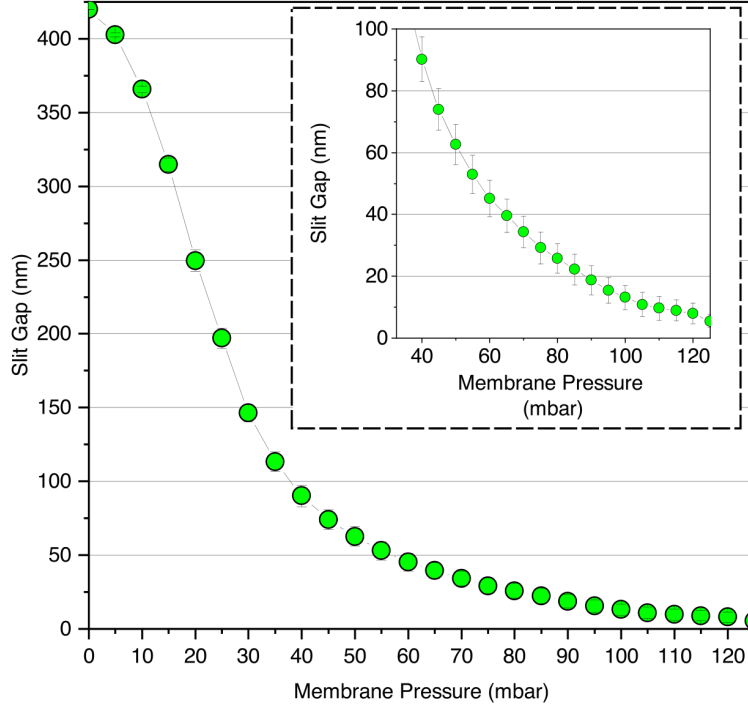


**Figure 5.8:** Relation between slit height and applied pressure used to deflect the membrane lid. The error bars show the variation of slit height in the center region of the membrane. The inset shows the zoom-in for the slit height smaller than 100 nm

#### 5.9.4 Flow Measurement

The flow rate in the nanochannels is measured using the following equation [17]:

$$\Delta P = R_h Q \quad (5.1)$$

with the  $R_h$  is hydrodynamic resistance,  $Q$  is the flow rate, and the  $\Delta P$  is the gradient of pressure between the inlet and outlet of the reagent channel. The hydrodynamic resistance for rectangular channels is:

$$R_h \approx \frac{12\mu L}{wh^3(1 - 0.630\frac{h}{w})} \quad (5.2)$$

with  $\mu$  is fluid viscosity (0.8 mPa.s at 30 °C and 0.43 mPa.s at 65 °C),  $h$  is height of channels (for microchannels is 420 nm and for nanochannels is 360 nm),  $w$  is width of channels (for microchannels is 200 $\mu$ m and for nanochannels is 300nm), and  $L$  is length of channels (for microchannels is 6300 $\mu$ m and nanochannels is 400 $\mu$ m). The hydrodynamic resistance of a network of channels can be measured based on the following laws that

- for two series channels  $R_h = R_{h1} + R_{h2}$
- for two parallel channels  $\frac{1}{R_h} = \frac{1}{R_{h1}} + \frac{1}{R_{h2}}$

The nanofluidic device can be presented in Fig. S5.4a. Considering 65 nanochannels ( $p = 65$ ), the total hydrodynamic resistance between the inlet and outlet of channels when the membrane is down is  $R_h = R_{m1} + R_{m2} + \frac{R_n \times R_g}{p \times R_g + R_n}$ . The  $R_m$ ,  $R_n$ , and  $R_g$  are resistance in microchannels, nanochannels, and the membrane slit height gap, respectively. The hydrodynamic resistance in the microchannels and nanochannels is fixed while the resistance of the membrane slit height gap changes by changing the slit height. In Fig. S5.9b-c, the variation of fluid velocity and flow rate is shown at different slit height values when 10 mbar applied pressure at reagents inlet is applied.

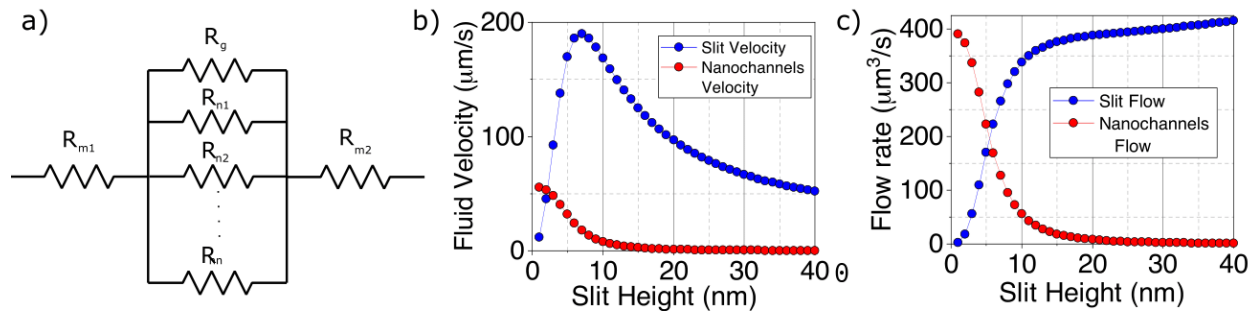


**Figure 5.9:** Flow and hydrodynamic resistance in the nanofluidic device computed from model a) Symbolic representation of hydrodynamic resistance circuit in the nanofluidic device. b) and c) Fluid velocity and flow rate, respectively, in the slit gap and nanochannels at different slit heights.



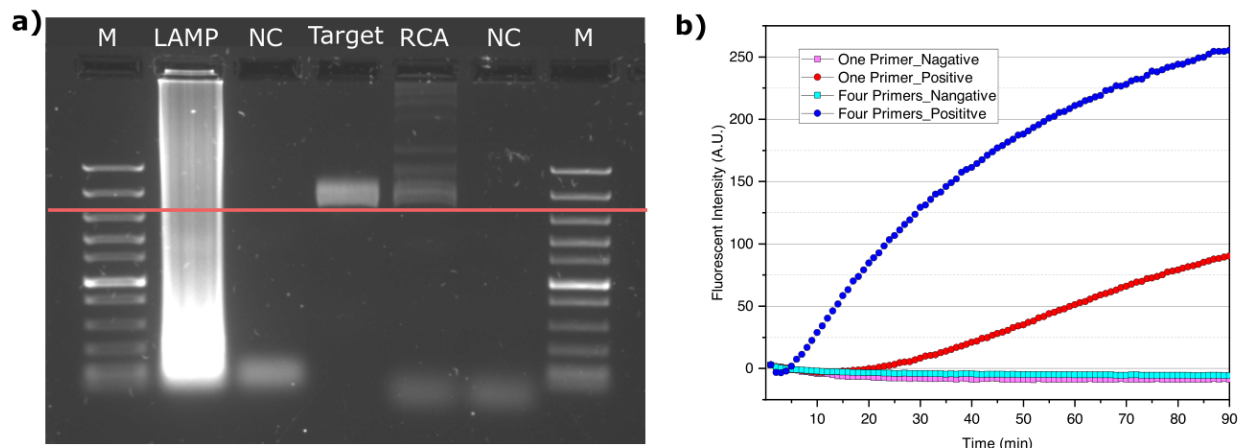


**Figure 5.10:** a) Comparison of LAMP and RCA results regarding the size of generated particles. b) Real-time PCR results for comparison of amplification rate for four primers and one primer RCA.

### 5.9.5 Gel electrophoresis and Real-Time PCR

In Fig. S5.10a, we show the difference between the LAMP and RCA methods regarding the size of synthesized amplicons. In the LAMP method, any sizes of amplicons (especially the very small NAs-  $< 100$ bps) are generated; however, in the RCA method, all the synthesized particles are larger than the target NA.

In RCA, we used four primers (two forward primers, and two backward primers) instead of one forward primer to accelerate the amplification rate. Here we tested the amplification rate using a real-time PCR machine to observe the fluorescent intensity increase (Roche Inc, LightCycler 480) Fig. S5.5b. We used the same fluorescent dye used in the nanofluidic experiment (NEB, LAMP fluorescent dye). The RCA amplification reagents are prepared according to the nanofluidic sample tests (mentioned in the Experimental part of the manuscript). The  $1\mu\text{g/ml}$  M13mp18 was added to the "positive" samples.

### 5.9.6 Particle size measurement

In our analysis, the approximate radius of gyration for different amplification continents is measured. For polymerases, the x-ray crystal structures of the proteins are obtained from the Protein DATA Bank (PDB). Then the data is imported into the VMD and a script is written to measure the size of particles based on the equation:

$$r_{RG}^2 = \frac{\sum_{i=1}^N m_i (r_i - r_{CM})^2}{\sum_{i=1}^N m_i} \quad (5.3)$$

the  $r_{CM}$  is the location of the center of mass,  $m_i$  and  $r_i$  are the mass and location of each atom, respectively. For YOYO1 fluorescent dye, due to the absence of its X-ray crystal structures in PDB, the TOTO1 Molecule (which is very similar to the YOYO1 molecule) is obtained from PDB and replaced the sodium atoms with oxygen (YOYO1 is  $C_{49}H_{58}I_4N_6O_2$  and TOTO1 is  $C_{49}H_{58}I_4N_6S_2$ ). The measured size for YOYO-1 Dyes is 0.69 nm. The radius of gyration for primers is measured using the equations proposed by reference [178]. For oligonucleotides with  $N < 35$  ( $N$  is the number of pairs), the radius of gyration can be measured by:

$$r_{RG}^2 = 2.92N^{1.62} \quad (5.4)$$

And, for oligonucleotides with  $N > 35$  pairs, the radius of gyration is measured by:

$$r_{RG}^2 = 8.94N^{1.16} \quad (5.5)$$

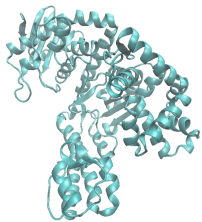
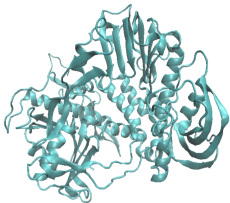
c

### 5.9.7 Primer Design

The M13mp18 vectors primers are obtained from the reference [160] (Tabel 5.1).

We designed the RCA primers and validated the designed primers as discussed in the qPCR and Gel electrophoresis results. Since the polymerase phi29 has an inherent

**Table 5.1:** Radius of gyration of polymerase.

Name of polymerase	PDB Name	Calculated Radius of Gyration (nm)
 BST	7K5O	2.66
 Phi29	2PYJ	3.76

**Table 5.2:** Radius of gyration of RCA primers.

	F1 (RCA)	F1(RCA)	B1(RCA)	B2(RCA)
Pairs	18	22	21	19
$r_{RG}$ (nm)	1.89	2.09	2.01	1.86

3' exonuclease effect, the four last nucleotides before the last nucleotides of RCA primer sets are phosphorothioated to hinder the exonuclease effect of phi29 polymerase on the designed primers. In table S 4, the letters "O", "E", "F", and "Z" are refereeing to the phosphorothioated cytosine (C), guanine (G), adenine (A), and thymine (T), respectively (Table 5.5).

**Table 5.3:** Radius of gyration of LAMP primers.

	FIP (LAMP)	BIP(LAMP)	F3(LAMP)	B3 (LAMP)
Pairs	51	52	17	21
$r_{RG}$ (nm)	2.92	2.96	1.80	2.01

**Table 5.4: LAMP primers**

Primer name	Sequence (5' to 3')	Concentration
BIP	CGACTCTAGAGGATCCCCGGGTAC TTTTTGTGTGTGGAATTGTGAGCGGAT	1.6 $\mu$ m
FIP	ACAACGTCGTGACTGGGAAAACCC TTTTTGTGCGGGCCTCTTCGCTATTAC	1.6 $\mu$ m
F3	GTTGGGAAGGGCGATCG	0.2 $\mu$ m
B3	ACTTTATGCTTCCGGCTCGTA	0.2 $\mu$ m

**Table 5.5: RCA primers**

Primer name	Sequence (5' to 3')	Concentration
F1	CCCAATTCTGCGAFOEFG	0.2 $\mu$ m
F2	CCAACGCTCAACAGTAGEEOT	0.2 $\mu$ m
B1	GGTGGCTCTGAGGGTGEOET	0.2 $\mu$ m
B2	GGTGGCTCTGAGGGZOEET	0.2 $\mu$ m

### 5.9.8 Point-spread function

We tested the effect of the point-spread function on fluorescent measurement. A captured rhodamine red-labelled liposome with 300 nm diameter is observed under the microscope. The objective used in all experiments is water dipping 60 $\times$  N.A. 1 (Nikon Inc). The results show that the effect of fluorescent intensity can be detected up to 1 $\mu$ m far from the cavity.

### 5.9.9 Supporting Movie

Supporting Video I shows the staining of fully confined pBR322 plasmid vectors inside cavities. Unlabeled pBR322 dsDNA is introduced and confined in nanocavities. Then, YoYo-1 fluorescent dye is introduced from the reagent-loading channel. The fluorescent intensity increases by 100 times when intercalating with the pBR322 dsDNA.

Supporting Video II and III shows the amplification of fully confined M13Mp18 using loop-mediated isothermal amplification and rolling circle amplification methods, respectively. The amplification reagents including the primers and fluorescent dye are loaded

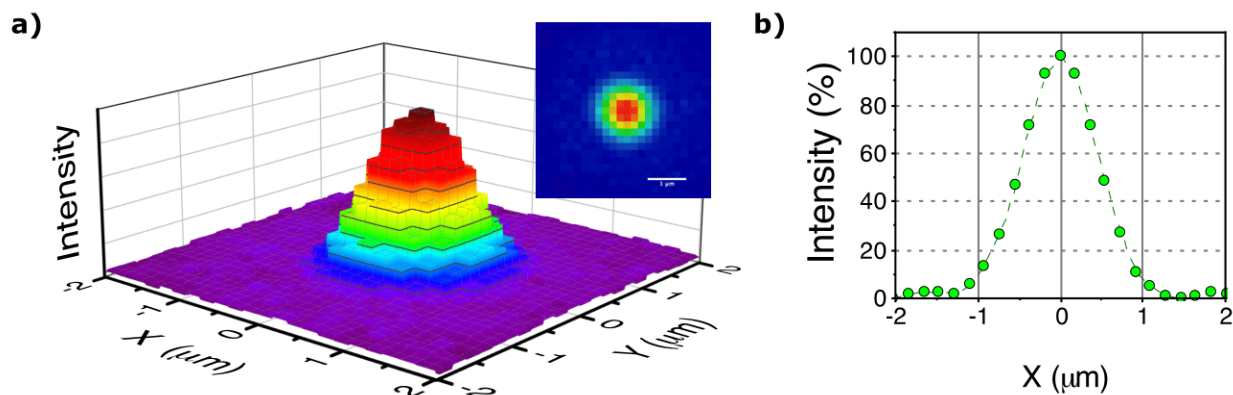


**Figure 5.11:** Point-spread function effect on the fluorescent measurements. a) 3D intensity profile of a 300 nm rhodamine red-labelled liposome imaged with 60× N.A. 1 objective. The scale bar of the inset is 1 μm. b) The fluorescent intensity vs the radius distance from the center.

from the reagent-loading channel. After reaching of reagent to the nanocavity area, the fluorescent intensity increases over time which shows the amplification procedure.

## Chapter 6

# Discussion and Conclusion

### 6.1 Discussion

In summary, we have applied our pneumatically actuated nanofluidic confinement system to EV analysis. Our system enables EV confinement via the pressure-induced deflection of a thin membrane bonding lid, which drives EVs into nanocavity structures embedded in a nanoslit. The system has the advantage that the gap between the membrane and nanoslit bottom surface can be adjusted with nm precision, enabling gaps sufficiently large to introduce reagent molecules into the nanocavities but thin enough to confine target molecules inside. We envision that this proposed approach can be used to isolate and analyze the molecular cargo encapsulated in single EVs. First, we explored the basic physics knowledge for the confinement and isolation of EVs, second, we can amplify nucleic acid chains inside the nano-bioreactors for potential detection of RNA/DNA encapsulated inside EVs.

In the first study, we investigated how lowering the membrane (reducing the channel height) can affect the confinement of nanoparticles in nanocavities. As a first step for the analysis of particles at single-level, isolation in a confined space is required. We showed that the EVs with negative surface charge are passively confined in nanocavities embedded in a slit channel which has a like-charge (negative). However, the EVs can

jump out of the nanocavities due to Brownian motion. We showed that particle escape time from the nanocavity is correlated with the degree of membrane deflection (channel height) which can be modulated in real-time via the applied pneumatic pressure. The level of confinement is also correlated to the surface charge of EVs as well as the geometry of the nanofluidic device. After calibration of the nanofluidic device using a plasmid vector with known chemistry, we used the device to compare the surface charge of EVs secreted from a brain tumor cell line with the surface charge of EVs secreted from a normal human brain cell line. The results show that the difference between the surface charge of EVs is detectable using the proposed nanofluidic device. The surface charge of EVs is correlated to the surface chemistry of the EVs. Work regarding the correlation between surface chemistry and surface charge is very limited. However, some studies have shown that the higher the level of sialic acids in the EV, the more negative the EV surface charge.

We believe that, although the surface charge of EVs might be used to differentiate the EVs from different cell lines, it is not alone sufficient for cancer detection. Our study on the physical parameters which affect the level of confinement of EVs in nanocavities reveals that at a certain height, EVs from one sample can experience a different level of confinement based on their size and surface chemistry considering the high heterogeneity of EVs in a sample. In the first study, we observed that it is possible to adjust the channel height with  $\approx 5$  nm accuracy. Also, there can be still a gap between the membrane and substrate while the particles are isolated for a long time in the cavities. The observations gave us the idea to use the nanofluidic device as label-free confinement method while allowing reagent molecules to access the cavity through a gap.

In the second project, we exploited the capability of the nanofluidic device for the detection of nucleic acid markers (DNA) with the aim of detecting markers on nucleic acids encapsulated inside EVs. The initial device design is modified by adding a second microchannel connected to nanochannels located below the membrane region adjacent to the nanocavities. This modification provides the opportunity for loading the detection reagents (e.g., fluorescent markers) very close to the nanocavities while not touching the

target molecules (DNA). Then, the reagents can be guided to the nanocavities by adjusting the height of microfluidic channels. First, we observed that the target molecules in nanocavities can be concentrated by adjusting the membrane height. This feature is very important for the samples in which the target molecule is diluted. Modulation of the channel height increases the concentration rate which is necessary for tests requiring several sequential confinement and release steps (high-throughput analysis of EVs). After the particle confinement in the nanocavities, we are able to adjust the channel height to keep the target DNA molecule fully confined (residing in the cavities for more than several hours) while still a tiny gap between the membrane and nanocavities is retained. The detection molecules can be loaded in the nanocavities through the tiny gap. We observed that there is not any depletion of target molecules inside the cavities, while the detection reagents are loaded in cavities or washed from the nanocavities. Also, we examined how the confinement is sensitive to the size of particles. In this regard, we examined two different batches of fluorescently labelled gold nanoparticles with different values of mean radii. The results indicate that we can control the size range of particles that pass by modulation of the channel height. Finally, we tested the capability of the device for performing two isothermal amplification methods- Loop-mediated isothermal amplification and Rolling circle amplification. single-stranded DNA vectors (M13Mp18) are confined in nanocavities and then amplification reagents are loaded in the nanocavities via a small gap maintained to allow reagents to pass from the side nanochannels.

In comparison with the single EVs methods, using the nano-fluidic coupled membrane approach provides the following features simultaneously:

1. **Label-free isolation:** In some previous methods, isolation was achieved via antibody capture. Use of capturing antibodies reduces detection sensitivity since all EVs do not carry the corresponding protein antigen. A maximum 50 – 60% of EVs carry proteins specific to a given capture antibody (e.g., CD9). In some studies EVs are biotinylated to capture all EVs by streptavidin conjugation; however, this requires pretreatment which might affect the biochemistry of EVs. Also, it is shown that



label-based capturing increases the steric hindrance between the detection reagents and consequently reduces the detection sensitivity. The other point is that, when a label-free method is used for particle isolation, it is possible to detect several rounds of particles in one position of the device by loading and reloading the sample. In contrast, in the immunoaffinity isolation methods, several extra detachment and device preparation steps are required for sequential rounds of detection.

2. **High throughput:** We were able to accommodate approximately 4300 cavities in  $200\mu\text{m} \times 200\mu\text{m}$  surface area. Considering our capability for concentrating particles inside the cavities, we hope that all the cavities will be filled with each EVs. Also, sequential analysis can be performed to increase the number of analyses for each sample. Another solution might be expanding the surface area. There will be two main challenges in this regard. 1- The maximum sensor size of the current commercially available microscope cameras is  $20.8\text{mm} \times 20.8\text{mm}$  (Kinetix sCMOS, Teledyne Photometrics). By using the 60X objective, the field of view will be limited to  $367\mu\text{m} \times 375\mu\text{m}$ . We can confront the challenge by using smaller magnification or scanning the Region Of Interest (ROI). Using smaller magnification reduces the resolution of detection and scanning the ROI increases the detection time. 2- Expanding the membrane area is restricted by the anodic bonding step of the device fabrication procedure. In our one attempt to expand the membrane area, two membrane sizes were included in one wafer with  $200\mu\text{m} \times 200\mu\text{m}$  and  $500\mu\text{m} \times 500\mu\text{m}$  surface areas. The fabrication of all the  $500\mu\text{m} \times 500\mu\text{m}$  devices failed by collapsing the SiNx membrane inside the microchannels, although all the  $200\mu\text{m} \times 200\mu\text{m}$  were successfully fabricated. In our first attempt, there is a big gap between two membrane sizes ( $200\mu\text{m}$  to  $500\mu\text{m}$ ). Therefore, in future studies, first, the threshold at which the collapsing happens should be tested by fabricating different membrane sizes. Next, we can optimize the following parameters to maximize the possible membrane area. The first parameter is the etched depth of the channels. We hypothesize that increasing the etched depth of the channel will enhance the fabrica-

tion yield. Also, different parameters can be adjusted during the anodic bonding step including the applied voltage, temperature, and pressure; however, changing the parameters can reduce the quality of bonding as well. Therefore, there would be an optimized value for the parameters which results in maximum yield. Also, it is possible to implement different membrane areas in one device, and the microscope stage sweep between the membrane areas automatically.

3. **Accessibility of the confined particles:** Current well-known methods for label-free single particle isolation (e.g, droplet generation or SiMoA technology) isolate the particles in such a way that the confined particles are inaccessible. The accessibility of particles will be important from different aspects. 1- Accessibility of the isolated particles let us have multidimensional/multiplex/multiomic analysis. Due to the overlap between spectra of different fluorescent dyes, only 4-6 fluorescent dyes (and consequently target biomarkers) can be detected simultaneously in one step. It should be mentioned that some studies have attempted to increase the number of detectable spectra in one step; however, this decreases sensitivity. The accessibility to the isolated particles opens up the opportunity for sequential staining/bleaching steps which results in the detection of non-limited number of biomarkers. 2- Clean up the confined particles from unfavourable solutions or contamination. For example, if there is a need for EV lysis, the lysis buffer (0.5-1X Triton) will interfere with the subsequent amplification or detection steps. The accessibility to the confined particles lets us wash out the nanocavity bioreactors from the added unfavourable solutions. Also, although the isolation methods can provide relatively high purity from contaminations (such as free proteins); however, we can wash out the remained small particles based on their size before detection steps which results in higher specificity. 3- Usually, label-free single-particle detection methods confine and isolate the target molecules and the detection reagents together. Then the detection sensitivity will be limited by the probability of confining the required detection reagents in the isolated spaces. In our method, however, the detection reagents can

be continuously loaded inside the confined space to make sure that they are at sufficiently high concentration.

4. **The possibility of accessing EV encapsulated cargo:** As discussed in the section on future work, we believe that using the platform to access encapsulated molecular cargo should be possible on the level of single EVs. In previous studies, the loading of the lysis buffer was not practical, or the particles were not fully isolated and by lysing the EVs, their contents will be dispersed in solution. However, in our device, it should be possible to lyse the EVs and keep their contents confined.

## 6.2 Future Work

In the future, this work can be extended in different directions. First, given the heterogeneity of Extracellular Vesicles in body fluids, a multidimensional analysis is required. For obtaining a multidimensional analysis, we should be able to barcode the target sequence of DNA/RNA. In the Rolling Circle Amplification method, the barcoding is achieved using a strategy called Pad-Lock-Probe (PLP). In the PLP strategy, a known sequence makes a circle while attached to the target molecule with cyclization achieved using a polymerase (e.g., T4 DNA ligase, which works at 70 °C). In the nanofluidic device, the cyclization reaction of T4 DNA ligase and DNA should be examined. Then using the PLP, we should be able to detect different sequences of DNA using different fluorescent dyes or even sequential quenching and re-staining steps. After this step, the nanofluidic device can be used for testing EVs for their RNA (e.g., mRNA, miRNA) detection. After the detection of EVs surface proteins using methods like SEA, EVs can be lysed using a lysis buffer or via a heat shock. Since the loading and unloading of detection reagents are performed based on the size of the particles, the initial target biomarker can be a large mRNA encapsulated in EVs, such as 9104 bp EGFR VIII which is encapsulated in EVs secreted from the Glioblastoma cell line. For other small RNAs (e.g., miRNAs) which have the same size as primers, the miRNAs can be captured on the surface of beads before adding

the detection reagents. In fact, our method can be combined with SiMoA technology. First, the beads which contain the capturing molecules can be loaded in the cavities and then the membrane is deflected to hold the particles. The EVs can be simultaneously confined with the capturing beads in the cavities. Then, the membrane can be pushed to achieve complete deflection, so that the solvent molecules can pass through between the membrane and substrate. The lysis buffer or heat shock can be applied to rupture the EVs membrane and release their contents and the released contents will be captured using the trapped beads. Afterwards, we can increase the gap for loading the detection reagents inside the cavities while the trapped beads are still confined in the cavities. The released EV inner contents are already captured on the bead surface.

# Bibliography

- [1] ABUSAMRA, A. J., ZHONG, Z., ZHENG, X., LI, M., ICHIM, T. E., CHIN, J. L., AND MIN, W.-P. Tumor exosomes expressing fas ligand mediate cd8+ t-cell apoptosis. *Blood Cells, Molecules, and Diseases* 35, 2 (2005), 169–173.
- [2] AHAMED, M. J., MAHSHID, S., BERARD, D. J., MICHAUD, F., SLADEK, R., REISNER, W. W., AND LESLIE, S. R. Continuous confinement fluidics: Getting lots of molecules into small spaces with high fidelity. *Macromolecules* 49, 7 (2016), 2853–2859.
- [3] AKAGI, T., AND ICHIKI, T. Evaluation of zeta-potential of individual exosomes secreted from biological cells using a microcapillary electrophoresis chip. *Encyclopedia of Biocolloid and Biointerface Science 2V Set* (2016), 469–473.
- [4] AKBAR, A., MALEKIAN, F., BAGHBAN, N., KODAM, S. P., AND ULLAH, M. Methodologies to isolate and purify clinical grade extracellular vesicles for medical applications. *Cells* 11, 2 (2022), 186.
- [5] AKGÜL, S., PATCH, A.-M., D’SOUZA, R. C., MUKHOPADHYAY, P., NONES, K., KEMPE, S., KAZAKOFF, S. H., JEFFREE, R. L., STRINGER, B. W., PEARSON, J. V., ET AL. Intratumoural heterogeneity underlies distinct therapy responses and treatment resistance in glioblastoma. *Cancers* 11, 2 (2019), 190.

- [6] AKTAS, G. B., RIBERA, A., SKOURIDOU, V., AND MASIP, L. Dna immobilization and detection using dna binding proteins. *Analytical and Bioanalytical Chemistry* 413, 7 (2021), 1929–1939.
- [7] ALVAREZ, M. L., KHOSROHEIDARI, M., RAVI, R. K., AND DISTEFANO, J. K. Comparison of protein, microrna, and mrna yields using different methods of urinary exosome isolation for the discovery of kidney disease biomarkers. *Kidney international* 82, 9 (2012), 1024–1032.
- [8] AUNER, V., KRIEGSHÄUSER, G., TONG, D., HORVAT, R., REINTHALLER, A., MUSTEA, A., AND ZEILLINGER, R. Kras mutation analysis in ovarian samples using a high sensitivity biochip assay. *BMC cancer* 9, 1 (2009), 1–8.
- [9] BACHURSKI, D., SCHULDNER, M., NGUYEN, P.-H., MALZ, A., REINERS, K. S., GRENZI, P. C., BABATZ, F., SCHAUSS, A. C., HANSEN, H. P., HALLEK, M., ET AL. Extracellular vesicle measurements with nanoparticle tracking analysis—an accuracy and repeatability comparison between nanosight ns300 and zetaview. *Journal of extracellular vesicles* 8, 1 (2019), 1596016.
- [10] BEBELMAN, M. P., SMIT, M. J., PEGTEL, D. M., AND BAGLIO, S. R. Biogenesis and function of extracellular vesicles in cancer. *Pharmacology & therapeutics* 188 (2018), 1–11.
- [11] BECHERER, L., BORST, N., BAKHEIT, M., FRISCHMANN, S., ZENGERLE, R., AND VON STETTEN, F. Loop-mediated isothermal amplification (lamp)—review and classification of methods for sequence-specific detection. *Analytical Methods* 12, 6 (2020), 717–746.
- [12] BERARD, D. J., AND LESLIE, S. R. Miniaturized flow cell with pneumatically-actuated vertical nanoconfinement for single-molecule imaging and manipulation. *Biomicrofluidics* 12 (2018), 054107.

- [13] BERARD, D. J., MIÇHAUD, F., MAHSHID, S., AHAMED, M. J., MCFaul, C. M. J., LEITH, J. S., BÉRUBÉ, PIERRE; SLADEK, R., REISNER, W., AND LESLIE, S. R. Convex lens-induced nanoscale templating. *Proced. Nat. Acad. Sci* 111 (2014), 13295–13300.
- [14] BERARD, D. J., MICHAUD, F., MAHSHID, S., AHAMED, M. J., MCFaul, C. M., LEITH, J. S., BÉRUBÉ, P., SLADEK, R., REISNER, W., AND LESLIE, S. R. Convex lens-induced nanoscale templating. *Proceedings of the National Academy of Sciences* 111, 37 (2014), 13295–13300.
- [15] BLOSSEY, R. *The Poisson-Boltzmann Equation: An Introduction*. Springer Nature, 2023.
- [16] BORDANABA-FLORIT, G., ROYO, F., KRUGLIK, S. G., AND FALCÓN-PÉREZ, J. M. Using single-vesicle technologies to unravel the heterogeneity of extracellular vesicles. *Nature Protocols* 16, 7 (2021), 3163–3185.
- [17] BRUUS, H. *Theoretical microfluidics*, vol. 18. Oxford university press, 2007.
- [18] BRYANT, K. L., MANCIAS, J. D., KIMMELMAN, A. C., AND DER, C. J. Kras: feeding pancreatic cancer proliferation. *Trends in biochemical sciences* 39, 2 (2014), 91–100.
- [19] BUSCAIL, L., BOURNET, B., AND CORDELIÉ, P. Role of oncogenic kras in the diagnosis, prognosis and treatment of pancreatic cancer. *Nature reviews Gastroenterology & hepatology* 17, 3 (2020), 153–168.
- [20] BUSCHMANN, D., KIRCHNER, B., HERMANN, S., MÄRTE, M., WURMSER, C., BRANDES, F., KOTSCHOTE, S., BONIN, M., STEINLEIN, O. K., PFAFFL, M. W., ET AL. Evaluation of serum extracellular vesicle isolation methods for profiling mirnas by next-generation sequencing. *Journal of extracellular vesicles* 7, 1 (2018), 1481321.

- [21] BUSTAMANTE, C. J., CHEMLA, Y. R., LIU, S., AND WANG, M. D. Optical tweezers in single-molecule biophysics. *Nature Reviews Methods Primers* 1, 1 (2021), 1–29.
- [22] BUZAS, E. I. The roles of extracellular vesicles in the immune system. *Nature Reviews Immunology* (2022), 1–15.
- [23] BUZAS, E. I., TOTH, E. A., SODAR, B. W., AND SZABO-TAYLOR, K. E. Molecular interactions at the surface of extracellular vesicles. *Seminars in Immunopathology* 40 (2018), 453–464.
- [24] CAI, Z., YANG, F., YU, L., YU, Z., JIANG, L., WANG, Q., YANG, Y., WANG, L., CAO, X., AND WANG, J. Activated t cell exosomes promote tumor invasion via fas signaling pathway. *The Journal of Immunology* 188, 12 (2012), 5954–5961.
- [25] CAPALDI, X., LIU, Z., ZHANG, Y., ZENG, L., REYES-LAMOTHE, R., AND REISNER, W. Probing the organization and dynamics of two dna chains trapped in a nanofluidic cavity. *Soft Matter* 14 (2018), 8455–8465.
- [26] CAPALDI, X., LIU, Z., ZHANG, Y., ZENG, L., REYES-LAMOTHE, R., AND REISNER, W. Probing the organization and dynamics of two dna chains trapped in a nanofluidic cavity. *Soft matter* 14, 42 (2018), 8455–8465.
- [27] CHAO, H., IM, H., CASTRO, C. M., BREAKFIELD, SANDRA; WEISSLEDER, R., AND LEE, H. New technologies for analysis of extracellular vesicles. *Chemical Reviews* 118 (2018), 1917–1950.
- [28] CHATELLARD-CAUSSE, C., BLOT, B., CRISTINA, N., TORCH, S., MISSOTTEN, M., AND SADOUL, R. Alix (alg-2-interacting protein x), a protein involved in apoptosis, binds to endophilins and induces cytoplasmic vacuolization. *Journal of Biological Chemistry* 277, 32 (2002), 29108–29115.



- [29] CHEN, C., ZONG, S., LIU, Y., WANG, Z., ZHANG, Y., CHEN, B., AND CUI, Y. Profiling of exosomal biomarkers for accurate cancer identification: Combining dna-paint with machine-learning-based classification. *Small* 15, 43 (2019), 1901014.
- [30] CHEN, F., CHEN, J., YANG, L., LIU, J., ZHANG, X., ZHANG, Y., TU, Q., YIN, D., LIN, D., WONG, P.-P., ET AL. Extracellular vesicle-packaged hif-1 $\alpha$ -stabilizing lncrna from tumour-associated macrophages regulates aerobic glycolysis of breast cancer cells. *Nature cell biology* 21, 4 (2019), 498–510.
- [31] CHOI, D., MONTERMINI, L., KIM, D.-E., MEEHAN, B., ROTH, F. P., AND RAK, J. The impact of oncogenic egfrviii on the proteome of extracellular vesicles released from glioblastoma cells. *Molecular Cellular Proteomics* 17 (2018), 1948–1964.
- [32] CHOI, D., MONTERMINI, L., KIM, D.-K., MEEHAN, B., ROTH, F. P., AND RAK, J. The impact of oncogenic egfrviii on the proteome of extracellular vesicles released from glioblastoma cells. *Molecular & Cellular Proteomics* 17, 10 (2018), 1948–1964.
- [33] CHOI, D., SPINELLI, C., MONTERMINI, L., AND RAK, J. Oncogenic regulation of extracellular vesicle proteome and heterogeneity. *Proteomics* 19, 1-2 (2019), 1800169.
- [34] COHEN, A. E. Force-extension curve of a polymer in a high-frequency electric field. *Physical review letters* 91, 23 (2003), 235506.
- [35] COHEN, A. E., AND MOERNER, W. Suppressing brownian motion of individual biomolecules in solution. *Proceedings of the National Academy of Sciences* 103, 12 (2006), 4362–4365.
- [36] COLOMBO, M., MOITA, C., VAN NIEL, G., KOWAL, J., VIGNERON, J., BENAROCH, P., MANEL, N., MOITA, L. F., THÉRY, C., AND RAPOSO, G. Analysis of escrt functions in exosome biogenesis, composition and secretion highlights the heterogeneity of extracellular vesicles. *Journal of cell science* 126, 24 (2013), 5553–5565.

- [37] CÚLUM, N. M., COOPER, T. T., BELL, G. I., HESS, D. A., AND LAGUGNÉ-LABARTHET, F. Characterization of extracellular vesicles derived from mesenchymal stromal cells by surface-enhanced raman spectroscopy. *Analytical and Bioanalytical Chemistry* 413, 20 (2021), 5013–5024.
- [38] DAABOUL, G. G., GAGNI, P., BENUSSI, L., BETTOTTI, P., CIANI, M., CRETICH, M., FREEDMAN, D. S., GHIDONI, R., OZKUMUR, A. Y., PIOTTO, C., ET AL. Digital detection of exosomes by interferometric imaging. *Scientific reports* 6, 1 (2016), 1–10.
- [39] DALLACASAGRANDE, V., AND HAJJAR, K. A. Annexin a2 in inflammation and host defense. *Cells* 9, 6 (2020), 1499.
- [40] D’ASTI, E., CHENNAKRISHNAIAH, S., LEE, T. H., AND RAK, J. Extracellular vesicles in brain tumor progression. *Cellular and Molecular Neurobiology* 36 (2016), 383–407.
- [41] DE JONG, O. G., KOOIJMANS, S. A., MURPHY, D. E., JIANG, L., EVERS, M. J., SLUIJTER, J. P., VADER, P., AND SCHIFFELERS, R. M. Drug delivery with extracellular vesicles: from imagination to innovation. *Accounts of chemical research* 52, 7 (2019), 1761–1770.
- [42] DE LA ESCOSURA-MUÑIZ, A., AND MERKOÇI, A. A nanochannel/nanoparticle-based filtering and sensing platform for direct detection of a cancer biomarker in blood. *Small* 7, 5 (2011), 675–682.
- [43] DE OLIVEIRA, G. P., ZIGON, E., ROGERS, G., DAVODIAN, D., LU, S., JOVANOVIĆ-TALISMAN, T., JONES, J., TIGGES, J., TYAGI, S., AND GHIRAN, I. C. Detection of extracellular vesicle rna using molecular beacons. *Isience* 23, 1 (2020).
- [44] DI BONITO, P., CHIOZZINI, C., ARENACCIO, C., ANTICOLI, S., MANFREDI, F., OLIVETTA, E., FERRANTELLI, F., FALCONE, E., RUGGIERI, A., AND FEDERICO, M. Antitumor hpv e7-specific ctl activity elicited by in vivo engineered exosomes

- produced through dna inoculation. *International journal of nanomedicine* 12 (2017), 4579.
- [45] DICKHOUT, A., AND KOENEN, R. R. Extracellular vesicles as biomarkers in cardiovascular disease; chances and risks. *Frontiers in cardiovascular medicine* 5 (2018), 113.
- [46] DOLDÁN, X., FAGÚNDEZ, P., CAYOTA, A., LAÍZ, J., AND TOSAR, J. P. Electrochemical sandwich immunosensor for determination of exosomes based on surface marker-mediated signal amplification. *Analytical chemistry* 88, 21 (2016), 10466–10473.
- [47] DONG, J., ZHANG, R. Y., SUN, N., SMALLEY, M., WU, Z., ZHOU, A., CHOU, S.-J., JAN, Y. J., YANG, P., BAO, L., ET AL. Bio-inspired nanovilli chips for enhanced capture of tumor-derived extracellular vesicles: toward non-invasive detection of gene alterations in non-small cell lung cancer. *ACS applied materials & interfaces* 11, 15 (2019), 13973–13983.
- [48] DONG, S., WANG, Y., LIU, Z., ZHANG, W., YI, K., ZHANG, X., ZHANG, X., JIANG, C., YANG, S., WANG, F., ET AL. Beehive-inspired macroporous sers probe for cancer detection through capturing and analyzing exosomes in plasma. *ACS applied materials & interfaces* 12, 4 (2020), 5136–5146.
- [49] EIJKEL, J. C., AND BERG, A. V. D. Nanofluidics: what is it and what can we expect from it? *Microfluidics and Nanofluidics* 1 (2005), 249–267.
- [50] ELSHARKASY, O. M., NORDIN, J. Z., HAGEY, D. W., DE JONG, O. G., SCHIFFELERS, R. M., ANDALOUSSI, S. E., AND VADER, P. Extracellular vesicles as drug delivery systems: Why and how? *Advanced Drug Delivery Reviews* 159 (2020), 332–343.
- [51] ESER, S., SCHNIEKE, A., SCHNEIDER, G., AND SAUR, D. Oncogenic kras signalling in pancreatic cancer. *British journal of cancer* 111, 5 (2014), 817–822.

- [52] FAEZ, S., LAHINI, Y., WEIDLICH, S., GARMANN, R. F., WONDRACZEK, K., ZEISBERGER, M., SCHMIDT, M. A., ORRIT, M., AND MANOHARAN, V. N. Fast, label-free tracking of single viruses and weakly scattering nanoparticles in a nanofluidic optical fiber. *ACS nano* 9, 12 (2015), 12349–12357.
- [53] FENG, C., MAO, X., YANG, Y., ZHU, X., YIN, Y., AND LI, G. Rolling circle amplification in electrochemical biosensor with biomedical applications. *Journal of Electroanalytical Chemistry* 781 (2016), 223–232.
- [54] FENG, Y.-H., AND TSAO, C.-J. Emerging role of microrna-21 in cancer. *Biomedical reports* 5, 4 (2016), 395–402.
- [55] FERGUSON, S., AND WEISSLEDER, R. Modeling ev kinetics for use in early cancer detection. *Advanced biosystems* 4, 12 (2020), 1900305.
- [56] FERGUSON, S., YANG, K. S., ZELGA, P., LISS, A. S., CARLSON, J. C., DEL CASTILLO, C. F., AND WEISSLEDER, R. Single-ev analysis (seva) of mutated proteins allows detection of stage 1 pancreatic cancer. *Science Advances* 8, 16 (2022), eabm3453.
- [57] FRAIKIN, J.-L., TEESALU, T., MCKENNEY, C. M., RUOSLAHTI, E., AND CLELAND, A. N. A high-throughput label-free nanoparticle analyser. *Nature nanotechnology* 6, 5 (2011), 308–313.
- [58] FRANCESCA, R., FRANZISKA, Z., NATALIE, M., MAGDELENA, R. M. W., ANDRZEJ, O., BENJAMIN, S., AND MADHAVI, K. Single-molecule electrometry. *Nature Nanotechnology* 12 (2017), 488–495.
- [59] FRYKHOLM, K., NYBERG, L. K., AND WESTERLUND, F. Exploring dna–protein interactions on the single dna molecule level using nanofluidic tools. *Integrative Biology* 9, 8 (2017), 650–661.

- [60] FUJIWARA, S., MORIKAWA, K., ENDO, T., HISAMOTO, H., AND SUEYOSHI, K. Size sorting of exosomes by tuning the thicknesses of the electric double layers on a micro-nanofluidic device. *Micromachines* 11, 5 (2020), 458.
- [61] GERSPACH, M. A., MOJARAD, N., SHARMA, D., EKINCI, Y., AND PFOHL, T. Pneumatically controlled nanofluidic devices for contact-free trapping and manipulation of nanoparticles. *Particle & Particle Systems Characterization* 35, 12 (2018), 1800161.
- [62] GERSPACH, M. A., MOJARAD, N., SHARMA, D., EKINCI, Y., AND PFOHL, T. Pneumatically controlled nanofluidic devices for contact-free trapping and manipulation of nanoparticles. *Part. Part. Syst. Charact.* 35 (2018), 1800161.
- [63] GERSPACH, M. A., MOJARAD, N., SHARMA, D., EKINCI, Y., AND PFOHL, T. Pneumatically controlled nanofluidic devices for contact-free trapping and manipulation of nanoparticles. *Part. Part. Syst. Charact.* 35 (2018), 1800161.
- [64] GERSPACH, M. A., MOJARAD, N., SHARMA, D., PFOHL, T., AND EKINCI, Y. Soft electrostatic trapping in nanofluidics. *Microsystems & nanoengineering* 3, 1 (2017), 1–10.
- [65] GIUSTI, I., DI FRANCESCO, M., POPPA, G., ESPOSITO, L., D’ASCENZO, S., AND DOLO, V. Tumor-derived extracellular vesicles activate normal human fibroblasts to a cancer-associated fibroblast-like phenotype, sustaining a pro-tumorigenic microenvironment. *Frontiers in Oncology* 12 (2022), 408.
- [66] GOYA, R., SUN, M. G., MORIN, R. D., LEUNG, G., HA, G., WIEGAND, K. C., SENZ, J., CRISAN, A., MARRA, M. A., HIRST, M., ET AL. Snvmix: predicting single nucleotide variants from next-generation sequencing of tumors. *Bioinformatics* 26, 6 (2010), 730–736.
- [67] GUAN, W., CHEN, L., RANE, T. D., AND WANG, T.-H. Droplet digital enzyme-linked oligonucleotide hybridization assay for absolute rna quantification. *Scientific reports* 5, 1 (2015), 13795.

- [68] HA, D., YANG, N., AND NADITHE, V. Exosomes as therapeutic drug carriers and delivery vehicles across biological membranes: current perspectives and future challenges. *Acta Pharmaceutica Sinica B* 6, 4 (2016), 287–296.
- [69] HAMBLIN, M. N., XUAN, J., MAYNES, D., TOLLEY, H. D., BELNAP, D. M., WOOLLEY, A. T., LEE, M. L., AND HAWKINS, A. R. Selective trapping and concentration of nanoparticles and viruses in dual-height nanofluidic channels. *Lab on a Chip* 10, 2 (2010), 173–178.
- [70] HANNAFON, B. N., AND DING, W.-Q. Intercellular communication by exosome-derived micrnas in cancer. *International journal of molecular sciences* 14, 7 (2013), 14240–14269.
- [71] HANNUN, Y. A., AND OBEID, L. M. Principles of bioactive lipid signalling: lessons from sphingolipids. *Nature reviews Molecular cell biology* 9, 2 (2008), 139–150.
- [72] HAPPEL, J., AND BRENNER, H. *Low Reynolds number hydrodynamics: with special applications to particulate media*. Springer Science and Business Media, Berlin, 2012.
- [73] HARMS, Z. D., HAYWOOD, D. G., KNELLER, A. R., SELZER, L., ZLOTNICK, A., AND JACOBSON, S. C. Single-particle electrophoresis in nanochannels. *Analytical chemistry* 87, 1 (2015), 699–705.
- [74] HE, D., WANG, H., HO, S.-L., CHAN, H.-N., HAI, L., HE, X., WANG, K., AND LI, H.-W. Total internal reflection-based single-vesicle in situ quantitative and stoichiometric analysis of tumor-derived exosomal micrnas for diagnosis and treatment monitoring. *Theranostics* 9, 15 (2019), 4494.
- [75] HECK, H. D., AND CASANOVA, M. Pharmacodynamics of formaldehyde: applications of a model for the arrest of dna replication by dna–protein cross-links. *Toxicology and applied pharmacology* 160, 1 (1999), 86–100.

- [76] HERRMANN, I. K., WOOD, M. J. A., AND FUHRMANN, G. Extracellular vesicles as a next-generation drug delivery platform. *Nature nanotechnology* 16, 7 (2021), 748–759.
- [77] HEYRIES, K. A., TROPINI, C., VANINSBERGHE, M., DOOLIN, C., PETRIV, O. I., SINGHAL, A., LEUNG, K., HUGHESMAN, C. B., AND HANSEN, C. L. Megapixel digital pcr. *Nature methods* 8, 8 (2011), 649–651.
- [78] HIDROVO, C. H. 2d thickness and temperature mapping of fluids by means of a two-dye laser induced fluorescence ratiometric scheme. *Journal of Flow Visualization and Image Processing* 9, 2&3 (2002).
- [79] HOSHINO, A., COSTA-SILVA, B., SHEN, T.-L., RODRIGUES, G., HASHIMOTO, A., TESIC MARK, M., MOLINA, H., KOHSAKA, S., DI GIANNATALE, A., CEDER, S., ET AL. Tumour exosome integrins determine organotropic metastasis. *Nature* 527, 7578 (2015), 329–335.
- [80] HOSSEINI, I. I., LIU, Z., CAPALDI, X., ABDEFATAH, T., MONTERMINI, L., RAK, J., REISNER, W., AND MAHSHID, S. Nanofluidics for simultaneous size and charge profiling of extracellular vesicles. *Nano Letters* 21, 12 (2021), 4895–4902.
- [81] HU, Y., FAN, J., LIANG, K., LIU, F., AND DALI, S. Nanoplasmonic quantification of tumor-derived extracellular vesicles in plasma microsamples for detection and treatment monitoring, Mar. 26 2020. US Patent App. 16/469,082.
- [82] HUGEL, B., MARTÍNEZ, M. C., KUNZELMANN, C., AND FREYSSINET, J.-M. Membrane microparticles: two sides of the coin. *Physiology* 20, 1 (2005), 22–27.
- [83] IAVELLO, A., FRECH, V. S., GAI, C., DEREGIBUS, M. C., QUESENBERRY, P. J., AND CAMUSSI, G. Role of alix in mirna packaging during extracellular vesicle biogenesis. *International journal of molecular medicine* 37, 4 (2016), 958–966.

- [84] IDEGUCHI, M., KAJIWARA, K., GOTO, H., SUGIMOTO, K., NOMURA, S., IKEDA, E., AND SUZUKI, M. Mri findings and pathological features in early-stage glioblastoma. *Journal of Neuro-Oncology* 123 (2015), 289–297.
- [85] IM, H., CHAO, H., PARK, Y. I., PETERSON, V. M., CASTRO, C. M., WEISSLEDER, R., AND LEE, H. Label-free detection and molecular profiling of exosomes with a nano-plasmonic sensor. *Nature Biotechnology* 32 (2014), 490–495.
- [86] IM, H., SHAO, H., PARK, Y. I., PETERSON, V. M., CASTRO, C. M., WEISSLEDER, R., AND LEE, H. Label-free detection and molecular profiling of exosomes with a nano-plasmonic sensor. *Nature biotechnology* 32, 5 (2014), 490–495.
- [87] INDA, M.-D.-M., BONAVIDA, R., AND SEOANE, J. Glioblastoma multiforme: A look inside its heterogeneous nature. *Cancers* 6 (2014), 226–239.
- [88] JALALI, M., HOSSEINI, I. I., ABDELFAH, T., MONTERMINI, L., HOGIU, S. W., RAK, J., AND MAHSHID, S. Plasmonic nanobowtiefluidic device for sensitive detection of glioma extracellular vesicles by raman spectrometry. *Lab on a Chip* 21, 5 (2021), 855–866.
- [89] JEONG, S., PARK, J., PATHANIA, D., CASTRO, C. M., WEISSLEDER, R., AND LEE, H. Integrated magneto–electrochemical sensor for exosome analysis. *ACS nano* 10, 2 (2016), 1802–1809.
- [90] JIA, R., ROTENBERG, S. A., AND MIRKIN, M. V. Electrochemical resistive-pulse sensing of extracellular vesicles. *Analytical Chemistry* 94, 37 (2022), 12614–12620.
- [91] JOBIN, M.-L., AND ALVES, I. D. Label-free quantification of cell-penetrating peptide translocation into liposomes. *Analytical Methods* 8, 23 (2016), 4608–4616.
- [92] JOHNSEN, K. B., GUDBERGSSON, J. M., ANDRESEN, T. L., AND SIMONSEN, J. B. What is the blood concentration of extracellular vesicles? implications for the use of



- extracellular vesicles as blood-borne biomarkers of cancer. *Biochimica et Biophysica Acta (BBA)-Reviews on Cancer* 1871, 1 (2019), 109–116.
- [93] JOHNSON, B. E., MAZOR, T., HONG, C., BARNES, M., AIHARA, K., MCLEAN, C. Y., FOUSE, S. D., YAMAMOTO, S., UEDA, H., TATSUNO, K., ET AL. Mutational analysis reveals the origin and therapy-driven evolution of recurrent glioma. *Science* 343, 6167 (2014), 189–193.
- [94] KAMPEN, N. Stochastic processes in physics and chemistry. elsevier, 2007.
- [95] KAMTEKAR, S., BERMAN, A. J., WANG, J., LÁZARO, J. M., DE VEGA, M., BLANCO, L., SALAS, M., AND STEITZ, T. A. Insights into strand displacement and processivity from the crystal structure of the protein-primed dna polymerase of bacteriophage  $\phi 29$ . *Molecular cell* 16, 4 (2004), 609–618.
- [96] KATSUDA, T., KOSAKA, N., TAKESHITA, F., AND OCHIYA, T. The therapeutic potential of mesenchymal stem cell-derived extracellular vesicles. *Proteomics* 13, 10-11 (2013), 1637–1653.
- [97] KERR, L. T., GUBBINS, L., GORZEL, K. W., SHARMA, S., KELL, M., MCCANN, A., AND HENNELLY, B. M. Raman spectroscopy and sers analysis of ovarian tumour derived exosomes (texs): a preliminary study. In *Biophotonics: Photonic Solutions for Better Health Care IV* (2014), vol. 9129, SPIE, pp. 482–490.
- [98] KIBRIA, G., RAMOS, E. K., LEE, K. E., BEDOYAN, S., HUANG, S., SAMAEKIA, R., ATHMAN, J. J., HARDING, C. V., LÖTVALL, J., HARRIS, L., ET AL. A rapid, automated surface protein profiling of single circulating exosomes in human blood. *Scientific reports* 6, 1 (2016), 36502.
- [99] KO, J., WANG, Y., SHENG, K., WEITZ, D. A., AND WEISSLEDER, R. Sequencing-based protein analysis of single extracellular vesicles. *ACS nano* 15, 3 (2021), 5631–5638.

- [100] KOJABAD, A. A., FARZANEHPOUR, M., GALEH, H. E. G., DOROSTKAR, R., JAFARPOUR, A., BOLANDIAN, M., AND NODOOSHAN, M. M. Droplet digital pcr of viral dna/rna, current progress, challenges, and future perspectives. *Journal of Medical Virology* 93, 7 (2021), 4182–4197.
- [101] KONRY, T., SMOLINA, I., YARMUSH, J. M., IRIMIA, D., AND YARMUSH, M. L. Ultrasensitive detection of low-abundance surface-marker protein using isothermal rolling circle amplification in a microfluidic nanoliter platform. *Small* 7, 3 (2011), 395–400.
- [102] KONTOPOULOU, E., STRACHAN, S., REINHARDT, K., KUNZ, F., WALTER, C., WALKENFORT, B., JASTROW, H., HASENBERG, M., GIEBEL, B., VON NEUHOFF, N., ET AL. Evaluation of dsdna from extracellular vesicles (evs) in pediatric aml diagnostics. *Annals of Hematology* 99 (2020), 459–475.
- [103] KÖRBER, V., YANG, J., BARAH, P., WU, Y., STICHEL, D., GU, Z., FLETCHER, M. N. C., JONES, D., HENTSCHEL, B., LAMSZUS, K., ET AL. Evolutionary trajectories of idhwt glioblastomas reveal a common path of early tumorigenesis instigated years ahead of initial diagnosis. *Cancer cell* 35, 4 (2019), 692–704.
- [104] KOTELEVETS, L., AND CHASTRE, E. Extracellular vesicles in colorectal cancer: From tumor growth and metastasis to biomarkers and nanomedications. *Cancers* 15, 4 (2023), 1107.
- [105] KOWAL, J., ARRAS, G., COLOMBO, M., JOUVE, M., MORATH, J. P., PRIMDAL-BENGTSON, B., DINGLI, F., LOEW, D., TKACH, M., AND THÉRY, C. Proteomic comparison defines novel markers to characterize heterogeneous populations of extracellular vesicle subtypes. *Proceedings of the National Academy of Sciences* 113, 8 (2016), E968–E977.
- [106] KRAMERS, H. A. Brownian motion in a field of force and the diffusion model of chemical reactions. *Physica* 7, 4 (1940), 284–304.

- [107] KRISHNAN, M. Electrostatic free energy for a confined nanoscale object in a fluid. *J. Chem. Phys.* 138 (2013), 114906.
- [108] KRISHNAN, M. Electrostatic free energy for a confined nanoscale object in a fluid. *The Journal of chemical physics* 138, 11 (2013), 114906.
- [109] KRISHNAN, M. A simple model for electrical charge in globular macromolecules and linear polyelectrolytes in solution. *J. Chem. Phys.* 146 (2017), 205101.
- [110] KRISHNAN, M., MOJARAD, N., KUKURA, P., AND SANDOGHDAR, V. Geometry-induced electrostatic trapping of nanometric objects in a fluid. *Nature* 467 (2010), 692–695.
- [111] KUATE, S., CINATL, J., DOERR, H. W., AND ÜBERLA, K. Exosomal vaccines containing the s protein of the sars coronavirus induce high levels of neutralizing antibodies. *Virology* 362, 1 (2007), 26–37.
- [112] KUSTANOVICH, A., SCHWARTZ, R., PERETZ, T., AND GRINSHPUN, A. Life and death of circulating cell-free dna. *Cancer biology & therapy* 20, 8 (2019), 1057–1067.
- [113] LANG, J. B., BUCK, M. C., RIVIÈRE, J., STAMBOULI, O., SACHENBACHER, K., CHOUDHARY, P., DIETZ, H., GIEBEL, B., BASSERMANN, F., OOSTENDORP, R. A., ET AL. Comparative analysis of extracellular vesicle isolation methods from human aml bone marrow cells and aml cell lines. *Frontiers in Oncology* 12 (2022).
- [114] LARA-VELAZQUEZ, M., AL-KHARBOOSH, R., JEANNERET, S., VAZQUEZ-RAMOS, C., MAHATO, D., TAVANAIEPOUR, D., RAHMATHULLA, G., AND QUINONES-HINOJOSA, A. Advances in brain tumor surgery for glioblastoma in adults. *Brain sciences* 7, 12 (2017), 166.
- [115] LAU, H. Y., AND BOTELLA, J. R. Advanced dna-based point-of-care diagnostic methods for plant diseases detection. *Frontiers in plant science* 8 (2017), 2016.

- [116] LEE, C., CARNEY, R. P., HAZARI, S., SMITH, Z. J., KNUDSON, A., ROBERTSON, C. S., LAM, K. S., AND WACHSMANN-HOGIU, S. 3d plasmonic nanobowl platform for the study of exosomes in solution. *Nanoscale* 7, 20 (2015), 9290–9297.
- [117] LEE, K., FRASER, K., GHADDAR, B., YANG, K., KIM, E., BALAJ, L., CHIOCCA, E. A., BREAKFIELD, X. O., LEE, H., AND WEISSLEDER, R. Multiplexed profiling of single extracellular vesicles. *ACS nano* 12, 1 (2018), 494–503.
- [118] LEE, K., SHAO, H., WEISSLEDER, R., AND LEE, H. Acoustic purification of extracellular microvesicles. *ACS nano* 9, 3 (2015), 2321–2327.
- [119] LEINS, A., RIVA, P., LINDSTEDT, R., DAVIDOFF, M. S., MEHRAEIN, P., AND WEIS, S. Expression of tenascin-c in various human brain tumors and its relevance for survival in patients with astrocytoma. *Cancer* 98, 11 (2003), 2430–2439.
- [120] LI, J.-W., SHI, D., WAN, X.-C., HU, J., SU, Y.-F., ZENG, Y.-P., HU, Z.-J., YU, B.-H., ZHANG, Q.-L., WEI, P., ET AL. Universal extracellular vesicles and pd-l1+ extracellular vesicles detected by single molecule array technology as circulating biomarkers for diffuse large b cell lymphoma. *Oncoimmunology* 10, 1 (2021), 1995166.
- [121] LI, M., YIN, F., SONG, L., MAO, X., LI, F., FAN, C., ZUO, X., AND XIA, Q. Nucleic acid tests for clinical translation. *Chemical Reviews* 121, 17 (2021), 10469–10558.
- [122] LIANG, C., ZHANG, L., LIAN, X., ZHU, T., ZHANG, Y., AND GU, N. Circulating exosomal socs2-as1 acts as a novel biomarker in predicting the diagnosis of coronary artery disease. *BioMed Research International* 2020 (2020).
- [123] LIGA, A., VLIEGENTHART, D. B., OOSTHUYZEN, W., DEAR, J. W., AND KERHOAS-KERSAUDY, M. Exosome isolation: a microfluidic road-map. *Lab-on-a-Chip* 15 (2015), 2388–2394.

- [124] LIN, Q., YE, X., HUANG, Z., YANG, B., FANG, X., CHEN, H., AND KONG, J. Graphene oxide-based suppression of nonspecificity in loop-mediated isothermal amplification enabling the sensitive detection of cyclooxygenase-2 mrna in colorectal cancer. *Analytical chemistry* 91, 24 (2019), 15694–15702.
- [125] LIU, C., XU, X., LI, B., SITU, B., PAN, W., HU, Y., AN, T., YAO, S., AND ZHENG, L. Single-exosome-counting immunoassays for cancer diagnostics. *Nano letters* 18, 7 (2018), 4226–4232.
- [126] LIU, C., YU, S., ZINN, K., WANG, J., ZHANG, L., JIA, Y., KAPPES, J. C., BARNES, S., KIMBERLY, R. P., GRIZZLE, W. E., ET AL. Murine mammary carcinoma exosomes promote tumor growth by suppression of nk cell function. *The Journal of Immunology* 176, 3 (2006), 1375–1385.
- [127] LIU, H., TIAN, Y., XUE, C., NIU, Q., CHEN, C., AND YAN, X. Analysis of extracellular vesicle dna at the single-vesicle level by nano-flow cytometry. *Journal of Extracellular Vesicles* 11, 4 (2022), e12206.
- [128] LIU, J., CHEN, Y., PEI, F., ZENG, C., YAO, Y., LIAO, W., AND ZHAO, Z. Extracellular vesicles in liquid biopsies: Potential for disease diagnosis. *BioMed Research International* 2021 (2021).
- [129] LIU, J., MAZZONE, P. J., CATA, J. P., KURZ, A., BAUER, M., MASCHA, E. J., AND SESSLER, D. I. Serum free fatty acid biomarkers of lung cancer. *Chest* 146, 3 (2014), 670–679.
- [130] LIU, Z., CAPALDI, X., ZENG, L., ZHANG, Y., REYES-LAMOTHE, R., AND REISNER, W. Confinement anisotropy drives polar organization of two dna molecules interacting in a nanoscale cavity. *Nature communications* 13, 1 (2022), 1–12.
- [131] LOEB, A. L., OVERBEEK, J. T. G., AND WIERSEMA, P. H. *The electrical double layer around a spherical colloidal particle*. MIT Press, Cambridge, 1961.

- [132] LONE, S. N., NISAR, S., MASOODI, T., SINGH, M., RIZWAN, A., HASHEM, S., EL-RIFAI, W., BEDOGNETTI, D., BATRA, S. K., HARIS, M., ET AL. Liquid biopsy: A step closer to transform diagnosis, prognosis and future of cancer treatments. *Molecular cancer* 21, 1 (2022), 1–22.
- [133] LOUIS, D. N., PERRY, A., REIFENBERGER, G., VON DEIMLING, A., FIGARELLA-BRANGER, D., CAVENEE, W. K., OHGAKI, H., WIESTLER, O. D., KLEIHUES, P., AND ELLISON, D. W. The 2016 world health organization classification of tumors of the central nervous system: a summary. *Acta neuropathologica* 131 (2016), 803–820.
- [134] LUO, P., MAO, K., XU, J., WU, F., WANG, X., WANG, S., ZHOU, M., DUAN, L., TAN, Q., MA, G., ET AL. Metabolic characteristics of large and small extracellular vesicles from pleural effusion reveal biomarker candidates for the diagnosis of tuberculosis and malignancy. *Journal of extracellular vesicles* 9, 1 (2020), 1790158.
- [135] MA, L., ZHU, S., TIAN, Y., ZHANG, W., WANG, S., CHEN, C., WU, L., AND YAN, X. Label-free analysis of single viruses with a resolution comparable to that of electron microscopy and the throughput of flow cytometry. *Angewandte Chemie International Edition* 55, 35 (2016), 10239–10243.
- [136] MAHSHID, S., AHAMED, M. J., BERARD, D., AMIN, S., SLADEK, R., LESLIE, S. R., AND REISNER, W. Development of a platform for single cell genomics using convex lens-induced confinement. *Lab-on-a-Chip* 15, 14 (2015), 3013–3020.
- [137] MAHSHID, S., LU, J., ABIDI, A. A., SLADEK, R., REISNER, W. W., AND AHAMED, M. J. Transverse dielectrophoretic-based dna nanoscale confinement. *Scientific reports* 8, 1 (2018), 1–12.
- [138] MALENICA, M., VUKOMANOVIĆ, M., KURTJAK, M., MASCIOTTI, V., DAL ZILIO, S., GRECO, S., LAZZARINO, M., KRUŠIĆ, V., PERČIĆ, M., JELOVICA BADOVINAC, I., ET AL. Perspectives of microscopy methods for morphology characterisation of extracellular vesicles from human biofluids. *Biomedicines* 9, 6 (2021), 603.

- [139] MAO, X. *Stochastic differential equations and applications*. Elsevier, 2007.
- [140] MARAGO, O. M., JONES, P. H., GUCCIARDI, P. G., VOLPE, G., AND FERRARI, A. C. Optical trapping and manipulation of nanostructures. *Nature nanotechnology* 8, 11 (2013), 807–819.
- [141] MARIE, R., PEDERSEN, J. N., MIR, K. U., BILENBERG, B., AND KRISTENSEN, A. Concentrating and labeling genomic dna in a nanofluidic array. *Nanoscale* 10, 3 (2018), 1376–1382.
- [142] MARTEL, R., SHEN, M. L., DECORWIN-MARTIN, P., DE ARAUJO, L. O. F., AND JUNCKER, D. Extracellular vesicle antibody microarray for multiplexed inner and outer protein analysis. *ACS sensors* (2022).
- [143] MARTINS, A. M., RAMOS, C. C., FREITAS, D., AND REIS, C. A. Glycosylation of cancer extracellular vesicles: Capture strategies, functional roles and potential clinical applications. *Cells* 10 (2021), 109.
- [144] MIN, S. K., KIM, W. Y., CHO, Y., AND KIM, K. S. Fast dna sequencing with a graphene-based nanochannel device. *Nature nanotechnology* 6, 3 (2011), 162–165.
- [145] MIOTKE, L., LAU, B. T., RUMMA, R. T., AND JI, H. P. High sensitivity detection and quantitation of dna copy number and single nucleotide variants with single color droplet digital pcr. *Analytical chemistry* 86, 5 (2014), 2618–2624.
- [146] MITRA, A., DEUTSCH, B., IGNATOVICH, F., DYKES, C., AND NOVOTNY, L. Nanofluidic detection of single viruses and nanoparticles. *ACS nano* 4, 3 (2010), 1305–1312.
- [147] MOJARAD, N., AND KRISHNAN, M. Measuring the size and charge of single nanoscale objects in solution using an electrostatic fluidic trap. *Nature Nanotechnology* 7 (2012), 448–452.

- [148] MONSERUD, J. H., AND SCHWARTZ, D. K. Mechanisms of surface-mediated dna hybridization. *Acs Nano* 8, 5 (2014), 4488–4499.
- [149] MORASSO, C., RICCIARDI, A., SPROVIERO, D., TRUFFI, M., ALBASINI, S., PICCOTTI, F., SOTTOTETTI, F., MOLLIKA, L., CEREDA, C., SORRENTINO, L., ET AL. Fast quantification of extracellular vesicles levels in early breast cancer patients by single molecule detection array (simoa). *Breast Cancer Research and Treatment* (2022), 1–10.
- [150] MULCAHY, L. A., PINK, R. C., AND CARTER, D. R. F. Routes and mechanisms of extracellular vesicle uptake. *Journal of Extracellular Vesicles* 3, 1 (2014), 24641.
- [151] NABHAN, J. F., HU, R., OH, R. S., COHEN, S. N., AND LU, Q. Formation and release of arrestin domain-containing protein 1-mediated microvesicles (armms) at plasma membrane by recruitment of tsg101 protein-graner2009proteomicgraner2009proteomic. *Proceedings of the National Academy of Sciences* 109, 11 (2012), 4146–4151.
- [152] NAKANO, I., GARNOER, D., MINATA, M., AND RAK, J. Extracellular vesicles in the biology of brain tumour stem cells – implications for inter-cellular communication, therapy and biomarker development. *Seminars in Cell and Developmental Biology* 40 (2015), 17–26.
- [153] NAROD, S. Tumour size predicts long-term survival among women with lymph node-positive breast cancer. *Current oncology* 19, 5 (2012), 249–253.
- [154] NARYZHNY, S., VOLNITSKIY, A., KOPYLOV, A., ZORINA, E., KAMYSHINSKY, R., BAIRAMUKOV, V., GARAIEVA, L., SHLIKHT, A., AND SHTAM, T. Proteome of glioblastoma-derived exosomes as a source of biomarkers. *Biomedicines* 8, 7 (2020), 216.



- [155] NEWMAN, J. Dynamic light scattering as a probe of superhelical dna–intercalating agent interaction. *Biopolymers: Original Research on Biomolecules* 23, 6 (1984), 1113–1119.
- [156] NEWTON, C. R., GRAHAM, A., AND ELLISON, J. S. *PcR*. BIOS Scientific Publishers Oxford, UK, 1997.
- [157] NORDIN, J. Z., LEE, Y., VADER, P., MÄGER, I., JOHANSSON, H. J., HEUSER-MANN, W., WIKLANDER, O. P., HÄLLBRINK, M., SEOW, Y., BULTEMA, J. J., ET AL. Ultrafiltration with size-exclusion liquid chromatography for high yield isolation of extracellular vesicles preserving intact biophysical and functional properties. *Nanomedicine: Nanotechnology, Biology and Medicine* 11, 4 (2015), 879–883.
- [158] NORMAN, M., TER-OVANESYAN, D., TRIEU, W., LAZAROVITS, R., KOWAL, E. J., LEE, J. H., CHEN-PLOTKIN, A. S., REGEV, A., CHURCH, G. M., AND WALT, D. R. L1cam is not associated with extracellular vesicles in human cerebrospinal fluid or plasma. *Nature methods* 18, 6 (2021), 631–634.
- [159] NØRØXE, D. S., POULSEN, H. S., AND LASSEN, U. Hallmarks of glioblastoma: a systematic review. *ESMO open* 1, 6 (2016), e000144.
- [160] NOTOMI, T., OKAYAMA, H., MASUBUCHI, H., YONEKAWA, T., WATANABE, K., AMINO, N., AND HASE, T. Loop-mediated isothermal amplification of dna. *Nucleic acids research* 28, 12 (2000), e63–e63.
- [161] OLIVEIRA-RODRÍGUEZ, M., LÓPEZ-COBO, S., REYBURN, H. T., COSTA-GARCÍA, A., LÓPEZ-MARTÍN, S., YÁÑEZ-MÓ, M., CERNUDA-MOROLLON, E., PASCHEN, A., VALES-GOMEZ, M., AND BLANCO-LÓPEZ, M. C. Development of a rapid lateral flow immunoassay test for detection of exosomes previously enriched from cell culture medium and body fluids. *Journal of extracellular vesicles* 5, 1 (2016), 31803.
- [162] OSTROM, Q. T., PRICE, M., NEFF, C., CIOFFI, G., WAITE, K. A., KRUCHKO, C., AND BARNHOLTZ-SLOAN, J. S. Cbtrus statistical report: Primary brain and other

- central nervous system tumors diagnosed in the united states in 2015–2019. *Neuro-oncology* 24, Supplement.5 (2022), v1–v95.
- [163] ÖZ, R., SRIRAM, K., AND WESTERLUND, F. A nanofluidic device for real-time visualization of dna–protein interactions on the single dna molecule level. *Nanoscale* 11, 4 (2019), 2071–2078.
- [164] O’BRIEN, K., BREYNE, K., UGHETTO, S., LAURENT, L. C., AND BREAKEYFIELD, X. O. Rna delivery by extracellular vesicles in mammalian cells and its applications. *Nature reviews Molecular cell biology* 21, 10 (2020), 585–606.
- [165] PARK, S.-J., AND SEO, M.-K. *Interface science and composites*, vol. 18. Academic Press, 2011.
- [166] PENDERS, J., NAGELKERKE, A., CUNNANE, E. M., PEDERSEN, S. V., PENCE, I. J., COOMBES, R. C., AND STEVENS, M. M. Single particle automated raman trapping analysis of breast cancer cell-derived extracellular vesicles as cancer biomarkers. *ACS nano* 15, 11 (2021), 18192–18205.
- [167] PENDERS, J., PENCE, I. J., HORGAN, C. C., BERGHOLT, M. S., WOOD, C. S., NAEGER, A., KAUSCHER, U., NAGELKERKE, A., AND STEVENS, M. M. Single particle automated raman trapping analysis. *Nature communications* 9, 1 (2018), 1–11.
- [168] PERKINS, G., LU, H., GARLAN, F., AND TALY, V. Droplet-based digital pcr: application in cancer research. *Advances in clinical chemistry* 79 (2017), 43–91.
- [169] PERSSON, F., AND TEGENFELDT, J. O. Dna in nanochannels—directly visualizing genomic information. *Chemical Society Reviews* 39, 3 (2010), 985–999.
- [170] PERSSON, F., UTKO, P., REISNER, W., LARSEN, N. B., AND KRISTENSEN, A. Confinement spectroscopy: probing single dna molecules with tapered nanochannels. *Nano letters* 9, 4 (2009), 1382–1385.

- [171] PFRIEGER, F. W., AND VITALE, N. Cholesterol and the journey of extracellular vesicles. *Journal of Lipid Research* 59, 12 (2018), 2255–2261.
- [172] PIETRAS, A., KATZ, A. M., EKSTRÖM, E. J., WEE, B., HALLIDAY, J. J., PITTER, K. L., WERBECK, J. L., AMANKULOR, N. M., HUSE, J. T., AND HOLLAND, E. C. Osteopontin-cd44 signaling in the glioma perivascular niche enhances cancer stem cell phenotypes and promotes aggressive tumor growth. *Cell stem cell* 14, 3 (2014), 357–369.
- [173] PIZZINAT, N., ONG-MEANG, V., BOURGAILH-TORTOSA, F., BLANZAT, M., PERQUIS, L., CUSSAC, D., PARINI, A., AND POINSOT, V. Extracellular vesicles of mscs and cardiomyoblasts are vehicles for lipid mediators. *Biochimie* 178 (2020), 69–80.
- [174] QI, Y., ZENG, L., KHORSHID, A., HILL, R. J., AND REISNER, W. W. Compression of nanoslit confined polymer solutions. *Macromolecules* 51, 2 (2018), 617–625.
- [175] RAIBORG, C., AND STENMARK, H. The esrt machinery in endosomal sorting of ubiquitylated membrane proteins. *Nature* 458, 7237 (2009), 445–452.
- [176] RAPOSO, G., AND STAHL, P. D. Extracellular vesicles: a new communication paradigm? *Nature Reviews Molecular Cell Biology* 20, 9 (2019), 509–510.
- [177] RAPOSO, G., AND STOORVOGEL, W. Extracellular vesicles: exosomes, microvesicles, and friends. *Journal of Cell Biology* 200, 4 (2013), 373–383.
- [178] RAWAT, N., AND BISWAS, P. Size, shape, and flexibility of proteins and dna. *The Journal of chemical physics* 131, 16 (2009), 10B616.
- [179] REED, T., SCHOREY, J., AND D’SOUZA-SCHOREY, C. Tumor-derived extracellular vesicles: a means of co-opting macrophage polarization in the tumor microenvironment. *Frontiers in Cell and Developmental Biology* 9 (2021), 746432.

- [180] RIAZIFAR, M., PONE, E. J., LÖTVALL, J., AND ZHAO, W. Stem cell extracellular vesicles: extended messages of regeneration. *Annual review of pharmacology and toxicology* 57 (2017), 125–154.
- [181] RIDOLFI, A., BRUCALE, M., MONTIS, C., CASELLI, L., PAOLINI, L., BORUP, A., BOYSEN, A. T., LORIA, F., VAN HERWIJNEN, M. J., KLEINJAN, M., ET AL. Afm-based high-throughput nanomechanical screening of single extracellular vesicles. *Analytical chemistry* 92, 15 (2020), 10274–10282.
- [182] RIELY, G. J., MARKS, J., AND PAO, W. Kras mutations in non-small cell lung cancer. *Proceedings of the American Thoracic Society* 6, 2 (2009), 201–205.
- [183] RISSIN, D. M., KAN, C. W., CAMPBELL, T. G., HOWES, S. C., FOURNIER, D. R., SONG, L., PIECH, T., PATEL, P. P., CHANG, L., RIVNAK, A. J., ET AL. Single-molecule enzyme-linked immunosorbent assay detects serum proteins at subfemtomolar concentrations. *Nature biotechnology* 28, 6 (2010), 595–599.
- [184] RUGGERI, F., AND KRISHNAN, M. Lattice diffusion of a single molecule in solution. *Physical Review E* 96, 6 (2017), 062406.
- [185] RUGGERI, F., AND KRISHNAN, M. Entropic trapping of a singly charged molecule in solution. *Nano Letters* 18, 6 (2018), 3773–3779.
- [186] RUGGERI, F., AND KRISHNAN, M. Spectrally resolved single-molecule electrometry. *J. Chem. Phys.* 148 (2018), 123307.
- [187] RUGGERI, F., ZOSEL, F., MUTTER, N., RÓŻYCKA, M., WOJTAS, M., OŻYHAR, A., SCHULER, B., AND KRISHNAN, M. Single-molecule electrometry. *Nature Nanotechnology* 12, 5 (2017), 488–495.
- [188] RYE, H. S., YUE, S., WEMMER, D. E., QUESADA, M. A., HAUGLAND, R. P., MATHIES, R. A., AND GLAZER, A. N. Stable fluorescent complexes of double-stranded

- dna with bis-intercalating asymmetric cyanine dyes: properties and applications. *Nucleic acids research* 20, 11 (1992), 2803–2812.
- [189] SANDERSON, R. D., BANDARI, S. K., AND VLODAVSKY, I. Proteases and glycosidases on the surface of exosomes: Newly discovered mechanisms for extracellular remodeling. *Matrix biology* 75 (2019), 160–169.
  - [190] SAUTER, E. R. Exosomes in blood and cancer. *Translational Cancer Research* 6 (2017), S1316–S1320.
  - [191] SAWNTON, C., PUSZTAI, L., AND FISHER, R. Cancer heterogeneity: implications for targeted therapeutics. *British Journal of Cancer* 108 (2013), 479–485.
  - [192] SCHLAEPFER, I. R., NAMBIAR, D. K., RAMTEKE, A., KUMAR, R., DHAR, D., AGARWAL, C., BERGMAN, B., GRANER, M., MARONI, P., SINGH, R. P., ET AL. Hypoxia induces triglycerides accumulation in prostate cancer cells and extracellular vesicles supporting growth and invasiveness following reoxygenation. *Oncotarget* 6, 26 (2015), 22836.
  - [193] SHAO, H., CHUNG, J., BALAJ, L., CHAREST, A., BIGNER, D. D., CARTER, B. S., HOCHBERG, F. H., BREAKFIELD, X. O., WEISSLEDER, R., AND LEE, H. Protein typing of circulating microvesicles allows real-time monitoring of glioblastoma therapy. *Nature medicine* 18, 12 (2012), 1835–1840.
  - [194] SHAO, H., IM, H., CASTRO, C. M., BREAKFIELD, X., WEISSLEDER, R., AND LEE, H. New technologies for analysis of extracellular vesicles. *Chemical reviews* 118, 4 (2018), 1917–1950.
  - [195] SHAYEGAN, M., TAHVILDARI, R., METERA, K., KISLEY, L., MICHNICK, S. W., AND LESLIE, S. R. Probing inhomogeneous diffusion in the microenvironments of phase-separated polymers under confinement. *Journal of the American Chemical Society* 141, 19 (2019), 7751–7757.

- [196] SHAYEGAN, M., TAHVILDARI, R., METERA, K., KISLEY, L., MICHNICK, S. W., AND SABRINA, L. R. Probing inhomogeneous diffusion in the microenvironments of phase-separated polymers under confinement. *J. Am. Chem. Soc.* 141 (2019), 7751–7757.
- [197] SHEN, F., DU, W., KREUTZ, J. E., FOK, A., AND ISMAGILOV, R. F. Digital pcr on a slipchip. *Lab on a Chip* 10, 20 (2010), 2666–2672.
- [198] SHEN, W., GUO, K., ADKINS, G. B., JIANG, Q., LIU, Y., SEDANO, S., DUAN, Y., YAN, W., WANG, S. E., BERGERSEN, K., ET AL. A single extracellular vesicle (ev) flow cytometry approach to reveal ev heterogeneity. *Angewandte Chemie International Edition* 57, 48 (2018), 15675–15680.
- [199] SHI, D., HUANG, J., CHUAI, Z., CHEN, D., ZHU, X., WANG, H., PENG, J., WU, H., HUANG, Q., AND FU, W. Isothermal and rapid detection of pathogenic microorganisms using a nano-rolling circle amplification-surface plasmon resonance biosensor. *Biosensors and Bioelectronics* 62 (2014), 280–287.
- [200] SHON, M. J., AND COHEN, A. E. Mass action at the single-molecule level. *Journal of the American Chemical Society* 134, 35 (2012), 14618–14623.
- [201] SHON, M. J., AND COHEN, A. E. Mass action at the single-molecule level. *Journal of the American Chemical Society* 134, 35 (aug 2012), 14618–14623.
- [202] SIDERIS, M., EMIN, E. I., ABDULLAH, Z., HANRAHAN, J., STEFATOU, K. M., SEVAS, V., EMIN, E., HOLLINGWORTH, T., ODEJINMI, F., PAPAGRIGORIADIS, S., ET AL. The role of kras in endometrial cancer: a mini-review. *Anticancer Research* 39, 2 (2019), 533–539.
- [203] SIRAVEGNA, G., MARSONI, S., SIENA, S., AND BARDELLI, A. Integrating liquid biopsies into the management of cancer. *Seminars in Cell and Developmental Biology* 14 (2017), 531–548.

- [204] SITAR, S., KEJZAR, A., PAHOVNIK, D., KOGEJ, K., TUSEK-ZNIDARIC, M., LENASSI, M., AND ZAGAR, E. Size characterization and quantification of exosomes by asymmetrical-flow field-flow fractionation. *Analytical chemistry* 87, 18 (2015), 9225–9233.
- [205] SKAUG, M. J., SCHWEMMER, C., FRINGES, S., RAWLINGS, C. D., AND KNOLL, A. W. Nanofluidic rocking brownian motors. *Science* 359, 6383 (2018), 1505–1508.
- [206] SMITH, J. T., WUNSCH, B. H., DOGRA, N., AHSEN, M. E., LEE, K., YADAV, K. K., WEIL, R., PEREIRA, M. A., PATEL, J. V., DUCH, E. A., ET AL. Integrated nanoscale deterministic lateral displacement arrays for separation of extracellular vesicles from clinically-relevant volumes of biological samples. *Lab on a Chip* 18, 24 (2018), 3913–3925.
- [207] SOLASSOL, J., RAMOS, J., CRAPEZ, E., SAIFI, M., MANGÉ, A., VIANÈS, E., LAMY, P.-J., COSTES, V., AND MAUDELONDE, T. Kras mutation detection in paired frozen and formalin-fixed paraffin-embedded (ffpe) colorectal cancer tissues. *International journal of molecular sciences* 12, 5 (2011), 3191–3204.
- [208] SPINELLI, C., MONTERMINI, L., MEEHAN, B., BRISSON, A. R., TAN, S., CHOI, D., NAKANO, I., AND RAK, J. Molecular subtypes and differentiation programmes of glioma stem cells as determinants of extracellular vesicle profiles and endothelial cell-stimulating activities. *J. of Extracellular Vesicles* 7 (2018), 1490144.
- [209] SPITZBERG, J. D., FERGUSON, S., YANG, K. S., PETERSON, H. M., CARLSON, J. C., AND WEISSLEDER, R. Multiplexed analysis of ev reveals specific biomarker composition with diagnostic impact. *Nature Communications* 14, 1 (2023), 1239.
- [210] STAHL, P. D., AND RAPOSO, G. Extracellular vesicles: Exosomes and microvesicles, integrators of homeostasis. *Physiology* 34 (2019), 169–177.

- [211] STATISTICS, J. C. Canadian cancer statistics advisory committee in collaboration with the canadian cancer society, statistics canada and the public health agency of canada. *Canadian Cancer Statistics* ((accessed February 2023)).
- [212] STEWART, M. L., TAMAYO, P., WILSON, A. J., WANG, S., CHANG, Y. M., KIM, J. W., KHABELE, D., SHAMJI, A. F., AND SCHREIBER, S. L. Kras genomic status predicts the sensitivity of ovarian cancer cells to decitabine. *Cancer research* 75, 14 (2015), 2897–2906.
- [213] STICHEL, D., EBRAHIMI, A., REUSS, D., SCHRIMPF, D., ONO, T., SHIRAHATA, M., REIFENBERGER, G., WELLER, M., HÄNGGI, D., WICK, W., ET AL. Distribution of egfr amplification, combined chromosome 7 gain and chromosome 10 loss, and tert promoter mutation in brain tumors and their potential for the reclassification of idh wt astrocytoma to glioblastoma. *Acta neuropathologica* 136 (2018), 793–803.
- [214] STREMERSCHE, S., MARRO, M., PINCHASIK, B.-E., BAATSEN, P., HENDRIX, A., DE SMEDT, S. C., LOZA-ALVAREZ, P., SKIRTACH, A. G., RAEMDONCK, K., AND BRAECKMANS, K. Identification of individual exosome-like vesicles by surface enhanced raman spectroscopy. *Small* 12, 24 (2016), 3292–3301.
- [215] STUPP, R., MASON, W. P., VAN DEN BENT, M. J., WELLER, M., FISHER, B., TAPHOORN, M. J., BELANGER, K., BRANDES, A. A., MAROSI, C., BOGDAHN, U., ET AL. Radiotherapy plus concomitant and adjuvant temozolomide for glioblastoma. *New England journal of medicine* 352, 10 (2005), 987–996.
- [216] SUZUKI, H., AOKI, K., CHIBA, K., SATO, Y., SHIOZAWA, Y., SHIRAISHI, Y., SHIMAMURA, T., NIIDA, A., MOTOMURA, K., OHKA, F., ET AL. Mutational landscape and clonal architecture in grade ii and iii gliomas. *Nature genetics* 47, 5 (2015), 458–468.
- [217] SZEMES, M., BONANTS, P., DE WEERDT, M., BANER, J., LANDEGREN, U., AND SCHOEN, C. D. Diagnostic application of padlock probes—multiplex detection of



- plant pathogens using universal microarrays. *Nucleic acids research* 33, 8 (2005), e70–e70.
- [218] TAKAHASHI, H., YAMAZAKI, H., AKANUMA, S., KANAHARA, H., SAITO, T., CHIMURO, T., KOBAYASHI, T., OHTANI, T., YAMAMOTO, K., SUGIYAMA, S., ET AL. Preparation of phi29 dna polymerase free of amplifiable dna using ethidium monoazide, an ultraviolet-free light-emitting diode lamp and trehalose. *PLoS One* 9, 2 (2014), e82624.
- [219] TANYERI, M., AND SCHROEDER, C. M. Manipulation and confinement of single particles using fluid flow. *Nano letters* 13, 6 (2013), 2357–2364.
- [220] TATISCHEFF, I., LARQUET, E., FALCÓN-PÉREZ, J. M., TURPIN, P.-Y., AND KRUGLIK, S. G. Fast characterisation of cell-derived extracellular vesicles by nanoparticles tracking analysis, cryo-electron microscopy, and raman tweezers microspectroscopy. *Journal of extracellular vesicles* 1, 1 (2012), 19179.
- [221] TENG, F., AND FUSSENEGGER, M. Shedding light on extracellular vesicle biogenesis and bioengineering. *Advanced Science* 8, 1 (2021), 2003505.
- [222] TER-OVANESYAN, D., NORMAN, M., LAZAROVITS, R., TRIEU, W., LEE, J.-H., CHURCH, G. M., AND WALT, D. R. Framework for rapid comparison of extracellular vesicle isolation methods. *Elife* 10 (2021), e70725.
- [223] THIOMBANE, N. K., COUTIN, N., BERARD, D., TAHVILDARI, R., LESLIE, S., AND NISLOW, C. Single-cell analysis for drug development using convex lens-induced confinement imaging. *BioTechniques* 67, 5 (2019), 210–217.
- [224] THOMAS, L. M., AND SALTER, R. D. Activation of macrophages by p2x7-induced microvesicles from myeloid cells is mediated by phospholipids and is partially dependent on tlr4. *The Journal of Immunology* 185, 6 (2010), 3740–3749.

- [225] THOMPSON, A. G., GRAY, E., HEMAN-ACKAH, S. M., MÄGER, I., TALBOT, K., ANDALOUSSI, S. E., WOOD, M. J., AND TURNER, M. R. Extracellular vesicles in neurodegenerative disease—pathogenesis to biomarkers. *Nature Reviews Neurology* 12, 6 (2016), 346–357.
- [226] TIAN, Q., HE, C., LIU, G., ZHAO, Y., HUI, L., MU, Y., TANG, R., LUO, Y., ZHENG, S., AND WANG, B. Nanoparticle counting by microscopic digital detection: selective quantitative analysis of exosomes via surface-anchored nucleic acid amplification. *Analytical chemistry* 90, 11 (2018), 6556–6562.
- [227] TIRINATO, L., GENTILE, F., DI MASCOLO, D., COLUCCIO, M., DAS, G., LIBERALE, C., PULLANO, S., PEROZZIELLO, G., FRANCARDI, M., ACCARDO, A., ET AL. Sens analysis on exosomes using super-hydrophobic surfaces. *Microelectronic Engineering* 97 (2012), 337–340.
- [228] TORCHILIN, V. P. Recent advances with liposomes as pharmaceutical carriers. *Nature reviews Drug discovery* 4, 2 (2005), 145–160.
- [229] TRAJKOVIC, K., HSU, C., CHIANTIA, S., RAJENDRAN, L., WENZEL, D., WIELAND, F., SCHWILLE, P., BRUGGER, B., AND SIMONS, M. Ceramide triggers budding of exosome vesicles into multivesicular endosomes. *Science* 319, 5867 (2008), 1244–1247.
- [230] UNGER, M. A., CHOU, H.-P., THORSEN, T., SCHERER, A., AND QUAKE, S. R. Monolithic microfabricated valves and pumps by multilayer soft lithography. *science* 288, 5463 (2000), 113–116.
- [231] VAN DER POL, E., BÖING, A. N., HARRISON, P., STURK, A., AND NIEUWLAND, R. Classification, functions, and clinical relevance of extracellular vesicles. *Pharmacological Reviews* 64 (2012), 676–705.
- [232] VAN DER POL, E., COUMANS, F., GROOTEMAAT, A., GARDINER, C., SARGENT, I. L., HARRISON, P., STURK, A., VAN LEEUWEN, T., AND NIEUWLAND, R. Particle

- size distribution of exosomes and microvesicles determined by transmission electron microscopy, flow cytometry, nanoparticle tracking analysis, and resistive pulse sensing. *Journal of Thrombosis and Haemostasis* 12, 7 (2014), 1182–1192.
- [233] VAN NIEL, G. Shedding light on the cell biology of extracellular vesicles. *Nature Reviews Molecular Cell Biology* 19 (2018), 213–228.
- [234] VAN NIEL, G., CARTER, D. R., CLAYTON, A., LAMBERT, D. W., RAPOSO, G., AND VADER, P. Challenges and directions in studying cell–cell communication by extracellular vesicles. *Nature Reviews Molecular Cell Biology* 23, 5 (2022), 369–382.
- [235] VAN NIEL, G., D’ANGELO, G., AND RAPOSO, G. Shedding light on the cell biology of extracellular vesicles. *Nature reviews Molecular cell biology* 19, 4 (2018), 213–228.
- [236] VENKATESAN, B. M., AND BASHIR, R. *Solid-state nanopore sensors for nucleic acid analysis*. Springer, 2011.
- [237] VINCI, M., BURFORD, A., MOLINARI, V., KESSLER, K., POPOV, S., CLARKE, M., TAYLOR, K. R., PEMBERTON, H. N., LORD, C. J., GUTTERIDGE, A., ET AL. Functional diversity and cooperativity between subclonal populations of pediatric glioblastoma and diffuse intrinsic pontine glioma cells. *Nature medicine* 24, 8 (2018), 1204–1215.
- [238] VOGEL, R., COUMANS, F. A., MALTESEN, R. G., BÖING, A. N., BONNINGTON, K. E., BROEKMAN, M. L., BROOM, M. F., BUZÁS, E. I., CHRISTIANSEN, G., HAJJI, N., ET AL. A standardized method to determine the concentration of extracellular vesicles using tunable resistive pulse sensing. *Journal of extracellular vesicles* 5, 1 (2016), 31242.
- [239] VORSELEN, D., MACKINTOSH, F. C., ROOS, W. H., AND WUITE, G. J. Competition between bending and internal pressure governs the mechanics of fluid nanovesicles. *ACS nano* 11, 3 (2017), 2628–2636.

- [240] VORSELEN, D., VAN DOMMELEN, S. M., SORKIN, R., PIONTEK, M. C., SCHILLER, J., DÖPP, S. T., KOOIJMANS, S. A., VAN OIRSCHOT, B. A., VERSLUIJS, B. A., BIERINGS, M. B., ET AL. The fluid membrane determines mechanics of erythrocyte extracellular vesicles and is softened in hereditary spherocytosis. *Nature communications* 9, 1 (2018), 4960.
- [241] WALKER, S., BUSATTO, S., PHAM, A., TIAN, M., SUH, A., CARSON, K., QUINTERO, A., LAFRENCE, M., MALIK, H., SANTANA, M. X., ET AL. Extracellular vesicle-based drug delivery systems for cancer treatment. *Theranostics* 9, 26 (2019), 8001.
- [242] WANG, C., BRUCE, R. L., DUCH, E. A., PATEL, J. V., SMITH, J. T., ASTIER, Y., WUNSCH, B. H., MESHRAM, S., GALAN, A., SCERBO, C., ET AL. Hydrodynamics of diamond-shaped gradient nanopillar arrays for effective dna translocation into nanochannels. *ACS nano* 9, 2 (2015), 1206–1218.
- [243] WANG, S., ZHANG, L., WAN, S., CANSIZ, S., CUI, C., LIU, Y., CAI, R., HONG, C., TENG, I.-T., SHI, M., ET AL. Aptasensor with expanded nucleotide using dna nanotetrahedra for electrochemical detection of cancerous exosomes. *ACS nano* 11, 4 (2017), 3943–3949.
- [244] WATERS, A. M., AND DER, C. J. Kras: the critical driver and therapeutic target for pancreatic cancer. *Cold Spring Harbor perspectives in medicine* 8, 9 (2018), a031435.
- [245] WEI, P., WU, F., KANG, B., SUN, X., HESKIA, F., PACHOT, A., LIANG, J., AND LI, D. Plasma extracellular vesicles detected by single molecule array technology as a liquid biopsy for colorectal cancer. *Journal of extracellular vesicles* 9, 1 (2020), 1809765.
- [246] WESTCOTT, P. M., AND TO, M. D. The genetics and biology of kras in lung cancer. *Chinese journal of cancer* 32, 2 (2013), 63.

- [247] WIKRAMARATNA, P. S., PATON, R. S., GHAFARI, M., AND LOURENÇO, J. Estimating the false-negative test probability of sars-cov-2 by rt-pcr. *Eurosurveillance* 25, 50 (2020), 2000568.
- [248] WILLIAMS, C., PAZOS, R., ROYO, F., GONZÁLEZ, E., ROURA-FERRER, M., MARTINEZ, A., GAMIZ, J., REICHARDT, N.-C., AND FALCÓN-PÉREZ, J. M. Assessing the role of surface glycans of extracellular vesicles on cellular uptake. *Scientific Reports* 9, 1 (2019), 1–14.
- [249] WITWER, K. W., AND THÉRY, C. Extracellular vesicles or exosomes? on primacy, precision, and popularity influencing a choice of nomenclature, 2019.
- [250] WORTZEL, I., DROR, S., KENIFIC, C. M., AND LYDEN, D. Exosome-mediated metastasis: communication from a distance. *Developmental cell* 49, 3 (2019), 347–360.
- [251] WU, D., YAN, J., SHEN, X., SUN, Y., THULIN, M., CAI, Y., WIK, L., SHEN, Q., OELRICH, J., QIAN, X., ET AL. Profiling surface proteins on individual exosomes using a proximity barcoding assay. *Nature communications* 10, 1 (2019), 3854.
- [252] WU, F., GU, Y., KANG, B., HESKIA, F., PACHOT, A., BONNEVILLE, M., WEI, P., AND LIANG, J. Pd-l1 detection on circulating tumor-derived extracellular vesicles (t-evs) from patients with lung cancer. *Translational Lung Cancer Research* 10, 6 (2021), 2441.
- [253] WUNSCH, B. H., SMITH, J. T., GIFFORD, S. M., WANG, C., BRINK, M., BRUCE, R. L., AUSTIN, R. H., STOLOVITZKY, G., AND ASTIER, Y. Nanoscale lateral displacement arrays for the separation of exosomes and colloids down to 20 nm. *Nature nanotechnology* 11, 11 (2016), 936–940.
- [254] XIA, Y., LIU, M., WANG, L., YAN, A., HE, W., CHEN, M., LAN, J., XU, J., GUAN, L., AND CHEN, J. A visible and colorimetric aptasensor based on dna-capped

- single-walled carbon nanotubes for detection of exosomes. *Biosensors and Bioelectronics* 92 (2017), 8–15.
- [255] XU, L., DUAN, J., CHEN, J., DING, S., AND CHENG, W. Recent advances in rolling circle amplification-based biosensing strategies-a review. *Analytica chimica acta* 1148 (2021), 238187.
- [256] XU, R., RAI, A., CHEN, M., SUWAKULSIRI, W., GREENING, D. W., AND SIMPSON, R. J. Extracellular vesicles in cancer—implications for future improvements in cancer care. *Nature reviews Clinical oncology* 15, 10 (2018), 617–638.
- [257] YADAV, S., BORACHEK, K., ISLAM, M. N., LOBB, R., MÖLLER, A., HILL, M. M., HOSSAIN, M. S. A., NGUYEN, N.-T., AND SHIDDIKY, M. J. An electrochemical method for the detection of disease-specific exosomes. *ChemElectroChem* 4, 4 (2017), 967–971.
- [258] YAMAMOTO, K., MORIKAWA, K., IMANAKA, H., IMAMURA, K., AND KITAMORI, T. Picoliter enzyme reactor on a nanofluidic device exceeding the bulk reaction rate. *Analyst* 145, 17 (2020), 5801–5807.
- [259] YAN, Z., DUTTA, S., LIU, Z., YU, X., MESGARZADEH, N., JI, F., BITAN, G., AND XIE, Y.-H. A label-free platform for identification of exosomes from different sources. *ACS sensors* 4, 2 (2019), 488–497.
- [260] YANG, S., CHE, S. P., KURYWCHAK, P., TAVORMINA, J. L., GANSMO, L. B., CORREA DE SAMPAIO, P., TACHEZY, M., BOCKHORN, M., GEBAUER, F., HALTOM, A. R., ET AL. Detection of mutant kras and tp53 dna in circulating exosomes from healthy individuals and patients with pancreatic cancer. *Cancer biology & therapy* 18, 3 (2017), 158–165.
- [261] YANG, Z., ATIYAS, Y., SHEN, H., SIEDLIK, M. J., WU, J., BEARD, K., FONAR, G., DOLLE, J. P., SMITH, D. H., EBERWINE, J. H., ET AL. Ultrasensitive single

- extracellular vesicle detection using high throughput droplet digital enzyme-linked immunosorbent assay. *Nano letters* 22, 11 (2022), 4315–4324.
- [262] YE, S., LI, W., WANG, H., ZHU, L., WANG, C., AND YANG, Y. Quantitative nanomechanical analysis of small extracellular vesicles for tumor malignancy indication. *Advanced Science* 8, 18 (2021), 2100825.
- [263] ZENG, Z., LI, Y., PAN, Y., LAN, X., SONG, F., SUN, J., ZHOU, K., LIU, X., REN, X., WANG, F., ET AL. Cancer-derived exosomal mir-25-3p promotes pre-metastatic niche formation by inducing vascular permeability and angiogenesis. *Nature communications* 9, 1 (2018), 5395.
- [264] ZHAI, H., ACHARYA, S., GRAVANIS, I., MEHMOOD, S., SEIDMAN, R. J., SHROYER, K. R., HAJJAR, K. A., AND TSIRKA, S. E. Annexin a2 promotes glioma cell invasion and tumor progression. *Journal of Neuroscience* 31, 40 (2011), 14346–14360.
- [265] ZHANG, H., FREITAS, D., KIM, H. S., FABIJANIC, K., LI, Z., CHEN, H., MARK, M. T., MOLINA, H., MARTIN, A. B., BOJMAR, L., ET AL. Identification of distinct nanoparticles and subsets of extracellular vesicles by asymmetric flow field-flow fractionation. *Nature cell biology* 20, 3 (2018), 332–343.
- [266] ZHANG, H.-G., AND GRIZZLE, W. E. Exosomes and cancer: A newly described pathway of immune suppressionexosomes and cancer. *Clinical Cancer Research* 17, 5 (2011), 959–964.
- [267] ZHANG, P., HE, M., AND ZENG, Y. Ultrasensitive microfluidic analysis of circulating exosomes using a nanostructured graphene oxide/polydopamine coating. *Lab on a Chip* 16, 16 (2016), 3033–3042.
- [268] ZHANG, Q., JEPPESEN, D. K., HIGGINBOTHAM, J. N., FRANKLIN, J. L., AND COFFEY, R. J. Comprehensive isolation of extracellular vesicles and nanoparticles. *Nature Protocols* (2023), 1–26.

- [269] ZHAO, Y., CHEN, F., QIN, J., WEI, J., WU, W., AND ZHAO, Y. Engineered janus probes modulate nucleic acid amplification to expand the dynamic range for direct detection of viral genomes in one microliter crude serum samples. *Chemical science* 9, 2 (2018), 392–397.
- [270] ZHAO, Z., YANG, Y., ZENG, Y., AND HE, M. A microfluidic exosearch chip for multiplexed exosome detection towards blood-based ovarian cancer diagnosis. *Lab-on-a-Chip* 16 (2016), 489–496.
- [271] ZHEN, K., WEI, X., ZHI, Z., ZHANG, S., CUI, L., LI, Y., CHEN, X., YAO, J., AND ZHANG, H. Comparison of different isolation methods for plasma-derived extracellular vesicles in patients with hyperlipidemia. *Life* 12, 11 (2022), 1942.
- [272] ZHOU, Q., RAHIMIAN, A., SON, K., SHIN, D.-S., PATEL, T., AND REVZIN, A. Development of an aptasensor for electrochemical detection of exosomes. *Methods* 97 (2016), 88–93.
- [273] ZHOU, W., FONG, M. Y., MIN, Y., SOMLO, G., LIU, L., PALOMARES, M. R., YU, Y., CHOW, A., O’CONNOR, S. T. F., CHIN, A. R., ET AL. Cancer-secreted mir-105 destroys vascular endothelial barriers to promote metastasis. *Cancer cell* 25, 4 (2014), 501–515.
- [274] ZHU, S., MA, L., WANG, S., CHEN, C., ZHANG, W., YANG, L., HANG, W., NOLAN, J. P., WU, L., AND YAN, X. Light-scattering detection below the level of single fluorescent molecules for high-resolution characterization of functional nanoparticles. *ACS nano* 8, 10 (2014), 10998–11006.
- [275] ZIMMERMAN, B., KELLY, B., MCMILLAN, B. J., SEEGAR, T. C., DROR, R. O., KRUSE, A. C., AND BLACKLOW, S. C. Crystal structure of a full-length human tetraspanin reveals a cholesterol-binding pocket. *Cell* 167, 4 (2016), 1041–1051.



- [276] ZONG, S., WANG, L., CHEN, C., LU, J., ZHU, D., ZHANG, Y., WANG, Z., AND CUI, Y. Facile detection of tumor-derived exosomes using magnetic nanobeads and sers nanoprobe. *Analytical Methods* 8, 25 (2016), 5001–5008.